FINNISH METEOROLOGICAL INSTITUTE
CONTRIBUTIONS

NO. 136

ROLES OF SUDDEN STRATOSPHERIC WARMING EVENTS AND ENERGETIC PARTICLE PRECIPITATION IN POLAR MIDDLE ATMOSPHERE: ODD NITROGEN AND OZONE

Sanna-Mari Päivärinta

Department of Physics
Faculty of Science
University of Helsinki
Helsinki, Finland

ACADEMIC DISSERTATION in meteorology

To be presented, with the permission of the Faculty of Science of the University of Helsinki, for public criticism in Auditorium Physicum E204 (Gustaf Hällströmin katu 2b) on December 8th, 2017, at 12 o'clock noon.

Finnish Meteorological Institute
Helsinki, 2017

Supervisor	Dr. Pekka T. Verronen Earth Observation Finnish Meteorological Institute, Helsinki, Finland
Pre-examiners	Prof. Esa Kallio Department of Electronics and Nanoengineering Aalto University, Espoo, Finland
	Dr. Alain Hauchecorne Laboratoire Atmosphères, Milieux, Observations Spatiales French National Centre for Scientific Research, Guyancourt, France
Opponent	Dr. Hauke Schmidt The Atmosphere in the Earth System Max Planck Institute for Meteorology, Hamburg, Germany
Custos	Prof. Heikki Järvinen Department of Physics University of Helsinki, Helsinki, Finland

ISBN 978-952-336-029-7 (paperback)
ISBN 978-952-336-030-3 (PDF)
ISSN 0782-6117

Erweko
Helsinki, 2017

FINNISH METEOROLOGICAL INSTITUTE

Published by
Finnish Meteorological Institute
P.O. Box 503, (Erik Palménin aukio 1)
FIN-00101 Helsinki, Finland

Series title, number and report code of publication
Finnish Meteorological Institute
Contributions 136, FMI-CONT-136

Date
December 2017

Author
Sanna-Mari Päivärinta

Title
Roles of sudden stratospheric warming events and energetic particle precipitation in polar middle atmosphere: odd nitrogen and ozone

Abstract

Odd nitrogen (NO_x = N + NO + NO_2) in the polar regions is mainly produced in the upper atmosphere through ionization processes by solar extreme ultraviolet radiation, soft X-rays and high energy particles originating from the space. During periods of high geomagnetic activity, normally close to the solar maximum, energetic particle precipitation (EPP) provides an in-situ source of NO_x also in the middle atmosphere. Understanding the behaviour of NO_x in the middle atmosphere is of great importance due to its capability to act as a catalyst in chemical reaction cycles destroying ozone in the stratosphere. This work considers EPP in the form of solar proton events (SPEs).

Atmospheric dynamics play an important role in determining the distributions of long-lived trace gases in the middle atmosphere. The main loss mechanism for NO_x is photolysis at the upper stratospheric and mesospheric altitudes, leading to long photochemical lifetime of NO_x during the dark polar winter. NO_x in the middle atmosphere, also if produced in-situ due to SPEs, is therefore affected by atmospheric dynamics, and transported from the mesosphere-lower thermosphere (MLT) region down to the middle atmosphere. This descent phenomenon can be intensified in the aftermath of sudden stratospheric warmings (SSWs), which are dynamical phenomena able to affect a wide range of altitudes in the Northern polar region atmosphere. The enhanced downward transport of NO_x can thus strengthen the NO_x-ozone connection in the stratosphere.

In this work we used both space born observations from several satellite instruments and a chemistry transport model in the examination of the SSW and SPE caused effects in the stratosphere and mesosphere. The scientific objectives of this work were to find out the individual and combined effects of SSWs and SPEs on the NO_x and ozone balance in the Northern middle atmosphere, and assess the relative contributions of dynamics (SSWs) and in-situ production of NO_x (SPEs) on ozone in the stratosphere. The results showed dramatic increases in NO_x in the middle atmosphere, even by a factor of 50, following both periods of enhanced NO_x descent in connection with SSWs and in-situ production of NO_x due to SPEs. A clear long-term (order of months) decrease in stratospheric ozone (10-90 %), coinciding with the enhanced amounts of NO_x, was evident and affected mostly by dynamics in the upper stratosphere.

The results of this work emphasize the importance of in-situ production of NO_x (SPEs) on the ozone balance in the upper stratosphere, but also the key role of dynamics (SSWs) in transporting the SPE effect to even lower altitudes and its capability to strengthen the effect.

Publishing unit
Finnish Meteorological Institute, Earth Observation

Classification (UDC)
523.9
551.5
551.510.532
551.510.533

Keywords
stratosphere, mesosphere, sudden stratospheric warmings, energetic particle precipitation, solar proton events, odd nitrogen ozone

ISSN and series title
0782-6117 Finnish Meteorological Institute Contributions

ISBN
978-952-336-029-7 (paperback), 978-952-336-030-3 (pdf)

Language
English

Pages
156

ILMATIETEEN LAITOS

Julkaisija
Ilmatieteen laitos
PL 503, (Erik Palménin aukio 1)
00101 Helsinki

Julkaisun sarja, numero ja raporttikoodi
Finnish Meteorological Institute
Contributions 136, FMI-CONT-136

Julkaisuaika
Joulukuu 2017

Tekijä
Sanna-Mari Päivärinta

Nimike
Stratosfäärin äkillisten lämpenemisten ja hiukkaspresipitaation roolit polaarialueen keski-ilmakehässä: pariton typpi ja otsoni

Tiivistelmä

Paritonta typpeä (NO_x = N + NO + NO_2) syntyy napa-alueilla pääasiassa yläilmakehässä ultraviolettisäteilyn, röntgensäteilyn ja avaruudesta peräisin olevien suurienergisten hiukkasten aiheuttaman ionisaation seurauksena. Korkean geomagneettisen aktiivisuuden aikana, yleensä lähellä aurinkopilkkujakson maksimia, suurienergiset hiukkaset tuottavat NO_x -yhdisteitä suoraan keski-ilmakehässä. NO_x -yhdisteiden käyttäytymisen ymmärtäminen keski-ilmakehässä on ensiarvoisen tärkeää, koska NO_x -yhdisteet toimivat katalyytteinä kemiallisissa reaktiosykleissä otsonia tuhoten. Tämä väitöstyö keskittyy Auringosta tuleviin suurienergisiin protoneihin eli niin kutsuttuihin Auringon protonimyrskyihin (SPE).

Ilmakehän dynamiikka vaikuttaa pitkäikästen yhdisteiden pitoisuuksiin keski-ilmakehässä. NO_x -yhdisteiden pääasiallinen tuhoutumiskeino ylästratosfäärissä ja mesosfäärissä on fotolyysi, joka johtaa NO_x -yhdisteiden pitkään fotokemialliseen elinikään napa-alueiden pimeän talven aikana. Tästä syystä NO_x, joita protonit voivat tuottaa keski-ilmakehään, on altis ilmakehän dynamiikalle ja sitä kulkeutuu helposti mesosfääristä ja alatermosfääristä alemmas keski-ilmakehään. Tämä alaspäin suuntautuva kuljetusliike voi voimistua pohjoisella napa-alueella stratosfäärin äkillisiksi lämpenemisiksi (SSW) kutsuttujen dynaamisten ilmiöiden jälkeen. Voimistunut NO_x -kuljetus keski-ilmakehään voi täten vahvistaa NO_x-otsoni kytkentää stratosfäärissä.

Tässä väitöstyössä käytettiin sekä satelliittihavaintoja useasta eri instrumentista että ilmakehän kemiakuljetusmallia tutkimaan SSW ja SPE vaikutuksia stratosfäärissä ja mesosfäärissä. Työn tieteelliset tavoitteet olivat selvittää lämpenemisten ja protonimyrskyjen yksittäiset ja yhteiset vaikutukset NO_x -yhdisteisiin ja otsoniin pohjoisen napa-alueen keski-ilmakehässä sekä määrittää dynamiikan (SSW) ja NO_x tuoton (SPE) suhteelliset merkitykset stratosfäärin otsoniin. Tulokset osoittivat NO_x -yhdisteiden pitoisuuksien dramaattisen nousun jopa 50-kertaiseksi sekä voimistuneen laskuliikkeen että protonimyrskyjen aikana. Selvä pitkäaikainen, kuukausia kestävä lasku (10-90 %) stratosfäärin otsonipitoisuuksissa tapahtui samaan aikaan NO_x pitoisuuksien kasvun kanssa. Ylästratosfäärissä tämä oli pääosin seurausta dynamiikasta ja voimistuneen laskuliikkeen mukanaan tuomista NO_x -yhdisteistä kyseiselle alueelle.

Tämän väitöstyön tulokset korostavat ilmakehän dynamiikan tärkeää roolia SPE vaikutusten kuljettamisessa alemmille korkeuksille ja sen mahdollisuudesta voimistaa otsonin tuhoutumista ylästratosfäärissä.

Julkaisijayksikkö
Ilmatieteen laitos, Uudet havaintomenetelmät

Luokitus (UDK)
523.9
551.5
551.510.532
551.510.533

Asiasanat
stratosfääri, mesosfääri, stratosfäärin äkillinen lämpeneminen, suurienergiset hiukkaset, protonimyrskyt, pariton typpi, otsoni

ISSN ja avainnimike
0782-6117 Finnish Meteorological Institute Contributions

ISBN
978-952-336-029-7 (nid.), 978-952-336-030-3 (pdf)

Kieli
Englanti

Sivumäärä
156

PREFACE

I would like to express my gratitude to Prof. Esa Kallio from the Aalto University School of Electrical Engineering and Dr. Alain Hauchecorne from the French National Centre for Scientific Research for the careful examination of this thesis. My gratitude also belongs to the University of Helsinki, especially to the Faculty of Science and the Department of Physics, where I got to conduct all my university studies. Thank you also Prof. Heikki Järvinen for teaching me meteorology, supporting me during my M.Sc. and Ph.D. studies, and acting as the Custos in the public examination of this thesis.

This work was carried out at the Finnish Meteorological Institute and was funded by the Academy of Finland. I would like to thank the management of the Earth Observation unit, both the former head of the unit Prof. Minna Palmroth and the current head Dr. Ari-Matti Harri, for being approachable, available for discussion, and providing me excellent working conditions. I would also like to express my gratitude to the Atmospheric Remote Sensing group, the best colleagues one can have, for making the working environment so inspiring. I would especially like to thank the head of the group, my awesome boss, Prof. Johanna Tamminen. Johanna, thank you for your support, always making time for me, listening to my outbursts of thoughts, trusting in me, and helping me find the right paths. Thank you Prof. Erkki Kyrölä for your support. It has been priceless, together with your sense of humour. Thank you Niilo Kalakoski for all your help related to work, but most importantly for always being there if I needed someone to talk to. Thank you Seppo Hassinen for all the countless discussions we have had during the past few years. It has meant a lot to me. Thank you Ella Kivimäki for all your help and your sense of humour. Great minds think alike! Thank you Kirsi Virolainen for taking care of me and for brightening the days with your happy personality.

I wish to thank Laura Thölix for all the help with FinROSE-CTM, but also for the tremendous support you have provided me during the years. I have enjoyed your company and our long discussions about work and life in general. I feel that we started working as colleagues, but ended up being very good friends. I would also like to thank all the people sitting at the 3rd floor coffee table for providing me distraction from work, but also helping me with science problems. Many questions have been solved during the coffee breaks!

I do not know how I can ever express the gratefulness I feel towards my closest colleagues, my friends, Dr. Annika Seppälä and Dr. Monika Andersson. Thank you for the countless discussions related to both work and everything else. Thank you for listening to me. Thank you for your everyday support, especially during the moments when I have doubted myself. Thank you for always being there for me. Thank you for being the wonderful personalities you are, do not ever change. We built this city!

Most of my indebtedness belongs to my supervisor Dr. Pekka Verronen. We have come a long way together: you were there for me when I started working at the Finnish Meteorological Institute as a university trainee in the summer of 2008, and you were there for me all the way to this point when I am defending my Ph.D. thesis. During these years I have learnt a lot from you. One of the most important lessons learnt has been the ability to treat problems as challenges. Thank you for your trust, support, guidance, and presence. Your help has been indispensable and it has made this possible.

Finally, I would like to thank my friends and family. My friends Taru Olsson and Johanna Aalto for being my very dear friends and for making me laugh. Kiitos ystävät. My parents Marita and Heikki for all the love, encouragement, and guidance. Kiitos äiti ja isä. My older sister Minna and her family for being my best friends and sister one can hope for. Kiitos sisko & co. My husband Ari for taking me as who I am and still standing next to me every single day. You are the love of my life. Kiitos rakas. My beautiful children Enni and Eevi for reminding me about the most important things in life. Kiitos murmelit. I love you all to the Moon and back!

Helsinki, December 2017
Sanna-Mari Päivärinta

Contents

List of Abbreviations

EPP	Energetic Particle Precipitation
SPE	Solar Proton Event
SSW	Sudden Stratospheric Warming
HO_x	Odd Hydrogen Family
NO_x	Odd Nitrogen Family
NO_y	Total Reactive Nitrogen
HNO_3	Nitric Acid
MLT	Mesosphere-Lower Thermosphere
ES	Elevated Stratopause
ECMWF	European Centre for Medium-Range Weather Forecasts
CTM	Chemistry Transport Model
UBC	Upper Boundary Condition
ACE-FTS	Atmospheric Chemistry Experiment-Fourier Transform Spectrometer
MIPAS	Michelson Interferometer for Passive Atmospheric Sounding (onboard Envisat)
MLS	Microwave Limb Sounder (onboard Aura)
SABER	Sounding of the Atmosphere using Broadband Emission Radiometry (onboard TIMED)

List of Original Publications and Author Contribution

I Salmi, S.-M., Verronen, P. T., Thölix, L., Kyrölä, E., Backman, L., Karpechko, A. Yu., and Seppälä, A. (2011): Mesosphere-to-stratosphere descent of odd nitrogen in February–March 2009 after sudden stratospheric warming event, *Atmos. Chem. and Phys.*, *11*, 4645–4655.

II Funke, B., Baumgaertner, A., Calisto, M., Egorova, T., Jackman, C. H., Kieser, J., Krivolutsky, A., López-Puertas, M., Marsh, D. R., Reddmann, T., Rozanov, E., Salmi, S.-M., Sinnhuber, M., Stiller, G. P., Verronen, P. T., Versick, S., von Clarmann, T., Vyushkova, T. Y., Wieters, N., and Wissing, J. M. (2011): Composition changes after the "Halloween" solar proton event: the High Energy Particle Precipitation in the Atmosphere (HEPPA) model versus MIPAS data intercomparison study, *Atmos. Chem. Phys.*, *11*, 9089–9139, doi:10.5194/acp-11-9089-2011.

III Päivärinta, S.-M., Seppälä, A., Andersson, M., Verronen, P. T., Thölix, L., and Kyrölä, E. (2013): Observed effects of solar proton events and sudden stratospheric warmings on odd nitrogen and ozone in the polar middle atmosphere, *J. Geophys. Res.*, *118*, 6837–6848, doi:10.1002/jgrd.50486.

IV Päivärinta, S.-M., Verronen, P. T., Funke, B., Gardini, A., Seppälä, A., and Andersson, M. E. (2016): Transport versus energetic particle precipitation: Northern polar stratospheric NO_x and ozone in January–March 2012, *J. Geophys. Res.*, *121*, 6085–6100, doi:10.1002/2015JD024217.

As the lead author of Publications I, III and IV, S.-M. Päivärinta (née Salmi) was responsible for designing and conducting the numerical model simulations (Publications I and IV), analyzing the satellite data (Publication III) and writing the manuscripts. S.-M. Päivärinta was also responsible of the initial ideas of Publications III and IV. Publication II is a large community wide numerical model intercomparison study where S.-M. Päivärinta was responsible for further development of the FinROSE chemistry-transport model for the purpose of the intercomparison, carrying out the FinROSE simulations and writing dedicated sections of the manuscript.

1 INTRODUCTION

The upper stratosphere and mesosphere together form the so called middle atmosphere (∼30–80 km) of the Earth (Fig. 1.1). The importance of ozone in the middle atmosphere has been recognised since the mid-1980s, after the first observations of the spring time ozone hole in the polar middle atmosphere (*Farman et al.*, 1985). Ozone has a major role both in the heat balance of the middle atmosphere and protecting living organisms at the ground-level by absorbing solar ultraviolet (UV) radiation. Changes in the ozone balance can thus have significant impacts in the middle atmosphere, possibly even beyond through coupling between the lower and middle atmosphere (e.g. *Seppälä et al.*, 2009; *Baumgaertner et al.*, 2011; *Rozanov et al.*, 2012). Today, the man-made impacts on ozone in the middle atmosphere are well established and more attention is drawn to the future behaviour of the ozone hole: while the mid-latitude spring time ozone seems to be recovering, it is not yet certain will the healing effect take place also in the polar areas (e.g. *Weatherhead et al.*, 2000; *Newchurch et al.*, 2003; *Solomon et al.*, 2016). Ozone is not only affected by anthropogenic sources, but also due to natural forcing mechanisms. This work focuses on ozone variability caused by solar forcing in the form of energetic particle precipitation (EPP), more precisely solar proton events (SPEs), and internal atmospheric dynamics during periods of so called sudden stratospheric warmings (SSWs).

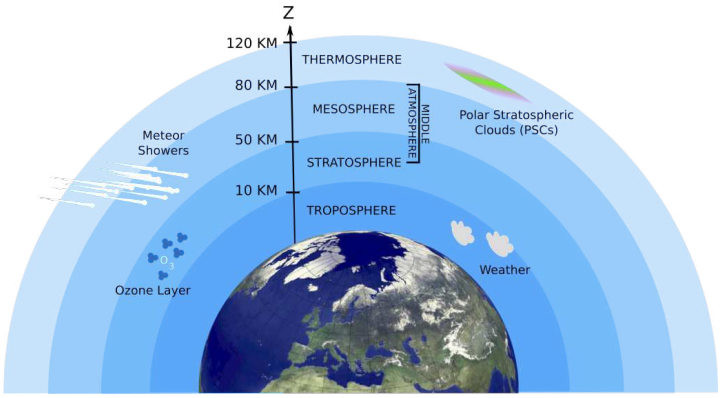

FIGURE 1.1.: A schematic view of the layers of the atmosphere and the definition of the middle atmosphere.

Solar forcing in the atmosphere does not provide a constant forcing factor on the middle atmosphere due to its dependence on the 11-year solar cycle of the Sun (e.g. *Richardson et al.*, 2000). During a solar cycle the activity of the Sun varies, including the amount of energetic particles released from the Sun and penetrating into the Earth's atmosphere. EPP is of great importance considering its effect in the atmosphere – it has been shown that energetic particles give rise to such chemical processes in the middle

atmosphere that can lead to a clear reduction in ozone in the polar regions during winter time above about 35 km (e.g. *Seppälä et al.*, 2004; *Jackman et al.*, 2005; *López-Puertas et al.*, 2005; *Verronen et al.*, 2005). As mentioned above, these type of changes in ozone can eventually have an impact also beyond the middle atmosphere, emphasizing the importance of this work and the understanding of the profound chemical and dynamical effects that EPP and solar forcing both have on the middle atmosphere in the time scale of a solar cycle. It is noteworthy, that the natural ozone variability related to EPP does not denote the same thing as the anthropogenic effect on ozone due to climate change, nor does it rule out the importance of the human-made global scale changes.

The atmospheric dynamics play a key role in determining the distributions of atmospheric constituents with long enough lifetimes. The winter time dynamics in the polar middle atmosphere have specific characteristics supporting the EPP effect to be transported further away from the area of particle precipitation to cover a wider range of altitudes (e.g. *Funke et al.*, 2005; *Randall et al.*, 2009; *Pérot et al.*, 2014). The prevailing winter dynamics can be disrupted by SSWs, extreme dynamical phenomena capable of affecting the atmospheric dynamics from the surface up to and even beyond the middle atmosphere. In optimal conditions SSWs can intensify the transport of ozone destroying substances and thus amplify the EPP–ozone connection in the middle atmosphere, an important factor that needs to be taken into account when considering the indirect EPP effects.

The work done for this thesis concentrates on the intricate roles of SSWs and EPP, in particular during solar proton events (SPEs), and how these contribute to upper statospheric ($\sim$30–50 km) and mesospheric ($\sim$50–80 km) ozone balance. The main scientific objectives are:

1. To assess the observed and simulated effects of SPEs and SSWs on the chemical composition of the Northern polar middle atmosphere

2. To contrast winters with different background conditions (SPE, SSW, SPE+SSW) with each other, and assess the implications of the individual and combined effects of the events on the middle atmosphere.

3. To account for the the relative importances of dynamics (SSW) and particle forcing (SPE) on stratospheric ozone.

The introductory review of this work begins with describing the relevant chemistry (Chapter 2) and dynamics (Chapter 3), including the SSWs, in the middle atmosphere considering the focus of this work. The characteristics of the SPEs are discussed in Chapter 4. Chapter 5 introduces the methods, here representing the satellite observations, the model and the parameterizations, crucial for carrying out this work. This thesis consists of four original publications listed on page 9, and they will be referred to as PUBLICATIONS I–IV. The main results of PUBLICATIONS I–IV are presented in Chapter 6. The importance of this work and the future prospects of the science related to EPP and SSWs are contemplated in Chapter 7.

2 Polar Stratosphere and Mesosphere: Chemistry

In the middle atmosphere, ozone is an important factor determining the chemical and radiative energy budgets (*Brasseur and Solomon*, 2005). It has been suggested that the solar-cycle signal could propagate down to the troposphere through changes in the middle atmospheric ozone balance and in the end also have an effect on the polar climate variability (e.g. *Seppälä et al.*, 2009; *Baumgaertner et al.*, 2011). Finding out the mechanisms affecting ozone in the middle atmosphere is of great importance in order to understand the coupling between the troposphere and middle atmosphere, as well as climate. This chapter concentrates on the stratospheric and mesospheric chemistry that is important for understanding the outcome of this thesis.

2.1 Ozone

Molecular oxygen (O_2) is the second most abundant ($\sim$21%) chemical constituent throughout the troposphere and middle atmosphere of the Earth. In a sunlit atmosphere, O_2 is photodissociated by ultraviolet radiation through reaction:

$$O_2 + h\nu \ (\lambda \leq 242.4 \text{ nm}) \rightarrow O + O. \tag{2.1}$$

The presence of atomic oxygen (O), produced via Reaction 2.1, enables the production of ozone (O_3), which in the middle atmosphere is produced by one reaction only: a three-body reaction between O, O_2, and either molecular nitrogen (N_2) or O_2 (denoted as M):

$$O + O_2 + M \rightarrow O_3 + M. \tag{2.2}$$

The presence of atomic oxygen is therefore necessary for ozone production. Despite the fact that O acts in reactions producing ozone, it can also work on the other direction and destroy ozone:

$$O + O_3 \rightarrow 2O_2. \tag{2.3}$$

Ozone is also destroyed by solar UV radiation:

$$O_3 + h\nu \ (\lambda \geq 320 \text{ nm}) \rightarrow O(^3P) + O_2 \tag{2.4}$$

$$O_3 + h\nu \ (\lambda \leq 320 \text{ nm}) \rightarrow O(^1D) + O_2 \tag{2.5}$$

where $O(^3P)$ denotes the ground state oxygen atom and $O(^1D)$ the excited state atom. Reactions 2.1–2.5 are known as the Chapman reactions based on the early work of *Chapman* (1930). These reactions, illustrated in Fig. 2.1, emphasize the importance of sunlit conditions in the production of ozone. In the polar regions, the intensity of solar

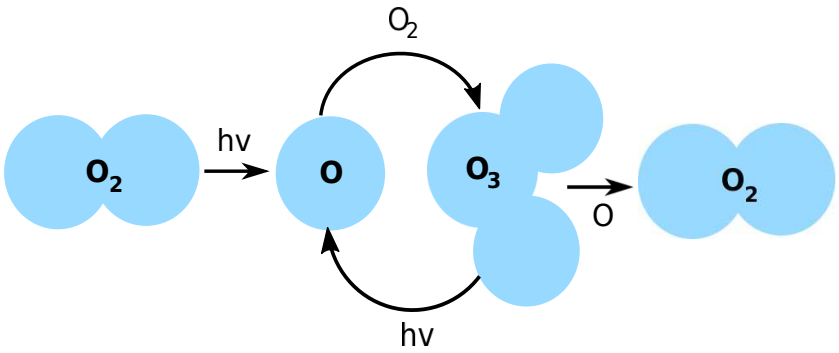

FIGURE 2.1.: Simplified illustration of the oxygen cycles in the middle atmosphere, also know as the Chapman reactions.

radiation starts to weaken rapidly during the autumn season and the radiation does not reach the highest latitudes during the winter period at all. This leads to a significant reduction in the formation of ozone as no atomic oxygen is produced. Simultaneously, other chemical constituents, activated in the cold temperatures, can destroy ozone in catalytic chemical reaction cycles. This can result in very low ozone concentrations inside the polar vortex (Chapter 3.2), including the well known ozone hole phenomena (*Farman et al.*, 1985). The next section provides a more thorough description of the catalytic cycles and catalysts mentioned above.

2.2 CATALYTIC REACTIONS

Some chemical constituents are able to destroy ozone in a very rapid and efficient manner. Such free radicals and catalysts can be divided into three groups: 1) halogen compounds (e.g. chlorine and bromine), 2) odd hydrogen family (HO_x), and 3) odd nitrogen family (NO_x). Some other minor constituents also act as catalysts, but the main contributors to ozone loss are the ones listed above. The following discussion focuses on the NO_x and HO_x families, and on the effects they have on ozone in the middle atmosphere.

2.2.1 Odd Nitrogen

The NO_x family comprises of the sum of atomic nitrogen (N), nitric oxide (NO) and nitrogen dioxide (NO_2):

$$NO_x = N + NO + NO_2.$$

In the stratosphere, NO is mainly produced by oxidation of nitrous oxide (N_2O):

$$N_2O + O(^1D) \rightarrow 2NO. \tag{2.6}$$

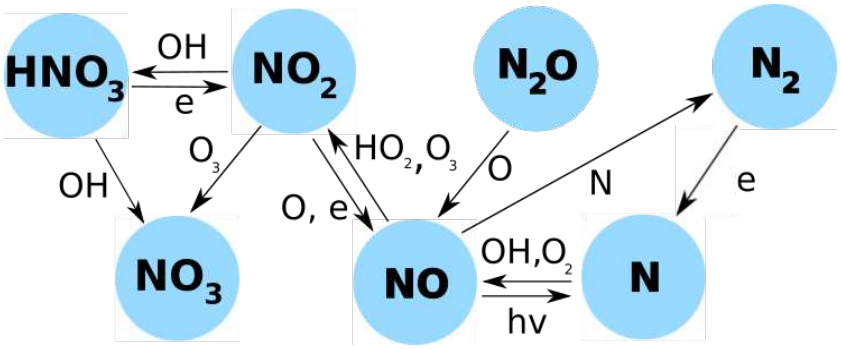

FIGURE 2.2.: A schematic view of the most important reactions related to NO_x chemistry.

Higher in the atmosphere, in the mesosphere and thermosphere, the main NO_x source is the photoionization of N_2 by solar extreme ultraviolet radiation and soft X-rays (*Barth*, 1992). During periods of high geomagnetic activity (Chapter 4), charged particles provide an additional source for NO_x as increased ionization/dissociation of the neutral molecules in the middle and upper atmosphere leads to enhanced production of N^+, N_2^+, O^+ and O_2^+ ions (*Sinnhuber et al.*, 2012):

$$O_2 + p \rightarrow O + O + p \tag{2.7}$$

$$N_2 + p \rightarrow N + N + p \tag{2.8}$$

$$N_2 + p \rightarrow N_2^+ + p + e^- \tag{2.9}$$

$$O_2 + p \rightarrow O_2^+ + p + e^- \tag{2.10}$$

$$N_2 + p \rightarrow N^+ + N + p + e^- \tag{2.11}$$

$$O + p \rightarrow O^+ + p + e^- \tag{2.12}$$

where p denotes a charged particle, e.g. a proton, and e an electron lost by the ionized molecule. The produced ions further react producing N (*Rusch et al.*, 1981):

$$N_2^+ + O \rightarrow NO^+ + N \tag{2.13}$$

$$N_2^+ + e \rightarrow N + N \tag{2.14}$$

$$O^+ + N_2 \rightarrow NO^+ + N \tag{2.15}$$

$$N^+ + O_2 \rightarrow O^+ + NO \rightarrow NO^+ + O \rightarrow O_2^+ + N \tag{2.16}$$

$$NO^+ + e \rightarrow N + O. \tag{2.17}$$

Atomic nitrogen (N), produced in Reactions 2.13–2.17 and including both the ground state ($N(^4S)$) and excited state ($N(^2D)$) atoms, can then react with O_2 in order to produce NO:

$$N + O_2 \rightarrow NO + O. \tag{2.18}$$

In the stratosphere and mesosphere, the reaction between $N(^2D)$ and O_2 is, however, much faster than the one between $N(^4S)$ and O_2 (*Rusch et al.*, 1981). NO can further react and produce NO_2 in various reactions, but most importantly in a reaction with ozone:

$$NO + O_3 \rightarrow NO_2 + O. \tag{2.19}$$

In sunlit conditions, NO_2 is quickly converted back to NO through photodissociation or oxidation (*Brasseur and Solomon*, 2005). The mesospheric and thermospheric NO_x production (Reactions 2.18–2.19) following the quite complicated ion chemistry is much more efficient than the NO_x production in the stratosphere (Reaction 2.6). This leads to thermospheric NO_x mixing ratios that are orders of magnitude larger than in the stratosphere.

The loss reactions for NO_x include photolysis at altitudes above the upper stratosphere during daytime (Reactions 2.20) and the following cannibalistic reaction with $N(^4S)$ (Reaction 2.21) (*Brasseur and Solomon*, 2005):

$$NO + h\nu \rightarrow N(^4S) + O \tag{2.20}$$

$$N(^4S) + NO \rightarrow N_2 + O. \tag{2.21}$$

The above reactions show clearly the dependence of NO_x loss on solar radiation. One more possible loss pathway for NO_x is the conversion of NO_x species to reservoir species of total reactive nitrogen NO_y ($NO_y = NO_x + NO_3 + 2N_2O_5 + HNO_3 + HO_2NO_2 + ClONO_2 + BrONO_2$). The conversion is more rapid in the lower stratosphere below about 45 km than in the upper stratosphere/mesosphere where $NO_x \simeq NO_y$. Assessing NO_y instead of NO_x takes the NO_x loss due to any conversion reactions into account. This was important, for example, in PUBLICATION II in order to evaluate the NO_x agreement between atmospheric models and satellite observations in the stratosphere.

During the polar winter, limited amount of solar radiation together with limited mixing between the vortex and non-vortex air (discussed more thoroughly in Chapter 3) supports the activation of catalytic chemical cycles where NO_x constituents act as the catalysts (denoted as X):

$$X + O_3 \rightarrow XO + O_2 \tag{2.22}$$

$$XO + O \rightarrow X + O_2 \tag{2.23}$$

$$Net : O + O_3 \rightarrow 2O_2. \tag{2.24}$$

During this cycle one oxygen atom and ozone molecule is depleted and two molecular oxygens are produced. Note that the Reactions 2.22–2.23 did not consume the catalyst

X. This way the catalyst, here NO_x, can continue destroying ozone for long periods of time, from days to even months, and is also affected by the atmospheric transport. This means that NO_x, and its ability to influence the composition of the middle atmosphere, can be transported tens of kilometres downwards from the area where it was originally produced, as shown in PUBLICATIONS I–IV.

2.2.2 Odd Hydrogen

HO_x family is the sum of atomic hydrogen (H), hydroxyl (OH) and hydroperoxyl (HO_2) in the middle atmosphere:

$$HO_x = H + OH + HO_2.$$

In the upper stratosphere and lower mesosphere HO_x is produced through oxidation of water vapour (H_2O, Reaction 2.25) and higher in the atmosphere through photodissociation of H_2O (Reaction 2.26) (*Solomon et al.*, 1981):

$$O(^1D) + H_2O \rightarrow 2OH \tag{2.25}$$

$$H_2O + h\nu \rightarrow H + OH. \tag{2.26}$$

Not only NO_x, but also HO_x is affected by the energetic particles penetrating into the Earth's atmosphere (Chapter 4). In case of HO_x, the ion chemistry is much more complicated than the one described above for NO_x, including for example the formation of water cluster ions. The eventual result of the ion chemistry is the conversion of one H_2O molecule into OH and H, both included in the HO_x family, and thus enhancing the amount of HO_x in the middle atmosphere rapidly. The ion chemistry related to HO_x is discussed more thoroughly in e.g. *Solomon et al.* (1981).

The main loss mechanisms for HO_x in the middle atmosphere are reactions with atomic oxygen and cannibalistic reactions. Examples of this type of reactions is given in Reactions 2.27 and 2.28, respectively:

$$OH + O \rightarrow O_2 + H \tag{2.27}$$

$$H + HO_2 \rightarrow OH + OH. \tag{2.28}$$

Similarly to NO_x, HO_x takes part in the catalytic chemical cycles (Reactions 2.22–2.23) destroying ozone in the middle atmosphere. NO_x dominates the cycles in the stratosphere whereas HO_x is the main contributor to ozone loss in the mesosphere. The photochemical lifetime of HO_x is very short: in the stratosphere the lifetime is order of minutes, in the mesosphere from hours to one day. This means that the photochemical lifetime of HO_x is significantly shorter than the timescales of atmospheric transport, and that the HO_x related effects in the middle atmosphere therefore remain local. The role of HO_x and its effects in the middle atmosphere are discussed also in PUBLICATIONS II and IV.

2.2.3 Nitric Acid

Nitric acid (HNO_3) is produced in the stratosphere in a reaction between NO_2 and OH (*Brasseur and Solomon*, 2005):

$$NO_2 + OH + M \rightarrow HNO_3 + M. \tag{2.29}$$

During periods of high geomagnetic activity, energetic particles provide an additional source of HNO_3 in the middle atmosphere as a consequence of the negative ion chemistry related to HO_x production (*Verronen et al.*, 2008; *Verronen et al.*, 2011).

The loss of HNO_3 is mainly governed by reactions with OH and photodissociation of HNO_3:

$$OH + HNO_3 \rightarrow H_2O + NO_3 \tag{2.30}$$

$$HNO_3 + h\nu \rightarrow OH + NO_2. \tag{2.31}$$

During the polar winter, when only limited amount of solar radiation is reaching the middle atmosphere, Reaction 2.31 is rather ineffective and the photochemical lifetime of HNO_3 becomes longer, even of the order of months. This is an important factor that needs to be taken into account, especially during geomagnetic storms (Chapter 4) when additional HNO_3 production takes place in the middle atmosphere (*Verronen et al.*, 2008; *Orsolini et al.*, 2009). In the night, HNO_3 builds up, but as soon as the amount of solar radiation increases during sunrise it becomes quickly photodissociated producing HO_x (Reaction 2.31) (*Verronen et al.*, 2006). At the same time, atomic oxygen, needed for the ozone destroying catalytic cycles, is abundant in the atmosphere after the phodissociation of O_2 (Reaction 2.1). Therefore, during periods of energetic particle precipitation, HNO_3 provides an additional source for HO_x at a crucial time point considering the catalytic ozone loss cycles. Neglecting this could in the end lead to underestimation of the HO_x related ozone loss in the mesosphere (*Verronen and Lehmann*, 2013). Recognising the importance of the ion chemistry leading to enhanced HNO_3 production in the middle atmosphere, this has been taken into account in PUBLICATIONS II and IV when simulating the atmospheric composition during and following geomagnetic disturbances.

3 Polar Stratosphere and Mesosphere: Dynamics

This chapter describes the dynamics of the middle atmosphere by going through the roles of atmospheric waves and other circulation patterns crucial for understanding the scope of this work. The chapter ends with discussion of NO_x descent and SSWs, both relevant in all the work presented in PUBLICATIONS I–IV. It should be noted that this chapter is not all-encompassing for the whole middle atmospheric dynamics.

3.1 Atmospheric Waves

The importance of atmospheric waves is dependent on the energy of the waves, and on the altitude region where the waves dissipate their energy. In the middle atmosphere, breaking of the waves leads to intense interaction between the waves and the mean flow, in the end giving rise to the observed circulation patterns. On the other hand, waves are also able to rapidly and completely change the prevalent dynamical conditions on a wide range of altitudes, spanning from the troposphere up to the thermosphere and beyond, particularly in the Northern polar region during the winter periods. The phenomena related to this, the SSWs, are discussed in Chapter 3.3 and in PUBLICATIONS I, III and IV. The results of these papers show that the ability of waves to propagate vertically not only plays an important role on the dynamics, but also on the distribution of trace gases.

Gravity waves are formed when air parcels are vertically displaced in a stably stratified atmosphere, i.e. when temperature decreases less than in a neutral atmosphere ($\sim$9.8 K/km) as a function of altitude. Due to buoyancy, the vertically shifted air parcels start to oscillate around the equilibrium state generating waves (*Fritts and Alexander*, 2003). Orographical sources, such as flow over mountains, are known to be one major source for the vertical displacements (*Whiteway and Duck*, 1996). Also non-orographical sources (e.g. convection, wind shear, frontal systems) can trigger gravity waves, but a complete list of these sources can not be established and is still beyond our knowledge (*Fritts and Alexander*, 2003). Satellite observations and numerical models have been of great value helping to determine the global distribution of long wavelength and low frequency gravity waves in the stratosphere and lower mesosphere by providing data with good time resolution and global coverage (*Miyoshi et al.*, 2014). Open questions still remain, especially concerning the shorter wavelength and higher frequency gravity waves, since satellite instruments can observe only part of the gravity wave spectra (*Gong et al.*, 2012). Issues in resolving gravity waves exist also in numerical modeling and significant amount of gravity waves in atmospheric models are parameterized and/or tuned in order to reproduce a realistic atmosphere.

Vertically propagating gravity waves are relatively short ($\sim$10–1000 km) in their horizontal wavelengths (*Brasseur and Solomon*, 2005). The propagation of gravity

waves depends greatly on the dynamical conditions in the surrounding atmosphere, one of the most important contributor being the wind distribution, (*Smith et al.*, 2010). If the component of the background wind speed in the direction of wave propagation at a certain altitude is the same as the phase speed of the wave, the wave will not propagate upward (*Whiteway and Duck*, 1996). Also, if the angle between the direction of propagation and the background wind is $\pm 90^{\circ}$, the wave becomes blocked (e.g. *Whiteway and Duck*, 1996; *Duck et al.*, 2001). The level of blocking is called the critical level and a wave will either dissipate all its energy underneath this level or be reflected when encountering the critical level and continue propagating in another direction. Gravity waves often propagate up to mesospheric altitudes, where the waves dissipate their energy between 60 and 80 km, and interact with the middle atmospheric circulation (*Chandran et al.*, 2013). The energy deposition from gravity waves in the mesosphere constrains the mean flow near the mesopause and thus drives a strong mean meridional circulation with upwelling and adiabatic cooling at the summer pole and downwelling and adiabatic heating at the winter pole (Fig. 3.1)(*Haynes et al.*, 1991; *Karlsson et al.*, 2007). Also, the westward zonal mean winds, dominating the zonal flow in the mesosphere, are primarily driven by gravity wave forcing (*Chandran et al.*, 2014).

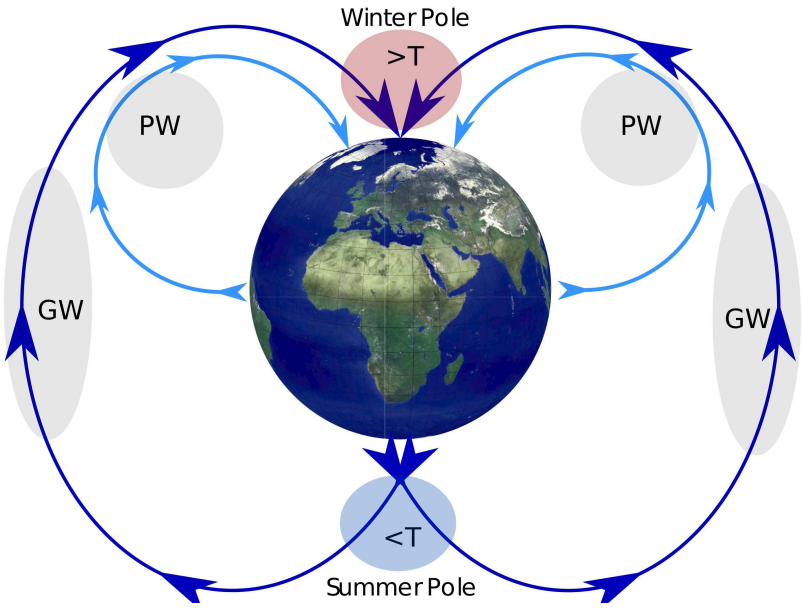

FIGURE 3.1.: A schematic illustration of the residual mean meridional circulation in the middle atmosphere. The gray shaded areas in the figure denote the breaking regions of atmospheric waves (GW: gravity waves, PW: planetary waves, i.e. the surf zone). The ascending motion in the summer mesosphere lead to very cold temperatures (blue area) whereas the descending motion in the winter pole warms the mesosphere (red region).

Planetary waves, also known as Rossby waves, are westward propagating relative to the mean flow or stationary oscillations with horizontal wavelengths of up to 10000–20000 km. Air parcels moving in the meridional direction across the latitudes induce a perturbation in the Coriolis parameter followed by changes in the potential vorticity. The air parcels aim to preserve their potential vorticity leading to a restoring force and oscillation about the equilibrium latitude of the air parcel (*Stull*, 2015). These oscillations develop into the polar stream and play an important role in determining the formation and evolution of the mid-latitude weather patterns and their variability.

Like gravity waves, planetary waves are also able to propagate vertically from the troposphere up to the middle atmosphere, and quasi-stationary waves have been observed even as high as in the upper mesosphere (*Smith*, 2003). Upward propagating planetary waves are forced modes generated in the troposphere by stationary sources such as the land-sea contrast or large-scale topography (*Holton and Alexander*, 2000). In order to propagate upwards the forced planetary waves require a eastward background flow, which is normally the case in the stratosphere during winter seasons. The velocity of the zonal flow also needs to be smaller than a critical value, a value that is dependent on the wavenumber of the planetary wave. In favourable conditions planetary waves propagate up to the stratosphere and dissipate their energy when the phase velocity of the wave is equal to the zonal mean wind (*Brasseur and Solomon*, 2005). The breaking zone (Fig. 3.1), also known as the surf zone, is bounded by strong gradients of potential vorticity in the winter subtropics and at the edge of the polar vortex at the mid-latitudes (*Plumb*, 2002).

By dissipating their energy in the stratosphere, planetary waves, together with synoptic scale waves in the very low stratosphere, interfere with the zonal-mean circulation in the same manner as gravity waves in the mesosphere (*Plumb and Eluszkiewicz*, 1999). Wave breaking in the stratosphere leads to a circulation pattern with upwelling in the tropical troposphere and downwelling in the high latitude stratosphere (Fig. 3.1). The descending motion of air in the polar areas produces adiabatic heating and thus several tens of Kelvin warmer winter stratosphere than the radiative equilibrium would suggest (*Callaghan and Salby*, 2001). This circulation pattern is widely referred to as the Brewer-Dobson circulation and it is strong in the winter hemisphere where the eastward flow dominates and strong wave disturbances can develop. Hemispheric differences are expected since the topography of the Southern Hemisphere (smaller landmass and the ocean surrounding the Antarctic continent) does not favour the generation of planetary waves, leading to significantly weaker Brewer-Dobson circulation during the Southern winter. The Brewer-Dobson circulation, together with the mesospheric downwelling due to gravity waves, also has a great influence on the distribution of trace species in the middle atmosphere. This is shown in PUBLICATIONS I–IV, which all focus on the mesosphere-to-stratosphere descent of NO_x, caused by the downwelling due to wave breaking, at different time points and with different background conditions.

3.2 POLAR VORTEX

The polar vortex is a low-pressure system that develops above the polar areas during winter time. The main driver of the cyclogenesis is the latitudinal gradient in the absorption of the solar short-wave radiation (e.g. *Schoeberl et al.*, 1992). The low pressure system results in strong circumpolar eastward winds that isolate the polar air from the surrounding mid-latitude air masses and form in that way a system known as the polar vortex. Isolation of air inside the vortex, together with the downwelling of mesosphere-lower thermosphere (MLT) air discussed above, plays an important role in determining the chemical composition of the polar middle atmosphere during winter. In order to reach the stratosphere, the timescale for the downward transport of MLT air needs to be shorter than the timescales of mixing with the surrounding air or significant photochemical production/loss (*Smith*, 2012). However, formation of the polar vortex supports the downward transport of NO_x by preventing mixing of mid-latitude NO_x poor air with the NO_x rich air inside the vortex.

The polar vortex extends from the lower stratosphere up to the mesosphere, but the cyclone is the strongest near the stratopause (*Scheiben et al.*, 2012). The vortex area varies significantly being usually larger in the mesosphere than in the stratosphere. This can be explained by the location of the strong eastward flow, also known as the polar night jet: in the mesosphere the jet is located at lower latitudes than in the stratosphere (*Harvey et al.*, 2009). If the planetary wave activity is on a modest level, the vortex can persist until the beginning of the spring. Less planetary waves are produced and forced into the middle atmosphere in the South leading to a more stable and longer persisting polar vortex than the one in the North (*Mitchell et al.*, 2011a). A schematic figure of the polar vortex and related phenomena is presented in Fig. 3.2.

Although located in the middle atmosphere, the polar vortex has a significant impact on dynamical variability in the troposphere. Variation in the polar vortex strength is very often followed by anomalies of the same sign in the tropospheric circulation, persisting couple of months in the North and even longer in the South (*Roy and Haigh*, 2011, and references therein). The main modulator of the polar vortices is planetary waves. In fact, the location of the vortex core is a function of the planetary wave activity. Planetary waves entering the middle atmosphere tend to stretch and increase the filamentation of the vortex (*Mitchell et al.*, 2011a). However, planetary waves are not the only factor affecting the strength of the polar vortex since other natural forcings such as the El Niño–Southern Oscillation (ENSO), the quasi-biennial oscillation, the 11-year solar cycle and volcanic eruptions influence the vortex in complex, nonlinear way that is still poorly understood (*Mitchell et al.*, 2011b).

There are several ways to define the edge of the polar vortex. Often used methods are defining the area of wind maximum or the strongest gradient in the potential vorticity field (*Scheiben et al.*, 2012, and references therein). Defining the vortex edge is crucial in order to understand the dynamics and the distribution of trace gases in the polar areas: the vortex edge acts as a mixing barrier and only little transport out of the

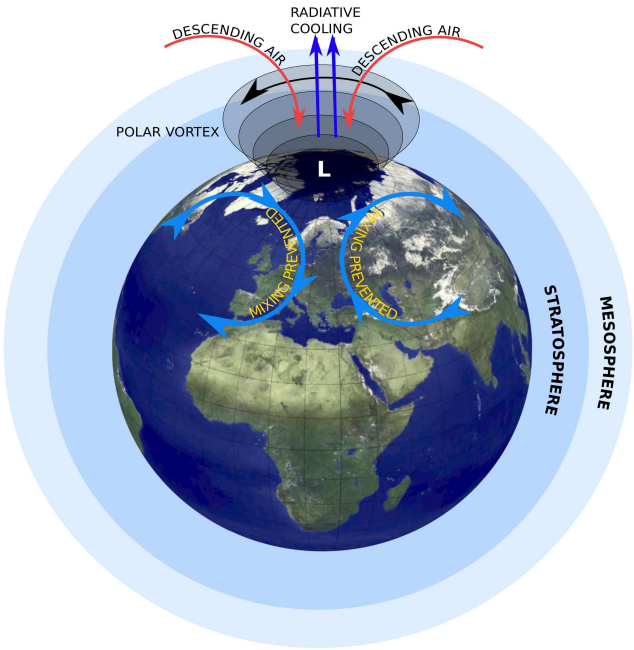

FIGURE 3.2.: A representative picture of the polar vortex. The vortex, reaching from the lower stratosphere up to the mesosphere, isolates the polar air masses from the mid-latitude air. Inside the polar vortex both downward transport, and related adiabatic warming (red arrows), and radiative cooling (blue arrows) of the air takes place.

vortex takes place before the vortex breakdown. Most of the mixing occurs in the lowest parts of the polar vortex, below ∼15–20 km (*Manney et al.*, 1994). The descending motion of the mesospheric air during polar winter concentrates near the core of the vortex in early winter and on/outside the edges in late winter (*Manney et al.*, 1994). When the vortex starts to erode, large amount of air is stripped away from the edge towards the mid and low latitudes.

3.3 SUDDEN STRATOSPHERIC WARMINGS

The downward transport of NO_x itself is somewhat regular wintry phenomena in the polar regions with yearly variations related to both the dynamical conditions (timing, altitudes affected) and the background production of NO_x due to energetic particles in the MLT region (the amount of NO_x descending) (e.g. *Funke et al.*, 2014a,b). The importance of NO_x descent is based on the dominating role of NO_x in the stratospheric ozone loss cycles if it reaches the stratosphere. The downward transport of NO_x is almost solely a dynamical phenomenon and can be strongly modulated by changes in the prevailing dynamics, such as the sudden stratospheric warmings (SSWs). The effect of SSWs on the NO_x descent is discussed in PUBLICATIONS I, III and IV.

SSWs are outstanding dynamical phenomena of the winter atmosphere, first reported by *Scherhag* (1952). The name sudden *stratospheric* warming is a bit misleading since the warmings affect not only the stratosphere, but couple the whole atmosphere from troposphere up to the thermosphere and beyond (e.g. *Funke et al.*, 2010; *Chau et al.*, 2012). The reason behind the warmings is vertically propagating planetary waves, first pointed out by *Matsuno* (1971): during the onset of SSWs, bursts of planetary waves enter the stratosphere and interact with the zonal flow. However, the role of gravity waves in the onsets of SSWs can not be ruled out since they might contribute by altering the vertical propagation of the planetary waves (*Richter et al.*, 2010).

Energy deposition from the waves decelerate the stratospheric eastward zonal wind leading to a meridional, poleward wind due to the imbalance between the pressure gradient and the Coriolis force, finally resulting in adiabatic downwelling over the polar areas due to continuity (*Hauchecorne et al.*, 2007). The downwelling leads to a sudden warming of the stratosphere giving the events its name. These events are observed almost solely in the Northern Hemisphere where majority of the planetary waves are produced and forced to propagate into the middle atmosphere. In fact, only one major SSW is known to have occurred in the Southern polar area (e.g. *Dowdy et al.*, 2004). Here we focus on SSWs taking place in the Northern Hemisphere.

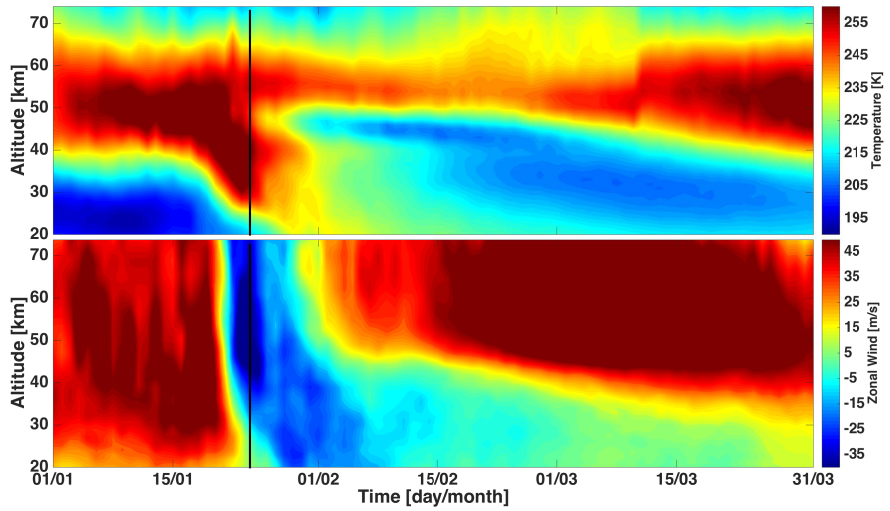

FIGURE 3.3.: Zonal mean temperature (K, top panel) and zonal mean zonal wind (ms^{-1}, bottom panel) at 75°N for the dynamically very active early 2009 from the European Centre of Medium-Range Weather Forecasts (ECMWF). In late January (black solid vertical lines), a major SSW forced the stratopause (layer of maximum temperature) to warm and drop below 30 km, accompanied by a rapid reversal of the zonal mean wind field (positive winds = eastward flow, negative winds = westward flow).

SSWs can be divided into minor and major SSWs, depending on the magnitude of the changes in the zonal mean zonal wind. According to the definition of the World Me-

teorological Organisation (WMO) (*Andrews et al.*, 1987), a *minor* warming occurs if the zonal mean zonal wind at or below 10 hPa and at 60° latitude is decelerated whereas during *major* events the zonal wind is reversed from eastward to westward. In addition, the poleward temperature gradient in the same region needs to be reversed from negative to positive. During major SSWs the stratospheric temperatures can increase by several tens of Kelvins as seen in Figure 3.3, which presents the temperature and zonal mean zonal wind changes for the 2009 major SSW (PUBLICATIONS I and III). Although the major warmings are defined at stratospheric altitudes, the wind changes are first visible in the mesosphere from where the changes propagate downwards in about one week (*Hoffmann et al.*, 2007; *Manney et al.*, 2009; *Lee et al.*, 2009; *Orsolini et al.*, 2010). Generally, the frequency of SSWs tends to be about one SSW every two years (*Andrews et al.*, 1987) or two SSWs every three years (*Charlton and Polvani*, 2007).

Another way to classify SSW events is to divide them according to the behaviour of the polar vortex during the SSW onsets. There exists two different pathways: 1) vortex displacement events accompanied by enhanced flux of wavenumber-1 (one wave length around a latitude circle) planetary waves, and 2) vortex split events with high activity of wavenumber-2 (two wave lengths around a latitude circle) planetary waves (*Mitchell et al.*, 2011a). During vortex displacement events the vortex is shifted off the pole with a comma-like shape whereas during the split events the vortex breaks into two almost equal size vortices. Depending on the methods used for defining the vortex breakdown pattern, there is an almost equal ratio between the vortex split and displacement events (*Chandran et al.*, 2014). The impact on the stratospheric temperatures and winds tends to last up to 20 days longer in the vortex split cases than in the displacement events (*Chandran et al.*, 2013). The split events are also more likely to affect the surface climate (*Nakagawa and Yamazaki*, 2006; *Mitchell et al.*, 2013).

Due to the deceleration of the eastward zonal flow during SSWs, the conditions become favourable for a more enhanced flux of planetary waves to propagate from the troposphere up to the stratosphere. The enhanced flux stays active as long as the flow is eastward. As soon as the flow reverses, a critical level is formed, and all the planetary waves will break and deposite their energy below this level. As a result, the westward gravity wave drag (GWD), contributing to the mesospheric circulation patterns and forcing the mesospheric flow to be westward in undisturbed conditions, is filtered out leading now to enhanced drag from the eastward propagating gravity waves. The missing westward GWD and the planetary wave forcing now taking place at lower altitudes, lead to downward propagation of the wind reversal and to a drop of the stratopause from its climatological position by up to 10–20 km (*Limpasuvan et al.*, 2012). The eastward GWD also affects mesospheric dynamics so that the usually westward flow can reverse to eastward, resulting in upwelling and thus mesospheric cooling by several tens of Kelvins (e.g. *Holton*, 1983; *Liu and Roble*, 2002; *Siskind et al.*, 2005; *Hoffmann et al.*, 2007).

After its sudden drop, the stratopause becomes indistinct for a short period of time in the whole polar middle atmosphere. However, radiative cooling in the mesosphere

due to the lack of GWD excites the recovery of the polar vortex and therefore also the recovery of the westtward polar night jet (*Orsolini et al.*, 2010). This leads to the reformation of the stratopause, sometimes at very high mesospheric altitudes (∼75–80 km). The origin of the elevated stratopause (ES) events, visible also in Fig. 3.3 (upper panel), is somewhat obscure. While it is widely recognised that both planetary and gravity waves play an important role in the ES events, their relative roles during the events are still under intense discussion and research. One explanation could be that the breaking zone for the gravity waves after a major SSW is higher in the mesosphere. This could force the meridional circulation to take place at higher altitudes, also leading to a elevated reformed stratopause (*Ern et al.*, 2016).

As the polar vortex strengthens, the ES descends down towards its climatological position in the upper stratosphere–lower mesosphere during the following couple of months. This descent is accompanied by enhanced downward transport of polar MLT air down to the lower mesosphere and stratosphere. Depending on the timing of the SSWs (Chapter 6.1 and PUBLICATION I) the SSWs and the related ES events can intensify the background downwelling of MLT air, possibly also the NO_x–ozone connection between the MLT region and stratosphere. The total downward transport that takes place during the ES events can be divided into eddy diffusion, molecular diffusion and advection, the main mechanism contributing to the downward transport being advection during ES events and the following descent (*Meraner and Schmidt*, 2016). The case studies presented in PUBLICATIONS I, III and IV show that the amount of NO_x entering the stratosphere following major/strong minor SSWs/ES events can be increased by several hundred percents.

4 SOLAR PROTON EVENTS

One highly varying source of NO_x in the polar region middle atmosphere is the geomagnetic activity in the form of EPP. Energetic particles, i.e. protons, electrons, and heavier ions, precipitate into the Earth's atmosphere continuously, but especially during geomagnetically disturbed conditions. This can lead to significant changes in the atmospheric composition on a wide range of altitudes from the thermosphere even down to the stratosphere (e.g. *Barth*, 1992; *Vitt et al.*, 2000). EPP can be divided into three categories according to the energies of the energetic particles: 1) solar proton events (SPEs), 2) relativistic electron precipitation, and 3) auroral electron precipitation. The first, SPEs, are a key component of PUBLICATIONS II–IV and will now be described further. For more information on the other types of EPP see e.g. *Turunen et al.* (2009)

SPEs are a major source of EPP in the atmosphere. The events originate from the surface of the Sun in the form of solar flares, or from coronal mass ejections (CMEs), lasting a few days. Solar flares and CMEs are large eruptions that are sporadic in their nature, but tend to be more frequent at the solar maximum (e.g. *Richardson et al.*, 2000; *Jackman et al.*, 2009). High energy protons emitted from the Sun travel fast in the space, even faster than the nominal solar wind ($\sim$400 km/h), and if the associated eruption took place towards the Earth, the protons are channeled by the Earth's magnetic field. Due to the geometry of the magnetic field lines, this leads to particle precipitation in the atmosphere of the polar areas, to be more precise, near the geomagnetic poles (Fig 4.1).

The altitudes affected by the energetic particles are strongly dependent on the particle energies (Fig. 4.2). In order to reach the mesosphere and stratosphere, the protons need to have energies of 4–20 MeV and $>$20 MeV, respectively, while several hundred MeV energies are required for the protons to reach the lower stratosphere (*Turunen et al.*, 2009). The flux of precipitating protons can be measured and observed

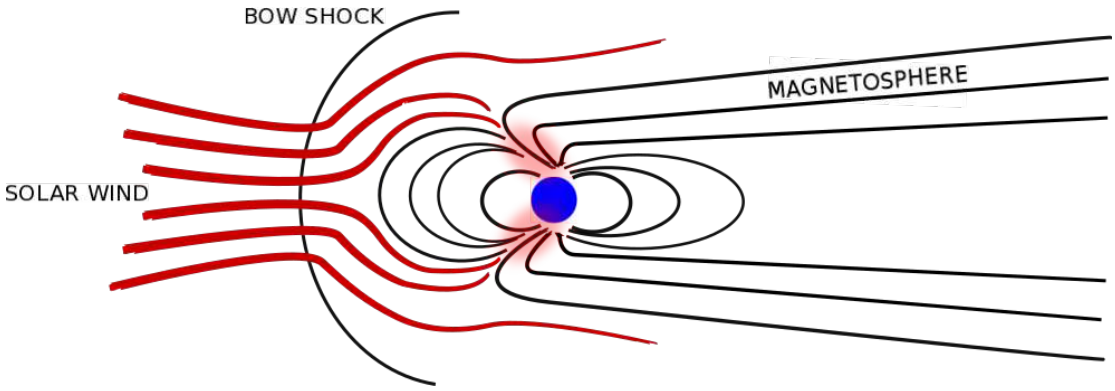

FIGURE 4.1.: An illustration of the Earth (the blue circle) and its magnetic field, the magnetosphere, the bow shock and the solar wind. High energy particles penetrate into the Earth?s atmosphere in the polar regions (red shaded areas).

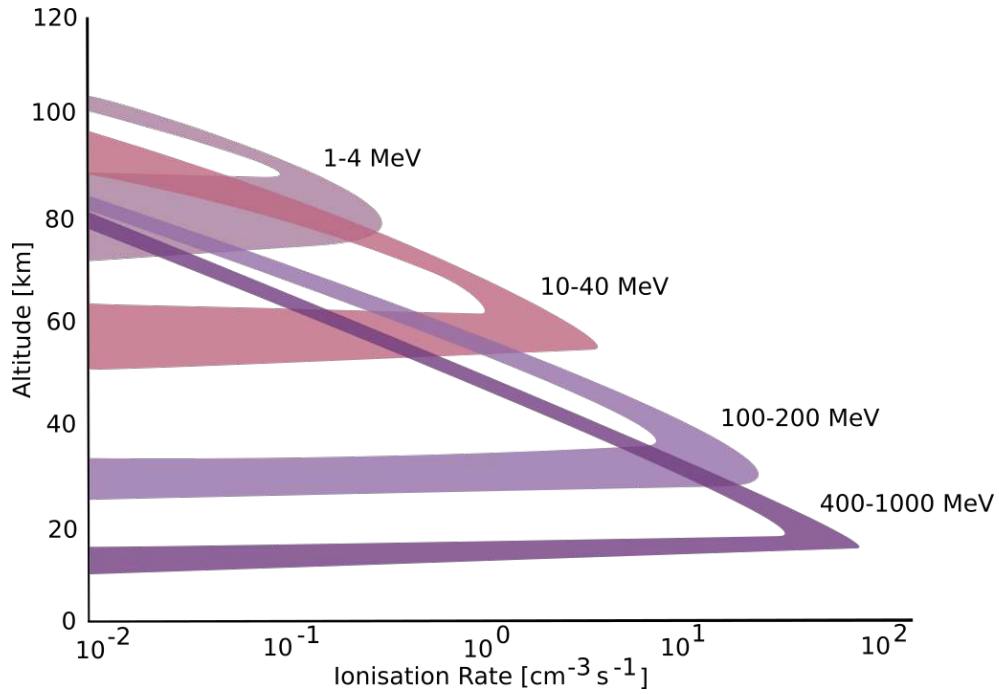

FIGURE 4.2.: A schematic view of the dependence of ionization rates on altitude and the energy of the protons. In order to penetrate in the stratosphere (∼30–80 km), protons need to have energies close to 40 MeV (e.g. *Turunen et al.*, 2009).

by satellites, e.g. by the GOES (Geostationary Operational Environmental Satellite), already since 1970s. PUBLICATIONS II–IV focuses on the SPEs that took place in late 2003 and early 2012. The proton flux during the so called "Halloween" event in October–November 2003 was nearly 30 000 pfu (particle flux unit, particles cm^{-2} s^{-1} sr^{-1}), meaning that the event was the fourth largest during the last four decades, whereas the event in 2012 was much smaller with a proton flux of about 6300 pfu. For both events, the fluxes are available from GOES measurements and for protons with energies >1 MeV.

When colliding with the neutral molecules of the atmosphere, protons loose energy and form ion pairs. The related ion chemistry is complicated and discussed shortly in Chapter 2. The ion chemistry results in the production of NO_x and HO_x so that one ion pair forms on average 1.2–1.3 NO molecules and about two or less HO_x species (e.g. *Sinnhuber et al.*, 2012; *Verronen and Lehmann*, 2013, and references therein). Taking into account the catalytic cycles destroying ozone and the contribution of both NO_x and HO_x in the cycles (Chapter 2), as well as the long-lived nature and transport of NO_x (Chapter 3), SPEs can have a significant effect on the middle atmospheric composition in much longer timescales than the actual event and at much wider altitude range than where the protons originally lost their energies.

5 METHODS

Atmospheric models and satellite observations both provide valuable information for research scientists of today: observations, considered as the ”truth”, show the prevailing state of the atmosphere whereas models help us understand the mechanisms and reasons behind that state. In order to get an up-to-date view of the middle atmosphere, continuous satellite observations are needed. However, the ongoing satellite era of middle atmospheric measurements is approaching its end and new satellite missions would be vital for continuing the high quality research of the middle atmosphere.

This chapter presents the chemistry transport model (CTM) FinROSE and all the satellite instruments used for the results presented in PUBLICATIONS I–IV and discussed in Chapter 6. These instruments were chosen because they provided high quality observations of NO_x, ozone and HNO_3 in the Northern polar region during early 2009 and 2012.

5.1 OBSERVATIONS

5.1.1 ACE-FTS

Atmospheric Chemistry Experiment (ACE), also known as SCISAT-1, is a Canadian-led mission launched in 2003 into a low Earth circular orbit at 650 km altitude (*Bernath et al.*, 2005). ACE carries two instruments: *Fourier Transform Spectrometer* (FTS), and *Measurement of Aerosol Extinction in the Stratosphere and Troposphere Retrieved by Occultation* (MAESTRO). FTS is the primary instrument and does observations in the 2.2–13.3 μm wavelength region with a high spectral resolution. The instrument measures vertical profiles of temperature, pressure, density and 18 atmospheric constituents in the altitude range of 10–150 km, with a vertical resolution of about $\sim$4 km in the whole altitude region. ACE-FTS uses the solar occultation measurement principle. This means that the measurements are carried out during sunset and sunrise as the satellite moves along its orbit. The instrument measures a series of spectra passing through the limb of the atmosphere as the Sun sets or rises relative to the satellite (Fig.5.1). This measurement technique leads to a limited latitudinal coverage, about 10–15 measurements per day north of 60°N during winter periods. Due to the measurement principle, the measurements represent almost the same latitudes from year to year. ACE-FTS NO_x and ozone have been used in PUBLICATIONS I and III.

5.1.2 MIPAS/Envisat

The European Space Agency’s Environmental Satellite ENVISAT was launched into a Sun-synchronous polar orbit at $\sim$800 km altitude in 2002, and it provided environmental observations until the connection was lost in the spring of 2012. In a Sun-

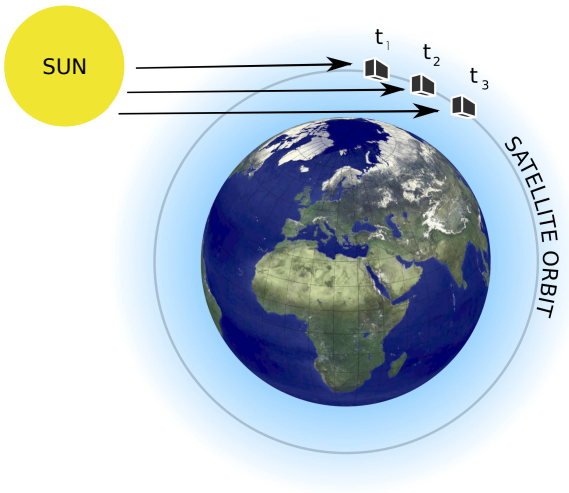

FIGURE 5.1.: A schematic view of the solar occultation measurement principle. Satellite instruments with this technique observe the Sun through the atmosphere while moving along the orbit of the satellite (t_1–t_3). The solar spectrum is measured repeatedly when the Sun appears to descend through the Earth's atmosphere during the measurements.

synchronous orbit, the satellite crosses a certain point at the same solar time. The polar orbit enables polar observations with a good time coverage. ENVISAT carried a total of ten instruments onboard, including e.g. the *Michelson Interferometer for Passive Atmospheric Sounding* (MIPAS) and the *Global Ozone Monitoring by Occultation of Stars* (GOMOS) instruments. MIPAS, a mid-infrared Fourier transform limb emission spectrometer designed and operated for measurement of atmospheric trace species (*Fischer et al.*, 2008), observations were utilized in PUBLICATIONS II and IV for several trace gases as well as for NO_x and ozone. The satellite passed the equator at 10 a.m. local time about 15 times in a day, leading to up to 1000 profiles per day measured by MIPAS in its standard observation mode. MIPAS observed the atmosphere during both day and night time from pole to pole so that the field of view was 30 km and 3 km in horizontal and vertical, respectively. The measured trace gas profiles can be retrieved from calibrated geolocated limb emission spectra with a processor developed and operated by the Institute of Meteorology and Climate Research (IMK) in Karlsruhe together with the Instituto de Astrofisica de Andalucia (IAA) in Granada, Spain.

5.1.3 MLS/Aura

The Microwave Limb Sounder (MLS) instrument onboard NASA's EOS Aura satellite was launched in 2004 and placed into a Sun-synchronous polar orbit at about 705 km altitude (*Waters et al.*, 2006). The scientific objectives of MLS are all closely related to ozone in the troposphere and stratosphere, and on processes affecting climate vari-

ability. MLS observes millimetre- and submillimetre- wavelength thermal microwave emissions, viewing forward along the satellite flight direction, and scanning from the ground up to 90 km every 25 s with daily global coverage of about 13 orbits per day, i.e. giving a latitudinal coverage of 82°S–82°N. This measurement technique allows reliable observations of many trace gases. The vertical resolution of the retrieved profiles in the middle atmosphere depends on the observed trace gas. For nitric acid (HNO_3) this varies between 3 and 5 km, and for ozone between 2 and 3 km. MLS ozone observations were utilized in PUBLICATION III and HNO_3 in PUBLICATION IV.

5.1.4 SABER/TIMED

Sounding of the Atmosphere using Broadband Emission Radiometry (SABER) is a 10-channel limb-scanning radiometer onboard NASA's Thermosphere Ionosphere Mesosphere Energetics Dynamics (TIMED) satellite launched in 2002 into low Earth orbit (*Russell et al.*, 1999). The scientific goal of SABER observations is to provide data of chemistry, dynamics, and transport in the altitude region of 60–180 km in order to enhance our understanding of MLT processes. SABER scans the Earth's limb from a 400 km tangent height to the ground, simultaneously recording profiles of radiance in the spectral range from 1.27 to 15.4 mm (*Mlynczak*, 1997). The observations provide vertical profiles for several trace gases, volume emission rates, cooling and heating rates as well as chemical heating rates. The instrument records approximately 1600 profiles per day. The vertical resolution of the observations is about 2 km, and the latitudinal coverage varies between 83°S–52°N and 52°S–83°N, depending on the yaw period of the satellite (*Rong et al.*, 2009). SABER observations of ozone were utilized in PUBLICATION III.

5.2 CHEMISTRY TRANSPORT MODEL FINROSE

The FinROSE-CTM is a 3-dimensional model designed for middle atmospheric studies (*Damski et al.*, 2007). The model is based on the ROSE model, developed at the National Center for Atmospheric Research (NCAR) in the United States, but was given the FinROSE acronym in order to separate it from the NCAR and other existing ROSE versions. FinROSE, as well as other CTMs, is forced with external meteorological input data, meaning that the model itself does not calculate the dynamics, i.e. temperature, horizontal winds and pressure. The vertical wind is an exception and is calculated from the continuity equation (*Holton*, 2004). Examples of the meteorological input data for the model include ECMWF operational data (PUBLICATION I), ECMWF Interim reanalysis data (PUBLICATION II) (see *Simmons et al.* (2006)) and the Modern Era Retrospective-analysis for Research and Applications data (MERRA, *Rienecker et al.* (2011)) available from NASA (PUBLICATION IV). It is important to keep in mind that, since the dynamics are fixed by an external source, changes in the modeled chemical

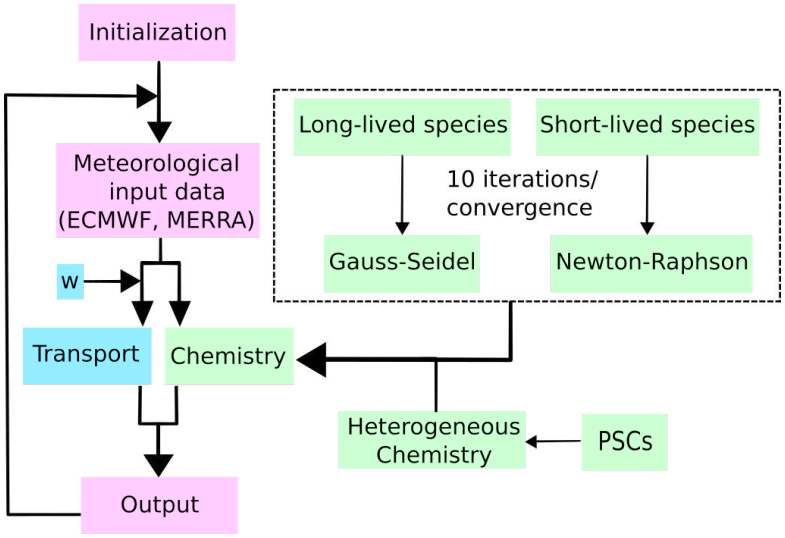

FIGURE 5.2.: A simplified diagram presenting the basic functions and operations in FinROSE. The chemistry part of the diagram is coloured with green and the transport section with blue. Those parts that are vital for both chemistry and transport in the model are coloured with fuchsia. W in the diagram denotes the vertical wind and PSCs the polar stratospheric clouds.

composition do not provide a feedback to the dynamics. A simple diagram showing the main functions of FinROSE is presented in Fig. 5.2.

Although the model dynamics are determined by an external source, they have a great influence on the modeled chemistry: many of the reaction rates, determining the speeds of chemical reactions, are dependent on temperature, and transport of long-lived trace gases is determined by the prevailing winds in the surrounding atmosphere. FinROSE calculates, taking into account both the chemistry and dynamics, the distributions of 41 species in the stratosphere and, depending on the vertical extent of the meteorological input data, possibly also in the mesosphere. The tropospheric abundances are given as boundary conditions: ozone and water vapour are defined with monthly averages from ECMWF and long-lived trace gases are relaxed towards long time trends, except methane, which is forced towards climatological distribution.

The middle atmospheric chemistry includes $\sim$120 homogenous reactions and $\sim$30 photodissociation processes. In addition to homogenous chemistry, FinROSE also includes heterogenous chemistry scheme which is responsible for the formation and sedimentation of polar stratospheric clouds (PSCs) and for the reactions on PSCs leading to the spring time ozone hole. The chemical kinetic data, reaction rate constants and absorption cross sections are all defined in advance based on the Jet Propulsion Laboratory compilation (*Sander et al.*, 2006) and updated from the available supplements. Photodissociation rates are calculated using the radiative transfer model PHODIS (*Kylling et al.*, 1997). Previous version of the FinROSE model (*Damski et al.*,

Table 5.1: Example of production/ionization (P/Q) ratios, calculated with the SIC model for HNO_3 for different combinations of altitude, ionization rate and solar zenith angle. See text for details.

Q	10^1	10^2	10^3	10^4	10^5	10^1	10^2	10^3	10^4	10^5	10^1	10^2	10^3	10^4	10^5
km		SZA	$\leq$	90°			SZA	=	95°			SZA	$\geq$	100°	
90	−0.00	−0.00	−0.00	−0.00	−0.00	−0.00	−0.00	−0.00	−0.00	−0.00	−0.00	−0.00	−0.00	−0.00	−0.00
85	−0.00	−0.00	−0.00	−0.00	−0.00	−0.00	−0.00	−0.00	−0.00	−0.00	−0.00	−0.00	−0.00	−0.00	−0.00
80	+0.00	+0.00	+0.00	+0.00	+0.00	+0.00	−0.00	+0.00	+0.00	+0.00	+0.01	+0.00	−0.00	+0.00	+0.00
75	+0.00	+0.00	+0.00	+0.00	+0.00	−0.01	−0.00	−0.00	−0.00	+0.00	+0.02	+0.01	+0.00	−0.00	−0.01
70	−0.00	−0.00	+0.00	−0.00	−0.01	−0.00	−0.00	−0.01	−0.01	−0.01	+0.05	+0.03	+0.03	+0.01	−0.00
65	−0.00	−0.00	−0.01	−0.01	−0.01	+0.00	−0.00	−0.01	−0.01	−0.01	+0.14	+0.07	+0.06	+0.04	+0.01
60	−0.01	−0.02	−0.02	−0.02	−0.01	+0.04	+0.01	+0.00	+0.00	−0.00	+0.33	+0.18	+0.13	+0.11	+0.05
55	−0.03	−0.04	−0.04	−0.03	+0.01	+0.15	+0.07	+0.04	+0.04	+0.04	+0.50	+0.33	+0.21	+0.21	+0.14
50	−0.05	−0.05	−0.06	−0.01	+0.06	+0.29	+0.20	+0.12	+0.12	+0.11	+0.59	+0.47	+0.31	+0.29	+0.28
45	−0.10	−0.06	−0.03	+0.04	+0.13	+0.46	+0.34	+0.22	+0.19	+0.22	+0.70	+0.55	+0.38	+0.33	+0.40
40	+0.32	+0.24	+0.14	+0.13	+0.17	+0.99	+0.77	+0.44	+0.26	+0.27	+1.19	+0.97	+0.60	+0.40	+0.41
35	+0.81	+0.73	+0.50	+0.28	+0.20	+1.14	+0.97	+0.65	+0.38	+0.30	+1.31	+1.14	+0.82	+0.53	+0.43
30	+1.07	+0.85	+0.49	+0.23	+0.14	+1.14	+0.81	+0.43	+0.24	+0.16	+1.32	+0.99	+0.58	+0.33	+0.24
25	+0.74	+0.53	+0.26	+0.12	+0.09	+0.43	+0.30	+0.14	+0.08	+0.06	+0.57	+0.39	+0.20	+0.11	+0.10
20	+0.40	+0.29	+0.14	+0.06	+0.05	+0.17	+0.13	+0.06	+0.03	+0.02	+0.23	+0.16	+0.08	+0.04	+0.03

2007) (PUBLICATION II) used a family approach in the chemistry for the short-lived species while the current version (PUBLICATIONS I and IV) solves the chemistry of these species individually. For these papers, significant model development work has been done for FinROSE. The following sections of this chapter describe this work, including the SPE parameterizations and the NO_x upper boundary conditions.

The horizontal resolution and the number of vertical levels in the model is dependent on the resolution of the external meteorological input data. For example in PUBLICATION I, where ECMWF operational data was used, FinROSE was run with 41 vertical levels ($\sim$0–80 km) and a horizontal resolution of $10^\circ \times 5^\circ$, in PUBLICATION II the model simulation had 35 vertical levels ($\sim$0–65 km) and the same horizontal resolution as in PUBLICATION I, and in PUBLICATION IV with 72 vertical levels ($\sim$0–80 km) and horizontal resolution of $5^\circ \times 4^\circ$.

5.2.1 Parameterization of Solar Proton Events

For investigation of solar proton events (SPEs) impact on the atmosphere (PUBLICATIONS II and IV), a new SPE parameterization was needed for FinROSE. The parameterization is set to replace the complicated ion chemistry related to the interactions between the energetic particles and the neutral atmosphere (Chapter 2). An approach often used in the models is to calculate already in advance the ratio between production rate (P, the number of molecules produced or lost per each produced ion pair) and ionization rate (Q, the number of ionized molecules in a unit of volume). Example of such P/Q ratios is given in Table 5.1.

The whole parameterization scheme in FinROSE is based on detailed calculations of ion chemistry and related P/Q ratios during geomagnetically perturbed conditions. The calculations have been conducted using the Sodankylä Ion and Neutral Chemistry (SIC) model (*Verronen et al.*, 2005, 2006; *Turunen et al.*, 2009), a 1-dimensional model

describing the ion and neutral chemistry between 20 and 150 km, taking into account also the external forcing due to solar flux and EPP. The actual production or loss rates of individual species is calculated during FinROSE simulations by multiplying the P/Q ratio from the SIC model with ionization rate q:

$$\text{Production/Loss} = (\frac{\text{P}}{\text{Q}})_{ratio} * \text{q}. \tag{5.1}$$

Eq. 5.1 is solved on every time step and in every grid point above 20 km altitude level in the geomagnetic polar cap area.

The ionization rate q, used to define the production/loss rates in Eq. 5.1, can be obtained in several different ways, and can differ from that used in SIC in the P/Q ratio calculations. For example in PUBLICATION II, ionization rate q was calculated using the Atmospheric Ionization Module Osnabrück (AIMOS) model (*Wissing and Kallenrode*, 2009) and then adjusted to the FinROSE model grid. In PUBLICATION IV, observed GOES 11 satellite proton flux data was used in order to calculate the ionization rate q with the SIC model (*Verronen et al.*, 2005).

In PUBLICATION II, P/Q ratios were implemented in the family chemistry of FinROSE for HO_x, NO_x, and HNO_3. For NO_x, a constant value based on the work of *Porter et al.* (1976) and *Rusch et al.* (1981) was used. They found that $N(^2D)$ and $N(^4S)$ are produced in ratio 40:60 of the total 1.25 produced N atoms per ion pair. FinROSE does not differentiate between the two excited states of N so the net effect on NO_x needed to be calculated in advance. Taking into account that $N(^2D)$ produces and $N(^4S)$ destroys NO_x (Chapter 2), the net effect and the P/Q ratio for NO_x was set to be 0.25. Adding a basic parameterization also for HNO_3 allowed us to account for processes which are still neglected in many other models. Dismissing the HNO_3 production can lead to underestimation of the SPE related ozone loss (Chapter 2.2.3). However, the parameterization does have its shortcomings as it does not consider the HNO_3 loss mechanisms due to negative ion chemistry and this leads to the overestimation of the SPE related HNO_3 increases in PUBLICATION II.

In PUBLICATION IV, FinROSE utilized a revised version of the parameterization where the loss of species due to ion chemistry, important especially for HNO_3, was taken into account. Instead of calculating only production rates, SIC calculations provided net change rates for the P/Q ratios (Eq. 5.2):

$$(\frac{\text{P}}{\text{Q}}) = \frac{(\text{P}_{\text{SPE}} - \text{L}_{\text{SPE}}) - (\text{P}_{\text{REF}} - \text{L}_{\text{REF}})}{\text{Q}} \tag{5.2}$$

where SPE and REF denote SPE and reference (non-SPE) model simulations, respectively, and L the loss rate due to ion chemistry (*Verronen and Lehmann*, 2013). The new P/Q ratios can be either positive (production) or negative (loss) depending on the altitude, ionization rate and solar zenith angle. The further developed model version (chemistry for short-lived species) enabled also a more detailed implementation of the parameterization in the model, and P/Q ratios were calculated for H, OH, HNO_3, N,

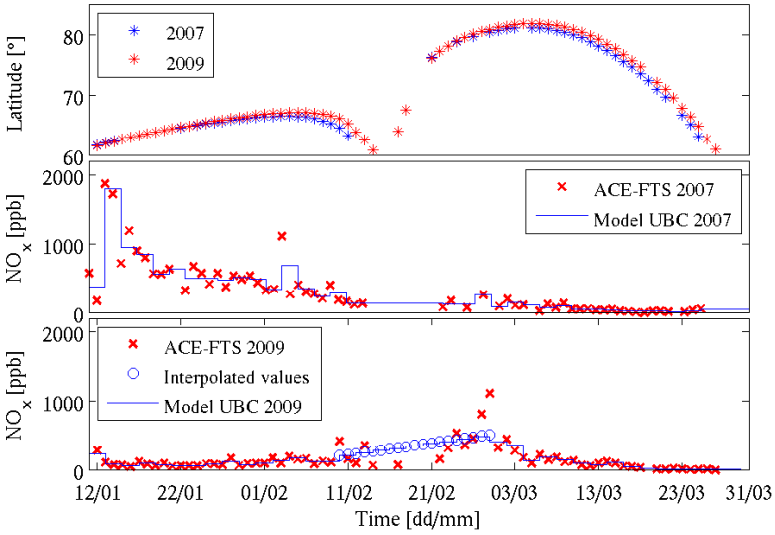

FIGURE 5.3.: Daily medians of the ACE-FTS measurement latitudes for 2007 and 2009 (top), and the NO_x upper boundary condition (UBC) values for 2007 (middle) and 2009 (bottom). The figure also shows the daily medians of the ACE-FTS NO_x observations. Note that in mid- to late-February 2009 the UBC is based on interpolated NO_x values. Figure is from PUBLICATION I.

NO, NO_2, NO_3 and N_2O_5. Therefore, this update introduced the same altitude and solar zenith angle dependence also on the P/Q ratios of NO_x, previously set to a constant value.

5.2.2 NO_x *Upper Boundary Condition*

The purpose of implementing an upper boundary condition (UBC) for NO_x is to represent a thermospheric source of NO_x in FinROSE. Without the UBC, the amount of mesospheric NO_x is significantly underestimated by the model, leading to unrealistic outcome when simulating the enhanced downward transport of NO_x from the lower thermosphere and the related effects. In PUBLICATIONS I and IV, two UBCs with different origins were implemented to FinROSE: in PUBLICATION I the UBC was based on ACE-FTS observations, and in PUBLICATION IV on MIPAS NO_x observations.

For PUBLICATION I the UBC was calculated both for the quiescent winter of 2007 and for the dynamically exceptional year 2009. The UBC from the ACE-FTS observations was obtained as follows: 1) calculation of daily NO_x medians for both winters, 2) calculation of two-day mean NO_x values from the daily medians, and 3) averaging the the two-day mean values over the altitude region of 75–85 km. These values were then implemented in FinROSE and used on every time step for two days

in a row, after which the next two-day mean value was used. In the case of missing values, the previous two-day mean was used. The obtained UBC was implemented only in the Northern polar cap area, i.e. 60°–90°N, and only for the time period of interest (January–March) at the upmost vertical level of FinROSE (0.01 hPa). The UBC values for both winters and zonal average of the ACE-FTS measurement latitudes is presented in Fig. 5.3. Note that between 10–28 February in 2009 the NO_x mixing ratio decreased rapidly according to the observations. This was due to the change of ACE-FTS measurement latitudes towards lower latitudes after early February. At lower latitudes the NO_x concentration is not as substantial as in the higher latitudes, leading to unrepresentative NO_x values in the polar region. Therefore, during that time period it was necessary to use interpolated values for the UBC.

For PUBLICATION IV the NO_x UBC was calculated using a different approach and it was derived for the NO_y family, including HNO_3, NO_2, NO, dinitrogen pentoxide (N_2O_5), and chlorine nitrate ($ClONO_2$) so that it takes into account the amount of excess NO_y produced by EPP. The method used for calculating the UBC is much more advanced than the one used in PUBLICATION I. This includes using a tracer correlation method based on MIPAS methane (CH_4) and carbon monoxide (CO) observations, as well as parameterization in terms of the geomagnetic index A_p and seasonal evolution (*Funke et al.*, 2014a). In principle, the UBC for NO_y is the sum of the model background NO_y and the MIPAS based excess NO_y. The UBC is then interpolated to fit the two upmost vertical levels of the model, i.e. about 75 and 80 km, and introduced in FinROSE on a daily basis northward of 70°.

6 MIDDLE ATMOSPHERE NO_x AND OZONE: ROLES OF SSWS AND SPES

This chapter describes the results of PUBLICATIONS I–IV. In order to assess the roles of SSWs and SPEs in the distribution of middle atmosphere NO_x and its impact on ozone, we need to utilize both atmospheric model simulations and observations. To reach this goal, we take the following stepwise approach, which includes testing the ability of our model to reproduce the state of the atmosphere following major events.

(i) Test the ability of FinROSE to reproduce the enhanced downward transport of NO_x following major SSWs and ES events.

(ii) Test the ability of FinROSE to reproduce the effects of SPEs in the middle atmosphere

(iii) Analyze the observed effects of SPEs and SSWs, both separately and together, on NO_x and ozone in the middle atmosphere.

(iv) Assess the relative importances of transport following SSWs and in-situ production during SPEs on the stratospheric NO_x and ozone.

6.1 DOWNWARD TRANSPORT OF NO_x

Models with a top in the upper mesosphere, such as FinROSE, do not consider the descent of lower thermospheric NO_x, i.e. NO_x outside the model domain, down to the middle atmosphere automatically. In order to assess our objective (i) as presented above and to reproduce the enhanced descent following the major SSW in early 2009, accompanied by an ES event, an UBC (described in Chapter 5.2.2) at the model top needs to be applied.

The meteorological conditions in early 2009 were quite exceptional due to one of the strongest recorded major SSWs taking place on the 24th January (Chapter 3.3 and Fig. 3.3). In PUBLICATION I we ran FinROSE model with the ECMWF operational data as meteorological input. For comparison, the rather stable winter of early 2007 was also analysed. ACE-FTS observations show (Fig. 6.1a) that in the dynamically stable year 2007 the lower edge of the NO_x enhancement extended down to the middle mesosphere, gradually moving above the model upper boundary during the spring. FinROSE results (Fig. 6.1b) replicate the observations, except that the NO_x maximum reached somewhat lower altitudes than observed. In 2009, a tongue-like structure of descending NO_x was visible almost immediately after the SSW and high amounts of NO_x were transported from 80 km down to 55 km with a descent rate of approximately 700 m day^{-1}. It is noteworthy that the descent stopped just above the stratopause and no elevated NO_x levels were observed or simulated in the stratosphere. The modeled

NO_x descent rates are in a good agreement with the observations, although the model underestimates the amount of NO_x reaching the lowest mesosphere by the end of the descent event by ∼10–55%.

Other minor species were also affected by the ES event and the accompanied descent of mesospheric air. Ozone in the same region decreased by 20–30% coinciding with the NO_x descent. In fact, the decrease continued below the stratopause level starting from early March. Analyses of the model results showed that the ozone losses were not driven by the enhanced amounts of NO_x in the middle atmosphere, but rather affected by transport of ozone poor air from altitudes above. Additional ozone loss in the stratosphere was related to the increased amount of solar radiation and the resulting activation of halogen compounds, i.e. a process taking place every spring and leading to the formation of the ozone hole.

Overall, FinROSE succeeds well in reproducing the NO_x descent with no in-situ production included. It has been suggested that meteorological driver data like the one used in PUBLICATION I might have shortcomings in the upper mesosphere (*Manney et al.*, 2008). However, our analysis in PUBLICATION I gave confidence in the use of ECMWF operational data in mesospheric modeling. Although no connection between the MLT NO_x and stratospheric ozone was observed or simulated in early 2009, it can not be disregarded in general. The results of PUBLICATION I show us that the connection might be strongly dependent on the time point of the major SSW: if the SSW takes place in early winter (at latest by early January), NO_x has more time to descend into the stratosphere and influence ozone there. On the other hand, if the SSW occurs later, the NO_x-ozone connection may be weaker. Of course, this is when no in-situ production of NO_x due to EPP takes place.

6.2 COMPOSITION CHANGES FOLLOWING SPES

PUBLICATION II was the result of the first international model-measurement intercomparison study undertaken by the HEPPA (High Energy Particle Precipitation in the Atmosphere) research community. The aim of the study was to simulate the historical "Halloween" SPE event, that took place in late October–early November 2003. Alltogether 11 atmospheric models took part and results were analyzed to test the ability of the different models to reproduce the atmospheric effects of the SPE. Our objective (ii) is thus of great importance in order to understand the solar-induced atmospheric variability on short and mid-term time scales. The results were compared with satellite observations from the MIPAS instrument.

The model results and observations all showed increased instantaneous amounts of NO_y in the regions poleward of 40°N. The agreement between the models and the observations was reasonable in general, within 50%, both in the stratosphere and mesosphere, although a systematic overestimation around 1 hPa was evident in all participating models. This overestimation was likely due to the ionization rates profile from the

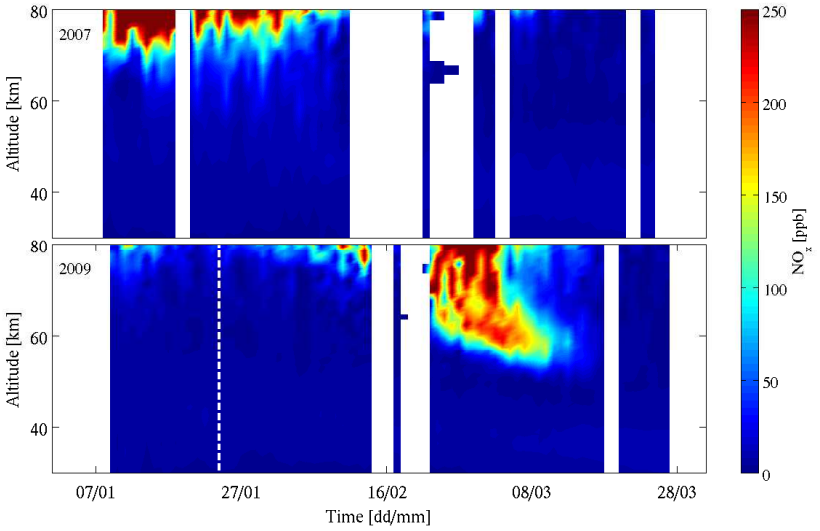

(a)

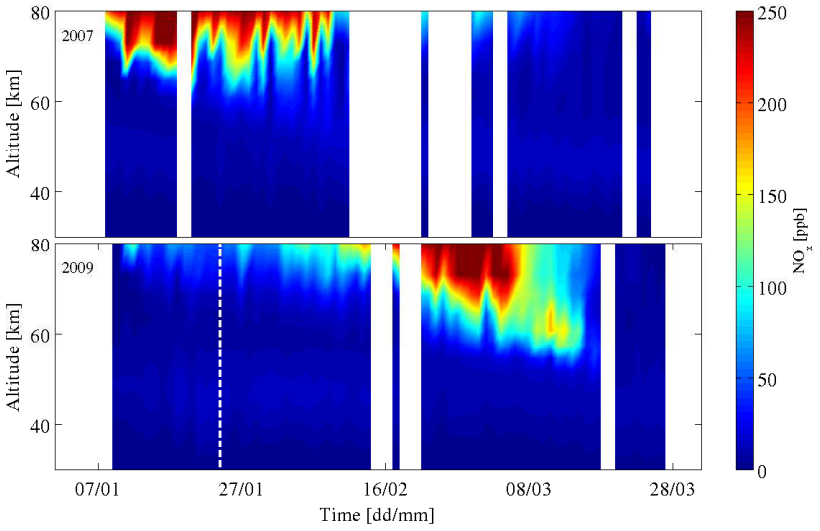

(b)

FIGURE 6.1.: (a) Daily median NO_x observed by ACE-FTS north of 60°N in 2007 (top panel) and 2009 (bottom panel). The white dashed line indicates the time point of the major SSW. (b) Same as (a), but calculated from FinROSE results using only the model grid points corresponding to ACE-FTS measurement locations. Figures from PUBLICATION I.

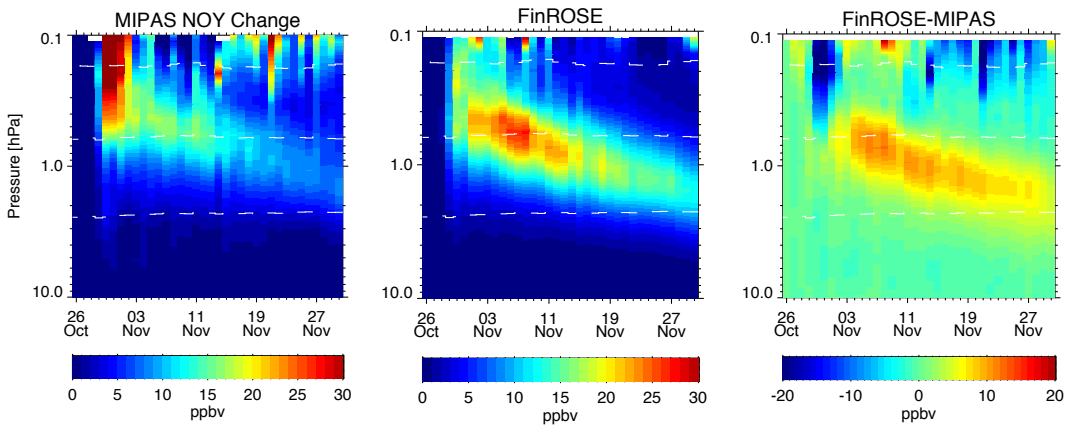

FIGURE 6.2.: Area weighted averages (40–90°N) of NO_y with respect to the onset date of the SPE according MIPAS (left) and FinROSE (middle). The figure also shows the absolute difference (ppbv) between these two (right). Original figure can be found in PUBLICATION II.

AIMOS model and uncertainties related to that. A large spread (up to 100%) between the models was evident but expected due to the different reaction paths for atomic nitrogen, background states of the atmosphere, and dynamics in the models. The impact of different dynamics was distinct already in October during the SPE, leading to significant spread of the model results: some models showed increased NO_y amounts north of 50°N whereas some models showed increases only north of 70°N, despite all models having the same source region for NO_y in-situ production. This implies that the response of the real atmosphere to SPEs is strongly dependent on atmospheric conditions at the time. The magnitude of descending NO_y inside the polar vortex was overestimated by most of the models due to the differences in the NO_y production during the proton forcing. However, the vertical distribution and the relative increase of NO_y was well reproduced by all the models. Fig. 6.2 shows the observed NO_y increase and its descent as well as the FinROSE results for this particular case. The performance of FinROSE was reasonable and the results found to be very close to the multi-model average of NO_y.

Instant HNO_3 enhancements during the Halloween event were generally underestimated by all the models. This was expected since most models did not account for the HNO_3 formation via ion-ion recombination processes. Only two models, FinROSE included, took this into account. In FinROSE, the ion chemistry (*Verronen et al.*, 2008) was taken into account in the SPE parameterization scheme, meaning that no actual ions or ion chemistry where added into the model. This led to HNO_3 overestimation by a factor of three. One possible explanation for the overestimation was that FinROSE, where no ions are included, used a parameterization calculated using a full ion chemistry scheme. However, the results emphasize the importance of inclusion of ion chemistry in models.

Ozone losses related to the Halloween event were simulated poleward of 60°N, in agreement with the proton forcing implemented in the models. The models showed generally more pronounced ozone loss compared with the MIPAS observations (Fig. 6.3). However, especially the mesospheric ozone decrease was well produced by most of the models indicating a very good overall ability of the models to reproduce the HO_x related ozone loss. Taking into account the differences in the modeled NO_y, more spread in the stratospheric ozone losses was evident, although the losses were still in a good agreement with the observations. The multi-model average shows that both the short-term (HO_x) and longer-term (NO_x) changes in the modeled ozone are within about 5% of the observations, indicating an excellent agreement. FinROSE was, again, very close to the multi-model average.

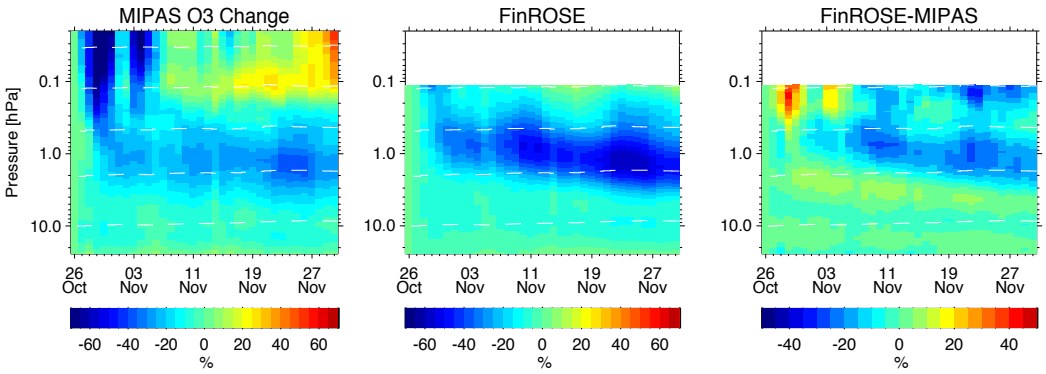

FIGURE 6.3.: Similar type of comparison as presented in Fig. 6.2, but for ozone. Original figure can be found in PUBLICATION II.

6.3 OBSERVED EFFECTS OF SSWS AND SPES

PUBLICATIONS I and II demonstrate the ability of FinROSE to reproduce the effects of SPEs and major SSWs separately. In PUBLICATION III three winters were compared: 1) 2005 with a SPE and in-situ production of NO_x, 2) 2009 with enhanced NO_x descent down to the middle atmosphere following a major SSW, and 3) 2012 with *both* of these effects. Our objective (iii) is to contrast, using observations alone, the separate effects of SPEs and SSWs, but also to look into the combined effects of these two types of events if they occur simultaneously, i.e. is there a more pronounced effect?

The existence of the wintry polar vortex is essential in order to get NO_x transported down to the stratosphere. During the winters of 2005, 2009 and 2012, the polar vortex formed or was already formed in December. The dynamical analyses showed that the mesospheric air descended down to about 25 km (descent rate of 380 m day^{-1}), 60 km (570 m day^{-1}), and 50 km (520 m day^{-1}) by mid-March in 2005, 2009 and 2012, respectively. NO_x increases related to the SPEs and SSWs were observed in every year, the most substantial mesospheric effect taking place in 2009 (SSW) and stratospheric effect in 2012 (SPEs + SSW). In fact, the amount of NO_x was actually higher in the

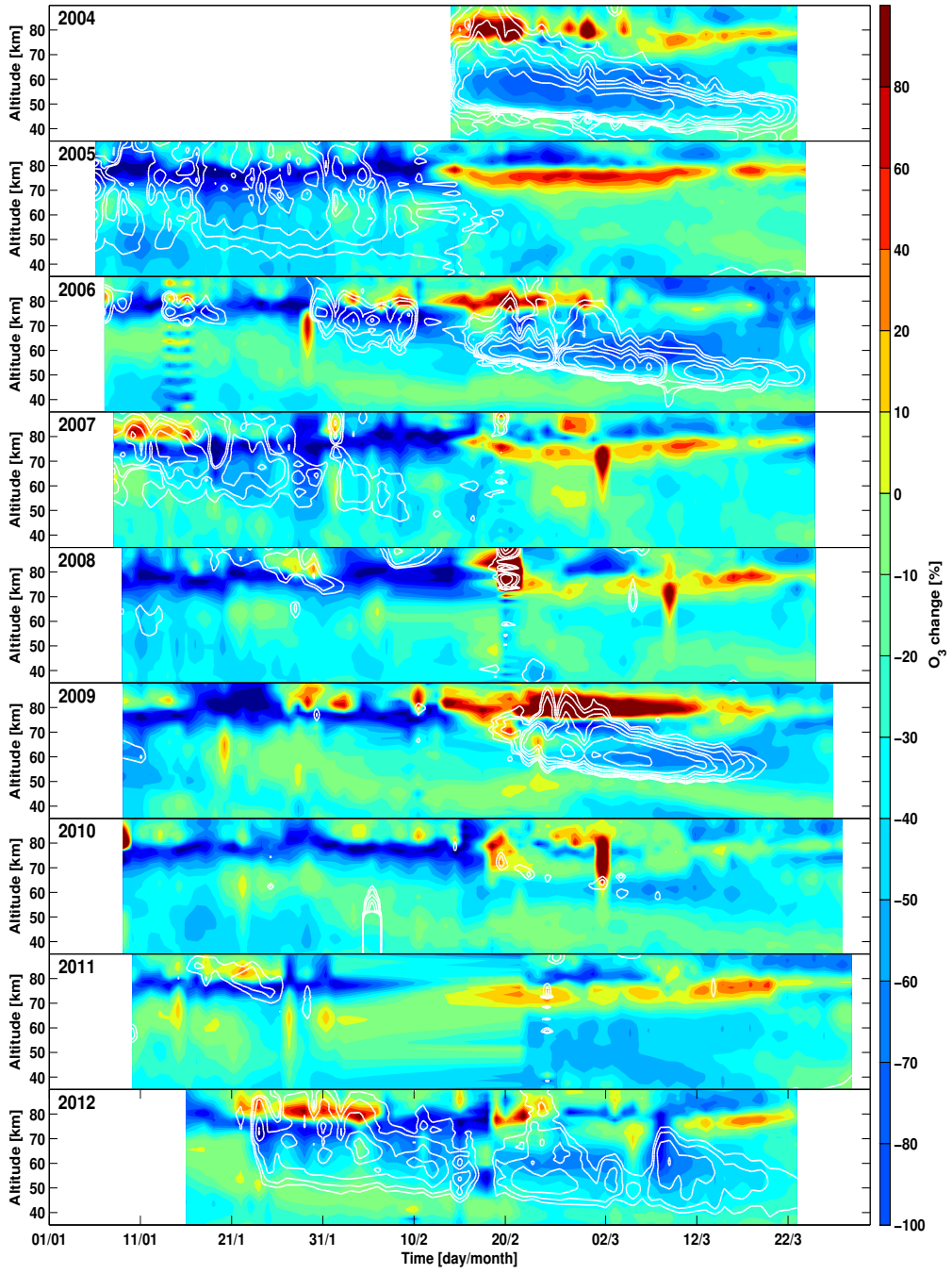

FIGURE 6.4.: Change (%) in O_3 as shown by ACE-FTS in 2004–2012. The changes are relative to the January–March mean in 2007–2008 northward of 60°N. The overlaid contours are values of positive NO_x changes (50, 100, 200, 400, 600, 1000, and 2000%) relative to the same period. Figure from PUBLICATION III.

altitude region of 46–56 km during years with a SSW, at least in the time period of 2005–2012. Compared to SPEs, the higher NO_x values following SSWs were visible in the middle atmosphere with a delay of about two months due to the time needed for NO_x to descend from mesospheric altitudes down to the stratopause region.

The effect on ozone was clear during all of the considered winters, both after SPEs and SSWs (Fig. 6.4). Ozone losses of up to 90% took place, the strongest destruction occurring in the mesosphere, often coinciding with the enhanced amounts of NO_x. The short-term losses lasting only few days can be clearly attributed to the dominant effect of HO_x in the mesosphere. Understanding the longer-term ozone changes in the mesosphere-upper stratosphere is not as straightforward. NO_x dominates the ozone loss cycles in the stratosphere (Chapter 2), but on longer time scales atmospheric dynamics play an important role in determining the vertical distribution of species with long photochemical lifetimes. Therefore, using observations only, it is challenging to separate the relative contributions of in-situ production and downward transport of NO_x on the middle atmospheric ozone balance.

Although the NO_x amounts in the middle atmosphere were increased by the SPEs and SSW in 2012, the combined effect did not lead to a clear NO_x dominated signal in ozone in the stratosphere. It is noteworthy that the SPEs 1) were only small/medium in strength, and 2) took place during solar minimum conditions when the background production of NO_x in the upper atmosphere is very low. Additionally, the timing of the SSW (end of January) was rather late and provided only limited amount of time for efficient amounts of NO_x to descend down to the stratosphere. The main result of PUBLICATION III was that the combination of optimal dynamics (SSW) and in situ production of NO_x (SPE) does not necessarily lead to longer-term NO_x dominated ozone losses in the stratosphere. The timing of the SSW and the background NO_x production, which is higher during and after solar maximum conditions, could actually be the determining factor of the possible NO_x-ozone connection in the middle atmosphere.

6.4 CONTRIBUTIONS OF TRANSPORT AND IN-SITU PRODUCTION ON NO_x AND OZONE

The goal of PUBLICATION IV, and also our objective (iv), was to assess the relative contributions of intensified downward transport following the strong SSW and in situ production of NO_x during the SPEs in early 2012 to the stratospheric ozone balance using FinROSE. For this study, FinROSE was used with the MERRA data as input for the dynamics. In PUBLICATION III we showed that longer-term (weeks/months) changes in middle atmospheric ozone took place in 2012 coinciding with the enhanced amounts of NO_x, but it was not possible to determine the separate contributors (SSW versus SPE) to the observed ozone losses. PUBLICATION IV concentrated on 1) model-measurement comparison in order to find out how reliable FinROSE results during this time period are, and 2) the actual contribution analysis performed with FinROSE. De-

tailed discussion on the SPE parameterization and the NO_x upper boundary condition (UBC) can be found in Chapters 5.2.1 and 5.2.2, respectively.

Comparison of FinROSE results with MIPAS observations showed that the simulated NO_x is in reasonable agreement with the observations. However, FinROSE overestimated the amount of descending and in situ produced NO_x, also leading to possibly overestimated effects of the NO_x related ozone losses. Moreover, the background levels of ozone were clearly lower in the model to start with, indicating that even small relative changes would lead to overestimation of the losses. One possible reason for the differences between the model and observations is the MIPAS based UBC, which does not take into account the effect from the SPEs, but also the meteorological data used as a input for the dynamics in the model. Still, implementation of the UBC and inclusion of the SPE parameterization improved the agreement between the model and observations drastically, both for NO_x and ozone.

PUBLICATION IV also assessed the overall behaviour of HNO_3. For this study, an improved and revised version of the HNO_3 parameterization was used instead of the earlier one used in PUBLICATION II. As discussed in Chapter 6.3, FinROSE was the one of the two models that took the HNO_3 parameterization into account in the studies for PUBLICATION II, but overestimated the HNO_3 production during the Halloween SPEs by a factor of three. The new parameterization in PUBLICATION IV, now for the early 2012 events, still led into an overestimation, but it was reduced down to a factor of 1.2, indicating a significant improvement in the parameterization.

The contribution analysis conducted utilizing the model results implied that the largest mesospheric NO_x enhancements took place after implementing the UBC in the model (Fig. 6.5a). The SPE parameterization, in turn, instantaneously affected all the middle atmospheric altitudes, the effect lasting for up to a month, especially in the stratosphere. The most substantial ozone losses ($< 90\%$) were simulated in the mesosphere during and shortly (few days) after the SPEs, closely related to the dominating HO_x chemistry in that region (Fig. 6.5b). In the stratosphere the indirect UBC effect (downward transport of NO_x) brought larger amounts of NO_x below the stratopause level than the direct effect from the SPEs, also leading to more substantial ozone losses (UBC 17%, SPE 9%) in that region. Taking into account the strength of the SPEs and the weak solar maximum condition, the results of PUBLICATION IV emphasize the importance of middle atmospheric dynamics in the stratospheric NO_x-ozone connection.

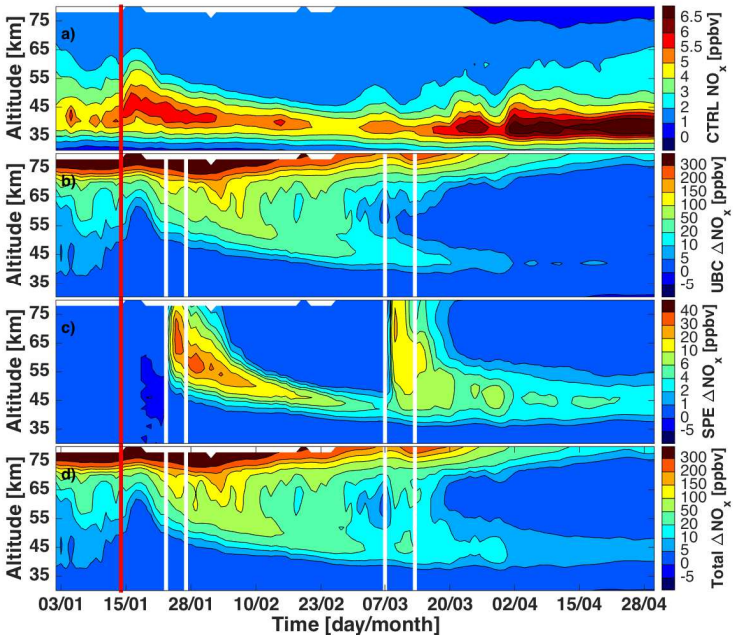

(a)

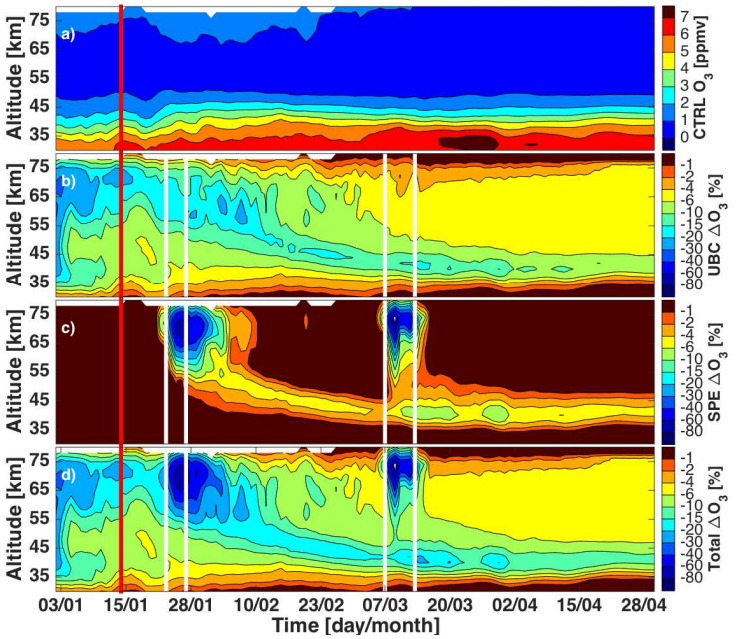

(b)

FIGURE 6.5.: (a) FinROSE NO_x in early 2012. a) Background NO_x b) NO_x changes due to the implementation of the UBC c) Effect of the SPE parameterization d) Total effect due to the implementation of the UBC and SPE parameterization compared with the background NO_x. (b) Similar type of comparison as presented in (a), but for ozone. Figures from PUBLICATION IV.

7 Future Prospects

The scientific objective of this work was to study the effects that SPEs and SSWs have on the middle atmospheric composition by assessing the respective and combined impacts of these events. Especially the combined effects were of great interest in order to find out if the NO_x–ozone connection between the MLT and stratosphere becomes more distinct during periods of intensified downward transport of NO_x together with in-situ production of NO_x.

The results of this work show the significant effect of solar forcing on the atmospheric composition of the middle atmosphere, and the role of atmospheric dynamics in modulating the effect in the Northern polar region. This raises the question, should the solar forcing in the form of EPP be included in all atmospheric models including a scheme for chemistry in the middle atmosphere? Inclusion of EPP and the following changes in the dynamics of the middle atmosphere would provide an additional pathway for the coupling between the middle atmosphere and troposphere. This could also improve the outcome of model simulations spanning from seasonal (the profound effect during polar winter) to decadal (solar cycle) time scales, eventually contributing even to the accuracy of climate predictions. So far, the Intergovernmental Panel on Climate Change (IPCC), the international body for assessing the science related to climate change, has recognised the solar forcing in the form of solar irradiance, but the effect of EPP is not well established (*IPCC*, 2013).

Although the first EPP effects were observed in the 1950s, research in the topic is still very much in progress. Today, the chemical response of the middle atmosphere to EPP events is fairly well understood, and the hot spot of research has moved towards the dynamical and surface responses. Research utilizing data ranging from model simulations to meteorological analyses have been conducted showing a solar signal at the surface level in the polar regions (e.g. *Rozanov et al.*, 2005; *Seppälä et al.*, 2009; *Baumgaertner et al.*, 2011; *Rozanov et al.*, 2012; *Arsenovic et al.*, 2016). The mechanism providing the signal with means to propagate from the middle atmosphere down to the troposphere is still not yet fully understood and is an important science question for the future studies of EPP–middle atmosphere–troposphere interaction in the sense of dynamics. One likely explanation for the detected surface signal is linked to the interaction between the atmospheric waves and the mean flow (e.g. *Lu et al.*, 2008; *Seppälä et al.*, 2013).

The profound effect of SSWs on atmospheric dynamics is known to affect the propagation of the EPP signal. Studies have shown (*Seppälä et al.*, 2013, and other references above) that by excluding SSWs from analysis the ground-level signal becomes clearer. Still, SSWs are a fairly frequent phenomenon of the Northern polar atmosphere, and in optimal conditions also capable of intensifying the EPP effect (descent of NO_x) in the middle atmosphere. In order to reach a comprehensive understanding of the im-

portance of the processes taking place following SSWs in periods of high geomagnetic activity, including the NO_x–ozone connection, more work needs to be done.

One significant challenge for the scientific community focusing on the middle atmosphere is the dramatic decrease in the number of satellites observing the middle atmosphere in the future. New satellite missions need to be planned and carried out in order to maintain the level of observations sufficient for reliably assess the atmospheric composition during both quiet and disturbed conditions in the middle atmosphere. Atmospheric models will continue providing us information also in the future, but the results need to be continuously verified with satellite measurements so that we know they are representing the atmosphere in the correct manner. This includes making sure that any future satellite missions take into account measurements of a wider range of species, including NO_x and HO_x.

BIBLIOGRAPHY

Andrews, D. G., J. R. Holton, and C. B. Leovy (1987), *Middle atmosphere dynamics.*, 259–260 pp., Academic Press, New York, NY, USA.

Arsenovic, P., E. Rozanov, A. Stenke, B. Funke, J. M. Wissing, K. Mursula, F. Tummon, and T. Peter (2016), The influence of middle range energy electrons on atmospheric chemistry and regional climate, *J. Atmos. Sol.-Terr. Phys.*, doi: 10.1016/j.jastp.2016.04.008.

Barth, C. A. (1992), Nitric oxide in the lower thermosphere, *Planet. Space Sci.*, *40*, 315-336.

Baumgaertner, A. J. G., A. Seppälä, P. Jöckel, and M. A. Clilverd (2011), Geomagnetic activity related NO_x enhancements and polar surface air temperature variability in a chemistry climate model: modulation of the NAM index, *Atmos. Chem. Phys.*, *11*, 4521–4531, doi:10.5194/acp-11-4521-2011.

Bernath, P. F., et al. (2005), Atmospheric Chemistry Experiment (ACE): Mission overview, *Geophys. Res. Lett.*, *3*, L15S01, doi:10.1029/2005GL022386.

Brasseur, G. P., and S. Solomon (2005), *Aeronomy of the Middle Atmosphere*, 3rd revised and enlarged ed., Springer, Dordrecht.

Callaghan, P. F., and M. L. Salby (2001), Three-Dimensionality and Forcing of the Brewer-Dobson Circulation., *J. Atmos. Sci.*, *59*, 976-991.

Chandran, A., R. L. Collins, R. R. Garcia, D. R. Marsh, V. L. Harvey, J. Yue, and L. de la Torre (2013), A climatology of elevated stratopause events in the whole atmosphere community climate model, *J. Geophys. Res.*, *118*, 1234–1246, doi: 10.1002/jgrd.50123.

Chandran, A., R. L. Collins, and V. L. Harvey (2014), Stratosphere-mesosphere coupling during stratospheric sudden warming events, *Adv. Space Res.*, *53*, 1265–1289, doi:10.1016/j.asr.2014.02.005.

Chapman, S. (1930), On ozone and atomic oxygen in the upper atmosphere, *Phil. Mag.*, *10*, 369–387.

Charlton, A. J., and L. M. Polvani (2007), A New Look at Stratospheric Sudden Warmings. Part I: Climatology and Modeling Benchmarks, *Journal of Climate*, *20*, 449, doi:10.1175/JCLI3996.1.

Chau, J. L., L. P. Goncharenko, G. G. Fejer, and H.-L. Liu (2012), Equatorial and Low Latitude Ionospheric Effects During Sudden Stratospheric Warming Events, *Space Sci Rev*, *168*, 385–417, doi:10.1007/s11214-011-9797-5.

Damski, J., L. Thölix, L. Backman, J. Kaurola, P. Taalas, J. Austin, N. Butchart, and M. Kulmala (2007), A chemistry-transport model simulation of middle atmospheric ozone from 1980 to 2019 using coupled chemistry GCM winds and temperatures, *Atmospheric Chemistry & Physics*, *7*, 2165-2181.

Dowdy, A. J., R. A. Vincent, D. J. Murphy, M. Tsutsumi, D. M. Riggin, and M. J. Jarvis (2004), The large-scale dynamics of the mesosphere–lower thermosphere during the Southern Hemisphere stratospheric warming of 2002, *Geophys. Res. Lett.*, *31*, L14102, doi:10.1029/2004GL020282.

Duck, T. J., J. A. Whiteway, and A. I. Carswell (2001), The Gravity Wave–Arctic Stratospheric Vortex Interaction, *J. Atmos. Sci.*, *58*, 3581–3596.

Ern, M., et al. (2016), Satellite observations of middle atmosphere gravity wave absolute momentum flux and of its vertical gradient during recent stratospheric warmings, *Atmos. Chem. Phys.*, *16*(15), 9983–10019, doi:10.5194/acp-16-9983-2016.

Farman, J. C., B. G. Gardiner, and J. D. Shanklin (1985), Large losses of total ozone in antarctica reveal seasonal ClO_x/NO_x interaction, *Nature*, *315*, 207–210.

Fischer, H., et al. (2008), MIPAS: an instrument for atmospheric and climate research, *Atmos. Chem. Phys.*, *8*, 2151–2188.

Fritts, D. C., and M. J. Alexander (2003), Gravity wave dynamics and effects in the middle atmosphere, *Reviews of Geophysics*, *41*, 1003-+, doi:10.1029/2001RG000106.

Funke, B., M. López-Puertas, S. Gil-Lopez, T. von Clarmann, G. P. Stiller, H. Fischer, and Kellmann (2005), Downward transport of upper atmospheric NOx into the polar stratosphere and lower mesosphere during the Antarctic 2003 and Arctic 2002/2003 winters, *J. Geophys. Res.*, *110*(D24), D24308, doi:10.1029/2005JD006463.

Funke, B., M. López-Puertas, D. Bermejo-Pantaleón, M. Garcia-Comas, G. P. Stiller, T. von Clarmann, M. Kiefer, and A. Linden (2010), Evidence for dynamical coupling from the lower atmosphere to the thermosphere during a major stratospheric warming, *Geophys. Res. Lett.*, *37*, L13803, doi:10.1029/2010GL043619.

Funke, B., M. López-Puertas, L. Holt, C. E. Randall, G. P. Stiller, and T. von Clarmann (2014a), Hemispheric distributions and interannual variability of NO_y produced by energetic particle precipitation in 2002–2012, *J. Geophys. Res.*, *119*, 13565–13582, doi:10.1002/2014JD022423.

Funke, B., M. López-Puertas, G. P. Stiller, and T. von Clarmann (2014b), Mesospheric and stratospheric NO_y produced by energetic particle precipitation during 2002–2012, *J. Geophys. Res.*, *119*, 4429–4446, doi:10.1002/2013JD021404.

Gong, J., D. L. Wu, and S. D. Eckermann (2012), Gravity wave variances and propagation derived from AIRS radiances, *Atmos. Chem. Phys.*, *12*, 1701–1720, doi: 10.5194/acp-12-1701-2012.

Harvey, V. L., C. E. Randall, and M. H. Hitchman (2009), Breakdown of potential vorticity-based equivalent latitude as a vortex-centered coordinate in the polar winter mesosphere, *J. Geophys. Res.*, *114*, D22105, doi:10.1029/2009JD012681.

Hauchecorne, A., J.-L. Bertaux, F. Dalaudier, J. M. Russell, M. G. Mlynczak, E. Kyrölä, and D. Fussen (2007), Large increase of NO_2 in the north polar mesosphere in January-February 2004: Evidence of a dynamical origin from GOMOS/ENVISAT and SABER/TIMED data, *Geophys. Res. Lett.*, *34*, L03810, doi: 10.1029/2006GL027628.

Haynes, P. H., C. J. Marks, M. E. McIntyre, T. G. Shepherd, and K. P. Shine (1991), On the 'Downward Control' of Extratropical Diabatic Circulations by Eddy-Induced Mean Zonal Forces, *J. Atm. Sci.*, *48(4)*, 651–678.

Hoffmann, P., W. Singer, D. Keuer, W. K. Hocking, M. Kunze, and Y. Murayama (2007), Latitudinal and longitudinal variability of mesospheric winds and temperatures during stratospheric warming events, *Journal of Atmospheric and Solar-Terrestrial Physics*, *69*, doi:http://dx.doi.org/10.1016/j.jastp.2007.06.010.

Holton, J. R. (1983), The influence of gravity wave breaking on the general circulation of the middle atmosphere, *J. Atm. Sci.*, *40*(10), 2497-2507.

Holton, J. R. (2004), *An Introduction to Dynamic Meteorology*, 4th ed., Elsevier Academic Press, ISBN: 0-12-354016-X.

Holton, J. R., and M. J. Alexander (2000), *The Role of Waves in the Transport Circulation of the Middle Atmosphere*, in Atmospheric Science Across the Stratopause (eds D. E. Siskind, S. D. Eckermann and M. E. Summers, American Geophysical Union, Washington, D. C., doi:10.1029/GM123p0021.

IPCC (2013), *Climate Change 2013: The Physical Science Basis*, Cambridge University Press, Cambridge, UK.

Jackman, C. H., M. T. DeLand, G. J. Labow, E. L. Fleming, D. K. Weisenstein, M. K. W. Ko, M. Sinnhuber, and J. M. Russell (2005), Neutral atmospheric influences of the solar proton events in October-November 2003, *J. Geophys. Res.*, *110*, A09S27, doi:10.1029/2004JA010888.

Jackman, C. H., D. R. Marsh, F. M. Vitt, R. R. Garcia, C. E. Randall, E. L. Fleming, and S. M. Frith (2009), Long-term middle atmospheric influence of very large solar proton events, *J. Geophys. Res.*, *114*, D11304, doi:10.1029/2008JD011415.

Karlsson, B., H. Körnich, and J. Gumbel (2007), Evidence for interhemispheric stratosphere-mesosphere coupling derived from noctilucent cloud properties, *Geophys. Res. Lett.*, *34*, L16806, doi:10.1029/2007GL030282.

Kylling, A., A. Albold, and G. Seckmeyer (1997), Transmittance of a cloud is wavelength – dependent in the uv-range: Physical interpretation, *Geophys. Res. Lett.*, *24(4)*, 397–400, doi:doi:10.1029/97GL00111.

Lee, J. N., D. L. Wu, G. L. Manney, and M. J. Schwartz (2009), Aura Microwave Limb Sounder observations of the Northern Annular Mode: From the mesosphere to the upper troposphere, *J. Geophys. Res.*, *36*, L20807, doi:10.1029/2009GL040678.

Limpasuvan, V., J. H. Richter, Y. J. Orsolini, F. Stordal, and O.-K. Kvissel (2012), The roles of planetray and gravity waves during a major stratospheric sudden warming as characterized in waccm, *J. Atmos. Sol.-Terr. Phys.*, *78–79*, 84–98, doi: 10.1016/j.jastp.2011.03.004.

Liu, H.-L., and R. G. Roble (2002), A study of a self-generated stratospheric sudden warming and its mesospheric–lower thermospheric impacts using the coupled TIME-GCM/CCM3, *J. Geophys. Res.*, *107*(D23), doi:10.1029/2001JD001533.

López-Puertas, M., B. Funke, S. Gil-López, T. von Clarmann, G. P. Stiller, M. Höpfner, S. Kellmann, H. Fischer, and C. H. Jackman (2005), Observation of NO_x enhancement and ozone depletion in the northern and southern hemispheres after the October-November 2003 solar proton events, *J. Geophys. Res.*, *110*, A09S43, doi: 10.1029/2005JA011050.

Lu, H., M. A. Clilverd, A. Seppälä, and L. L. Hood (2008), Geomagnetic perturbations on stratospheric circulation in late winter and spring, *J. Geophys. Res.*, *113*, D16106, doi:10.1029/2007JD008915.

Manney, G. L., R. W. Zurek, A. O'Neill, and R. Swinbank (1994), On the Motion of Air through the Stratospheric Polar Vortex., *J. Atmos. Sci.*, *51*, 2973-2994.

Manney, G. L., et al. (2008), The evolution of the stratopause during the 2006 major warming: Satellite data and assimilated meteorological analyses, *J. Geophys. Res.*, *113*, D11115, doi:10.1029/2007JD009097.

Manney, G. L., M. J. Schwartz, K. Krüger, M. L. Santee, S. Pawson, J. N. Lee, W. H. Daffer, R. A. Fuller, and N. J. Livesey (2009), Aura Microwave Limb Sounder observations of dynamics and transport during the record-breaking 2009 Arctic stratospheric major warming, *Geophys. Res. Lett.*, *36*, L12815, doi: 10.1029/2009GL038586.

Matsuno, T. (1971), A dynamical model of the sudden stratospheric warming, *Journal of Atmospheric Sciences*, *28*, 1479–1494.

Meraner, K., and H. Schmidt (2016), Transport of nitrogen oxides through the winter mesopause in HAMMONIA, *J. Geophys. Res.*, *121*(6), 2556–2570, doi: 10.1002/2015JD024136.

Mitchell, D. M., A. J. Charlton-Perez, and L. J. Gray (2011a), Characterizing the variability and extremes of the stratospheric polar vortices using 2d moment analysis, *J. Atmos. Sci.*, *68*, 1194–1213, doi:10.1175/2010JAS3555.1.

Mitchell, D. M., L. J. Gray, and A. J. Charlton-Perez (2011b), The structure and evolution of the stratospheric vortex in response to natural forcings, *J. Geophys. Res.*, *116*, D15110, doi:10.1029/2011JD015788.

Mitchell, D. M. M., L. J. Gray, J. Anstey, M. P. Baldwin, and A. J. Chartlon-Perez (2013), The influence of stratospheric vortex displacements and splits on surface climate, *Journal of Climate*, *26*(8), 2668-2682, doi:10.1175/JCLI-D-12-00030.1.

Miyoshi, Y., H. Fujiwara, H. Jin, and H. Shinagawa (2014), A global view of gravity waves in the thermosphere simulated by a general circulation model, *J. Geophys. Res.*, *119*, 5807–5820, doi:10.1002/2014JA019848.

Mlynczak, M. G. (1997), Energetics of the mesosphere and lower thermosphere and the SABER experiment, *Advance in Space Research*, *20*, 1177–1183.

Nakagawa, K. I., and K. Yamazaki (2006), What kind of stratospheric sudden warming propagates to the troposphere?, *Geophys. Res. Lett.*, *33*(4), L04801, doi: 10.1029/2005GL024784.

Newchurch, M. J., E.-S. Yang, D. M. Cunnold, G. C. Reinsel, J. M. Zawodny, and J. M. Russell (2003), Evidence for slowdown in stratospheric ozone loss: First stage of ozone recovery, *Journal of Geophysical Research (Atmospheres)*, *108*, 4507, doi: 10.1029/2003JD003471.

Orsolini, Y. J., J. Urban, and D. P. Murtagh (2009), Nitric acid in the stratosphere based on Odin observations from 2001 to 2007 - Part 2: High-altitude polar enhancements, *Atmos. Chem. Phys.*, *9*, 7045–7052, doi:10.5194/acp-9-7045-2009.

Orsolini, Y. J., J. Urban, D. P. Murtagh, S. Lossow, and V. Limpasuvan (2010), Descent from the polar mesosphere and anomalously high stratopause observed in 8 years of water vapor and temperature satellite observations by the odin sub-millimeter radiometer, *J. Geophys. Res.*, *115*, D12305, doi:doi:10.1029/2009JD013501.

Pérot, K., J. Urban, and D. P. Murtagh (2014), Unusually strong nitric oxide descent in the Arctic middle atmosphere in early 2013 as observed by Odin/SMR, *Atmos. Chem. Phys.*, *14*(15), 8009–8015, doi:10.5194/acp-14-8009-2014.

Plumb, R. A. (2002), Stratospheric transport, *J. Meteor. Soc. Japan*, *80*, 793-809.

Plumb, R. A., and J. Eluszkiewicz (1999), The brewer–dobson circulation: Dynamics of the tropical upwelling, *J. Atmos. Sci.*, *56*, 868–890.

Porter, H. S., C. H. Jackman, and A. E. S. Green (1976), Efficiencies for production of atomic nitrogen and oxygen by relativistic proton impact in air, *J. Chem. Phys.*, *65*, 154–167.

Randall, C. E., V. L. Harvey, D. E. Siskind, J. France, P. F. Bernath, C. D. Boone, and K. A. Walker (2009), NO_x descent in the Arctic middle atmosphere in early 2009, *Geophys. Res. Lett.*, *36*, L18811, doi:10.1029/2009GL039706.

Richardson, I. G., E. W. Cliver, and H. V. Cane (2000), Sources of geomagnetic activity over the solar cycle: Relative importance of coronal mass ejections, high speed streams, and slow solar wind, *J. Geophys. Res.*, *105*(A8), 18203âĂŞ18213.

Richter, J. H., F. Sassi, and R. R. Garcia (2010), Toward a physically based gravity wave source parameterization in a general circulation model, *J. Atm. Sci.*, *67*(1), 136–156, doi:10.1175/2009JAS3112.1.

Rienecker, M. M., et al. (2011), MERRA: NASA's Modern-Era Retrospective Analysis for Research and Applications, *Journal of Climate*, *24*, 3624-3648, doi: 10.1175/JCLI-D-11-00015.1.

Rong, P. P., J. M. Russell, M. G. Mlynczak, E. E. Remsberg, B. T. Marshall, L. L. Gordley, and M. López-Puertas (2009), Validation of Thermosphere Ionosphere Mesosphere Energetics and Dynamics/Sounding of the Atmosphere using Broadband Emission Radiometry (TIMED/SABER) v1.07 ozone at 9.6 μm in altitude range 15-70 km, *J. Geophys. Res.*, *114*, D04306, doi:10.1029/2008JD010073.

Roy, I., and J. D. Haigh (2011), The influence of solar variability and the quasi-biennial oscillation on lower atmospheric temperatures and sea level pressure, *Atmos. Chem. Phys.*, *11*, 11679–11687, doi:10.5194/acp-11-11679-2011.

Rozanov, E., L. Callis, M. Schlesinger, F. Yang, N. Andronova, and V. Zubov (2005), Atmospheric response to NO_y source due to energetic electron precipitation, *Geophys. Res. Lett.*, *32*, L14811, doi:10.1029/2005GL023041.

Rozanov, E., M. Calisto, T. Egorova, T. Peter, and W. Schmutz (2012), The influence of precipitating energetic particles on atmospheric chemistry and climate, *Surveys in Geophys.*, *33*, 483-501, doi:10.1007/s10712-012-9192-0.

Rusch, D. W., J.-C. Gérard, S. Solomon, P. J. Crutzen, and G. C. Reid (1981), The effect of particle precipitation events on the neutral and ion chemistry of the middle atmosphere – I. Odd nitrogen, *Planet. Space Sci.*, *29*, 767–774.

Russell, I., J. M., M. G. Mlynczak, L. L. Gordley, J. Tansock, and R. Esplin (1999), An overview of the saber experiment and preliminary calibration result, *Proc. Soc. Photo-Opt. Instrum. Eng.*, *3756*, 277–288.

Sander, S. P., et al. (2006), *Chemical kinetics and photochemical data for Use in Atmospheric Studies, Evaluation Number 15*, JPL Publication 06-2, Jet Propulsion Laboratory, California Institute of Technology, Pasadena, USA.

Scheiben, D., C. Straub, K. Hocke, P. Forkman, and N. Kämpfer (2012), Observations of middle atmospheric h_2o and o_3 during the 2010 major sudden stratospheric warming by a network of microwave radiometers, *Atmos. Chem. Phys.*, *12*, 7753–7765, doi:10.5194/acp-12-7753-2012.

Scherhag, R. (1952), Die explosionsartigen stratosphärenerwärmungen des spätwinters 1951/52, *Berichte des Deutschen Wetterdienstes in de US zone*, *38*, 51–63.

Schoeberl, M. R., L. R. Lait, P. A. Newman, and J. E. Rosenfield (1992), The structure of the polar vortex, *J. Geophys. Res.*, *97*, 7859–7882.

Seppälä, A., P. T. Verronen, E. Kyrölä, S. Hassinen, L. Backman, A. Hauchecorne, J. L. Bertaux, and D. Fussen (2004), Solar proton events of October-November 2003: Ozone depletion in the Northern Hemisphere polar winter as seen by GOMOS/Envisat, *Geophys. Res. Lett.*, *31*(19), L19107, doi:10.1029/2004GL021042.

Seppälä, A., C. E. Randall, M. A. Clilverd, E. Rozanov, and C. J. Rodger (2009), Geomagnetic activity and polar surface air temperature variability, *J. Geophys. Res.*, *114*, A10312, doi:10.1029/2008JA014029.

Seppälä, A., H. Lu, M. A. Clilverd, , and C. J. Rodger (2013), Geomagnetic activity signatures in wintertime stratosphere wind, temperature, and wave response, *J. Geophys. Res.*, *118*, 2169-2183, doi:10.1002/jgrd.50236.

Simmons, A., S. Uppala, D. Dee, and S. Kobayashi (2006), *ERA-Interim: New ECMWF reanalysis products from 1989 onvards*, ECMWF Newsletter 110 – Winter 2006/07, Data Services ECMWF, Shinfield Park, Reading, UK.

Sinnhuber, M., H. Nieder, and N. Wieters (2012), Energetic particle precipitation and the chemistry of the mesosphere/lower thermosphere, *Surv. Geophys.*, *33*, 1281–1334, doi:10.1007/s10712-012-9201-3.

Siskind, D. E., L. Coy, and P. Espy (2005), Observations of stratospheric warmings and mesospheric coolings by the TIMED SABER instrument, *Geophys. Res. Lett.*, *32*, L09804, doi:10.1029/2005GL022399.

Smith, A. K. (2003), The origin of stationary planetary waves in the upper mesosphere, *J. Atmos. Sci.*, *60*, 3033–3041.

Smith, A. K. (2012), Interactions between the lower, middle and upper atmosphere, *Space Sci. Rev.*, *168:1*, doi:10.1007/s11214-011-9791-y.

Smith, A. K., R. R. Garcia, D. R. Marsh, D. E. Kinnison, and J. H. Richter (2010), Simulations of the response of mesospheric circulation and temperature to the antarctic ozone hole, *Geophys. Res. Lett.*, *37*, L22803, doi:10.1029/2010GL045255.

Solomon, S., D. W. Rusch, J.-C. Gérard, G. C. Reid, and P. J. Crutzen (1981), The effect of particle precipitation events on the neutral and ion chemistry of the middle atmosphere: II. Odd hydrogen, *Planet. Space Sci.*, *8*, 885–893.

Solomon, S., D. J. Ivy, D. Kinnison, M. J. Mills, R. R. Neely III, and A. Schmidt (2016), Emergence of healing in the Antarctic ozone layer, *Science*, *353*, 269–274, doi:10.1126/science.aae0061.

Stull, R. (2015), *Practical Meteorology: An Algebra-based Survey of Atmospheric Science*, 938 pp., Univ. of British Columpia, ISBN: 978-0-88865-176-1.

Turunen, E., P. T. Verronen, A. Seppälä, C. J. Rodger, M. A. Clilverd, J. Tamminen, C.-F. Enell, and T. Ulich (2009), Impact of different precipitation energies on NO_x generation during geomagnetic storms, *J. Atmos. Sol.-Terr. Phys.*, *71*, 1176–1189, doi:10.1016/j.jastp.2008.07.005.

Verronen, P. T., and R. Lehmann (2013), Analysis and parameterisation of ionic reactions affecting middle atmospheric HO_x and NO_y during solar proton events, *Ann. Geophys.*, *31*, 909–956, doi:10.5194/angeo-31-909-2013.

Verronen, P. T., A. Seppälä, M. A. Clilverd, C. J. Rodger, E. Kyrölä, C.-F. Enell, T. Ulich, and E. Turunen (2005), Diurnal variation of ozone depletion during the October-November 2003 solar proton events, *J. Geophys. Res.*, *110*, A09S32, doi: 10.1029/2004JA010932.

Verronen, P. T., A. Seppälä, E. Kyrölä, J. Tamminen, H. M. Pickett, and E. Turunen (2006), Production of odd hydrogen in the mesosphere during the January 2005 solar proton event, *Geophys. Res. Lett.*, *33*, L24811, doi:10.1029/2006GL028115.

Verronen, P. T., B. Funke, M. López-Puertas, G. P. Stiller, T. von Clarmann, N. Glatthor, C.-F. Enell, E. Turunen, and J. Tamminen (2008), About the increase of HNO_3 in the stratopause region during the Halloween 2003 solar proton event, *Geophys. Res. Lett.*, *35*, L20809, doi:10.1029/2008GL035312.

Verronen, P. T., M. L. Santee, G. L. Manney, R. Lehmann, S.-M. Salmi, and A. Seppälä (2011), Nitric acid enhancements in the mesosphere during the January 2005 and December 2006 solar proton events, *J. Geophys. Res.*, *116*, D17301, doi: 10.1029/2011JD016075.

Vitt, F. M., T. P. Armstrong, T. E. Cravens, G. A. M. Dreschhoff, C. H. Jackman, and C. M. Laird (2000), Computed contributions to odd nitrogen concentrations in the Earth's polar middle atmopshere by energetic charged particles, *J. Atmos. Sol.-Terr. Phys.*, *62*, 669–683.

Waters, J. W., et al. (2006), The Earth Observing System Microwave Limb Sounder (EOS MLS) on the Aura satellite, *IEEE Trans. Geosci. Remote Sens.*, *44*, 1075–1092, doi:10.1109/TGRS.2006.873771.

Weatherhead, E. C., et al. (2000), Detecting the recovery of total column ozone, *J. Geophys. Res.*, *105*, 22201–22210.

Whiteway, J. A., and T. J. Duck (1996), Evidence for critical level filtering of atmospheric gravity waves, *Geophys. Res. Lett.*, *23(2)*, 145-148, doi:10.1029/95GL03784.

Wissing, J. M., and M.-B. Kallenrode (2009), Atmospheric Ionization Module Osnabrück (AIMOS): A 3-D model to determine atmospheric ionization by energetic charged particles from different populations, *J. Geophys. Res.*, *114*, A06104, doi: 10.1029/2008JA013884.

PUBL. I

Reprinted, with permission, from
Atmospheric Chemistry and Physics, 11, 4645-4655,
doi: 10.5194/acp-11-4645-2011

Atmos. Chem. Phys., 11, 4645–4655, 2011
www.atmos-chem-phys.net/11/4645/2011/
doi:10.5194/acp-11-4645-2011

Atmospheric Chemistry and Physics

Mesosphere-to-stratosphere descent of odd nitrogen in February–March 2009 after sudden stratospheric warming

S.-M. Salmi[1,2], **P. T. Verronen**[1], **L. Thölix**[1], **E. Kyrölä**[1], **L. Backman**[1], **A. Yu. Karpechko**[1], **and A. Seppälä**[1,3]

[1]Finnish Meteorological Institute, Helsinki, Finland
[2]Department of Physics, University of Helsinki, Helsinki, Finland
[3]British Antarctic Survey (NERC), Cambridge, UK

Received: 23 November 2010 – Published in Atmos. Chem. Phys. Discuss.: 18 January 2011
Revised: 27 April 2011 – Accepted: 5 May 2011 – Published: 18 May 2011

Abstract. We use the 3-D FinROSE chemistry transport model (CTM) and Atmospheric Chemistry Experiment Fourier Transform Spectrometer (ACE-FTS) observations to study connections between atmospheric dynamics and middle atmospheric NO_x ($NO_x = NO + NO_2$) distribution. Two cases are considered in the northern polar regions: (1) descent of mesospheric NO_x in February–March 2009 after a major sudden stratospheric warming (SSW) and, for comparison, (2) early 2007 when no NO_x descent occurred. The model uses the European Centre for Medium-Range Weather Forecasts (ECMWF) operational data for winds and temperature, and we force NO_x at the model upper altitude boundary (80 km) with ACE-FTS observations. We then compare the model results with ACE-FTS observations at lower altitudes. For the periods studied, geomagnetic indices are low, which indicates absence of local NO_x production by particle precipitation. This gives us a good opportunity to study effects of atmospheric transport on polar NO_x. The model results show no NO_x descent in 2007, in agreement with ACE-FTS. In contrast, a large amount of NO_x descends in February–March 2009 from the upper to lower mesosphere at latitudes larger than 60° N, i.e. inside the polar vortex. Both observations and model results suggest NO_x increases of 150–200 ppb (i.e. by factor of 50) at 65 km due to the descent. However, the model underestimates the amount of NO_x around 55 km by 40–60 ppb. According to the model results, chemical loss of NO_x is insignificant during the descent period, i.e. polar NO_x is mainly controlled by dynamics. The descent is terminated and the polar NO_x amounts return to pre-descent levels in mid-March, when the polar vortex breaks. The break-up prevents the descending NO_x from reaching the upper stratosphere, where it could participate in catalytic ozone destruction. Both ACE-FTS observations and FinROSE show a decrease of ozone of 20–30 % at 30–50 km from mid-February to mid-March. In the model, these ozone changes are not related to the descent but are due to solar activation of halogen and NO_x chemistry.

Correspondence to: S.-M. Salmi
(sanna-mari.salmi@fmi.fi)

1 Introduction

In the stratosphere odd nitrogen ($NO_x = NO + NO_2$) is produced mainly by oxidation of nitrous oxide (N_2O). Significant production occurs also in the lower thermosphere, around 110 km, through photoionization of N_2 by extreme ultraviolet (EUV) and soft X-ray radiation. In the polar regions, another important and highly varying source of NO_x is ionizing energetic particle precipitation directly affecting a wide range of altitudes from the thermosphere down to the stratosphere (Barth, 1992; Vitt et al., 2000). Because NO_x loss is driven by photodissociation, in the absence of solar radiation NO_x is chemically long-lived and therefore strongly affected by atmospheric dynamics.

In the recent years, observations have shown that during winter times NO_x can be effectively transported downwards inside the polar vortex (Funke et al., 2005, 2007; Hauchecorne et al., 2007; Seppälä et al., 2007; Randall et al., 2009), after NO_x is produced by particle precipitation in the mesosphere-lower thermosphere (MLT). Although the satellite observations of NO_x often cover altitudes up to middle mesosphere only, the connection to lower thermospheric NO_x production has been established using VLF (Very Low-Frequency) radio propagation data in the case of the 2004 descent event (Clilverd et al., 2006). Previously it had already been suggested that NO_x transport could provide a connection mechanism between particle precipitation in the MLT region and stratospheric ozone (Solomon et al., 1982; Siskind et al., 1997; Callis and Lambet, 1998). Several recent studies based on atmospheric modelling support the importance of wintertime NO_x enhancements to middle

Published by Copernicus Publications on behalf of the European Geosciences Union.

atmospheric composition (Vogel et al., 2008; Baumgaertner et al., 2009; Reddmann et al., 2010). Callis et al. (2000) suggested that changes in NO_x concentrations due to particle precipitation and variations in transport could have a comparable effect on the amount of ozone in the upper stratosphere as changes in UV radiation at lower latitudes. At middle to high latitudes this coupling between NO_x and ozone may have a significant effect, again comparable in magnitude to that of UV radiation, also on the dynamics (Callis et al., 2001; Langematz et al., 2005). It has even been suggested that these changes could affect the polar regional ground-level climate although the linking mechanisms are not yet understood (Rozanov et al., 2005; Seppälä et al., 2009; Baumgaertner et al., 2010). Also other mechanisms connecting geomagnetic activity and middle atmospheric dynamics have been proposed. Arnold and Robinson (2001) suggested a coupling of geomagnetic activity to atmospheric waves. Lu et al. (2008) suggested that geomagnetic and far-UV perturbations might have an indirect connection to the stratosphere. Along the lines of Arnold and Robinson (2001), Lu et al. (2008) also concluded that this is likely due to coupling between the mean flow and atmospheric waves. Satellite observations have shown that exceptionally strong NO_x descent events occurred in 2004, 2006 and 2009 after sudden stratospheric warming events (Randall et al., 2009; Manney et al., 2009). These events are related to reformation of the vortex following its split/displacement. One of the strongest major SSWs on record occurred in the Northern Hemisphere in January 2009 (Manney et al., 2009). According to observations of the Microwave Limb Sounder (MLS), the stratopause broke down in late January and then reformed at very high altitudes around 80 km. During the major SSW the polar vortex split, but reformed after the SSW in the upper stratosphere where it became stronger than it initially was. Randall et al. (2009) used ACE-FTS data and showed that following the SSW stratospheric NO_x increased due to strong downward transport by factor of approximately 50 compared to winters without descent events. Because geomagnetic activity was low at the time, indicating that there was no significant NO_x production by particle precipitation occurring, the NO_x enhancement in 2009 was likely driven by the meteorology. Randall et al. (2009) further concluded that significant effects on ozone were neither expected nor observed since the descending NO_x enhancements never reached altitudes where NO_x is most effective at catalytic ozone destruction. However, they also pointed out the limitations of these conclusions, which were based on data not covering the whole polar night region.

In this paper we analyse the dynamics and meteorology of the winter of 2009 in the northern polar region using ECMWF operational analyses. Building on the observational analysis of Randall et al. (2009), we use the FinROSE chemistry transport model (CTM) to simulate this winter and the strong descent event of NO_x. This is done by constraining the model NO_x by enforcing a time-dependent upper boundary condition (UBC) based on ACE-FTS observations between 75 and 85 km altitude. Compared to earlier studies of other NO_x descent events utilizing ECMWF data (e.g. Vogel et al., 2008; Reddmann et al., 2010), in this study we use ECMWF operational analyses for dynamics up to 80 km, which gives us the opportunity to study the NO_x descent starting as high as from the upper mesosphere. The 3-dimensional CTM used in this study provides a complete coverage of the polar area, which thus enables also the study of any possible changes in ozone concentrations not seen by ACE-FTS due to its limited spatial coverage. For comparison, we also simulate the winter of 2007 when no comparable SSWs or NO_x descent was observed.

2 Model and measurements

2.1 Chemistry transport model FinROSE

FinROSE is a global 3-dimensional CTM designed for middle atmospheric studies (Damski et al., 2007). The model dynamics (i.e. temperature, horizontal winds and pressure) are from external sources i.e. changes in atmospheric composition do not affect the model dynamics. Vertical wind is calculated inside the model by using the continuity equation. In this study FinROSE is run with 41 vertical levels (0–80 km), a horizontal resolution of $10° \times 5°$ and is driven by operational analyses from ECMWF. The analyses are based on ECMWF simulations of a general circulation model (GCM) using four dimensional data assimilation (4D-VAR). The horizontal resolution and the number of vertical levels in FinROSE can be modified depending on the resolution of the meteorological data. The model calculates distributions of 40 species and families taking into account both chemistry and dynamics. However, only to the long-lived constituents are transported. The model includes about 120 homogeneous reactions and 30 photodissociation processes. Chemical kinetic data, reaction rate coefficients and absorption cross-sections are taken from look-up-tables based on the Jet Propulsion Laboratory compilation by Sander et al. (2006), including updates from the available supplements. Photodissociation frequencies are calculated using a radiative transfer model (Kylling et al., 1997). In addition to homogeneous chemistry, the model also includes heterogeneous chemistry, i.e. formation and sedimentation of PSCs and reactions on PSCs. Chemistry is not defined in the troposphere, but the tropospheric abundances are given as boundary conditions. At the lower boundary, monthly averages from ECMWF are used for ozone and water vapour, while methane is relaxed towards climatological distribution and other long-lived trace gases towards long time trends.

2.2 Observations

We have used observations from the FTS (Fourier Transform Spectrometer) instrument onboard the ACE satellite

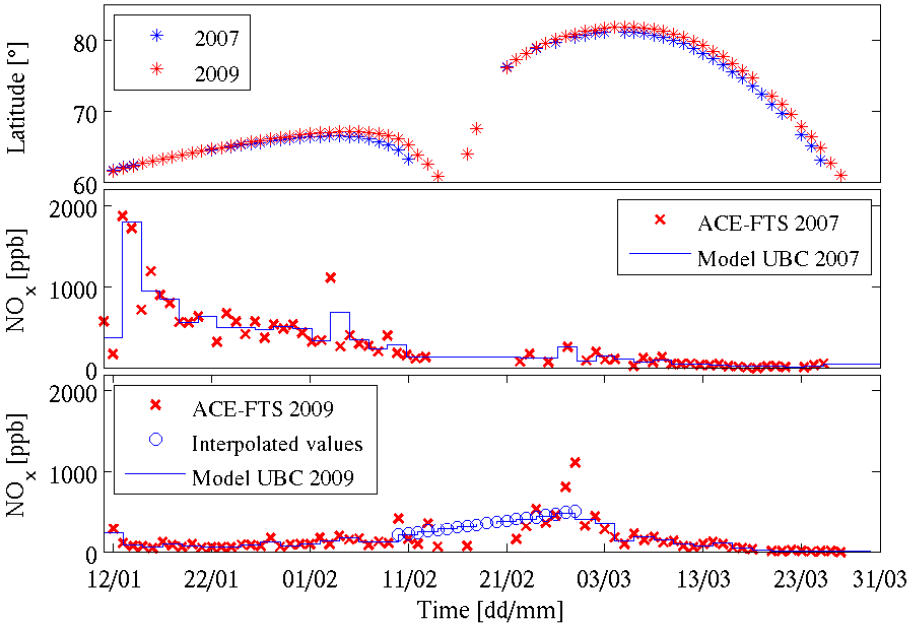

Fig. 1. Daily medians of ACE-FTS measurement locations north of 60° N (top) in 2007 (blue asterisk) and 2009 (red asterisk). The figure also shows mean NO_x concentrations measured by ACE-FTS between 75–85 km altitudes (red crosses) and two-day means calculated from the observations (blue line) for 2007 (middle) and 2009 (bottom). Two-day means for 2009 are based on interpolated values between 10 and 28 February (blue circles).

(Atmospheric Chemistry Experiment) (Bernath et al., 2005). ACE-FTS is a solar occultation instrument launched in 2003. The instrument operates in the wavelength region of 2.2–13.3 μm and measures vertical profiles of temperature, pressure, density and 18 atmospheric constituents in the altitude range of 10–150 km. Figure 1 shows the daily medians of the measurement locations north of 60° N in January–March 2007 and 2009. We have calculated the median only when there are at least five measurements available during a day. Otherwise the measurements for that particular day have been neglected. In most cases ACE-FTS makes about 10 measurements per day. The figure also shows that the measurements represent almost the same latitudes from year to year. Measuring error for NO_x depends on altitude and concentration (not shown) so that at 80 km altitude the error is 1–3 % for mixing ratios such as in late February–early March in 2009 and increases up to 10–15 % for NO_x amounts observed in January 2009.

In this study we use ACE-FTS observations of NO_x as an UBC for FinROSE (Fig. 1). We first calculated daily medians from the observations northward of 60° N for 2007 and 2009. As a result we got one value per day representing approximately a zonal average at the median latitude. Using these daily values we then calculated two-day means, which we in this study use at the upper boundary of the model. This two-day mean value is used on every time step for two days after which the next two-day mean is used. In case of missing data for both of the days in question, we use the previous two-day mean. The UBC is taken uniform at every grid point between 60° N–90° N. It should be noted that the instrument changed the direction of the measurements towards lower latitudes after the 5 February, which can be seen as a decrease of about 400 ppb in the 2009 NO_x mixing ratios (Fig. 1). Around 16 February ACE-FTS continued measuring on northern latitudes (>60° N) and NO_x concentrations increased because of this. The effect can be seen as a minimum in the 2009 NO_x mixing ratios between 10 and 28 February in Fig. 1. This means that the ACE-FTS measurements do not give a representative general view of the situation in the polar region during this time period. To reduce the influence of the change in the measuring direction, we replaced the 2009 ACE-FTS observations with interpolated values over the minimum (blue circles in Fig. 1) and neglected the largest values. This is somewhat arbitrary, but perhaps the best approach taking into account the lack of usable data in this time period.

3 Results

3.1 Meteorological conditions

In this section we use the ECMWF operational data to analyse the meteorological conditions and their differences in early 2007 and 2009. We are aware of the possible shortcomings of the data (Manney et al., 2008), but for this study it is important that the ECMWF fields extend up to 80 km,

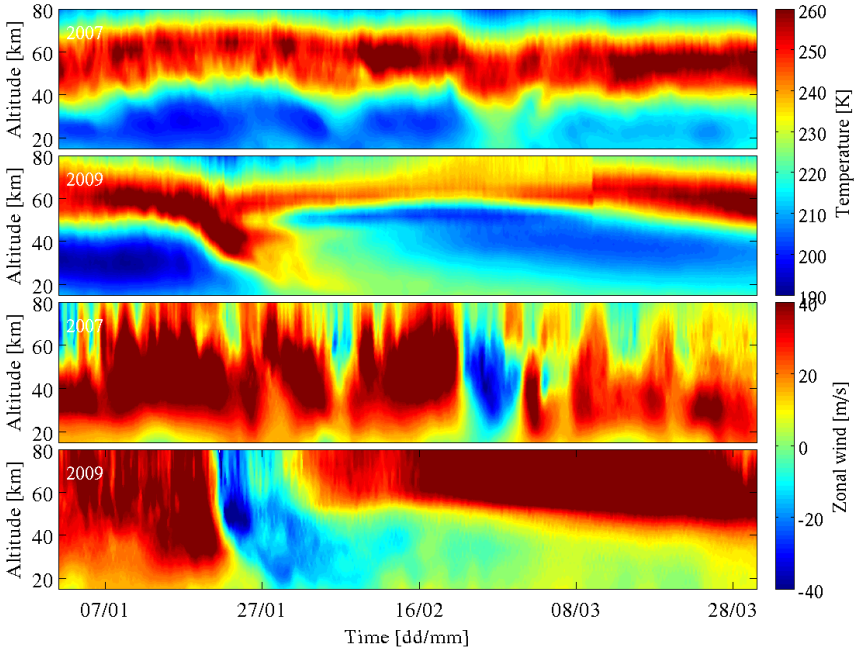

Fig. 2. ECMWF zonal mean temperature (K) and zonal mean zonal wind (m s^{-1}) at 75° N as a function of time and altitude for winters 2007 and 2009.

allowing us to model the NO_x descent starting as high as from the upper mesosphere.

Figure 2 shows zonal mean temperature (two top panels) and zonal mean zonal wind (two bottom panels) at 75° N for 2007 and 2009 as a function of time and altitude. The meteorological conditions show remarkable differences between these two years. The winter of 2007 was rather stable whereas early 2009 was dynamically quite exceptional as the stratopause warmed and dropped below 30 km in late January. In early February the stratopause reformed around 80 km, which led to very low temperatures between 30 and 50 km. The same figure also shows that the warming in 2009 was accompanied by a rapid change in the direction of the zonal flow (from positive/westerly to negative/easterly), which persisted until early March. This one month period of easterly winds in 2009 led to low wave activity above the critical level, which for stationary waves corresponds to a level where the zonal wind speed equals to zero, and enabled the formation of a strong polar vortex, which did not break until early March. Changes in the wind direction took place also in early and late February 2007, but these changes lasted only for at most ≈10 days. Extreme changes in stratopause temperatures, as in 2009, did not occur.

According to McInturff (1978), the criteria for a major SSW are fulfilled when the latitudinal mean temperature at 10 hPa (≈30 km) or below increases poleward of 60° N and the zonal winds are reversed from westerly to easterly in the same area. Figure 3 shows the zonal mean temperature and zonal mean zonal wind at 10 hPa as a function of time and latitude. The poleward temperature gradient reversed during both winters. In 2007 the temperature increase was fairly small (≈10 K) and lasted only about 10 days. The warming in 2009 was more pronounced and the temperature gradient was positive for approximately 20 consecutive days in the polar region. The figure also shows that the zonal mean wind at 10 hPa reversed from westerly to easterly at the same time when the temperature gradient became positive. This indicates that a major SSW occurred in both winters. However, the situation in 2007 returned to undisturbed winter conditions in a few days, which is more common for minor SSWs. In 2009 the wind reversal to westerly took about one month, giving enough time for the vortex to recover in the upper stratosphere/lower mesosphere. The criteria for a major SSW in 2009 were first met on the 24 January (black vertical dashed line).

It has been suggested by Manney et al. (2008) that the ECMWF operational analyses underestimate the variations in the stratopause altitude during extreme meteorological conditions. The operational analyses agree, however, well with satellite observations of MLS and SABER (Sounding of the Atmosphere using Broadband Emission Radiometry) in early winter stratopause temperatures. Compared to the MLS measurements (Manney et al., 2009) the ECMWF operational analyses underestimate the altitude of the stratopause reformation in 2009 by about 5 km. The zonal wind, instead, resembles MLS measurements also at higher altitudes. Below 50 km altitude the MLS observations and operational analyses are in very good agreement.

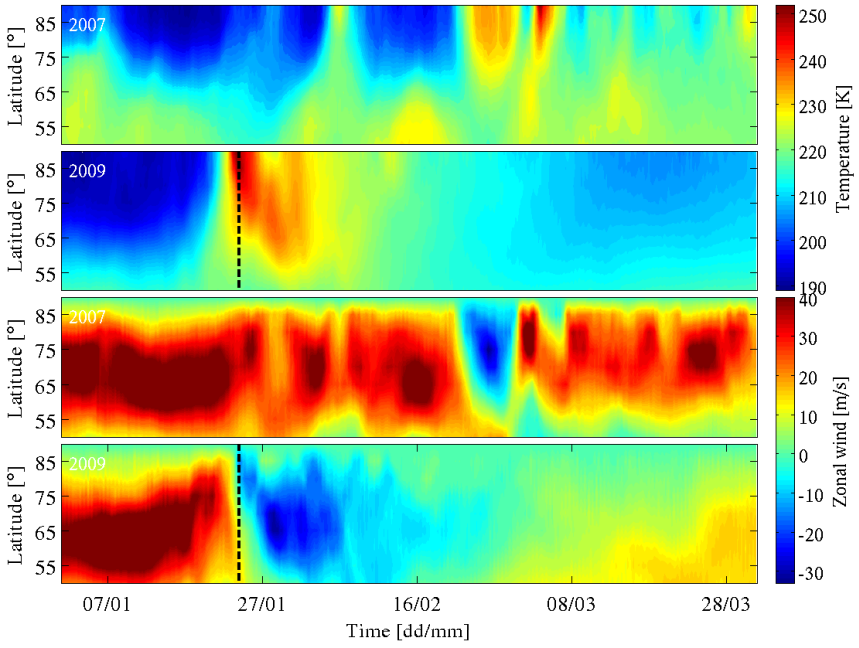

Fig. 3. ECMWF zonal mean temperature (K) and zonal mean zonal wind ($m\,s^{-1}$) at 10 hPa (≈30 km) as a function of time and latitude. The vertical black dashed lines in figures representing the year 2009 show the date when the criteria for the major SSW were fulfilled.

3.2 NO_x descent

Figure 4 presents NO_x observations measured by ACE-FTS in 2007 (top) and 2009 (bottom). Plotted are daily medians north of 60° N, which correspond to measurement locations shown in Fig. 1. The observations show that there were large differences in the distribution of NO_x between years 2007 and 2009. In 2007 the mesospheric maximum of NO_x reached 60–65 km in the beginning of the year and then ascended towards the spring. This can be explained by changes in the zonal mean temperature and wind fields (Figs. 2 and 3). The stratopause was quite stable until the beginning of February, when the temperatures increased for a few days and the westerly winds weakened. Warm midlatitude air with low NO_x concentrations mixed with the colder polar air and decreased the NO_x concentrations. This warming did not dislocate the stratopause and the temperatures remained quite high even after the warming. The warming in late February produced no significant effects on NO_x.

In contrast, the major SSW in 2009 had a great impact on NO_x. A tongue-like structure of descending NO_x from the mesosphere to the stratosphere after the SSW is clearly seen in Fig. 4. High NO_x amounts were transported from 80 to 55 km altitude in about 40 days. The descent took place during the recovery of the polar vortex and is also discussed by Randall et al. (2009). Comparison of NO_x and isentrops calculated from ECMWF operational data indicates that the NO_x concentration isolines crossed the isentrops (not shown), suggesting that the descent was diabatic. The situation is thus similar to the upper stratospheric vortex recovery that occurred after a SSW in winter 2005/2006 (Manney et al., 2008). In mid-March the descent stopped and NO_x concentrations decreased back to the level on which they were before the SSW. At this time the stratopause had already reformed and the zonal winds had started to reverse back to westerly (Fig. 2) allowing planetary waves to propagate upward, interact with the vortex, and mix the low-NO_x air from outside the vortex with high-NO_x air inside the vortex.

Figure 5 shows NO_x timeseries calculated from FinROSE-CTM results. The data are daily means, calculated using only the grid points corresponding to ACE-FTS measurement locations (Fig. 1). The model reproduces the distribution of NO_x reasonably well compared to the observations shown in Fig. 4. The maximum of NO_x in the beginning of 2007 at about 75 km is of the same order of magnitude (800–900 ppb) as in the observations, but extends 3–5 km lower in the middle atmosphere. In 2009, the observations and model results show an increase of NO_x to 150–200 ppb at 65 km. The modelled and observed NO_x both descend to about 55 km, but at this altitude the amount of NO_x is underestimated in the model by 40–60 ppb. The descent also starts 3–5 days earlier and lasts 3–5 days longer in the model than in the observations.

In order to test the robustness of the results, we averaged the model NO_x over the whole polar cap (60° N–90° N) instead of sampling at ACE locations, but found this to have only a slight effect on the results (not shown). Compared to the sampled results (Fig. 5) the descent stopped a couple

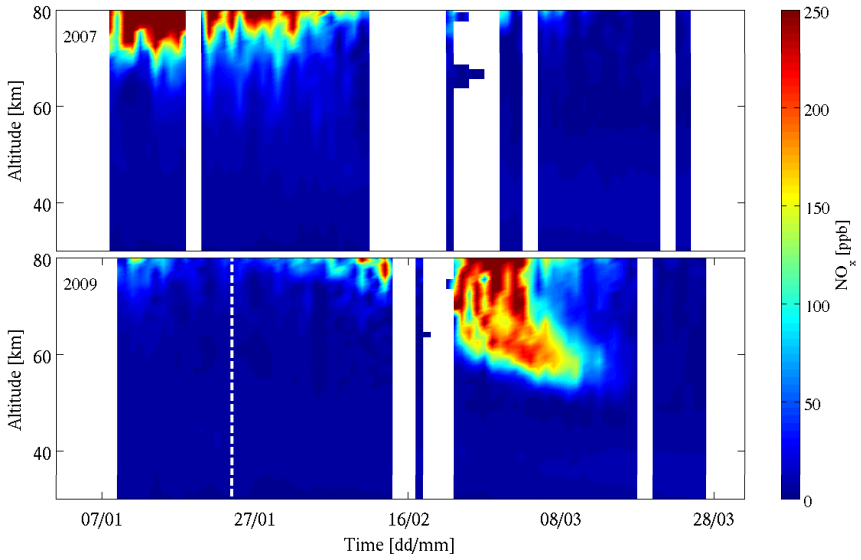

Fig. 4. NO_x time series (ppb) as daily medians measured by ACE-FTS. White dashed line indicates the time point, when the criteria for the major SSW were fulfilled in 2009. The upper panel is for 2007 and the lower for 2009. White regions indicate missing data or not enough data.

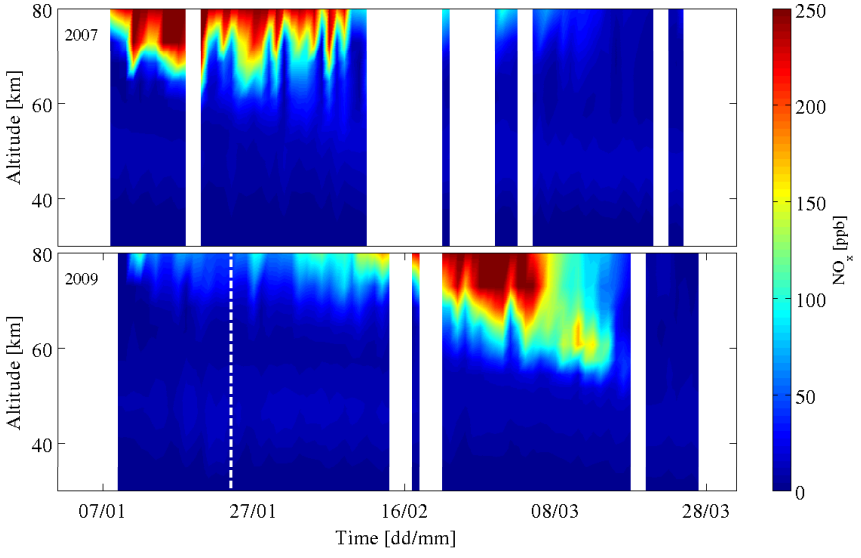

Fig. 5. NO_x time series (ppb) as daily means from FinROSE-CTM. White dashed line indicates the time point, when the criteria for the major SSW were fulfilled in 2009. The upper panel is for 2007 and the lower for 2009. White regions indicate missing ACE-FTS data or not enough ACE-FTS data.

of days earlier above 60 km, but continued longer until late March between 60 and 50 km with NO_x mixing ratios of 50–100 ppb. Otherwise the concentrations were of the same magnitude as in the sampled results. The similarity between the sampled and whole-polar-cap results from the model suggests that NO_x did not reach upper stratosphere anywhere in the polar cap region.

To estimate the effect of different UBCs on the NO_x descent we made two additional model runs. In these runs we used the following upper boundaries: (1) a constant value (~670 ppb) between the 11 February and the 4 March and (2) a two-step increment of NO_x so that the first step (~190 ppb) is located between the 11 and 21 February and the second one (~540 ppb) between the 22 February and the 4 March. The results (not shown) for case 2 are in agreement with those obtained with the interpolated upper boundary shown in Fig. 1. In contrast, case 1 produces about 100 ppb higher NO_x mixing ratios between 60 and 80 km during the

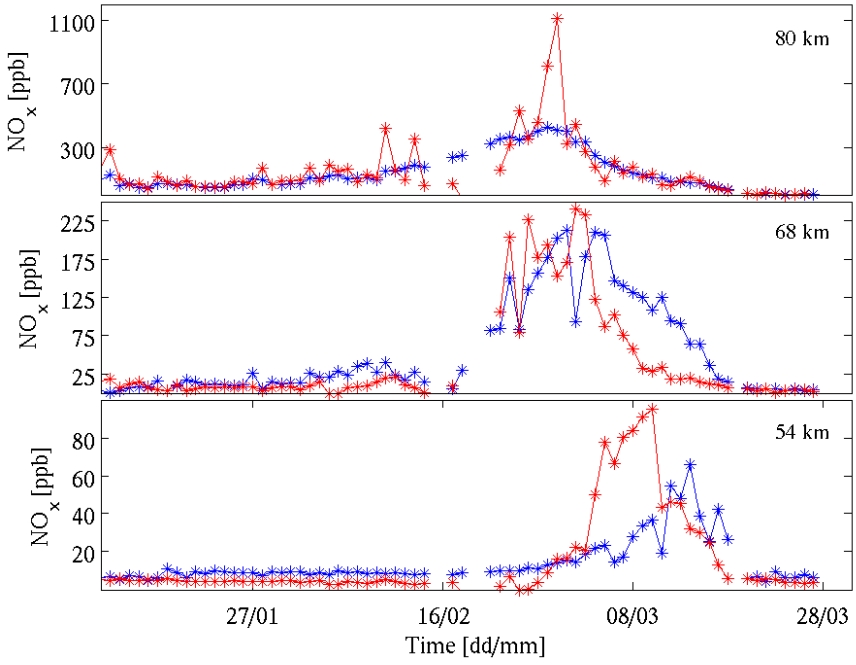

Fig. 6. ACE-FTS NO_x observations (red line) and model results (blue line) in ppb at 80 (top), 68 (middle) and 54 km (bottom) altitudes as a function of time in 2009.

descent event until early March. At this time the mixing ratios are about 50 ppb higher. However, NO_x descent stops at the same altitude as with the interpolated upper boundary. As expected, the different upper boundaries change only the amount of descending NO_x because in all model runs the descent is driven by the same ECMWF meteorological data.

Figure 6 shows the model results and ACE-FTS observations at 80, 68 and 54 km altitudes. Differences at 80 km altitude during 10–28 February are due to the interpolated UBC at that time. However, the modified UBC improves the agreement between the model and observations at lower altitudes. There is a reasonable agreement between the model and the observations at 68 km altitude. An overestimation of about 100 ppb occurs after the 8 March, consistent with the fact that the descent lasted longer in the model than observed by ACE-FTS. Significant differences are found at 54 km where the model produces 40–60 ppb smaller values than found in the observations. The observed maximum of NO_x occurs about 10 days earlier compared to the model results. Overall, the model succeds to reproduce the descent of NO_x, with no in-situ production included in the model, reasonably well compared to the observations and confirms the results of Randall et al. (2009) about the importance of dynamics on the distribution of NO_x. Although this is not a direct measure, the NO_x comparison suggest that the ECMWF data are in this case usable in atmospheric modelling also at mesospheric altitudes.

Figure 7 illustrates the modelled distribution of NO_x in the northern polar region (50° N–90° N). The descending NO_x reaches 69 km altitude already on 6 February with amounts of 80–100 ppb. The circular structure of NO_x in the polar region is due to the existing or evolving polar vortex. The effect of photochemistry can be considered negligible during the polar winter on latitudes poleward of 60° N. As Fig. 6 already showed, with time NO_x is transported at lower altitudes with mixing ratios of 60–80 ppb finally reaching 54 km on 15 March. ACE-FTS measurement locations are marked in the figure with filled white circles. As mentioned already in section 2.2 ACE-FTS makes about 10 measurements per day. In cases when some of the data are corrupted and excluded from the analysis, even fewer observations are left to represent the whole polar cap region. This might lead to differences between observations and the model results, especially close to the polar vortex edge. In addition, the closest model grid to ACE-FTS measurement covers by definition a larger area ($10° \times 5°$) than the point-form observation does and can also be inside the vortex, although the measurement was made outside the vortex. This can partly explain the differences between the model and observations.

To estimate the effect of chemistry on descending NO_x, we have analysed the NO_x tracer in the model. The tracer uses the same boundary condition as NO_x, but is not affected by chemistry. Transport is thus the only factor that affects the tracer. The relative effect of chemistry can be calculated by dividing the difference between NO_x and the tracer with the

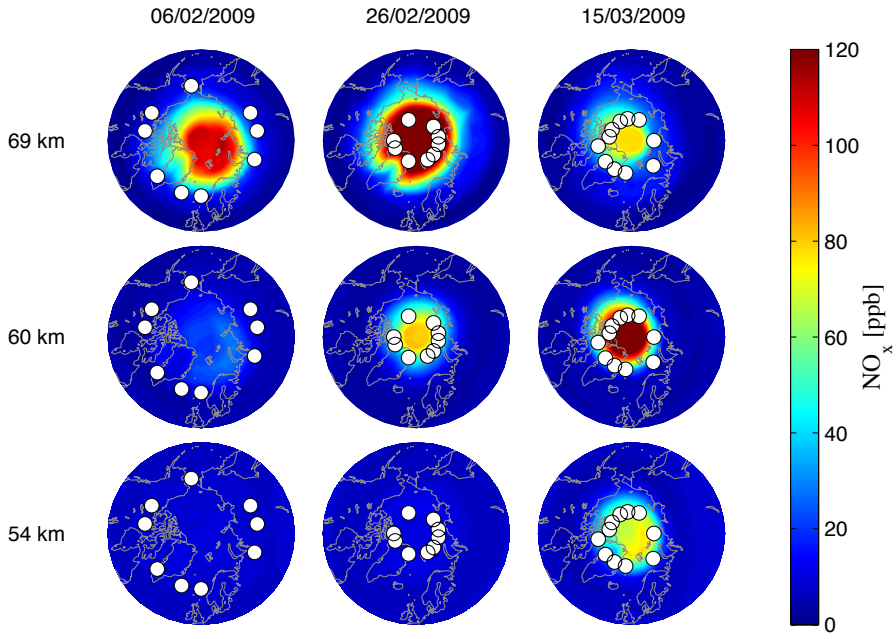

Fig. 7. Distribution of NO_x in ppb at 69, 60 and 51 km altitudes (rows) on 6 and 26 February and 15 March (columns) in the northern polar region (50° N–90° N) calculated from the model results. White circles indicate the measurement locations of ACE-FTS on that particular day.

amount of NO_x. The model results indicate that the chemical production of NO_x is not effective during polar winter and, furthermore, the relative chemical loss is only 3 % or less (not shown), meaning that chemistry does not affect the NO_x concentrations during the polar night. Therefore NO_x can descend inside the arctic vortex with only little interference by chemistry. In addition to gas phase chemistry, also photodissociation processes affect the amount of NO_x in the middle and upper atmosphere. The time period from January to March in the northern polar area is very dark leading to only weak photodissociation processes and thus to longer photochemical lifetimes. The photochemical lifetime of NO_x was nearly two months in early January decreasing to about 5 days towards the end of March in the altitude range of 60–80 km. This is a further evidence that NO_x was mainly influenced by atmospheric dynamics during the time period under investigation.

3.3 Effects on O_3

The descent event of NO_x in 2009 was one of the strongest observed. If transported down to the stratosphere, NO_x affects ozone balance through well-known catalytic reaction cycles (Grenfell et al., 2006). Although we do not expect to see any NO_x related changes in stratospheric ozone in this case (the descending NO_x did not reach stratosphere before vortex breakdown) we are interested in any effects this meteorological event might have had on ozone. Figure 8 shows ACE-FTS observations and FinROSE model results of ozone in early 2009. Analysing the O_x tracer in the model (not shown), similarly to the NO_x tracer earlier, we find that the behaviour of ozone until mid-February, including ozone decrease in late January and early February, was largely determined by the dynamics. The model results show lower ozone mixing ratios around 40 km compared to the observations, which can partially be explained by the non-perfect correspondence of the closest model grid point with the daily median of the observations.

Both ACE-FTS and FinROSE show ozone decrease after mid-February 2009 starting from around 50 km (Fig. 8). The observations indicate a decrease of about 20 % between 30–50 km lasting one month and recovery in early March. In the model, ozone depletion is about 10 % stronger than observed while the recovery takes place later in mid-March. Although coinciding with the NO_x descent, the ozone decrease is not directly linked to the descent as discussed earlier. The dynamics could, on the other hand, lead to ozone decrease at 40 km through transport of low ozone concentrations from above. The O_x tracer analysis, however, indicates that transport of air with low O_x concentrations cannot explain its decrease. Similar to NO_x descent, the descent of low O_x air did not affect altitudes below 50 km. Below 50 km the downward transport was too weak to explain the observed structure of ozone. In the model, ozone destroying substances, such as HO_x, bromine and chlorine, were produced after mid-February as the solar radiation increased and

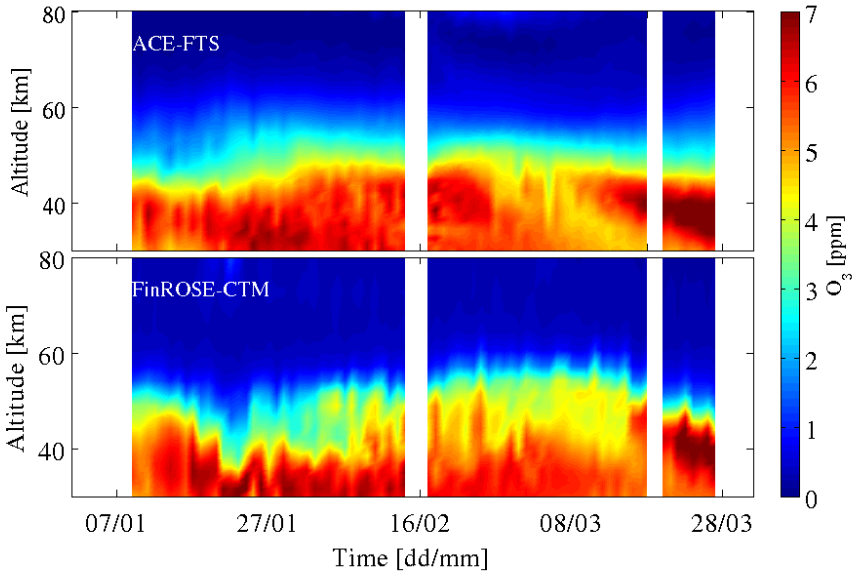

Fig. 8. ACE-FTS (top) and FinROSE-CTM (bottom) ozone time series in ppm as a function of altitude for early 2009 in ACE-FTS measurement locations.

the chemical processes, including photodissociation, started to play an important role on atmospheric composition. These substances, with the help of a strong polar vortex, enabled the catalytic cycles destroying ozone and caused the observed depletion at 40 km. When the solar radiation increased, the production of ozone began to dominate. This led to increase of ozone in both the observations and model results in early March at 45 km altitude and then gradually also at lower altitudes as shown in Fig. 8.

4 Discussion

In the case of 2009, even though a strong descent event occurred, enhanced mesospheric NO_x did not reach the upper stratosphere and thus did not affect ozone. The model results show this behaviour throughout the northern polar cap region, in agreement with the spatially limited ACE-FTS observations. However, based on a single case of descent presented in this paper, we cannot in general dismiss the possible connection between descending NO_x, upper stratospheric ozone decrease, and subsequent changes in dynamics. If the SSW had occurred earlier, NO_x would have had more time to descend and reach the stratosphere before the vortex break-up/split. According to the model results, NO_x rapidly descended from mesosphere to stratosphere with a velocity of about 700 m day^{-1} in February and early March 2009. In contrast, average descent rates in the polar vortex are typically less than 200 m day^{-1}. Assuming velocity of 700 m day^{-1}, the descent should have started 10–30 days earlier in order to reach 50–35 km altitude.

We would like to point out that Randall et al. (2009) and Vogel et al. (2008) have shown that the observed ozone loss in early 2004 can be attributed to a NO_x descent event similar to that of 2009. Compared to the 2009 event, the SSW that caused the NO_x descent in early 2004 occurred about one month earlier, i.e. in late December, allowing enhanced NO_x to reach the stratosphere. Therefore, strong NO_x descent events seem to decrease stratospheric ozone only if the corresponding SSW occurs early enough in the winter period (by ∼early January), although this time condition would obviously be relaxed if in-situ production of NO_x by energetic particle precipitation occurred at altitudes below 80 km. If the SSW occurred later than early January, it might actually lead to weaker connection between MLT NO_x production and stratospheric ozone, i.e. any enhanced NO_x amounts already in the mesosphere would be mixed with outside-vortex air during the SSW, and the after-SSW descent would start too late to transport NO_x from the upper mesosphere to the stratosphere, as in the case of the 2009 descent event. In such conditions, the effect of EEP-NO_x on stratospheric ozone in SSW years could be equal or smaller compared to years without a SSW. This could be one potential reason for the findings of Lu et al. (2008) and Seppälä et al. (2009), who have demonstrated that changes in stratospheric and tropospheric dynamics actually correlate with geomagnetic Ap index better when the SSW-years were excluded from their analyses. It is evident to us that more research is needed to answer the questions concerning NO_x–O_3 interaction and possible connection to stratospheric/tropospheric dynamics.

5 Conclusions

In this paper, we have used the FinROSE-CTM and ACE-FTS observations to study the effect of polar vortex dynamics on the distribution of NO_x in the winter polar region. Two different Northern Hemisphere cases, 2007 and 2009, were considered. The latter was characterized by a strong NO_x descent event in February–March, which begun after a record-breaking SSW. In the modelling, we used ECMWF operational winds, temperature, and pressure up to 0.01 hPa ($\sim$80 km) and a NO_x upper boundary at 80 km based on ACE-FTS observations, and then compared the results with the observations at lower altitudes.

In contrast to 2007, when a SSW did not have any significant effects on the atmospheric composition, in 2009 large amounts of NO_x descended from the upper mesosphere to the stratosphere following a major SSW. Analysis of ECMWF data shows that the descent was enabled by the formation of a strong polar vortex facilitated by easterly zonal flow that prevented the vertical propagation of planetary waves. Based on ACE-FTS observations, the NO_x descent continued until mid-March, by which time the high-NO_x amounts of 150–200 ppb reached down to 55 km. The FinROSE-CTM results are in reasonable agreement with ACE-FTS, except that the amount of NO_x at 55 km is underestimated by 40–60 ppb compared to the observations. Although the ACE-FTS observations have a restricted spatial coverage, the model results indicate that the measurements give a good representation of the NO_x descent throughout the polar cap. The FinROSE-CTM results also show that chemical production and loss of NO_x was insignificant during the descent in the polar night region, so that NO_x distribution was controlled by the vortex dynamics. The reasonably good agreement between observations and the model gives confidence in the usability of the ECMWF operational data in mesospheric modelling.

Although a strong descent event occurred in February–March 2009 after a major SSW, we find that in this case the high NO_x amounts did not reach upper stratosphere and thus did not catalytically deplete ozone. Instead, both ACE-FTS and FinROSE-CTM show ozone decreased by about 20 % at 30–50 km in late February–early March, which according to the model was due to increasing amount of solar radiation and activation of HO_x and halogen compounds. However, if a similar descent event had begun about a month earlier, NO_x would have reached stratospheric altitudes. Therefore, it seems that a connection between EEP-NO_x production in the MLT region and stratospheric ozone variability requires suitable timing of descent events, and our case study does not exclude the possibility of this connection. More research on EPP-NO_x and stratospheric ozone is needed, keeping in mind the links to dynamics and ground-level temperature and pressure anomalies that have been suggested.

Acknowledgements. S.-M. Salmi would like to thank Viktoria Sofieva for helpful comments. All the authors thank also Cora Randall, Lynn Harvey and Kaley Walker for their help with the ACE-FTS data. Funding from the Academy of Finland through the THERMES, SPOC, SAARA and MIDAT projects is gratefully acknowledged. A. Seppälä was supported by the European Commission project FP7-PEOPLE-IEF-2008/237461. The Atmospheric Chemistry Experiment (ACE) data were provided by the European Space Agency (ESA). ACE is a Canadian-led mission mainly supported by the Canadian Space Agency and the Natural Sciences and Engineering Research Council of Canada.

Edited by: A. J. G. Baumgaertner

References

Arnold, N. F. and Robinson, T. R.: Solar magnetic flux influences on the dynamics of the winter middle atmosphere, Geophys. Res. Lett., 28(12), 2381–2384, doi:10.1029/2000GL012825, 2001.

Barth, C. A.: Nitric oxide in the lower thermosphere, Planet. Space Sci., 40, 315–336, 1992.

Baumgaertner, A. J. G., Jöckel, P., and Brühl, C.: Energetic particle precipitation in ECHAM5/MESSy1 – Part 1: Downward transport of upper atmospheric NOx produced by low energy electrons, Atmos. Chem. Phys., 9, 2729–2740, doi:10.5194/acp-9-2729-2009, 2009.

Baumgaertner, A. J. G., Seppälä, A., Jöckel, P., and Clilverd, M. A.: Geomagnetic activity related NOx enhancements and polar surface air temperature variability in a chemistry climate model: modulation of the NAM index, Atmos. Chem. Phys. Discuss., 10, 30171–30203, doi:10.5194/acpd-10-30171-2010, 2010.

Bernath, P. F., McElroy, C. T., Abrams, M. C., Boone, C. D., Butler, M., Camy-Peyret, C., Carleer, M., Clerbaux, C., Coheur, P.-F., Colin, R., DeCola, P., DeMaziére, M., Drummond, J. R., Dufour, D., Evans, W. F. J., Fast, H., Fussen, D., Gilbert, K., Jennings, D. E., Llewellyn, E. J., Lowe, R. P., Mahieu, E., McConnell, J. C., McHugh, M., McLeod, S. D., Michaud, R., Midwinter, C., Nassar, R., Nichitiu, F., Nowlan, C., Rinsland, C. P., Rochon, Y. J., Rowlands, N., Semeniuk, K., Simon, P., Skelton, R., Sloan, J. J., Soucy, M.-A., Strong, K., Tremblay, P., Turnbull, D., Walker, K. A., Walkty, I., Wardle, D. A., Wehrle, V., Zander, R., and Zou, J.: Atmospheric Chemistry Experiment (ACE): Mission overview, Geophys. Res. Lett., 32, L15S01, doi:10.1029/2005GL022386, 2005.

Callis, L. B. and Lambeth, J. D.: NO_y formed by precipitating electron events in 1991 and 1992: Descent into the stratosphere as observed by ISAMS, Geophys. Res. Lett., 25, 1875–1878, doi:10.1029/98GL01219, 1998.

Callis, L. B., Natarajan, M., and Lambeth, J. D.: Calculated upper stratospheric effects of solar UV flux and NO_y variations during the 11-year solar cycle, Geophys. Res. Lett., 27(23), 3869–3872, doi:10.1029/2000GL011622, 2000.

Callis, L. B., Natarajan, M., and Lambeth, J. D.: Solar-atmospheric coupling by electrons (SOLACE) 3, Comparisons of simulations and observations, 1979-1997, issues and implications, J. Geophys. Res., 106, 7523–7539, doi:10.1029/2000JD900615, 2001.

Clilverd, M. A., Seppälä, A., Rodger, C. J., Verronen, P. T., and Thomson, N. R.: Ionospheric evidence of thermosphere-

to-stratosphere descent of polar NO_x, Geophys. Res. Lett., 33, L19811, doi:10.1029/2006GL026727, 2006.

Damski, J., Thölix, L., Backman, L., Taalas, P. and Kulmala, M.: FinROSE – middle atmospheric chemistry transport model, Boreal Env. Res., 12, 535–550, 2007.

Funke, B., Lopéz-Puertas, M., Gil-López, S., von Clarmann, T., Stiller, G. P., Fischer, H., and Kellmann, S.: Downward transport of upper atmospheric NO_x into the polar stratosphere and lower mesosphere during the Antarctic 2003 and Arctic 2002/2003 winters, J. Geophys. Res., 110, D24308, doi:10.1029/2005JD006463, 2005.

Funke, B., Lopéz-Puertas, M., Fischer, H., Stiller, G. P., von Clarmann, T., Wetzel, G., Carli, B., and Belotti, C.: Comment on "Origin of the January–April 2004 increase in stratospheric NO_2 observed in northern polar latitudes", by: Jean-Baptiste Renard et al., Geophys. Res. Lett., 34, L07813, doi:10.1029/2006GL027518, 2007.

Grenfell, J. L., Lehmann, R., Mieth, P., Langematz, U., and Steil, B.: Chemical reation pathways affecting stratospheric and mesospheric ozone, J. Geophys. Res., 111, D17311, doi:10.1029/2004JD005713, 2006.

Hauchecorne, A., Bertaux, J.-L., Dalaudier, F., Russell III, J. M., Mlynczak, M. G., Kyrölä, E., and Fussen, D., : Large increase of NO_2 in the north polar mesosphere in January–February 2004: Evidence of a dynamical origin from GOMOS/ENVISAT and SABER/TIMED data, Geophys. Res. Lett., 34, L03810, doi:10.1029/2006GL027628, 2007.

Kylling, A., Albold, A. and Seckmeyer, G.: Transmittance of a cloud is wavelength – dependent in the UV-range: Physical interpretation, Geophys. Res. Lett., 24(4), 397–400, doi:10.1029/97GL00111, 1997.

Langematz, U., Grenfell, J. L., Matthes, K., Mieth, P., Kunze, M., Steil, B., and Brühl, C.: Chemical effects in 11-year solar cycle simulations with the Freie Universität Berlin Climate Middle Atmosphere Model with online chemistry (FUB-CMAM-CHEM), Geophys. Res. Lett., 32, L13803, doi:10.1029/2005GL022686, 2005.

Lu, H., Clilverd, M. A., Seppälä, A., and Hood, L. L.: Geomagnetic perturbations on stratospheric circulation in late winter and spring, J. Geophys. Res., 113, D16106, doi:10.1029/2007JD008915, 2008.

Manney, G. L., Daffer, W. H., Strawbridge, K. B., Walker, K. A., Boone, C. D., Bernath, P. F., Kerzenmacher, T., Schwartz, M. J., Strong, K., Sica, R. J., Krüger, K., Pumphrey, H. C., Lambert, A., Santee, M. L., Livesey, N. J., Remsberg, E. E., Mlynczak, M. G., and Russell III, J. R.: The high Arctic in extreme winters: vortex, temperature, and MLS and ACE-FTS trace gas evolution, Atmos. Chem. Phys., 8, 505–522, doi:10.5194/acp-8-505-2008, 2008.

Manney, G. L., Schwartz, M. J., Krüger, K., Santee, M. L., Pawson, S., Lee, J. N., Daffer, W. H., Fuller, R. A., and Livesey, N. J.: Aura Microwave Limb Sounder observations of dynamics and transport during the record-breaking 2009 Arctic stratosphere major warming, Geophys. Res. Lett., 36, L12815, doi:10.1029/2009GL038586, 2009.

McInturff, R.: Stratospheric warmings: Synoptic, dynamic and general-circulation aspects, NASA Reference Publ. NASA-RP-1017, NASA, Natl. Meteorol. Cent., Washington, DC, 1978.

Randall, C. E., Harvey, V. L., Siskind, D. E., France, J., Bernath, P. F., Boone, C. D., and Walker, K. A.: NO_x descent in the Arctic middle atmosphere in early 2009, Geophys. Res. Lett., 36, L18811, doi:10.1029/2009GL039706, 2009.

Reddmann, T., Ruhnke, R., Versick, S., and Kouker, W.: Modeling disturbed stratospheric chemistry during solar-induced NO_x enhancements observed with MIPAS/ENVISAT, J. Geophys. Res., 115, D00I11, doi:10.1029/2009JD012569, 2010.

Rozanov, E., Callis, L., Schlesinger, M., Yang, F., Andronova, N., and Zubov, V.: Atmospheric response to NO_y source due to energetic electron precipitation, Geophys. Res. Lett., 32, L14811, doi:10.1029/2005GL023041, 2005.

Sander, S. P., Friedl, R. R., Golden, D. M., Kurylo, M. J., Moortgat, G. K., Keller-Rudek, H., Wine, P. H., Ravishankara, A. R., Kolb, C. E., Molina, M. J., Finlayson-Pitts, B. J., Huie, R. E., and Orkin, V. L.: Chemical kinetics and photochemical data for Use in Atmospheric Studies, Evaluation Number 15, Publication 06-2, JPL, Pasadena, USA, 2006.

Seppälä, A., Verronen, P. T., Clilverd, M. A., Randall, C. E., Tamminen, J., Sofieva, V., Backman, L., and Kyrölä, E.: Arctic and Antarctic polar winter NO_x and energetic particle precipitation in 2002–2006, Geophys. Res. Lett., 34, L12810, doi:10.1029/2007GL029733, 2007.

Seppälä, A., Randall, C., Clilverd, M. A., Rozanov, E., and Rodger, C. J.: Geomagnetic activity and polar surface air temperature variability, J. Geophys. Res., 114, A10312, doi:10.1029/2008JA014029, 2009.

Siskind, D. E., Bacmeister, J. T., Summers, M. E., and Russell III, J. M.: Two-dimensional model calculations of nitric oxide transport in the middle atmosphere and comparison with Halogen Occultation Experiment data, J. Geophys. Res., 102, 3527–3546, doi:10.1029/96JD02970, 1997.

Solomon, S., Crutzen, P. J., and Roble, R. G.: Photochemical coupling between the thermosphere and the lower atmosphere: 1. odd nitrogen from 50 to 120 km, J. Geophys. Res., 87(C9), 7206–7220, 1982.

Vitt, F. M., Armstrong, T. P., Cravens, T. E., Dreschhoff, A. M., Jackman, C. H., and Laird, C. M.: Computed contributions to odd nitrogen concentrations in the Earth's polar middle atmosphere by energetic charged particles, J. Atmos. Sol.-Terr. Phys., 62, 669–683, 2000.

Vogel, B., Konopka, P., Grooß, J.-U., Müller, R., Funke, B., López-Puertas, M., Reddmann, T., Stiller, G., von Clarmann, T., and Riese, M.: Model simulations of stratospheric ozone loss caused by enhanced mesospheric NO_x during Arctic Winter 2003/2004, Atmos. Chem. Phys., 8, 5279–5293, doi:10.5194/acp-8-5279-2008, 2008.

PUBL. II

Reprinted, with permission, from
Atmospheric Chemistry and Physics, 11, 9089-9139
doi: doi:10.5194/acp-11-9089-2011

Atmos. Chem. Phys., 11, 9089–9139, 2011
www.atmos-chem-phys.net/11/9089/2011/
doi:10.5194/acp-11-9089-2011

Atmospheric Chemistry and Physics

Composition changes after the "Halloween" solar proton event: the High Energy Particle Precipitation in the Atmosphere (HEPPA) model versus MIPAS data intercomparison study

B. Funke[1], A. Baumgaertner[2], M. Calisto[3], T. Egorova[4], C. H. Jackman[5], J. Kieser[6], A. Krivolutsky[7], M. López-Puertas[1], D. R. Marsh[8], T. Reddmann[9], E. Rozanov[3,4], S.-M. Salmi[11,12], M. Sinnhuber[9,10], G. P. Stiller[9], P. T. Verronen[11], S. Versick[9,14], T. von Clarmann[9], T. Y. Vyushkova[7], N. Wieters[10], and J. M. Wissing[13]

[1]Instituto de Astrofísica de Andalucía, CSIC, Granada, Spain
[2]Max Planck Institute for Chemistry, Mainz, Germany
[3]Institute for Atmospheric and Climate Science ETH, Zurich, Switzerland
[4]Physical-Meteorological Observatory/World Radiation Center, Davos, Switzerland
[5]NASA Goddard Space Flight Center, Greenbelt, MD 20771, USA
[6]Max Planck Institute for Meteorology, Hamburg, Germany
[7]Central Aerological Observatory (CAO), Dolgoprudny, Moscow Region, Russia
[8]National Center for Atmospheric Research, Boulder, CO, USA
[9]Karlsruhe Institute of Technology, Institute for Meteorology and Climate Research, Karlsruhe, Germany
[10]Institute of Environmental Physics, University of Bremen, Bremen, Germany
[11]Earth Observation Unit, Finnish Meteorological Institute, Helsinki, Finland
[12]Department of Physics, University of Helsinki, Helsinki, Finland
[13]FB Physik, University of Osnabrück, Osnabrück, Germany
[14]Steinbuch Centre for Computing, Karlsruhe, Germany

Received: 23 December 2010 – Published in Atmos. Chem. Phys. Discuss.: 22 March 2011
Revised: 27 June 2011 – Accepted: 21 August 2011 – Published: 5 September 2011

Abstract. We have compared composition changes of NO, NO_2, H_2O_2, O_3, N_2O, HNO_3, N_2O_5, HNO_4, ClO, HOCl, and $ClONO_2$ as observed by the Michelson Interferometer for Passive Atmospheric Sounding (MIPAS) on Envisat in the aftermath of the "Halloween" solar proton event (SPE) in late October 2003 at 25–0.01 hPa in the Northern Hemisphere (40–90° N) and simulations performed by the following atmospheric models: the Bremen 2-D model (B2dM) and Bremen 3-D Chemical Transport Model (B3dCTM), the Central Aerological Observatory (CAO) model, FinROSE, the Hamburg Model of the Neutral and Ionized Atmosphere (HAMMONIA), the Karlsruhe Simulation Model of the Middle Atmosphere (KASIMA), the ECHAM5/MESSy Atmospheric Chemistry (EMAC) model, the modeling tool for SOlar Climate Ozone Links studies (SOCOL and SOCOLi), and the Whole Atmosphere Community Climate Model (WACCM4). The large number of participating models allowed for an evaluation of the overall ability of atmospheric models to reproduce observed atmospheric perturbations generated by SPEs, particularly with respect to NO_y and ozone changes. We have further assessed the meteorological conditions and their implications for the chemical response to the SPE in both the models and observations by comparing temperature and tracer (CH_4 and CO) fields.

Simulated SPE-induced ozone losses agree on average within 5 % with the observations. Simulated NO_y enhancements around 1 hPa, however, are typically 30 % higher than indicated by the observations which are likely to be related to deficiencies in the used ionization rates, though other error sources related to the models' atmospheric background state and/or transport schemes cannot be excluded. The analysis of the observed and modeled NO_y partitioning in the aftermath of the SPE has demonstrated the need to implement additional ion chemistry (HNO_3 formation via ion-ion recombination and water cluster ions) into the chemical schemes. An overestimation of observed H_2O_2 enhancements by all models hints at an underestimation of the OH/HO_2 ratio in the upper polar stratosphere during the SPE. The analysis of chlorine species perturbations has shown that the encountered

Correspondence to: B. Funke
(bernd@iaa.es)

differences between models and observations, particularly the underestimation of observed $ClONO_2$ enhancements, are related to a smaller availability of ClO in the polar night region already before the SPE. In general, the intercomparison has demonstrated that differences in the meteorology and/or initial state of the atmosphere in the simulations cause a relevant variability of the model results, even on a short timescale of only a few days.

1 Introduction

Energetic particle precipitation has important implications for atmospheric chemistry. In particular, protons and associated electrons, generated during solar eruptions, cause sporadical in-situ production of NO_x and HO_x radicals involved in catalytic ozone destruction. These solar proton events (SPEs) thus represent an important Sun-Earth connection which contributes to the natural ozone variability. The quasi-instantaneous increase of odd nitrogen and hydrogen due to SPEs induces perturbations of the chemical composition of the middle atmosphere on a short-time scale. In this sense, SPE-induced perturbations of the atmospheric composition represent an ideal natural laboratory for studying stratospheric and mesospheric chemistry (see also Jackman and McPeters, 1987).

In recent years, there have been two large SPEs (October/November 2003 and January 2005) (Jackman et al., 2008) which have been intensively observed by several instruments on different satellite platforms, including, for example, NOAA 16 SBUV/2 and HALOE data (Jackman et al., 2005a,b; Randall et al., 2005); MIPAS, GOMOS and SCIAMACHY on Envisat (López-Puertas et al., 2005a,b; von Clarmann et al., 2005; Orsolini et al., 2005; Seppälä et al., 2004; Rohen et al., 2005); and MLS on AURA (Verronen et al., 2006). In particular, during late October and early November 2003, three active solar regions produced solar flares and solar energetic particles of extremely large intensity, including the fourth largest event observed in the past forty years (Jackman et al., 2005b, 2008), known as the "Halloween" storm. During and after this event, the MIPAS instrument observed global changes (e.g. in both the Northern and Southern polar regions, during day and nighttime) in the stratospheric and lower mesospheric composition. This includes enormous enhancements in NO_x, e.g. in NO and NO_2, and large depletions in O_3 (López-Puertas et al., 2005a) as well as significant changes in other NO_y species, such as HNO_3, N_2O_5, $ClONO_2$ (López-Puertas et al., 2005b), and N_2O (Funke et al., 2008). In addition, there also have been observed changes in ClO and HOCl as evidence of perturbations by solar protons on the HO_x and chlorine species abundances (von Clarmann et al., 2005).

Several model studies, aiming at reproducing observed short- and medium-term composition changes after this particular event (Jackman et al., 2008; Verronen et al., 2008; Funke et al., 2008; Baumgaertner et al., 2010; Egorova et al., 2011) and evaluating SPE-induced long-term effects (Jackman et al., 2009) have been carried out in the past.

The High Energy Particle Precipitation in the Atmosphere (HEPPA) model vs. data intercomparison initiative has brought together scientists involved in atmospheric modeling using state-of-the art general circulation models (GCMs) and chemistry-transport models (CTMs) on the one hand and scientists involved in the analysis and generation of observational data on the other hand. The objective of this community effort is (i) to assess the ability of state-of-the-art atmospheric models to reproduce composition changes induced by particle precipitation, (ii) to identify and – if possible – remedy deficiencies in chemical schemes, and (iii) to serve as a platform for discussion between modelers and data producers. This is achieved by a quantitative comparison of observed and modeled composition changes after particle precipitation events, as well as by inter-comparing the simulations performed by the different models.

In this study we report results from the intercomparison of MIPAS/Envisat data obtained during 26 October–30 November 2003, before and after the Halloween SPE, at altitudes from 25–75 km (25–0.01 hPa) with simulations performed using the following GCMs and CTMs: the Bremen 2d Model (B2dM) (Sinnhuber et al., 2003a; Winkler et al., 2009), the Bremen 3d Chemical Transport Model (B2dM and B3dCTM) (Sinnhuber et al., 2003b), the Central Aerological Observatory (CAO) model (Krivolutsky and Vyushkova, 2002), FinROSE (Damski et al., 2007b), the Hamburg Model of the Neutral and Ionized Atmosphere (HAMMONIA) (Schmidt et al., 2006), the Karlsruhe Simulation Model of the Middle Atmosphere (KASIMA) (Kouker et al., 1999), the ECHAM5/MESSy Atmospheric Chemistry (EMAC) model (Jöckel et al., 2006), the modeling tool for SOlar Climate Ozone Links studies (SOCOL and SOCOLi) (Egorova et al., 2005; Schraner et al., 2008; Egorova et al., 2011), and the Whole Atmosphere Community Climate Model (WACCM4) (Garcia et al., 2007). Among the species affected by SPEs we focus here on NO, NO_2, H_2O_2, O_3, N_2O, HNO_3, N_2O_5, HNO_4, ClO, HOCl, and $ClONO_2$. For these species a significant perturbation well above the detection limit has been observed by MIPAS. We have further assessed the meteorological background conditions in both the models and the real atmosphere as observed by MIPAS by comparing temperature and tracer fields (CH_4 and CO). Although SPE-induced composition changes during the Halloween event have been reported in both hemispheres, we restrict our analysis to the Northern Hemisphere (NH) in the latitude range 40–90° N where most pronounced effects have been observed and composition changes can be well distinguished from the background variability.

Apart from the initial particle forcing leading to atmospheric ionization, SPE-induced composition changes are controlled by several other factors such as the neutral and

Table 1. Used MIPAS data versions (indicated by the last digits of the retrieval version) for all species on a daily basis within the period 26 October–30 November 2003.

Day	26	27	28	29	30	31	1	2	3	4	5	6	7	8	9	10	11	12	13	14	15	16	17	18	19	20	21	22	23	24	25	26	27	28	29	30
Temp.	9	10	10	9	9	9	9	9	9	9	9	10	10	9	9	9	9	10	10	10	9	9	9	9	9	9	9	9	10	10	10	10	9	9	9	9
CH_4	12	12	12	12	12	12	12	12	12	12	12	12	12	12	12	12	12	12	12	12	12	12	12	12	12	12	12	12	12	12	12	12	12	12	12	12
CO	9	11	11	9	10	10	9	9	10	10	9	11	11	10	10	10	9	11	11	11	10	10	10	9	10	10	9	10	11	11	11	11	9	10	10	10
NO	14	14	14	14	14	14	14	14	14	14	14	14	14	14	14	14	14	14	14	14	14	14	14	14	14	14	14	14	14	14	14	14	14	14	14	14
NO_2	14	13	13	14	11	11	14	14	11	11	14	13	13	11	11	11	14	13	13	13	11	11	11	14	11	11	14	11	13	13	13	13	14	11	11	11
N_2O	12	12	12	12	12	12	12	12	12	12	12	12	12	12	12	12	12	12	12	12	12	12	12	12	12	12	12	12	12	12	12	12	12	12	12	12
HNO_3	9	9	9	9	9	9	9	9	9	9	9	9	9	9	9	9	9	9	9	9	9	9	9	9	9	9	9	9	9	9	9	9	9	9	9	9
N_2O_5	9	10	10	10	10	10	9	10	10	10	10	10	10	10	10	10	9	10	10	10	10	10	10	10	10	10	9	10	10	10	10	10	10	10	10	10
HNO_4	12	12	12	12	12	12	12	12	12	12	12	12	12	12	12	12	12	12	12	12	12	12	12	12	12	12	12	12	12	12	12	12	12	12	12	12
O_3	9	9	9	9	9	9	9	9	9	9	9	9	9	9	9	9	9	9	9	9	9	9	9	9	9	9	9	9	9	9	9	9	9	9	9	9
H_2O_2	4	4	4	4	4	4	4	4	4	4	4	4	4	4	4	4	4	4	4	4	4	4	4	4	–	4	4	4	4	4	4	4	4	4	4	4
ClO	10	11	11	11	11	11	10	11	11	11	11	11	11	11	11	11	10	11	11	11	11	11	11	11	11	11	10	11	11	11	11	11	11	11	11	11
HOCl	3	4	4	3	3	3	3	3	3	3	3	4	4	3	3	3	3	4	4	4	3	3	3	3	3	3	3	3	4	4	4	4	3	3	3	3
$ClONO_2$	11	12	12	12	12	12	11	12	12	12	12	12	12	12	12	12	11	12	12	12	12	12	12	12	12	12	11	12	12	12	12	12	12	12	12	12

ion chemistry responsible for the repartitioning of primarily generated species, the background composition interfering with the chemical repartitioning, and the meteorological/dynamical conditions. The large number of controlling factors and their interaction introduce a significant spread in the model results and make their analysis difficult. In order to reduce the model variability and to make differences between the simulations more traceable, we have simplified the intercomparison setup such that a common particle-induced ionization source has been used in all models. These ionization rates, accounting for protons (154 eV–500 MeV) and electrons (154 eV–5 MeV) have been provided by the AIMOS model (Wissing and Kallenrode, 2009). Different model responses to the particle forcing are hence reduced to differences of the intrinsic model properties, e.g. chemical and dynamical schemes. A major aim of this paper is the assessment of these differences and their implications for the models' ability to correctly describe particle precipitation effects which represent an important source of natural, solar-induced climate variability on short and mid-term scales. Additionally, conclusions on the quality of the description of the external forcing provided by the ionization model can be drawn from the overall agreement of the short-time response of primarily generated constituents (i.e. NO_x).

The paper is organized as follows: in Sect. 2 we give an overview on MIPAS observations and data products used in this study, followed by Sect. 3 describing the ionization model AIMOS and Sect. 4 describing the participating global circulation and chemistry transport models. The intercomparison method is described in Sect. 5, followed by the discussion of the results (Sect. 6).

2 MIPAS observations

The Michelson Interferometer for Passive Atmospheric Sounding (MIPAS) is a mid-infrared Fourier transform limb emission spectrometer designed and operated for measurement of atmospheric trace species from space (Fischer et al., 2008). It is part of the instrumentation of the European Environmental Satellite (ENVISAT) which was launched into its sun-synchronous polar orbit of 98.55° N inclination at about 800 km altitude on 1 March 2002. MIPAS passes the equator in a southerly direction at 10:00 a.m. local time 14 to 15 times a day, observing the atmosphere during day and night with global coverage from pole to pole. The instrument's field of view is 30 km in horizontal and approximately 3 km in vertical direction. MIPAS operated during October/November 2003 at full spectral resolution of 0.035 cm^{-1} (unapodized) in terms of full width at half maximum. During this period, MIPAS recorded a rear-viewing limb sequence of 17 spectra each 90 s, corresponding to an along track sampling of approximately 500 km and providing about 1000 vertical profiles per day in its standard observation mode. Tangent heights covered the altitude range from 68 down to 6 km with tangent altitudes at 68, 60, 52, 47, and then at 3 km steps from 42 to 6 km.

Trace gas profiles have been retrieved from calibrated geolocated limb emission spectra with the scientific MIPAS level 2 processor developed and operated by the Institute of Meteorology and Climate Research (IMK) in Karlsruhe together with the Instituto de Astrofísica de Andalucía (IAA) in Granada. The general retrieval strategy, which is a constrained multi-parameter non-linear least squares fitting of measured and modeled spectra, is described in detail in von Clarmann et al. (2003). Its extension to retrievals under consideration of non-LTE (i.e. CO, NO, and NO_2) is described in Funke et al. (2001). Non-LTE vibrational populations of these species are modeled with the Generic RAdiative traNsfer AnD non-LTE population Algorithm (GRANADA) (Funke et al., 2007) within each iteration of the retrieval.

In contrast to previous work describing MIPAS observations of composition changes during the Halloween SPE (López-Puertas et al., 2005a,b; von Clarmann et al., 2005), we base our analysis here on reprocessed IMK/IAA MIPAS data which have substantially improved with respect to previous data versions. These improvements include updates in the L1B processing (version 4.61/62 instead of 4.59) performed by ESA as well as changes in the L2 processing performed at IMK/IAA. The new data set also offers full temporal coverage over the period of interest (26 October–

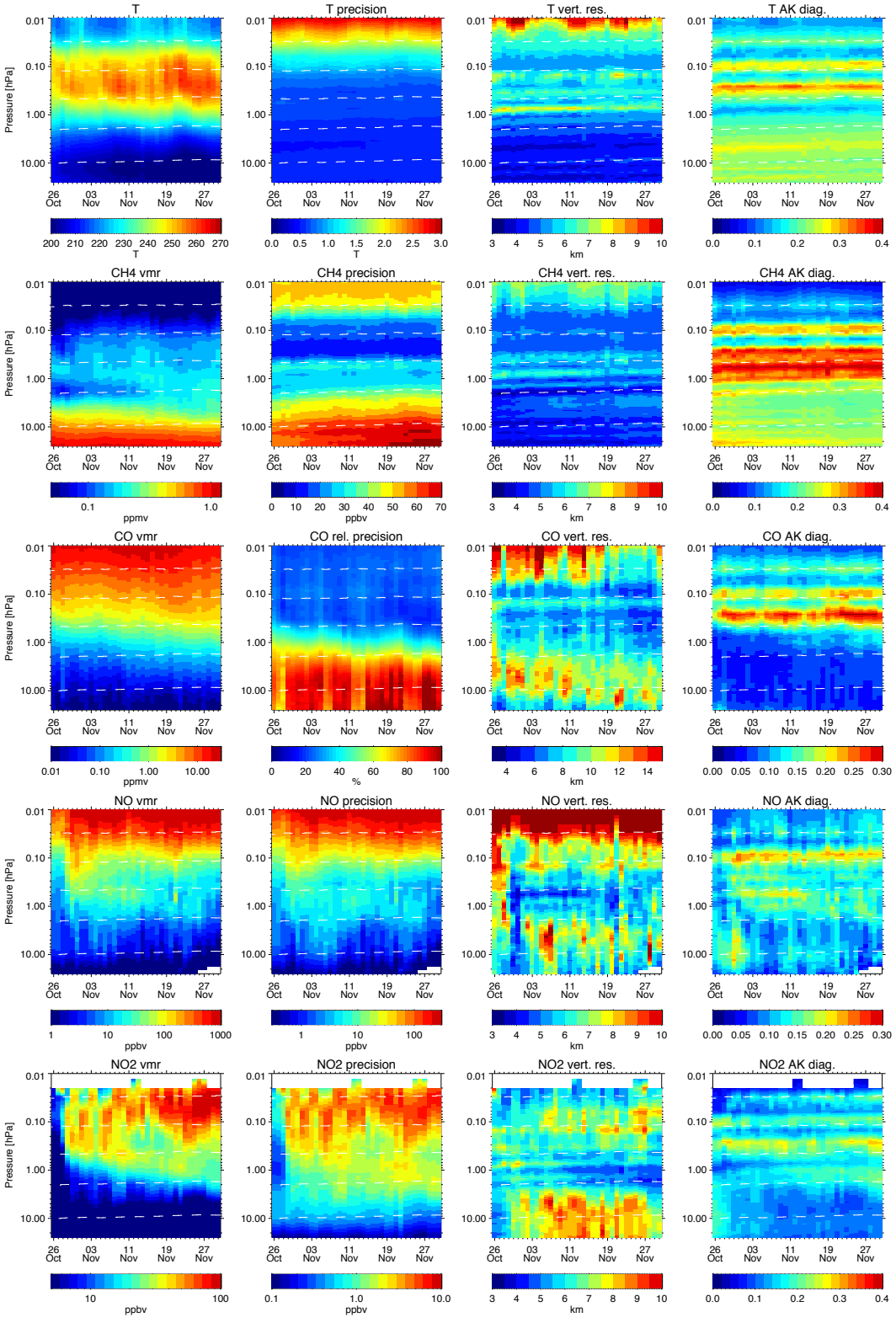

Fig. 1. Temporal evolution of MIPAS temperature, CH_4, CO, NO, NO_2, (from top to bottom) volume mixing ratio, single measurement precision, vertical resolution, and AK diagonal element profiles (left to right) during 26 October–30 November 2003 averaged over 60–90° N. White dashed lines indicate 30, 40, 50, 60, and 70 km geometric altitude levels. White regions reflect meaningless data (AK diagonal elements smaller than 0.03).

30 November 2003). In the following, we summarize the improvements of the retrieval setups for each species/parameter and characterize the data used in our analysis in terms of estimated single measurement precision and vertical resolution obtained from the full width at half maximum of the rows of the averaging kernel (AK) matrix (Rodgers, 2000). The AK diagonal elements are also discussed as a measure of the sensitivity of the retrieval at a given profile grid point to the "true" profile. Values close to zero (typically <0.03) indicate that there is no significant sensitivity to the retrieval parameter at the corresponding altitude and hence are excluded from our analysis. This value may appear unreasonably small but since IMK/IAA retrievals are not constrained by optimal estimation (Rodgers, 2000) but by a first order smoothing constraint using a Tikhonov (1963) formalism, low values do not hint at a large a priori content of the retrieval but only at extensive smearing of information over altitude. A detailed discussion of systematic retrieval errors can be found in previous works describing the individual constituent retrievals which are referenced in the following.

2.1 Temperature

Temperature data versions used here are V3O_T_9 and V3O_T_10 (see Table 1), both including as an extension to the original retrieval setup described in von Clarmann et al. (2003) the joint retrieval of horizontal temperature gradients. Differences between both versions are of minor nature and do not noticeably affect the data characteristics. In the period of interest, observed temperatures range at 60–90° N from around 200 K in the lower stratosphere to around 270 K at the stratopause (see Fig. 1). The single measurement precision ranges from 0.5 K to 1.5–2.5 K above the stratopause. Vertical resolution is 3–4 km below 1 hPa and 5–7 km above. Meaningful data are obtained in the whole vertical range of interest (25–70 km).

2.2 CH_4

We use version V3O_CH4_12 (see Table 1) which has been jointly retrieved with N_2O (V3O_N2O_12). The retrieval setup is similar to that described in Glatthor et al. (2005). The single measurement precision ranges from 10–20 ppbv in the upper stratosphere to 50–70 ppbv above and below (see Fig. 1) Vertical resolution is 3–6 km below 0.03 hPa and slightly higher above. Meaningful data is obtained in the whole vertical range of interest (25–70 km).

2.3 CO

CO data versions used here are V3O_CO_9, V3O_CO_10, described in detail in Funke et al. (2009), as well as the most recent version V3O_CO_11 (see Table 1). Improvements implemented in the latter version include an extended set of spectral fitting windows resulting in a better precision and vertical resolution in the lower and middle stratosphere. In the period of interest, the temporal evolution of MIPAS CO abundances at 60–90° N indicate polar winter descent of mesospheric air masses of about 10 km around 1 hPa (see Fig. 1). The single measurement precision ranges from 20–30 % above 1 hPa to 70–80 % in the lower stratosphere. Vertical resolution is 6–12 km below 0.1 hPa. Meaningful data are obtained in the whole vertical range of interest (25–70 km).

2.4 NO

We use version V3O_NO_14 (see Table 1), available for the whole time period. This version has substantially improved with respect to the retrieval setup described in Funke et al. (2005) and the data discussed in López-Puertas et al. (2005a) by (i) the use of log(vmr) instead of vmr (volume mixing ratio) in the retrieval vector, (ii) a revised correction scheme for line of sight variations of the NO_x partitioning close to the terminator, and iii) joint-fitted vmr horizontal gradients at constant longitudes and latitudes. NO increases of several 100 ppbv have been observed at 60–90° N during the intense proton forcing during 29 October–4 November in the upper stratosphere around 0.2 hPa (see Fig. 1). Above, NO increases were mainly produced by polar winter descent of upper atmospheric air masses, resulting in vmrs up to 1 ppmv below 70 km. The single measurement precision is of the order of 10 %. Vertical resolution ranges from 4 to 8 km below 70 km. Meaningful data are obtained in the whole vertical range of interest (25–70 km).

2.5 NO_2

NO_2 data versions used here are V3O_NO2_11, V3O_NO2_13, and V3O_NO2_14 (see Table 1). Including the same modifications as described above for NO, these versions have substantially improved with respect to the retrieval setup described in Funke et al. (2005) and the data discussed in López-Puertas et al. (2005a). While differences between the latter two versions do not affect noticeably the data characteristics, a modified regularization scheme and terminator treatment implemented after version V3O_NO2_11 gave rise to non-negligible differences in the newer versions with respect to the previous setup. These differences are visible in the vertical resolution in the mesosphere and middle stratosphere (see Fig. 1, third column) and go along with generally smaller vmrs around the terminator at 70° N around 0.1 hPa. Similar to NO, increases of 50–80 ppbv were observed during the proton forcing in the upper stratosphere, descending by approximately 10 km by the end of November. Polar winter descent of NO_x led to mesospheric NO_2 increases of more then 100 ppbv, particularly in the second half of November. The single measurement precision is of the order of 5–10 %. Vertical resolution ranges from 4 to 8 km below 70 km. Meaningful

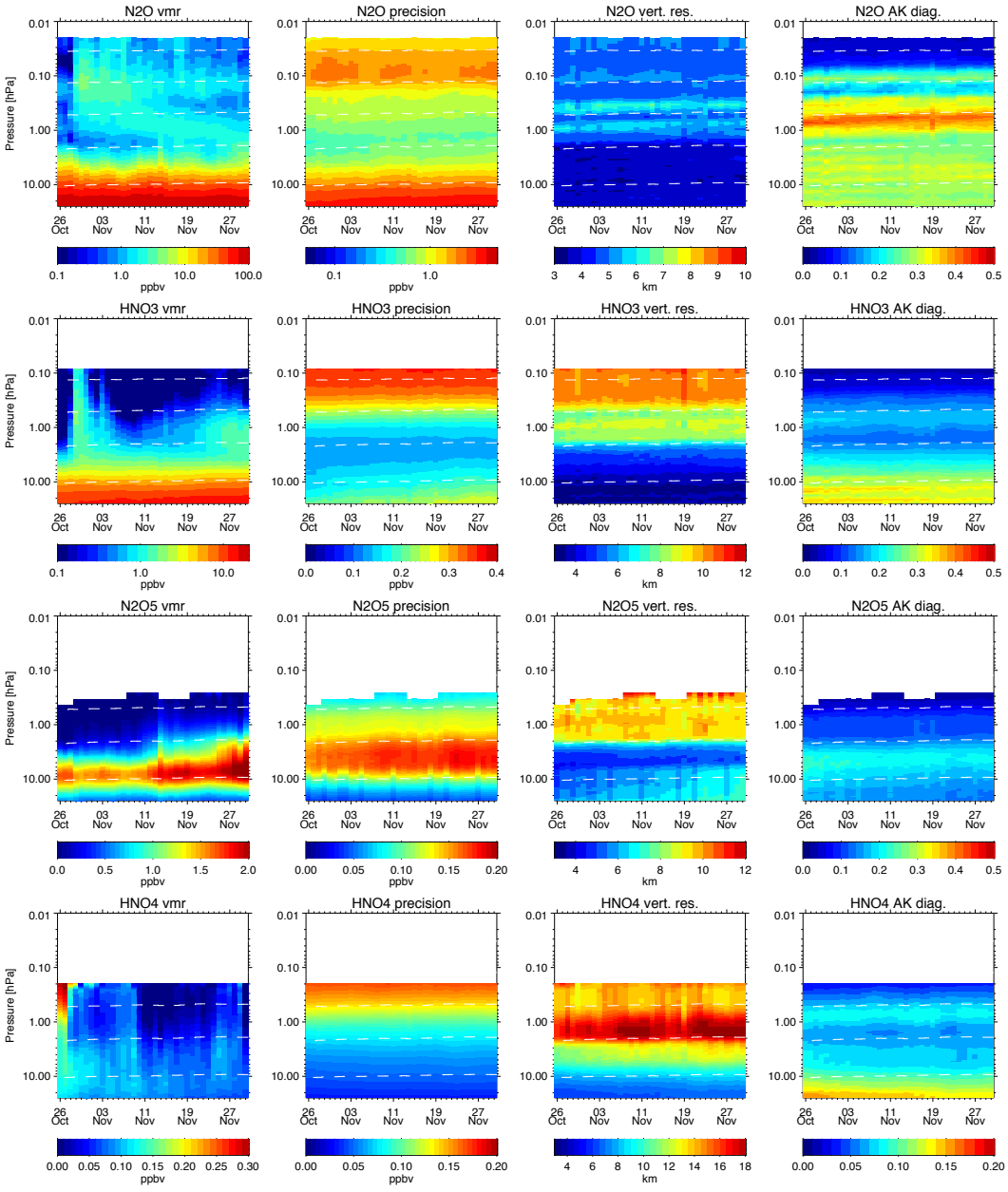

Fig. 2. Same as Fig. 1, but for N_2O, HNO_3, N_2O_5, and HNO_4.

data are obtained in the whole vertical range of interest (25–70 km).

2.6 N_2O

We use version V3O_N2O_12 (see Table 1), available for the whole time period. This version has already been used for the previous analysis of N_2O abundance changes during the Halloween SPE (Funke et al., 2008) and differs from other versions by a relaxed regularization above approximately 40 km, which allows for vertically resolving the upper stratospheric and mesospheric enhancements. At 60–90° N, these enhancements of around 5–7 ppbv appeared around 30 October and descended during November to the middle stratosphere (see Fig. 2). The single measurement precision ranges from 0.5 ppbv in the upper stratosphere to 2 ppbv in the mesosphere. Vertical resolution is 4–6 km. Meaningful data are obtained in the whole vertical range of interest (25–70 km).

2.7 HNO_3

We use version V3O_HNO3_9 (see Table 1), available for the whole time period, and which is based on the retrieval setup described in Wang et al. (2007). HNO_3 increases of around

3 ppbv up to altitudes of 0.1 hPa during the proton forcing and a further buildup at slightly lower altitudes at the end of November are visible in Fig. 2, consistent with previous findings (López-Puertas et al., 2005b). The single measurement precision ranges from 0.1 ppbv in the middle stratosphere to 0.35 ppbv around the stratopause. Vertical resolution is 3–4 km below 12 hPa and 7–10 km above. Meaningful data are obtained below 0.1 hPa (60 km).

2.8 N_2O_5

N_2O_5 data versions used here are V3O_N2O5_9 and V3O_N2O5_10 (see Table 1), all based on the retrieval setup described in Mengistu Tsidu et al. (2004). Differences between both versions are of minor nature and do not affect noticeably the data characteristics. N_2O_5 increases related to the proton event are visible in Fig. 2 in the second half of November around 2–0.5 hPa, consistent with previous findings (López-Puertas et al., 2005b; Orsolini et al., 2005). The single measurement precision ranges from 0.05 ppbv to 0.15 ppbv in the middle stratosphere. Vertical resolution is 5–7 km below 2 hPa and 9–10 km above. Meaningful data are obtained below approximately 0.3 hPa (52 km).

2.9 HNO_4

We use version V3O_HNO4_12 (see Table 1) which differs from the original retrieval setup described in Stiller et al. (2007) by the application of a weaker regularization in the middle stratosphere, where most pronounced SPE effects are expected. Unfortunately, this version is sensitive to systematic oscillations in the radiance baseline related to an imperfect gain calibration of the instrument (see also Stiller et al., 2008). In consequence, retrieved HNO_4 profiles are systematically biased during each gain calibration period (typically a few days) with a randomly changing magnitude from one calibration period to another. The variable bias is noticeable in the temporal evolution of the observed HNO_4 distributions at 60–90° N (see Fig. 2) as sharp increases/decreases in the upper stratosphere, coincident with the onsets of new gain calibration periods (i.e. 28 October, 10 November, and 24 November). Therefore, we restrict our analysis of SPE-related HNO_4 increases in Sect. 6 to data observed during one particular gain calibration period, 28 October–5 November, covering the onset of the proton forcing which led to short-term HNO_4 increases of the order of 0.15 ppbv (hardly visible in Fig. 2). The single measurement precision ranges from 0.03 ppbv to 0.15 ppbv around the stratopause. Vertical resolution is 6–10 km below 5 hPa and around 10 km above. Meaningful data are obtained below approximately 0.2 hPa (55 km).

2.10 O_3

We use version V3O_O3_9 (see Table 1), available for the whole time period. Retrieval setup and characteristics are similar to those described in Steck et al. (2007), except for a slightly different selection of spectral intervals (microwindows) and the inclusion of pre-fitted horizontal temperature gradients. A pronounced O_3 depletion during the intense proton forcing as already reported in López-Puertas et al. (2005a) is visible above the stratopause at 60–90° N, competing with seasonal mesospheric O_3 buildup in the following weeks (see Fig. 3). Also, the previously reported NO_x-induced losses at lower altitudes are seen on a mid-term scale. The single measurement precision ranges from 0.1 ppmv around the stratopause to 0.25 ppbv above and below. Vertical resolution is 3–4 km below 1 hPa and 5–7 km above. Meaningful data are obtained in the whole vertical range of interest (25–70 km).

2.11 H_2O_2

We use version V3O_H2O2_4, available for the whole time period (see Table 1) which is based on the retrieval setup described in Versick (2010). H_2O_2 increases up to 0.15 ppbv have been observed at 60–90° N during the intense proton forcing on 29 October–4 November in the upper stratosphere around 0.2 hPa (see Fig. 3). The single measurement precision in the middle stratosphere ranges from 0.1 to 0.2 ppbv, being thus of the order of the observed enhancements. In consequence, averaging is required for the analysis. Vertical resolutions larger than 10 km indicate that no relevant information on the vertical distribution of the middle/upper stratospheric enhancements can be extracted from the measurements. Meaningful data are obtained below approximately 0.2 hPa (55 km).

2.12 ClO

ClO data versions used here are V3O_CLO_10 and V3O_CLO_11 (see Table 1), all based on the retrieval setup described in Glatthor et al. (2004). Differences between both versions are of minor nature and do not affect noticeably the data characteristics. As in the case of HNO_4, ClO data is affected by systematic oscillations in the radiance baseline related to an imperfect gain calibration of the instrument, however, to a lesser degree than in the case of HNO_4. The single measurement precision ranges from 0.2 ppbv in the lower stratosphere to 0.7 ppbv around 2 hPa, being thus higher than 100 % at the ClO peak height (see Fig. 3). In consequence, averaging is required for its analysis. Vertical resolution is 6–10 km below 2 hPa and 15–20 km above. Meaningful data are obtained below approximately 0.5 hPa (40 km).

2.13 HOCl

HOCl data versions used here are V3O_HOCL_3 and V3O_HOCL_4 (see Table 1), all based on the retrieval setup described in von Clarmann et al. (2006). Differences between both versions are of minor nature and do not affect noticeably the data characteristics. HOCl increases of around

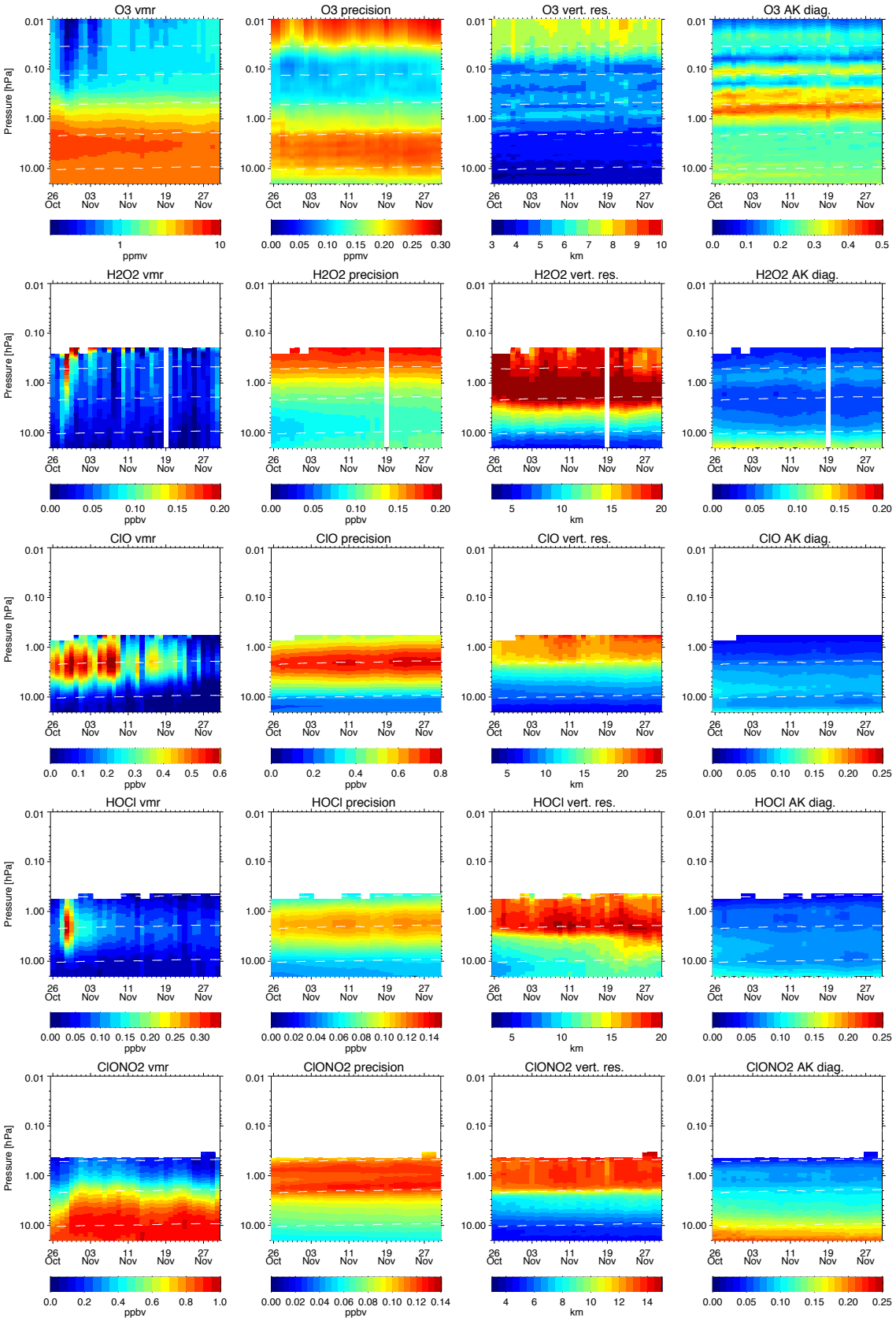

Fig. 3. Same as Fig. 2, but for O_3, H_2O_2, ClO, HOCl, and $ClONO_2$.

0.3 ppbv show up in Fig. 3 immediately after the main proton forcing at the beginning of November, consistent with previous findings (von Clarmann et al., 2005). The single measurement precision ranges from 0.05 to 0.1 ppbv around 2 hPa. Vertical resolution 8–12 km below 2 hPa and coarser than 15 km above. Meaningful data is obtained below approximately 0.5 hPa (40 km).

2.14 $ClONO_2$

$ClONO_2$ data versions used here are V3O_CLONO2_11 and V3O_CLONO2_12 (see Table 1), all based on the retrieval setup described in Höpfner et al. (2007). Differences between both versions are of minor nature and do not affect noticeably the data characteristics. $ClONO_2$ increases of around 0.5 ppbv are visible in Fig. 3 after the main proton forcing above 5 hPa and last until the end of November. This is consistent with previous findings based on data version V1_CLONO2_1 (López-Puertas et al., 2005b) in qualitative terms, however, the peak height of the increases is slightly higher (∼5 km) in the newer data versions included here. This difference is mainly related to a change of the height-dependent regularization strength in order to allow for more sensitivity at lower and higher altitudes. The single measurement precision ranges from 0.06 to 0.12 ppbv, increasing with altitude. Vertical resolution is 5–8 km below 2 hPa and 12–14 km above. Meaningful data is obtained below approximately 0.5 hPa (40 km).

3 Ionization rates

The model intercomparison is based on ionization rates calculated with Atmospheric Ionization Module OSnabrück (AIMOS). The reason is to avoid different model results due to different ionization rates as to better understand the differences in the dynamical and chemistry schemes of the models under assessment. AIMOS calculates ionization rates due to precipitating solar and magnetospheric particles. The altitude range of calculated ionization rates is defined by the energy range of the particles considered, which is specific to the satellite instruments used. The data used here and their altitude coverage are listed in Table 2. Given by the altitude range of this study, the focus lies on solar particles. As particle precipitation strongly depends on the geomagnetic field, the model accounts for different spatial precipitation zones. A detailed description of AIMOS can be found in Wissing and Kallenrode (2009).

AIMOS is composed of two parts. One describes the spatial particle flux on top of the atmosphere while the second calculates the resulting ionization rate. Both parts will be discussed in the following.

Table 2. AIMOS particle energy ranges and the corresponding pressure and altitude levels. As the upper altitude border for protons and electrons lies in the thermosphere, it varies by solar activity. The first number indicates solar minimum conditions while the second number represents solar maximum.

Species	Energy	Pressure (hPa)	Approx. altitude (km)
protons	154 eV–500 MeV	10^{-7}–100	18–240/440
electrons	154 eV–5 MeV	10^{-7}–1	48–240/440

3.1 Spatial particle flux

The particle flux on top of the atmosphere is measured by the TED and MEPED instruments on POES 15/16 as well as the SEM instrument on GOES 10. As all particle measurements are in-situ, the main challenge is to derive a global coverage at any time. Inside an empirically determined polar cap where particle precipitation is homogeneous, the high energy particle flux from GOES and the mean flux values from polar cap crossings of the POES satellites are used. Outside the polar cap, particle precipitation depends on geomagnetic latitude, geomagnetic activity and local time. Therefore, mean precipitation maps for the POES TED and MEPED channels, based on a 4 year data set, have been produced, sorted by the geomagnetic Kp-index and local time. These mean precipitation maps represent the spatial distribution, including, e.g. the movement of the auroral oval. According to the recent Kp-level, the mean precipitation maps are selected and scaled to recent POES particle flux.

In summary, the first part of the model describes the incoming particle flux at every grid point. The spatial resolution is 96 zonal cells, divided into 48 meridional sections. Regions of similar particle flux are combined as, e.g. the polar cap. Given by the scaling of the mean precipitation maps, the temporal resolution is limited by the POES orbit and has been set to 2 h.

3.2 Modeling ionization rates

The second part of AIMOS is the atmospheric particle detector model, which simulates particle interactions based on the GEANT4-Simulation Toolkit (Agostinelli et al., 2003). GEANT4 provides Monte-Carlo based algorithms to model energy deposition/ionization of protons and electrons. The atmospheric detector model is divided into 67 logarithmically equidistant pressure levels, ranging from sea level to 1.7×10^{-5} Pa. Since the atmospheric parameters (density, altitude, composition and temperature) depend on latitude, season and solar activity, model versions for 80° N, 60° N, 60° S and 80° S, 3 different F10.7 flux values and 4 different months are used. These parameters are adopted from the HAMMONIA (Schmidt et al., 2006) and MSIS (Picone et al.,

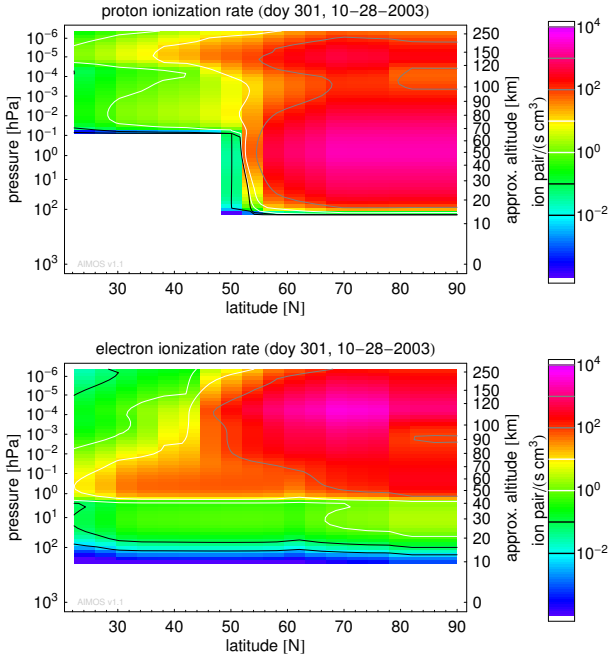

Fig. 4. Altitude-latitude sections of AIMOS ion pair production rates for protons (top) and electrons (bottom) on 28 October 2003.

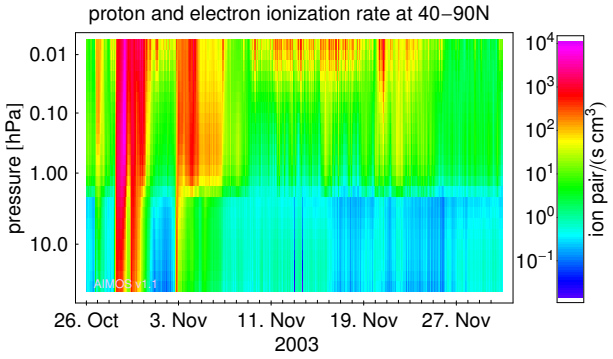

Fig. 5. Temporal evolution of area-weighted averages (40–90° N) of AIMOS ion pair production rates for protons and electrons during the period of interest. Electron ionization rate below 1 hPa is induced by bremsstrahlung only.

2002) models. The ionization rates for mono-energetic and isotropic particle ensembles are determined. As a final step, the mono-energetic ionization rates are combined with multiple power-law fits of the particle flux at various regions. The latitudinal distribution of the proton and electron contributions to the modeled ionization rates is shown in Fig. 4 for 28 October 2003.

Figure 5 shows the temporal evolution of the resulting ion pair production rates averaged over 40–90° N during the period of interest. Prior to the main event, a X1.1 flare on 23 October was accompanied by a coronal mass ejection (CME), affecting moderately the Earth atmosphere on the evening of 26 October (Dst: −72 nT). The main event was caused by a series of three consecutive flares (X1.2, X17 and X10) from 26 October to 29 October, accompanied by strong precipitation of energetic particles as well as interplanetary shocks causing high geomagnetic disturbance (Dst: −42 nT, −363 nT and −401 nT) when they arrived at 1 AU after 20 to 32 h. This "Halloween" SPE provoked two very strong increases in the ion pair production rates on 28–30 October and led to significant atmospheric ionization down to the middle stratosphere around 10 hPa. Modeled peak rates at 0.1 hPa were in the order of several thousand ion pairs per cm^{-3}. The second, less intense event was a consequence of a X8.3 flare in the evening of 2 November. The following shock arrived at Earth on 4 November, leading to geomagnetic disturbance (Dst: −68 nT) and moderate ionization restricted to higher altitudes. The most intensive flare (and fastest CME) during this period (and solar cycle 23 in total) reaches class X28 on 4 November. However, as it was moving orthogonal to the Sun-Earth line, the impact to the Earth's atmosphere was small (Dst: −27 nT) as indicated by the little red peak in the evening of 6 November. The last major forcing during this period was the large storm on 20 November (Dst: −472 nT) originating from a CME on 18 November. A more detailed description of the October–November 2003 SPE period is given in Gopalswamy et al. (2005).

The ionization rates should provide a similar forcing for all models, therefore the original data set has been adopted to every model grid. The data set and the adoption routine for a used specific grid is available at http://aimos.physik.uos.de.

4 Description of participating models

4.1 Bremen 2d model (B2dM)

The Bremen two-dimensional model is based on the two-dimensional transport, chemistry and radiation model formerly described in Sinnhuber et al. (2009) and Chipperfield and Feng (2003). It uses the dynamical core of the so-called "two-and a half-dimensional" model THIN AIR (Kinnersley, 1998), which calculates temperature, pressure, and horizontal transport on isentropic surfaces, interactively with the model chemistry. The model covers the altitude range from the surface to ∼100 km in 29 isentropic surfaces, providing a vertical spacing of about 3.5 km. The horizontal resolution is about 9.5 degree. Stratospheric dynamics are forced by the amplitudes of waves 1 to 3 of the Montgomery potential from meteorological analyses with a repeating annual cycle for the period of May 1980 to April 1981. There is no quasi biennial oscillation (QBO) in the model, i.e. the modeled tropical stratospheric wind is always in a weak easterly state. In this sense, the Bremen 2d model is a two-dimensional chemistry-climate model which is forced to repeat a very similar scenario by the repeating annual cycle of the Montgomery potential.

The chemistry is based on the SLIMCAT chemistry (Chipperfield and Jones, 1999), but adapted for the use in the mesosphere in several ways: (1) above ∼50 km, no family approach is used; (2) H_2O and CO_2 are treated as short-lived species explicitly, and H_2 is varied as well, to provide a realistic description of mesospheric HO_x and CO. (3) NO_x and HO_x production by atmospheric ionization is parameterized based on Porter et al. (1976) and Solomon et al. (1981), i.e. 1.25 NO_x are produced, of which 45 % are produced as N, and 55 % as NO, and up to 2 HO_x are produced per ion pair depending on pressure and ionization rate, equally distributed to H and OH. Ionization due to Galactic Cosmic Rays in the stratosphere has been included based on Heaps (1978); the additional ionization due to solar and magnetospheric particles is considered by introducing atmospheric ionization rates of protons and electrons provided by the AIMOS model (see Sect. 3).

All reaction and photolysis rates are taken from Sander et al. (2006). The Bremen 2d model has been used in the past to investigate the impact of large solar proton events on the composition of the middle atmosphere (Sinnhuber et al., 2003a; Rohen et al., 2005; Winkler et al., 2008). For the HEPPA intercomparison, the two-dimensional model has been combined with a one-dimensional model sharing the same description of chemistry in the following way:

25 model runs with the two-dimensional model are carried out at different longitudes, to take into account the tilt of the geomagnetic poles. The B2dM runs started in 1959. Tropospheric trace gases (FCKWs, halons, and green-house gases) were prescribed into the lowest model box from WMO (2010). For every MIPAS measurement used in the intercomparison, a one-dimensional model run is initialized with output of the 2-dimensional model runs interpolated to the geo-location of the measurement, at local noon of the day before the measurement took place. One-dimensional model runs are then carried out until the time of the measurement, providing model output at the exact time and geo-location of the measurement.

4.2 Bremen 3d Chemistry and Transport model (B3dCTM)

The Bremen three-dimensional Chemistry and Transport Model is a combination of the Bremen transport model (Sinnhuber et al., 2003b) and the chemistry code of the Bremen 2d model (Sinnhuber et al., 2003a; Winkler et al., 2008), which is based on the SLIMCAT model (Chipperfield and Jones, 1999).

The model has 28 isentropic levels ranging from 330 to 3402 K (approx. 10–60 km) and has a horizontal resolution of 3.75° × 2.5°. Output is provided hourly. The vertical transport across the isentropes is calculated through diabatic heating and cooling rates. These rates are calculated using the radiation scheme MIDRAD (Shine, 1987). The horizontal transport is driven by external wind fields. Advection is calculated by using the second order moments scheme by Prather (1986). Meteorological data, such as horizontal wind speeds and temperatures, are taken from ECMWF ERA Interim (Simmons et al., 2006). Concentrations at the lower model box are kept constant from the initialization. No transport over the lower and upper vertical boundary into and out of the model boxes is considered. The model run calculated with B3DCTM was initialized at the beginning of January 2003.

The model calculates the behavior of 58 chemical species, using a family approach for short-lived species (HO_x, NO_x, O_x, ClO_x, BrO_x, and CHO_x). It includes about 180 gas phase, photochemical, and heterogeneous reactions and uses the recent set of recommendations for kinetic and photochemical data established by the Jet Propulsion Laboratory (Sander et al., 2006).

To account for ion chemistry reactions within the neutral code, the production of NO_x and HO_x is parameterized as suggested by Porter et al. (1976) and Solomon and Crutzen (1981). Hence 1.25 N atoms and about 2 HO_x are produced per ion pair. Atmospheric ionization due to solar and magnetospheric particles is considered by introducing atmospheric ionization rates of protons and electrons provided by the AIMOS model (see Sect. 3).

4.3 CAO

The Central Aerological Observatory (CAO) model consists of a CTM and a 3-D dynamical core with a horizontal resolution of 10° × 10° and vertical resolution of 2 km. The radiative scheme used in the dynamical core below 60 km is based on parameterizations described in Chou and Suarez (1994, 1999). Above, parameterizations from Kutepov and Fomichev (1993); Fomichev et al. (1998); Kockarts (1980); Strobel (1978) are applied. The CTM calculates the concentrations of 30 minor components, involved in 70 chemical and 35 photochemical reactions, in the range 0–90 km. Output is provided hourly. The reaction rate constants, absorption cross-sections, solar radiation intensity, and quantum outputs were assigned in the tabulated form according to Sander et al. (2003). The annual and daily variations of the solar zenith angle at a given point and its dependence on the height above the Earth's surface were taken into account. For zenith angle higher than 75°, Chapman's functions have been used in accordance with Swinder and Gardner (1967). Photolysis rates have been recalculated every hour during the integration of the model. A family approach (Turco and Whitten, 1974) has been used for solving the chemical equations, including O_x ($O_3 + O + O(^1D)$), NO_y ($N + NO + NO_2 + NO_3 + 2N_2O_5 + HNO_3 + HNO_4 + ClONO_2$), Cl_y ($Cl + ClO + OClO + ClOO + HOCl + HCl$), and hydrogen compounds ($H + OH + HO_2 + 2H_2O_2$). Other long-lived species (N_2O, CCl_4, $CFCl_3$, CF_2Cl_2, CH_3Cl_3, CH_4, H_2O, H_2 and CO_2) were included also in simulations. The CAO model applies additionally to electron and proton-induced

Table 3. Summarized description of the models involved in this study.

Model	Type	Vertical domain	Vert. range (km)	Horizontal resolution	Vert. res. (km)	Meteorological data nudging	Family approach[a]	Kinetic data[b]
B2dM	CTM/GCM -2D	isentropic	∼0–100	9.5°	∼3.5	GCM	<50 km	S06
B3dCTM	CTM	isentropic	∼10–60	3.75° × 2.5°	∼3.5	ECMWF ERA Interim	yes	S06
CAO	CTM/GCM	altitude	0–90	10° × 10°	2	GCM	yes	S03
FinROSE	CTM	hybrid	∼0–65	10° × 5°	∼2	ECMWF ERA Interim	yes	S06
HAMMONIA	CCM	pressure	∼0–200	4° × 4°	∼3.5	ECMWF below 179 hPa	no	S06
KASIMA	CCM	pressure	∼7–120	5.6° × 5.6°	0.75–3.8	ECMWF below 1 hPa	no	S03
EMAC	CCM	hybrid	∼0–80	2.8° × 2.8°	∼1	ECMWF below 200 hPa	no	S06
SOCOL(i)	CCM	hybrid	∼0–80	3.75° × 3.75°	∼2	free-running	no	S00
WACCM	CCM	pressure	∼0–135	1.9° × 2.5°	∼1.5	MERRA below 50 km	no	S06

[a] See model descriptions in Sect. 4 for details. [b] S00: Sander et al. (2000), S03: Sander et al. (2003), S06: Sander et al. (2006).

ionization also ionization rates caused by alpha-particles provided by the AIMOS model (Wissing and Kallenrode, 2009).

The vertical profiles of molecular oxygen and air density were fixed during photochemical calculations. Heterogeneous removal of H_2O_2, HNO_3, HCl, and HNO_4 was included in the troposphere. Fixed mixing ratios for long-lived and "chemical families" components at lower and upper boundaries were assumed during the calculations in order to formulate the boundary conditions. Corresponding mixing ratio values were taken from Park et al. (1999). An accurate, non-diffuse method for three-dimensional advection of trace species suggested by Prather (1986) was used to solve the continuity equation for each transported species ("families" and long-lived species). The chemical constituents were initialized with profiles obtained from a one-dimensional model (Krivolutsky et al., 2001). Wind components used for transport by advection were obtained from the simulation with the 3-D dynamical model for each day of the year. The simulation was started in January 2003. Daily averaged global zonal, meridional, vertical wind components, and temperature have then been used in the CTM runs. More details concerning the chemical 3-D model can be found in Krivolutsky and Vyushkova (2002). This model was used to study the response in composition and dynamics after the July 2000 SPE (Krivolutsky et al., 2006). The CAO simulation included in this study covers the period 26 October–4 November.

4.4 FinROSE

FinROSE is a global 3-D chemistry transport model (Damski et al., 2007a). The model dynamics are from external sources except the vertical wind, which is calculated inside the model using the continuity equation. In this study FinROSE has 35 vertical levels (0–65 km), a horizontal resolution of 10° × 5° and uses ECMWF Interim analyses (Simmons et al., 2006) for dynamics. Output is provided every 3 h. The model produces distributions of 40 species and includes about 120 homogeneous reactions and 30 photodissociation processes, using a family approach for short-lived species (HO_x, NO_x, O_x, ClO_x, BrO_x, Cl_x, and Br_x. Chemical kinetic data, reaction rate coefficients and absorption cross-sections are taken from look-up-tables based on the Jet Propulsion Laboratory compilation by Sander et al. (2006). Photodissociation frequencies are calculated using a radiative transfer model (Kylling et al., 1997). The model also includes formation and sedimentation of polar stratospheric clouds (PSCs) and reactions on PSCs. Tropospheric abundances are given as boundary conditions and long-lived trace gases are relaxed towards long time trends. The spin-up period used for this model run was 1 month. The FinROSE model applies additionally to electron and proton-induced ionization also ionization rates caused by alpha-particles provided by the AIMOS model (Wissing and Kallenrode, 2009).

4.5 HAMMONIA

The Hamburg Model of the Neutral and Ionized Atmosphere (HAMMONIA) is a 3-dimensional GCM and chemistry model covering an altitude range from the surface up to 1.7×10^{-7} hPa. A detailed description of the model is given by Schmidt et al. (2006). Simulations of particle precipitation effects use a modified version of HAMMONIA. It treats 54 photochemical, 139 bi- and termolecular, 5 ion-electron recombination, and 12 ion-neutral reactions involving 50 neutral and 6 charged (O^+, O_2^+, N^+, N_2^+, NO^+, e^-) components. Neutral bi- and termolecular reactions and the corresponding rate coefficients are taken from Sander et al. (2006). Photochemistry involves 7 ionizing and dissociating reactions through solar irradiance of wavelengths shorter than Lyman-alpha using a parametrization of Solomon and Qian (2005) and observed solar spectral irradiance. Additionally, 6 ionizing, dissociating, and exciting reactions represent the direct influence of precipitating primary and secondary particles on thermospheric chemistry. Corresponding reaction rates are calculated using the particle induced

ionization rates and branching ratios given by Roble and Ridley (1987) and Rusch et al. (1981). Below 10^{-3} hPa, particle impact on chemistry is represented by the production of $N(^2D)$, $N(^4S)$ and HO_x. Here, HAMMONIA uses parametrizations of Jackman et al. (2005a) based on formulations of Porter et al. (1976) and Solomon et al. (1981). The simulations use 67 pressure levels. Linear terms of dynamics are calculated using triangular truncation at wavenumber 31 (T31), while nonlinear terms of dynamics and spatially dependent physical and chemical quantities are computed on a Gaussian grid of approximately $3.75 \times 3.75°$. Output is provided every 2 h. Up to 179 hPa, the model is relaxed to ECMWF analyzed temperature, divergence, vorticity, and surface pressure. The HAMMONIA simulation starts on 1st March 2003 using ionization rates for the entire time period.

4.6 KASIMA

The KASIMA model is a 3-D mechanistic model of the middle atmosphere including full middle atmosphere chemistry (Kouker et al., 1999). The model can be coupled to specific meteorological situations by using analyzed lower boundary conditions and nudging terms for vorticity, divergence and temperature. Here we use the version as described by Reddmann et al. (2010). It has a horizontal resolution of about $5.6° \times 5.6°$ with 63 pressure levels between 7 and 120 km and a vertical resolution in the lower stratosphere of 750 m, gradually increasing to 3.8 km at the upper boundary. The frequency of output is every 6 h. The model is nudged to ECMWF analyses below 1 hPa. A numerical time step of 12 min was used in the experiments. The chemistry uses JPL 2002 data (Sander et al., 2003) and is calculated up to 90 km, above which only transport is applied. The chemical fields of long-lived tracers have been initialized from a multi-annual run starting in the year 1960. For the HEPPA experiments, the transport scheme has been revised to allow transport of the members of chemical families NO_x and HO_x individually in the mesosphere. In addition, the ozone heating rate is calculated interactively. The rate constants of the gas phase and heterogeneous reactions are taken from Sander et al. (2003). For the production of HO_x the parameterization of Solomon et al. (1981) is used, for the production of NO_x, 0.7 NO molecules are produced per ion pair and 0.55 N atoms in ground state, including reactions of $N + O_2$, $N + NO$, $N + NO_2$. The HNO_3 production from proton hydrates (de Zafra and Smyshlyaev, 2001) has been modied to be dependent on actual ionization rates.

4.7 EMAC

The ECHAM5/MESSy Atmospheric Chemistry (EMAC) model is a numerical chemistry and climate simulation system that includes sub-models describing tropospheric and middle atmosphere processes and their interaction with oceans, land and human influences (Jöckel et al., 2006). It uses the Modular Earth Submodel System (MESSy, see Jöckel et al., 2005) to link multi-institutional computer codes. The core atmospheric model is the 5th generation European Centre Hamburg general circulation model (ECHAM5, Roeckner et al., 2006). Here, EMAC (ECHAM5 version 5.3.02, MESSy version 1.8^+) was applied in the T42L90MA-resolution, i.e. with a spherical truncation of T42 (corresponding to a quadratic Gaussian grid of approximately 2.8 by 2.8° in latitude and longitude) with 90 vertical hybrid pressure levels up to 0.01 hPa. The frequency of output is every 2 h. The model is weakly nudged at 200–700 hPa to ECMWF reanalysis data. The chemistry submodel includes 104 chemical species and 250 homogeneous and heterogeneous reactions based on Sander et al. (2006). The simulation was initialized from a free-running simulation which was started in 1958. For more details on the setup used here refer to Baumgaertner et al. (2010).

4.8 SOCOL and SOCOLi

SOCOL (modeling tool for SOlar Climate Ozone Links studies) is a combination of the GCM MA-ECHAM4 and the chemistry-transport model MEZON. It is a spectral model with T30 horizontal truncation resulting in a grid spacing of about 3.75; in the vertical direction the model has 39 levels in a hybrid sigma-pressure coordinate system spanning the model atmosphere from the surface to 0.01 hPa. Time step for dynamical and physical processes is 15 min and 2 h for radiative transfer calculations and chemical reactions. The original version of the chemistry-climate model SOCOL was described by Egorova et al. (2005), and updated version in Schraner et al. (2008). For the HEPPA comparison, two versions of SOCOL have been used. One is with parameterized production of odd nitrogen, where for the NO_x sources, the fact that 1.25 NO molecules were produced was taken into account (Porter et al., 1976), for the HO_x sources, the table given by Solomon et al. (1981) has been used. The other version (SOCOLi) includes the chemistry of ionized species. SOCOLi is described in Egorova et al. (2011). As sources for ionization the model uses galactic cosmic rays (Heaps, 1978), energetic electron precipitation, solar proton events and observed solar irradiance. SOCOLi takes into account 580 reactions involving 43 neutral of the oxygen, hydrogen, nitrogen, carbon, chlorine and bromine groups, electrons, 31 positive and 17 negative charge species including clusters of $O2^+$, H^+ and NO^+. The rate constants of the gas phase and heterogeneous reactions are taken from Sander et al. (2000). The experiment runs with SOCOL and SOCOLi were initialized in September 2003 from the restart files of SPARC CCMVal2 REF-B1 run started in 1960 (Morgenstern et al., 2010). SOCOL and SOCOLi models apply additionally to electron and proton-induced ionization also ionization rates caused by alpha-particles provided by AIMOS model (Wissing and Kallenrode, 2009). This choice is based on the assumption that AIMOS describes all physical processes

relevant to particle precipitation during the event. Output is provided at the local time and location of the MIPAS overpass.

4.9 WACCM

The fourth version of the Whole Atmosphere Community Climate Model (WACCM4) is part of the Community Earth System Model (http://www.cesm.ucar.edu/). It is a coupled chemistry climate model with horizontal resolution of 1.9° latitude by 2.5° longitude. For this study WACCM4 has 88 vertical levels and is forced with meteorological fields from the Modern Era Retrospective-analysis for Research and Applications (MERRA, http://gmao.gsfc.nasa.gov/research/merra/). MERRA is a NASA reanalysis for the satellite era using the Goddard Earth Observing System Data Assimilation System Version 5 (Rienecker et al., 2008). The forcing is achieved by relaxing horizontal winds and temperatures with a time constant of approximately 50 h from the surface to 40 km. Above that level the forcing is reduced linearly, so that the model is free-running between 50 km and the model top at approximately 135 km (4.5×10^{-6} hPa). Heating rates and photolysis are calculated using observed daily solar spectral irradiance and geomagnetic activity effects in the auroral region are parameterized in terms of the Kp index (Marsh et al., 2007). A description of simulations of the effects of solar proton events using an earlier free-running version of WACCM and comparison with measurements is given in Jackman et al. (2008, 2009). The standard WACCM chemistry is described and evaluated extensively in WMO (2010). Reaction rates are from Sander et al. (2006). For these simulations we have modified the $N + NO_2$ reaction to include two additional pathways as described in Funke et al. (2008). It should be noted that both WACCM and HAMMONIA use the same chemical solver based on the MOZART3 chemistry (Kinnison et al., 2007), include the same set of ionized species, and use the parameterized EUV ionization rates from Solomon and Qian (2005). For these simulations the latter parameterization has been extended to include the photoionization of CO_2 in the EUV. Proton and electron ionization rates, used in the nominal simulation, are taken from AIMOS, however above 5×10^{-4} hPa ($\sim$100 km) ionization from electrons is instead calculated by the WACCM parameterized aurora. An additional simulation using proton ionization, only, has also been performed (in the following denoted as WACCMp). The HO_x production per ion pair is included in WACCM using a lookup table from Jackman et al. (2005b, Table 1), which is based on the work of Solomon et al. (1981). It is assumed that 1.25 N atoms are produced per ion pair and divide the N atom production between ground state, $N(^4S)$, at 0.55 per ion pair and excited state, $N(^2D)$, at 0.7 per ion pair (Jackman et al., 2005b; Porter et al., 1976). In this study, the "spin-up" period was one year. The nudged simulation was started 1 January 2003, from an initial condition file based on a free running transient simulation performed for the SPARC CCMVal2 exercise that covered the second half of the 20th Century ("REF 1B" scenario). WACCM constituent and temperature profiles were saved at the model grid point and time-step (model time-step is 30 min) closest to each of the MIPAS observation locations.

5 Intercomparison method

In order to reduce errors related to the different sampling of the MIPAS observations and gridded model data (i.e. B3dCTM, CAO, FinROSE, HAMMONIA, KASIMA, and EMAC) , we have linearly interpolated the model results to the MIPAS measurement locations and times, as well as to the corresponding pressure levels of the vertical retrieval grid of the species under consideration. This approach has the further advantage that diurnal variations of particular species are implicitly taken into account. Comparison of MIPAS measurements and model results requires the transformation of modeled profiles to MIPAS altitude resolution. Based on the formalism by Rodgers (2000), we calculate the model profiles adjusted to MIPAS resolution $\boldsymbol{x}_{\mathrm{adj}}$ as

$$\boldsymbol{x}_{\mathrm{adj}} = \boldsymbol{A}\,\boldsymbol{x}_{\mathrm{mod}} + (\boldsymbol{I} - \boldsymbol{A})\boldsymbol{x}_{\mathrm{a}}, \quad (1)$$

where $\boldsymbol{A}$ is the MIPAS averaging kernel matrix, $\boldsymbol{x}_{\mathrm{mod}}$ is the original model profile, $\boldsymbol{I}$ is unity, and $\boldsymbol{x}_{\mathrm{a}}$ is the a priori information used in the MIPAS retrievals. This adjustment procedure yields species profiles that MIPAS would see if it were to sound the model atmosphere. Assuming that the altitude resolution of the models is much finer than that of the MIPAS retrievals, the comparison of $\boldsymbol{x}_{\mathrm{adj}}$ and MIPAS measurements is not affected by any smoothing error.

This procedure has been applied to each model result resampled at the corresponding measurement location. As an example, Fig. 6 compares HOCl zonal mean distributions at 40–90° N, averaged over the period 29 October to 4 November 2003, as observed by MIPAS and as modeled by WACCM with and without application of averaging kernels. In the former case, the vertical distribution is broader and slightly shifted towards lower altitudes compared to the original model data, similar to the retrieved MIPAS profiles. Also, the absolute vmr peak values are smaller than without application of the averaging kernel. It should be noted that the apparent better agreement of the maximum vmr values between MIPAS and the unconvolved WACCM simulations are related to the fact that background HOCl vmrs are underestimated in the model. The relative vmr increase related to the SPE is in better agreement when comparing observed and convolved model data (see also Sect. 6).

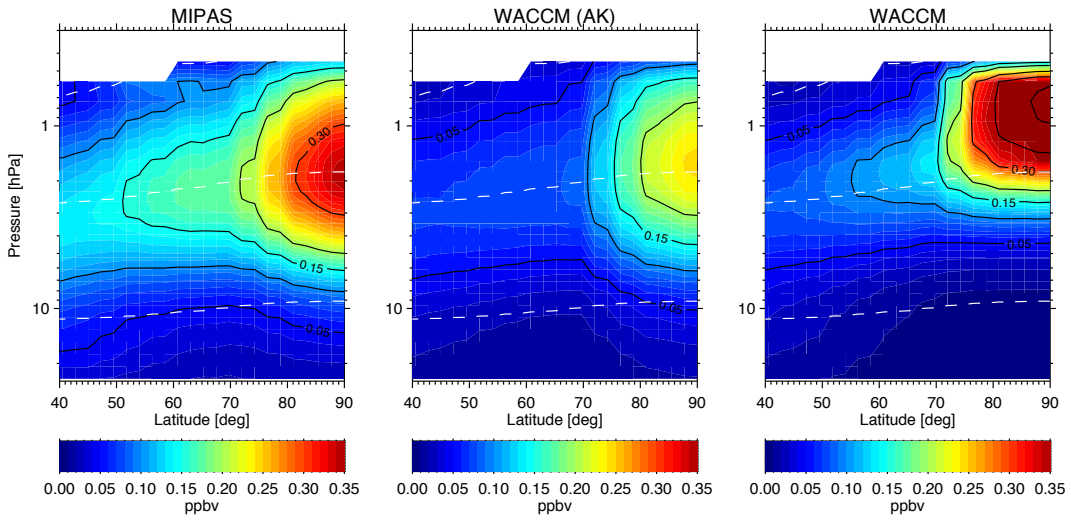

Fig. 6. Effect of application of averaging kernels (AKs) to the model data on the example of MIPAS and WACCM4 HOCl zonal mean distributions (40–90° N) averaged over the period 29 October to 4 November 2003. Left: MIPAS, middle: WACCM4 with MIPAS averaging kernels applied, right: WACCM4, original model results.

6 Results and discussion

6.1 Meteorological background conditions

Meteorological background conditions, particularly the thermal structure and the prevailing dynamics, can have an important impact on the magnitude and spatial distribution of SPE-induced composition changes. Temperature differences between models and observed data have, on the one hand, a significant impact on SPE-related chemistry due to involvement of highly temperature-dependent reactions (i.e. $N + O_2$ or $NO_2 + O_3$). On the other hand, meridional transport and mixing, depending largely on the development stage of the early winter polar vortex, control the redistribution of air masses between polar night and illuminated regions and hence, the efficiency of photochemical losses. Also, the strength of polar winter descent plays an important role in the vertical redistribution of some species on the time scale of the intercomparison period.

Figure 7 shows the MIPAS temperature zonal mean distribution at 40–90° N averaged over the period of the main proton forcing, 29 October to 4 November 2003, and the corresponding differences between the models and the observations. It is evident that models which are driven or strongly forced by assimilated meteorological data up to the upper stratosphere (i.e. B3dCTM, FinROSE, KASIMA, and WACCM) reproduce reasonably well the observed temperatures below approximately 1 hPa. On the other hand, free-running models (B2dM and SOCOLi) and those which are nudged to meteorological in the troposphere only (i.e. HAMMONIA) tend to overestimate the observations inside the polar vortex by more than 15 K around approximately 1 hPa or slightly below, while polar mesospheric temperatures are considerably underestimated by these models (more than 25 K in the case of SOCOLi). This behavior is related to a lower polar stratopause height compared to the observations. Slightly too high stratopause temperatures are found in EMAC, CAO, B3dCTM, FinROSE, and WACCM simulations. These models also tend to have a higher stratopause compared to the observations, particularly in the case of WACCM. The KASIMA model yields generally good agreement with the observations in the polar regions, however, overestimates stratopause temperatures in the 50–60° N region.

The temporal evolution of observed polar temperatures (70–90° N) and the corresponding differences between model and observations are shown in Fig. 8. No significant trend in either, observations or model data, can be observed during the period of interest, while short-term temperature fluctuations of more than 10 K compared to the observations, most likely related to differences in the planetary wave activity, show up particularly in the case of the free-running or weakly nudged models (B2dM, CAO, HAMMONIA, and SOCOLi).

Differences in the magnitude of meridional redistribution between models and observations have been assessed by comparing CH_4 zonal mean distributions provided by all models except CAO. Since the global stratospheric CH_4 abundances differ noticeably among the models, we used the relative meridional CH_4 anomaly as indicator for meridional redistribution rather than absolute vmrs. The relative meridional anomaly is defined as percentage deviation from the 40–90° N average at each vertical level. Figure 9 shows the observed and modeled meridional CH_4 anomalies at 40–90° N averaged over the whole period. A pronounced gradient in the observed anomalies around 60° N indicates the

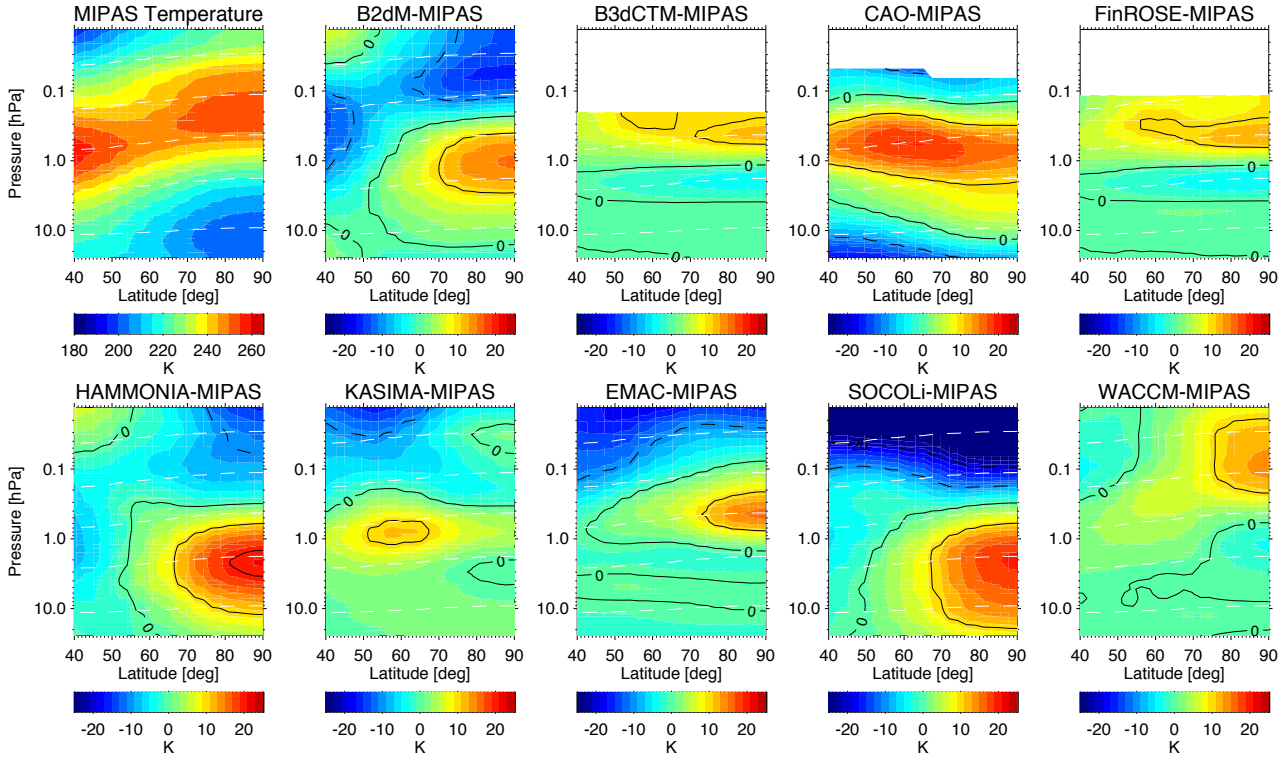

Fig. 7. Observed and modeled temperature zonal mean distributions at 40–90° N averaged over the period 29 October to 4 November 2003.

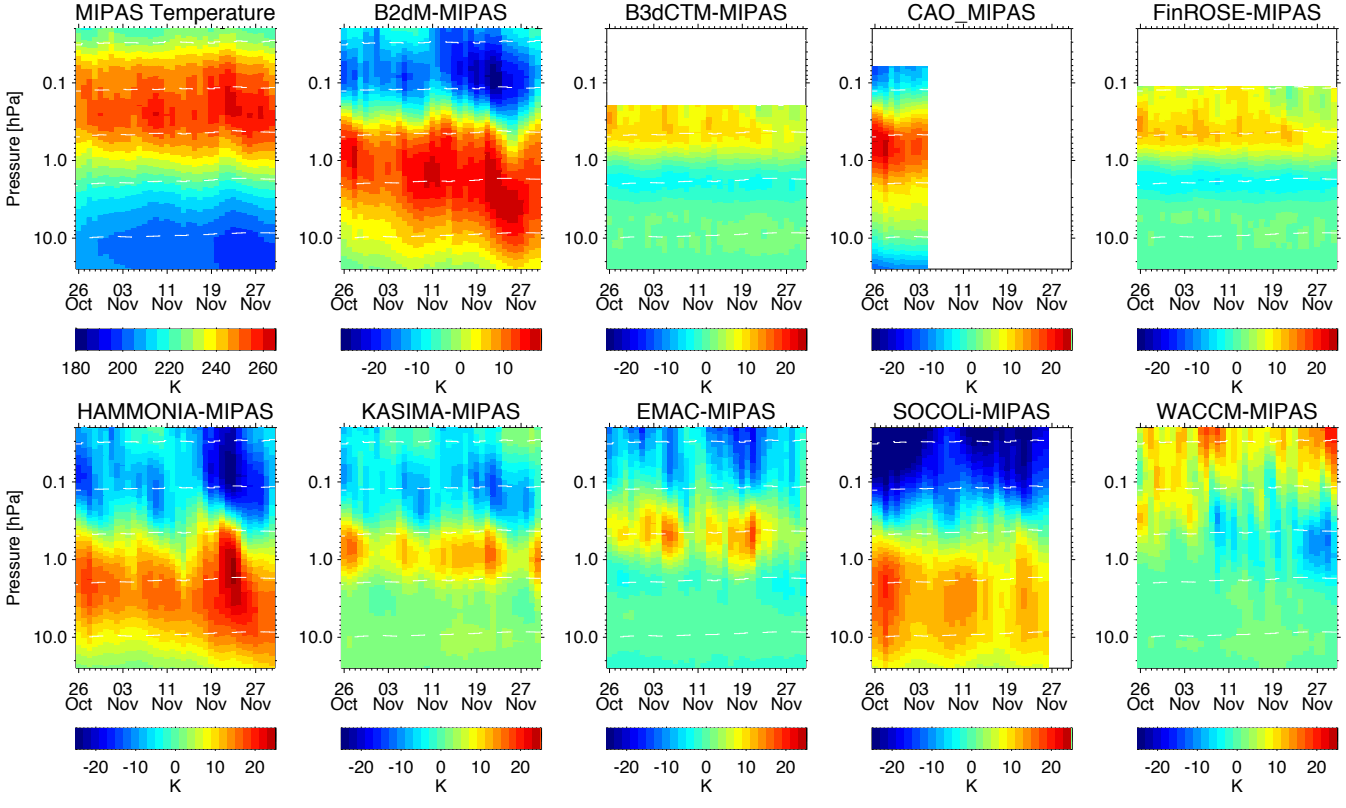

Fig. 8. Temporal evolution of MIPAS temperature and model - MIPAS differences averaged over 70–90° N.

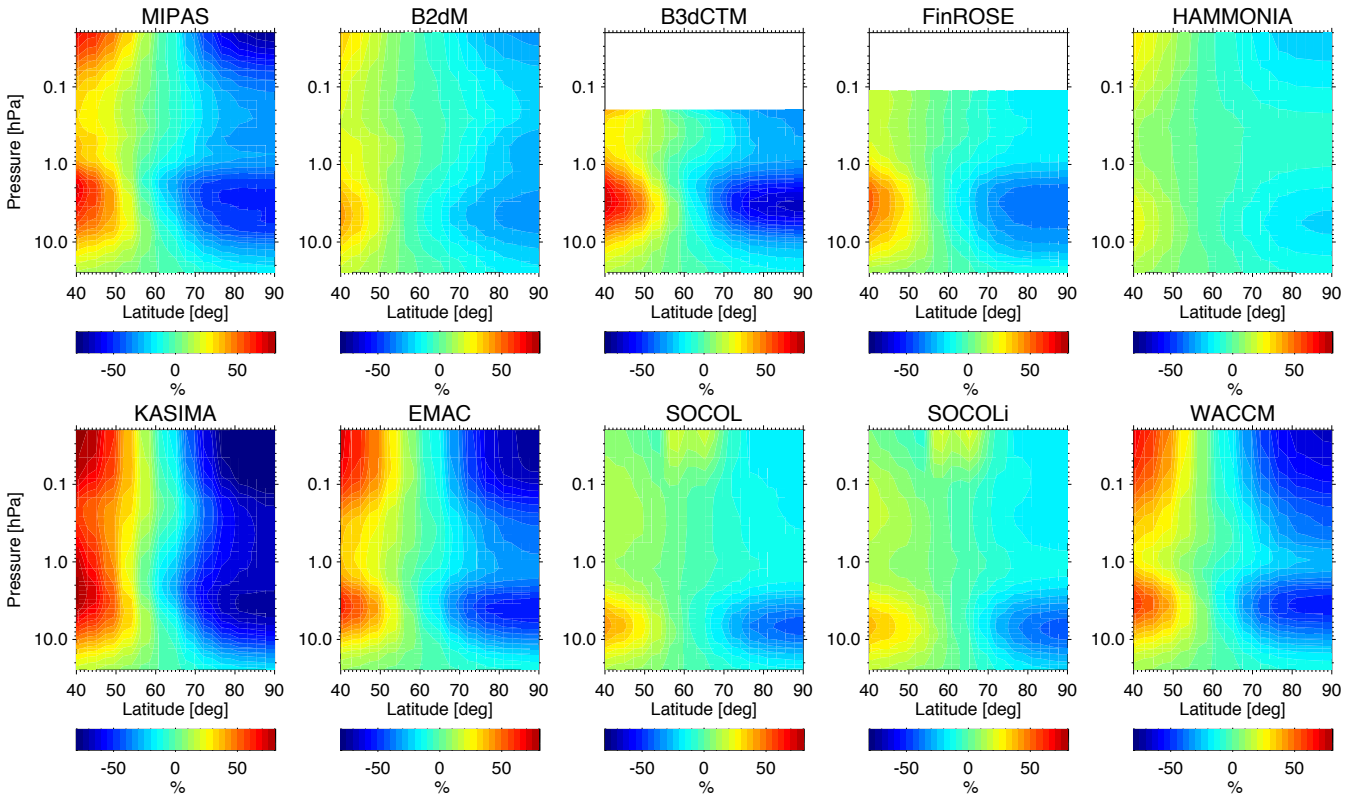

Fig. 9. Relative meridional CH_4 anomalies in MIPAS observations and model simulations at 40–90° N averaged over the whole time period.

early winter vortex boundary. In general, the vortex boundary position is well reproduced by all models, although there are significant differences in the overall CH_4 change from mid-latitudes to the pole between the models. Strongest latitudinal gradients (i.e. weakest redistribution) were found in the KASIMA simulations, while smallest gradients (i.e. strongest redistribution) are visible in HAMMONIA. The reason for the underestimation of meridional redistribution in KASIMA is not fully understood, particularly because other ECMWF-driven models have simulated considerably stronger mixing. The too strong mixing in HAMMONIA is most probably related to wave-1 activity, being present in the whole time period. The vertical distribution of the observed CH_4 meridional anomaly shows a broadening in the stratopause region (1–0.1 hPa). Spatial CH_4 distributions at these vertical levels (not shown) indicate that this broadening is related to a weakened transport barrier at the vortex top rather than to increased planetary wave activity in the mesosphere. This behavior is reproduced by the models in general although there are differences with respect to the altitude and magnitude of the broadening region. In B2dM, it is shifted slightly upwards while the opposite is observed in EMAC, SOCOL, and SOCOLi simulations. In these latter models, meridional redistribution seems also to be slightly overestimated around the stratopause. It should be noted that our analysis of CH_4 meridional anomalies does not allow to distinguish between meridional redistribution by eddy diffusion and large-scale transport by planetary waves, the latter being of higher importance for the redistribution of air masses between polar night and illuminated regions.

The variability of the polar vortex strength has been assessed by comparing the temporal evolution of the relative change of CH_4 abundances with respect to 26 October averaged over 70–90° N (see Fig. 10). The observed evolution indicates a vortex intensification and descent in the lower and middle stratosphere while a CH_4 increase above 0.3 hPa, particularly during the proton forcing at the beginning of November, hints at an increase of meridional mixing in the mesosphere. This general behavior is partly reproduced by the models but important differences with respect to the vertical structure and magnitude exist. These differences have to be taken into account when analyzing the temporal evolution of SPE-induced composition changes (see next sections).

Carbon monoxide is an ideal tracer for upper stratospheric and mesospheric dynamics. Particularly, it allows to identify air masses which have descended from the upper mesosphere and contain enhanced NO_x related to energetic electron precipitation (EEP). Since polar winter descent of NO_x generated by EEP prior to the SPE event is not resolved by all models, and since we focus here on SPE-related effects, observed NO_x enhancements due to descending upper mesospheric air masses perturb our analysis and should hence be excluded.

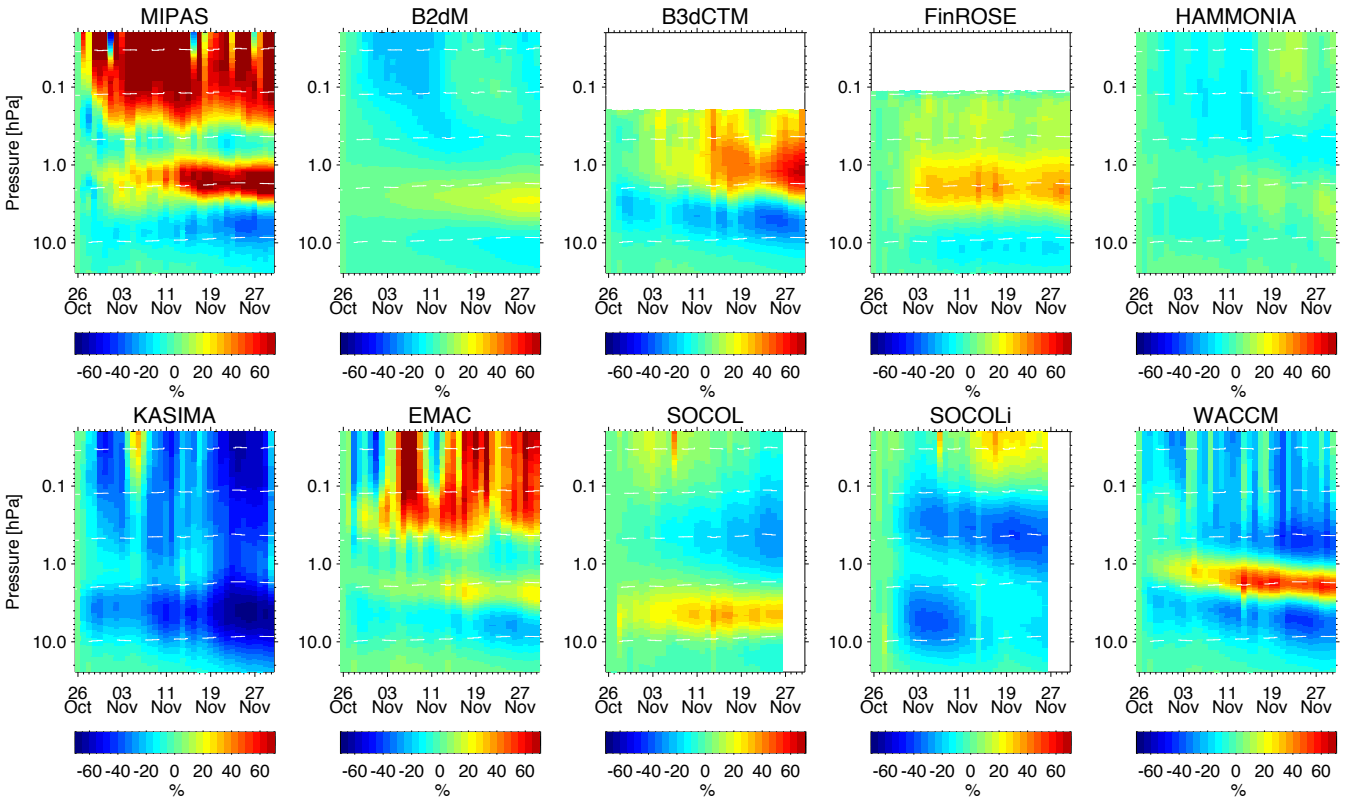

Fig. 10. Temporal evolution of CH_4 changes with respect to 26 October 2003 in MIPAS observations and model simulations averaged over 70–90° N.

MIPAS CO observations provide an excellent criterion for identification of EEP-related enhancements (see Sect. 6.2).

CO distributions also allow for the characterization of descent and vortex perturbations by large-scale wave activity and isentropic mixing across the vortex boundary in the upper stratosphere and mesosphere. Figure 11 shows the observed and modeled temporal evolution of CO abundances averaged over 70–90° N. In general, the continuous decrease in altitude of CO vmr isolines in the upper stratosphere, related to polar winter descent, agrees well in models and data. Around 1 hPa, polar air masses descended approximately 5 km in both models and observations during the time period under investigation.

A higher variability is found in the mesosphere. Observed CO abundances decreased around the beginning of November, at the same time when CH_4 increased significantly (see Fig. 10). A pronounced CO increase occurred around 20 November, hinting at enhanced descent and vortex intensification. Modeled CO distributions show a different temporal evolution in the mesosphere, although some similarities can be found. For instance, EMAC, KASIMA and WACCM reproduce the CO increase in late November, however, with a smaller magnitude and slightly shifted in time. A CO decrease around 0.1 hPa at the beginning of November, as observed by MIPAS, is also visible in SOCOL, SOCOLi, and – to a lesser extent – in WACCM simulations.

In contrast to the observations, these modeled decreases occur nearly instantaneously on 31 October, suggesting that the simulated CO changes might be related to the proton event rather than dynamical modulations. Indeed, CO is removed by the reaction with OH, which is strongly enhanced during the SPE at nighttime. The isolation of a possible SPE-induced chemical CO loss from dynamical effects is difficult in both observations and simulations. Nevertheless, we have analyzed the observed CO abundances at fixed CH_4 levels in the vertical range of 0.2–0.05 hPa in order to exclude CO variations related to isentropic mixing or meridional redistribution. CO abundances observed simultaneously with CH_4 vmrs of less than 40 ppbv decreased by approximately 1 ppmv from 29 October to 1 November, thus suggesting a chemical removal of the order of 10 % which could be related to enhanced OH. The CO decreases found in the WACCM simulations have a similar magnitude, while SOCOL and SOCOLi simulations show a CO decrease around 30 %.

6.2 Enhancements of NO_y and N_2O

The most important impact of proton precipitation on the middle atmosphere is the immediate formation of NO_x ($= NO + NO_2$) via dissociation of molecular nitrogen by ionization and subsequent recombination with oxygen. Due to its relatively long chemical lifetime in the stratosphere,

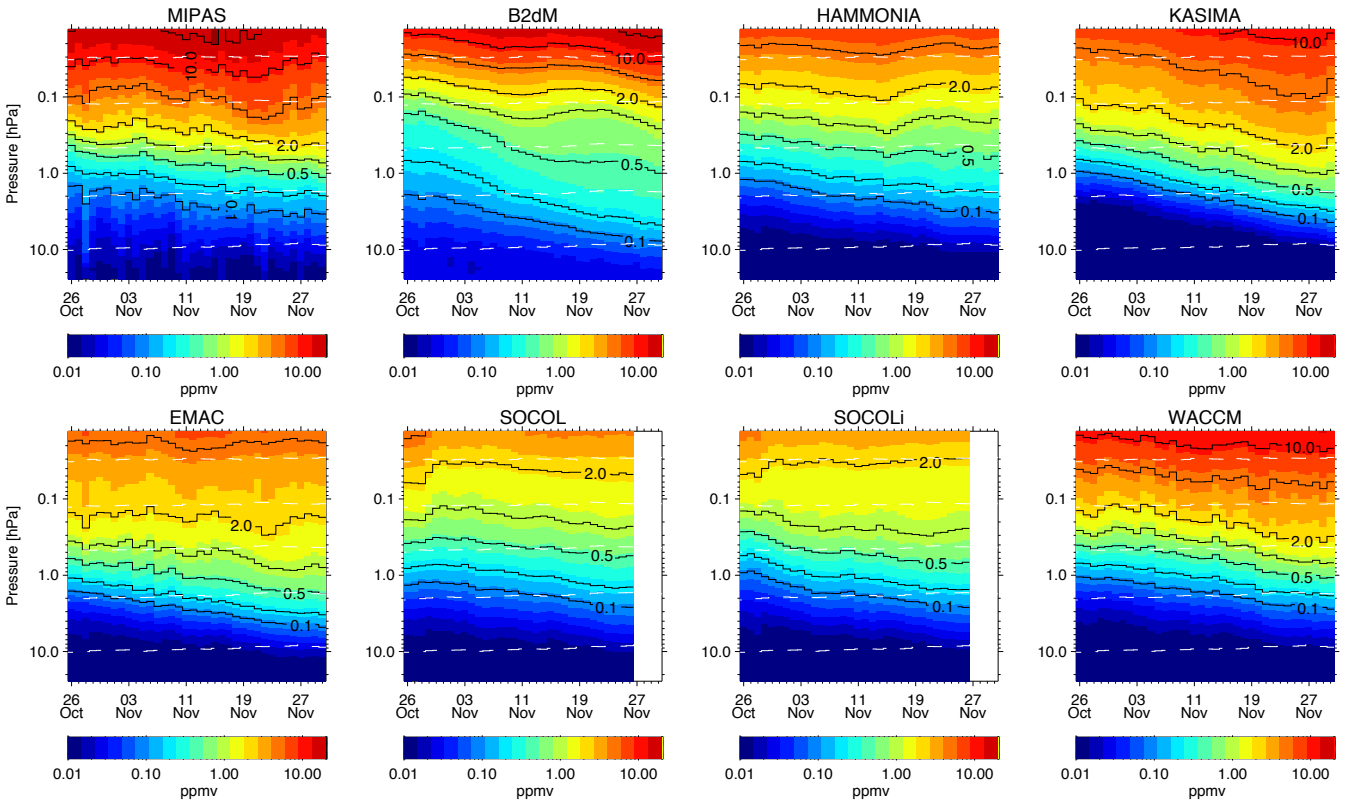

Fig. 11. Temporal evolution of CO abundances in MIPAS observations and model simulations averaged over 70–90° N. The 0.1, 0.2, 0.5, 1, 2, 5, 10, and 20 ppmv contours are shown by solid lines.

SPE-induced NO_x enhancements have a strong potential to deplete ozone on a mid- to long-term scale via catalytic cycles. A fraction of excess NO_x produced by proton forcing is subsequently buffered into NO_y reservoir species (i.e. N_2O_5, HNO_3, and $ClONO_2$) by a series of chemical processes (see next section) at different time scales. In general, the NO_x deactivation is very slow in the upper stratosphere. At lower altitudes, however, observed HNO_3 and $ClONO_2$ increases immediately after the onset of the proton forcing during the Halloween event indicate a much faster conversion. In order to assess the agreement of observed and modeled SPE-related odd nitrogen enhancements, we have thus compared, at first instance, total NO_y ($= NO + NO_2 + HNO_3 + 2N_2O_5 + ClONO_2 + HNO_4$) rather than NO_x. Since meridional redistribution is an issue (see discussion in the previous subsection), we have separately analyzed area-weighted averages of NO_y enhancements with respect to 26 October within 70–90° N and 40–90° N, the latter area covering entirely the source region.

As a first step, we analyze the instantaneous NO_y enhancements during the main proton forcing around 29 October–1 November. Figure 12 shows the observed and modeled NO_y enhancements during this period, ranging from a few ppbv in the middle stratosphere to several 100 ppbv in the mesosphere. As expected from the latitudinal distribution of SPE-induced ionization (see Fig. 4), higher NO_y enhancements are found at 70–90° N compared to 40–90° N. The agreement between the observations and the multi-model average, the latter providing a measure of the overall ability of current atmospheric models to reproduce SPE-related NO_y increases, is reasonable, exhibiting differences below 50 % in the whole altitude range. There is, however, a systematic overestimation of the models around 1 hPa, being more pronounced over the pole. Above 0.3 hPa, the models tend to underestimate observed NO_y enhancements at 40–90° N, while they agree on average with the observations in the polar region.

The NO_y underestimation of the models above 0.3 hPa in the sunlit 40–90° N region could be related to an overestimation of NO photolysis, the principal NO_y loss mechanism in the illuminated mesosphere. It has been pointed out by Minschwaner and Siskind (1993) that absorption of solar irradiance by thermospheric NO, being significantly enhanced during SPEs, has an important impact on the photolysis rates of nitric oxide in the middle atmosphere. An overestimation of NO photolysis is also supported by the fact that modeled NO_y enhancements agree on average with the observations in the polar region (70–90° N) where photochemical losses of NO are small.

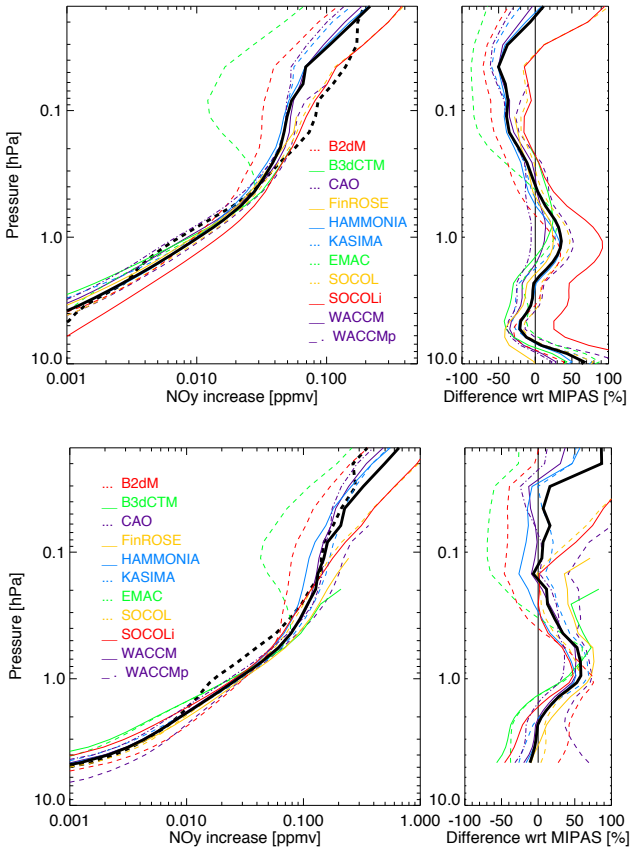

Fig. 12. Area-weighted averages of observed and modeled NO_y enhancements for 40–90° N (top) and 70–90° N (bottom) during 30 October–1 November with respect to 26 October (left) and relative deviations of modeled averages from the MIPAS observations (right). Thick solid and dashed lines represent the multi-model mean and MIPAS observations, respectively. WACCMp denotes the WACCM simulation including proton ionization only (excluded from the multi-model mean).

The systematic behavior of the NO_y overestimation around 1 hPa suggests that these differences are related – at least partly – to the simulated ionization rate profile. In this pressure range, uncertainties in the modeling of electron precipitation at 300 keV to 5 MeV, contributing to the total ionization by approximately 15 %, represent an important error source in the AIMOS calculations. As the highest electron channel on POES does not provide data up to 5 MeV, the energy spectrum was extended according to Klassen et al. (2005). In addition, the energy range of the highest electron channel *mep0e3* is not known for sure (private communication, Janet Green, NOAA) and it might be smaller than the published 300 keV–2.5 MeV (Evans and Greer, 2000). A smaller energy range would also result in increased NO_y production within 40–90° N at 0.1 hPa in agreement with the observations. A possible overestimation of electron ionization alone, however, cannot explain the mismatch between modeled and observed NO_y increases of up to 50 %. Around 1 hPa, the WACCM simulation without electrons (WACCMp) yields 20 % less enhanced NO_y than the nominal simulation, including protons and electrons. Even when assuming that electrons do not contribute to the SPE-induced ionization at stratospheric altitudes, only about half of the differences between modeled and observed enhancements could be explained. Additional ionization by alpha particles, included in CAO, FinROSE, SOCOL, and SOCOLi contributes only by approximately 5 % to the total ionization within 40–90° N, hence increasing the SPE-related NO_y enhancements only marginally. Other possible error sources in the ionization rate calculation are related to uncertainties of the GOES proton flux observations and to the spatial interpolation scheme for particle fluxes from the POES satellites. Also, uncertainties of atmospheric parameters (density, altitude, composition, and temperature) used in the AIMOS calculations could produce errors in the ionization rates. These parameters, taken from HAMMONIA and MSIS calculations, might differ from the actual atmospheric conditions during the Halloween SPE. Apart from possible deficiencies in the ionization rate calculation, also differences of the true and modeled atmospheric background state and/or dynamical conditions could contribute to the encountered model overestimation of NO_y enhancements. However, such differences are likely to produce a spread in the modeled NO_y increases rather than a systematic bias compared to the observations.

Indeed, such a spread of up to 100 % among the modeled NO_y enhancements can be observed, particularly in the 40–90° N region. NO_y enhancements are most strongly overestimated (up to 100 %) by SOCOLi, SOCOL, and CAO in the stratosphere around 1 hPa. In the mesosphere, smallest NO_y increases are obtained by B2dM and EMAC (up to 80 % less than observed), while SOCOL and SOCOLi simulations agree well with the MIPAS observations.

In order to investigate possible reasons for the dispersion among the model results, a more detailed look into the NO_x production mechanism is required. Generally, it is assumed that each ion pair produces 1.25 atomic nitrogen atoms, distributed between the electronic ground state $N(^4S)$ and the excited $N(^2D)$ state with a branching ratio of 0.45 and 0.55, respectively (Jackman et al., 2005b). The value of 1.25 atomic nitrogen atoms per ion pair has been adapted by all models involved in this study, except for EMAC and SOCOLi. In the latter model, N production is implicitly modeled by means of the involved ion chemistry scheme. In EMAC, an altitude-dependent N production has been assumed which has been determined empirically by the adjustment of the simulations to observed NO_2 and N_2O abundances (Baumgaertner et al., 2010). The resulting N production profile is slightly higher than that used by the other models in the upper stratosphere (around 1.5 N per ion pair) and considerably lower in the mesosphere (less than 0.3 N per ion pair) which explains to a major extent the behavior of the EMAC NO_y enhancements compared to other models.

An important source of variability in the NO_y production is related to the reaction paths of the produced atomic nitrogen in its ground and excited states. While the reaction of $N(^2D)$ with oxygen to form NO is very fast such that practically all $N(^2D)$ is immediately converted to NO below the thermosphere, the corresponding reaction of the nitrogen ground state

$$N(^4S) + O_2 \rightarrow NO + O \quad (R1)$$

is slower and highly temperature-dependent. Hence, it competes with other reactions, namely:

$$N(^4S) + NO \rightarrow N_2 + O \quad (R2)$$

$$N(^4S) + NO_2 \rightarrow N_2O + O, \quad (R3)$$

both destroying NO_x. As a consequence, only a fraction of the initially produced NO_x remains available after the proton forcing. This fraction depends strongly on temperature due to Reaction (R1) and to a lesser extent on the repartitioning between NO and NO_2, driven by illumination and odd oxygen availability. In order to assess the sensitivity of the SPE-related NO_x production to these parameters, we have integrated the relevant chemical equations for the period 28 October–1 November with a simple box model including AIMOS ionization rates and assuming initial atmospheric conditions as observed by MIPAS at 70–90° N before the SPE, as well as the $N(^4S)/N(^2D)$ branching ratio recommended by Jackman et al. (2005b) . The modeled NO_x enhancements have then been compared to a similar simulation, but setting the rate coefficient for Reactions (R2) and (R3) to zero (i.e. assuming that all initially produced NO survives). The ratio of both simulations reflects the NO_x production efficiency. It is shown in Fig. 13 for nighttime and daytime conditions (solid and dotted black lines, respectively), exhibiting maximum value of 0.55–0.7 around the stratopause and smaller values (0.15–0.4) above and below. Reduced values below the stratopause are related to the background NO_x: if initial NO_x abundances are set to zero, the production efficiency increases with pressure to values close to unity in the lower stratosphere (see Fig. 13, dotted green line). A temperature increase (decrease) of 20 K results in an enhancement (reduction) of this quantity by approximately 30–50 % (see red and blue lines in Fig. 13). On the other hand, assuming a two times higher ozone abundance results in an increase of the NO_x production efficiency by only a few percent.

The chemical scheme described above (including a $N(^4S)$ and $N(^2D)$ branching ratio of 0.45 and 0.55) has been employed in most of the atmospheric models included in the intercomparison, with some exceptions: B3dCTM and CAO use a family approach which implies the immediate conversion of all atomic nitrogen to NO (equivalent to a ratio of 1 in Fig. 13), explaining – at least partly – the relatively high NO_y increases above 2 hPa in these models. Also FinROSE applies a family approach, however, in this model it is implicitly assumed that all $N(^4S)$ produced by ionization destroys

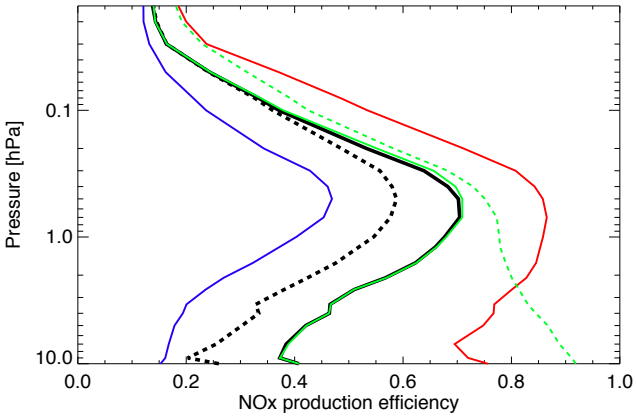

Fig. 13. NO_x production efficiency (ratio of the net NO_x increase and the integrated initial N production) during the period of the main proton forcing (28 October–1 November) from box model calculations for night- and daytime conditions (solid and dashed black lines, respectively), assuming initial atmospheric conditions as observed by MIPAS in the polar cusp region. The following variations for dark conditions are also shown: a 20 K temperature increase (red) and decrease (blue), a factor of 2 increase of O_3 (solid green), and initial NO_x abundances set to zero (dashed green).

NO via Reaction (R2), resulting in a net NO_x production of 0.25 per ion pair (i.e. an altitude-independent production efficiency of 0.2 in Fig. 13). However, although a considerably smaller NO_y production is hence expected, FinROSE model results show more excess NO_y than found in the observations. EMAC uses a $N(^4S)$ and $N(^2D)$ branching ratio of approximately 0.2 and 0.8, respectively. Box model calculations using this atomic nitrogen branching yield weakly altitude-dependent NO_x production efficiencies of 0.6–0.8, considerably higher than the nominal efficiency of ∼0.2 in the mesosphere. Therefore, the smaller atomic nitrogen production in the mesosphere applied in EMAC is partly compensated by the modified $N(^4S)$ and $N(^2D)$ branching ratio.

As shown above, temperature differences might explain the differences of the NO_y enhancements simulated by the remaining models. B2dM underestimates the observed temperatures in the mesosphere by about 15 K, consistent with the relatively low NO_y enhancements compared to the other models and observations, there. In contrast, HAMMONIA and SOCOLi simulations, exhibiting relatively low mesospheric temperatures, show much larger NO_y enhancements. Stratospheric temperatures are significantly overestimated by B2dM, CAO, HAMMONA, and SOCOLi. However, only the latter model shows stratospheric NO_y enhancements well above the model average. Thus, temperature differences among the models cannot be the only reason for the spread encountered in the modeled NO_y enhancements.

Therefore, we have looked at the spatial NO_y distribution in order to investigate if the spread in the modeled NO_y could also be related to dynamical effects. Figure 14 shows the observed and modeled NO_y distributions in the upper

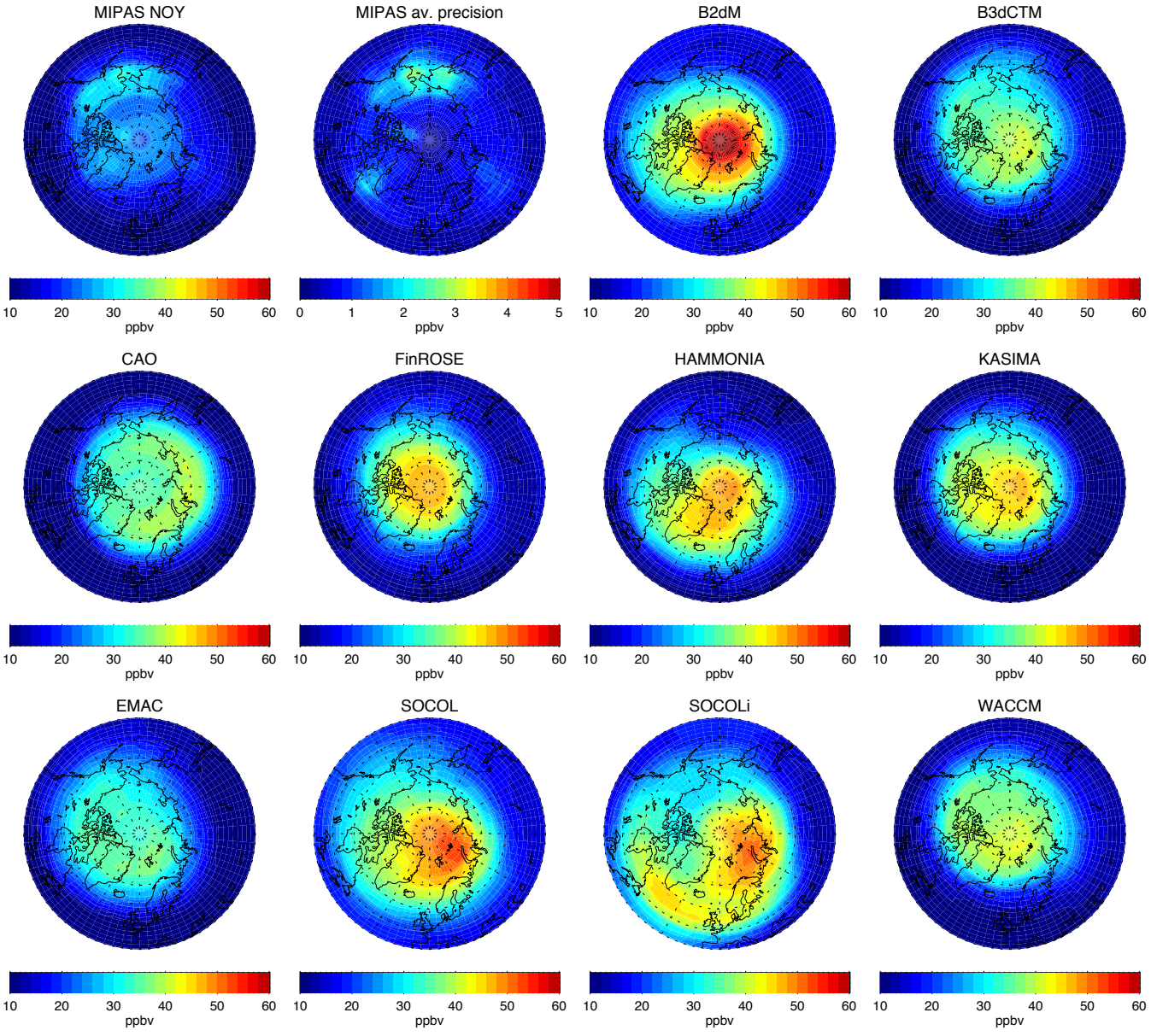

Fig. 14. Spatial distributions of observed and modeled NO_y at 1 hPa averaged over the period of the main proton forcing during 30 October–1 November. The average precision of MIPAS observations is also shown (upper second panel from the left).

stratosphere (1 hPa) averaged over the period 30 October–1 November. The spatial extension of the modeled NO_y enhancements exhibits pronounced differences. In some cases, NO_y enhancements are confined to the polar region northward of 70° N (i.e. B2dM, KASIMA, FinROSE) while in other cases they extend even to regions equatorwards of 50°N (i.e. SOCOL and SOCOLi). Taking into account that the spatial extension of the source region is the same in all models, these differences must be related to transport acting on a very short time scale. As discussed above, SOCOLi shows higher NO_y averages than other models with similar stratospheric temperatures (i.e. HAMMONIA, B2dM). The spatial NO_y distribution of SOCOLi at 1 hPa indicates strong wave activity resulting in a deformation of the pole-centered shape of the NO_y distribution. Thus, it cannot be excluded that tropical NO_y, transported into the 40–90° N region, contributed to the large NO_y enhancements identified in this simulation. Further, the fast transport of SPE-generated NO_y out of the source region in the SOCOLi simulations might result in a higher net NO_y production since NO_x destruction by reactions with atomic nitrogen (Reactions R2 and R3) is then less efficient. On the other hand, B2dM shows the most pole-centered NO_y distribution among the models. As a consequence, NO_y enhancements in the 70–90° N region reach

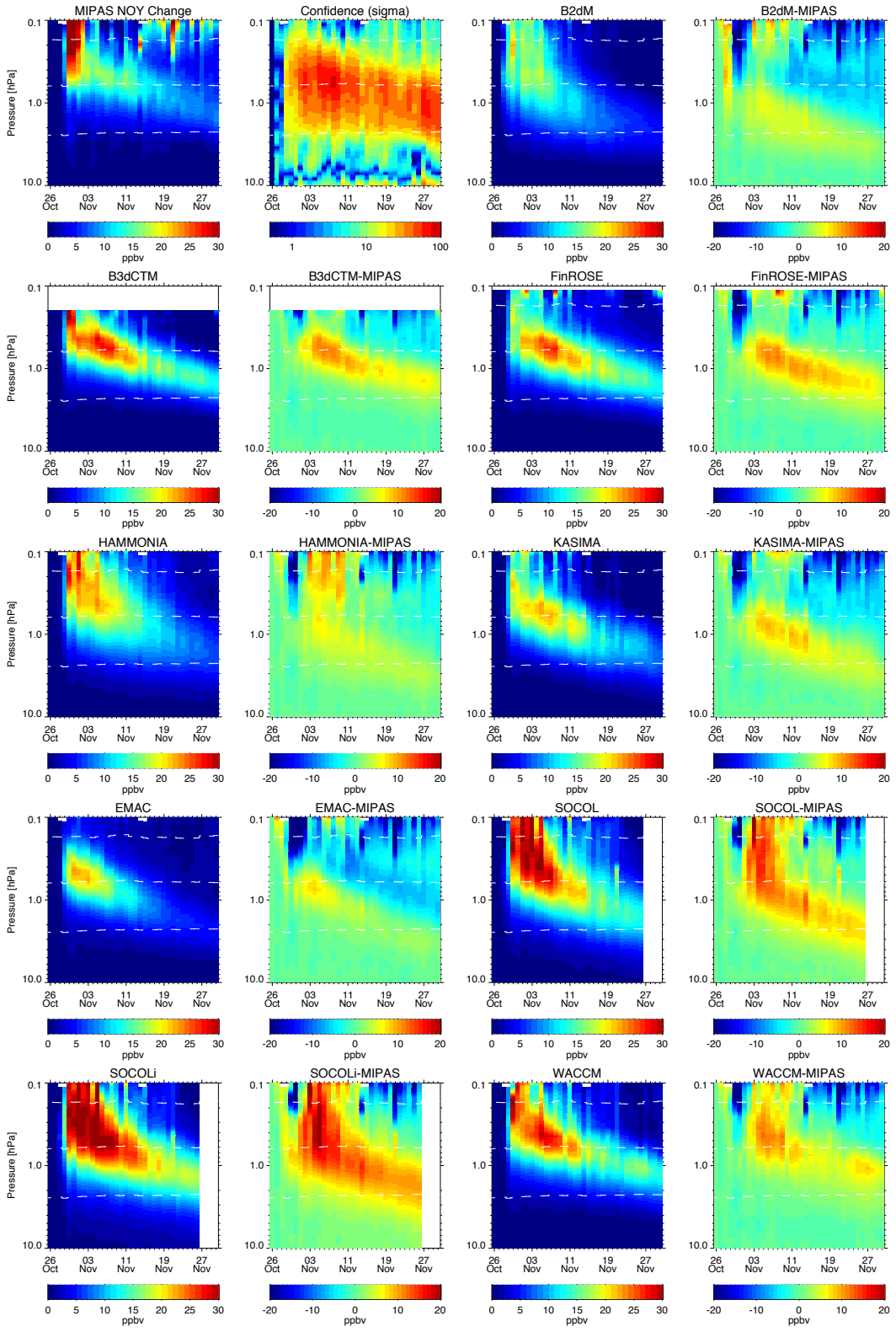

Fig. 15. Temporal evolution of area-weighted averages of NO_y changes with respect to 26 October 2003 in MIPAS observations and model simulations at 40–90° N, as well as differences between modeled and observed averages. The significance of observed NO_y changes (in units of σ) is shown in the upper second panel (from the left). Note that observations exhibiting CO abundances higher than 1 ppmv have been omitted in the averaging in order to exclude the contributions from descended NO_x produced by EEP at higher altitudes before the Halloween stroms. See text for further details.

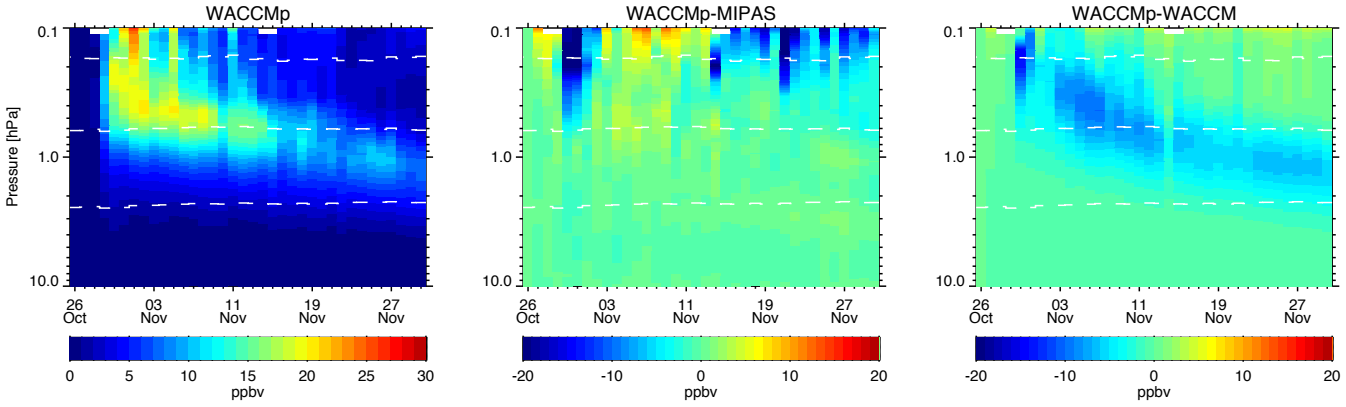

Fig. 16. As Fig. 15, but showing area-weighted averages for WACCMp (proton ionization, only, left), differences between WACCMp and MIPAS (middle), and differences between WACCMp and WACCM (right).

highest values of up to 60 ppbv (twice as much as observed), although the 40–90° N average (see Fig. 12) is below the multi-model mean at this pressure level. This behavior is related to the very strong but small vortex in this particular model, probably as a result of its relatively poor horizontal resolution. The high dispersion in the latitudinal extent of the modeled NO_y distributions, showing up already two days after the onset of the main proton forcing, is rather unexpected and highlights the importance of transport processes on a very short timescale.

During the following month, the SPE-induced NO_y enhancements were transported downwards with the meridional circulation, forming a NO_y layer around 45 km at the end of November (López-Puertas et al., 2005a). At the same time, NO_x, generated by continuous EEP in the lower thermosphere before the Halloween storm, reached the upper stratosphere and began to merge with the upper part of the SPE-induced layer (see also Fig. 1). This behavior is not reproduced by the simulations since low and mid-energy EEP is not included in the majority of the models. In order to facilitate the comparison of observed and modeled SPE-induced NO_y enhancements in the following month after the proton forcing, we have excluded those parts of all observed and modeled NO_y profiles where MIPAS CO abundances were higher than 1 ppmv. This value has been chosen such that the major fraction of EEP-induced NO_y enhancements has been filtered out without removing too many MIPAS locations, particularly at higher altitudes.

Figure 15 shows the temporal evolution of the observed and modeled NO_y enhancements (related to the SPE-induced in-situ production, only) with respect to 26 October within 40–90° N for the following month. While the magnitude of the enhancements is generally larger than in the observations and further shows a significant spread related to the differences in the NO_y production during the proton forcing (see discussion above), the observed evolution of the SPE-induced NO_x layer is well reproduced by all models in terms of vertical distribution and relative vmr decrease. A more detailed look into the temporal NO_y evolution of individual models shows that smaller fluctuations can be attributed to dynamical variability.

It is interesting to notice that the WACCM simulation without electron-induced ionization yields better agreement with the observations than the nominal simulation throughout the period under investigation (see Fig. 16). Additional NO_y buildup related to electron-induced ionization is even more pronounced during the second event (4–5 November) below 0.4 hPa compared to the main proton forcing (see right panel of this figure). The NO_y increase caused by electrons during the second event contributes with 5–10 ppbv to the excess NO_y layer, descending during the following weeks.

The meridional distributions of the observed and modeled NO_y enhancements exhibit important differences towards the end of November (see Fig. 17, showing NO_y distributions at 2 hPa averaged over 20–27 November). The observed and modeled latitudinal gradients correlate well with the meridional CH_4 anomalies (see Fig. 9), highlighting the important role of mixing and large-scale transport. The meridional redistribution of the SPE-induced NO_y enhancements, particularly the transport out of the polar night region, has important implications for the NO_y repartitioning which is to a major part driven by photochemistry (see next subsection).

An interesting detail of the observed evolution of SPE-induced NO_y enhancements (Fig. 15, upper left panel) is the appearance of several "spikes" at mesospheric altitudes, which are temporally correlated with peaks in the ionization related to high energy (>300 keV) electron precipitation, the most pronounced event occurring on 21 November. Ionization by high energy electrons is included in the models which, however, do not reproduce such sudden NO_y increases. It is therefore unlikely the observed mesospheric NO_y peaks are related to in situ production by EEP associated with the Halloween event. Instead, they could be related to residual contributions of descending NO_x from the

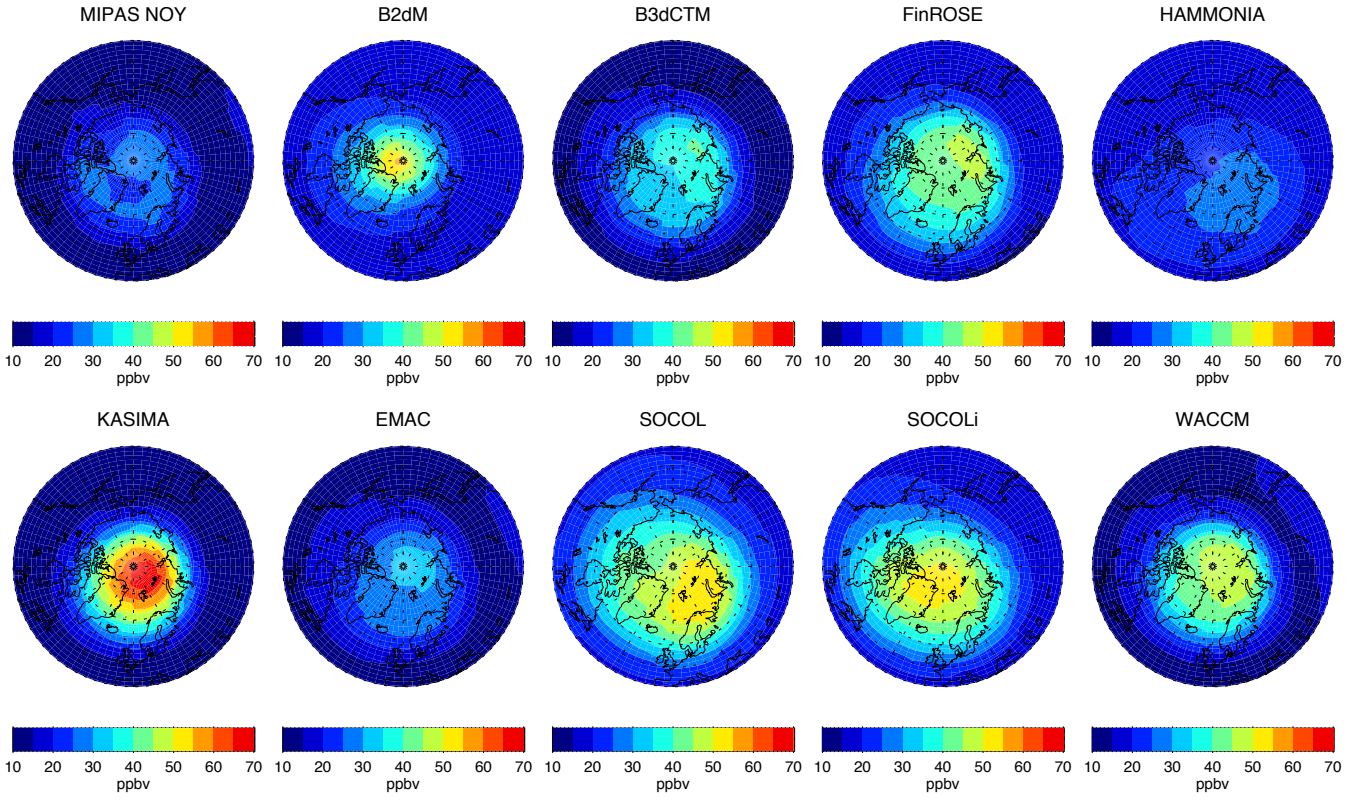

Fig. 17. Spatial distributions of observed and modeled NO_y at 2 hPa averaged of the period 20–27 November.

upper mesosphere which have not completely been filtered out. It should be noted that the observed CO temporal evolution (see Fig. 11) indicates particularly strong descent around 20 November.

A fraction of the NO_x deactivation by reaction with atomic nitrogen during the proton forcing discussed above occurred via Reaction (R3), giving rise to the buildup of N_2O. Upper stratospheric and mesospheric nitrous oxide increases up to 7 ppbv have been observed by MIPAS during the Halloween SPE and have been attributed to this reaction channel (Funke et al., 2008). Reasonable agreement with CMAM model calculations has been obtained by assuming that only half of the products of Reaction (R3) is N_2O and O, while the other half is N_2 and O_2. Figure 18 shows the observed and modeled N_2O zonal mean enhancements averaged over the period of the main proton forcing (29 -31 October). Except for FinROSE and B2dM, which do not include the reaction channel R3, N_2O increases are simulated by all models. The observed enhancements, however, are generally overestimated by a factor 2 to 10, except for EMAC which shows smaller N_2O increases than observed by MIPAS. In the latter model, this can be clearly attributed to the modified $N(^4S)$ and $N(^2D)$ branching ratio (see discussion above). Except for WACCM, the remaining models do not include the additional reaction channel of (R3), responsible for the formation of N_2 and O_2, which has been included in the CMAM simulations (Funke et al., 2008). But even when taking into account a reduction by a factor of 2 of the simulated enhancements, these models tend to overestimate the observations and further show a significant spread among the individual results. As in the case of NO_y, also the total SPE-induced N_2O production depends on temperature, NO_x partitioning, and dynamical redistribution. However, a dominant relationship of none of these quantities with the differences of the magnitudes of the modeled N_2O increases can be established.

6.3 Repartitioning of nitrogen species

After having assessed the observed and modeled total NO_y and N_2O enhancements generated by the Halloween event, we analyze in this subsection the repartitioning of initially produced nitric oxide into other NO_y species in the aftermath of the SPE.

6.3.1 NO_x

The conversion of the excess NO generated by the proton forcing into NO_2 acts on a very short timescale (seconds to minutes) and is controlled at dark conditions by the reactions

$$NO + O_3 \rightarrow NO_2 + O_2 \quad \text{(R4)}$$

$$NO_2 + O \rightarrow NO + O_2, \quad \text{(R5)}$$

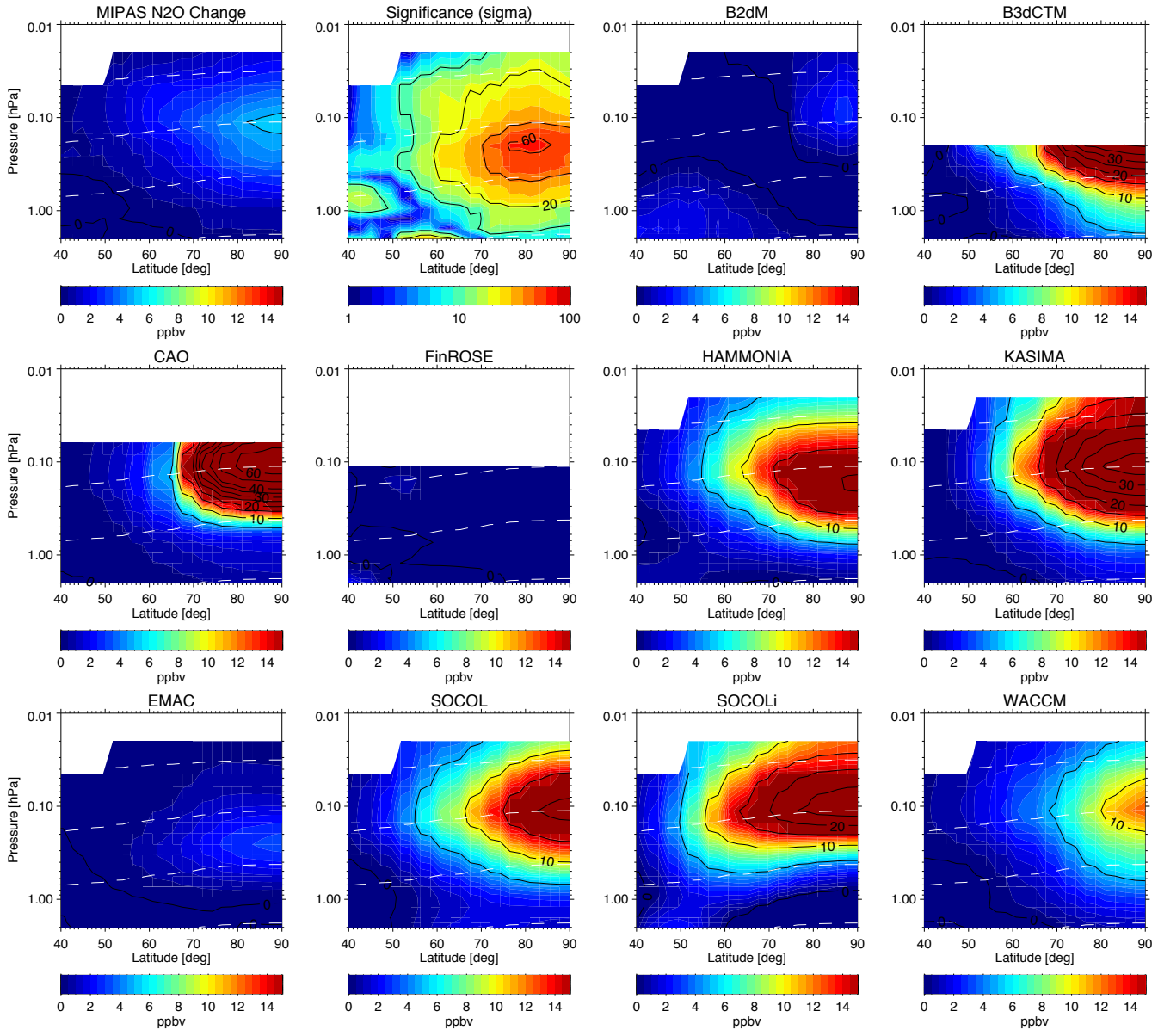

Fig. 18. Zonal mean N_2O changes with respect to 26 October 2003 in MIPAS observations and model simulations averaged over the period 29–31 October. The significance of observed N_2O changes (in units of σ) is shown in the upper second panel (from the left).

giving rise to a NO_2/NO_x ratio close to one in the stratosphere, but decreasing in the mesosphere due to the availability of atomic oxygen. This decrease occurs at higher altitudes in the polar night region compared to midlatitudes. Figure 19 shows the observed and modeled nighttime NO_2/NO_x ratios averaged over the initial SPE period. The observed decrease of this ratio above 0.3 hPa at midlatitudes and 0.1 hPa in the polar region is generally well reproduced by the models which resolve the mesosphere, except for B2dM and EMAC, which both overestimate the polar NO_2 fraction at these altitudes. The higher mesospheric NO_2 abundances in these two models might be related to lower atomic oxygen concentrations at high altitudes and/or less efficient mixing between polar night and illuminated regions. At sunlit conditions, photolysis of NO_2 and higher atomic oxygen abundances shift the NO_2/NO_x ratio to lower values compared to dark conditions. Figure 20 shows the observed and modeled daytime ratios. The observed values are well reproduced by B2dM, B3dCTM, SOCOL, and SOCOLi, while other models tend to overestimate the polar upper stratospheric and mesospheric NO_2 fraction close to the terminator. In the case of CAO, EMAC, FinROSE, and HAMMONIA, this behavior can be explained by cut-off solar zenith angles lower than 95° applied in the photolysis rate calculation. The encountered

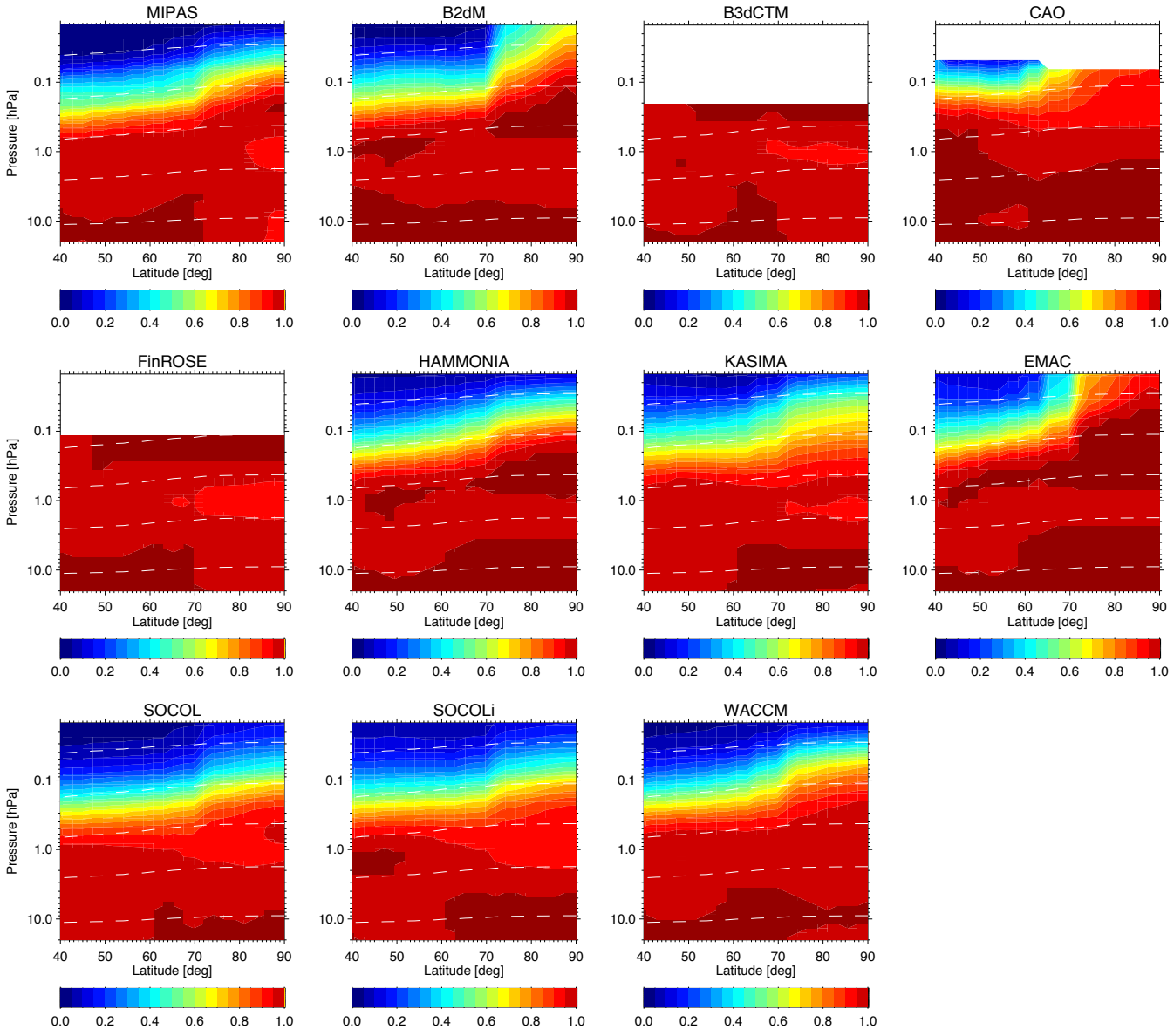

Fig. 19. Zonal mean nighttime NO_2/NO_x ratios averaged over the period 28 October–15 November in MIPAS observations and model simulations.

differences in the NO_x partitioning among the models and observations highlight the difficulties in drawing conclusions on the SPE-induced total NO_x enhancements from the comparison if only one of its components is considered.

6.3.2 N_2O_5 and HNO_3

In the stratosphere, excess NO_x produced by the proton forcing is slowly converted into N_2O_5 in the following weeks after the SPE by the reactions

$$NO_2 + O_3 \rightarrow NO_3 + O_2 \quad \text{(R6)}$$

$$NO_2 + NO_3 + M \rightarrow N_2O_5 + M. \quad \text{(R7)}$$

The rate-limiting reaction of this conversion is Reaction (R6) which exhibits a strong temperature dependence. N_2O_5 enhancements around 1–2 ppbv, appearing 10–15 days after the Halloween event, have been observed by MIPAS around 70–90° N and have been attributed to the repartitioning of SPE-induced excess NO_x (López-Puertas et al., 2005b). This conversion is further accelerated in the course of November by the growth of the polar night region, reducing the efficiency of N_2O_5 losses by photolysis.

Figure 21 shows the observed and modeled temporal evolutions of the N_2O_5 enhancements with respect to 26 October averaged over 70–90° N. A stratospheric N_2O_5 buildup, being most pronounced in the second half of November, is

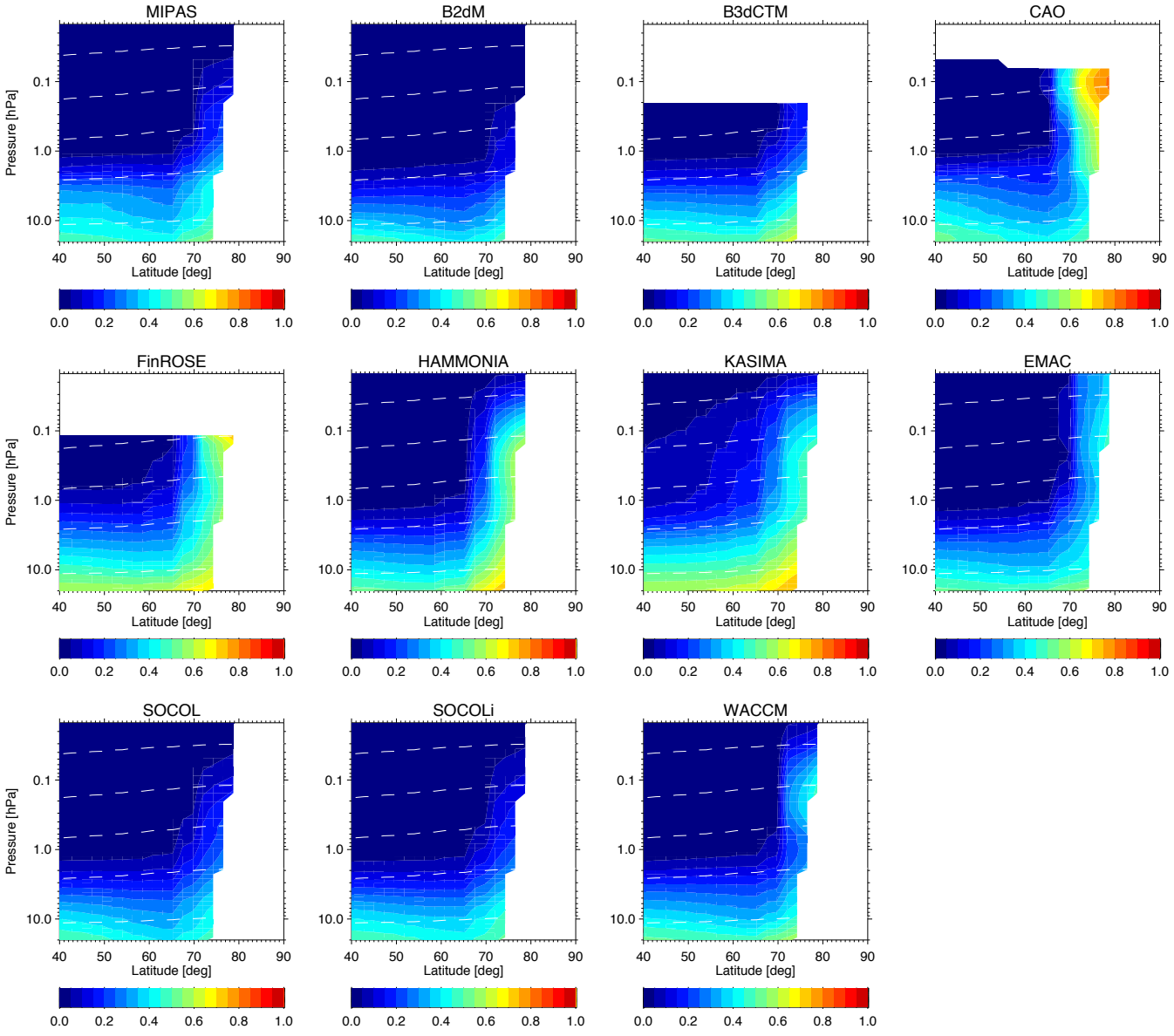

Fig. 20. Zonal mean daytime NO_2/NO_x ratios averaged over the period 28 October–15 November in MIPAS observations and model simulations.

simulated by all models, qualitatively reproducing the observed behavior. The modeled N_2O_5 increases are, however, generally overestimated (except for KASIMA) and exhibit a wide spread among the models. Taking into account that the magnitude of the N_2O_5 increase depends on various factors such as NO_x availability, temperature, ozone abundances, and the efficiency of $N_2O_5 \rightarrow HNO_3$ conversion (see below), a large spread of the model results is expected. B2dM and EMAC, however, overestimate the observed N_2O_5 increases by factors of 4 and 6, respectively. While in the case of B2dM the extraordinarily high N_2O_5 amounts can be explained by the very pole-centered distribution of the precursor NO_x, implying insignificant photochemical losses in the source region (see also discussion below), the reason for the unreasonably high N_2O_5 abundances of up to 12 ppbv in the case of EMAC is still under investigation. N_2O_5 enhancements simulated by CAO until 4 November are likely to be caused by seasonal variations rather than by the SPE. The overestimated seasonal N_2O_5 buildup in this model is most likely related to the use of a family approach for NO_y.

Two distinct HNO_3 enhancements were observed by MIPAS in the aftermath of the Halloween SPE (López-Puertas et al., 2005b). The first one, reaching vmrs around 2 ppbv, occurred immediately after the SPEs at altiudes above 40 km and has been initially attributed to the gas-phase reaction $NO_2 + OH + M \rightarrow HNO_3 + M$. Verronen et al. (2008),

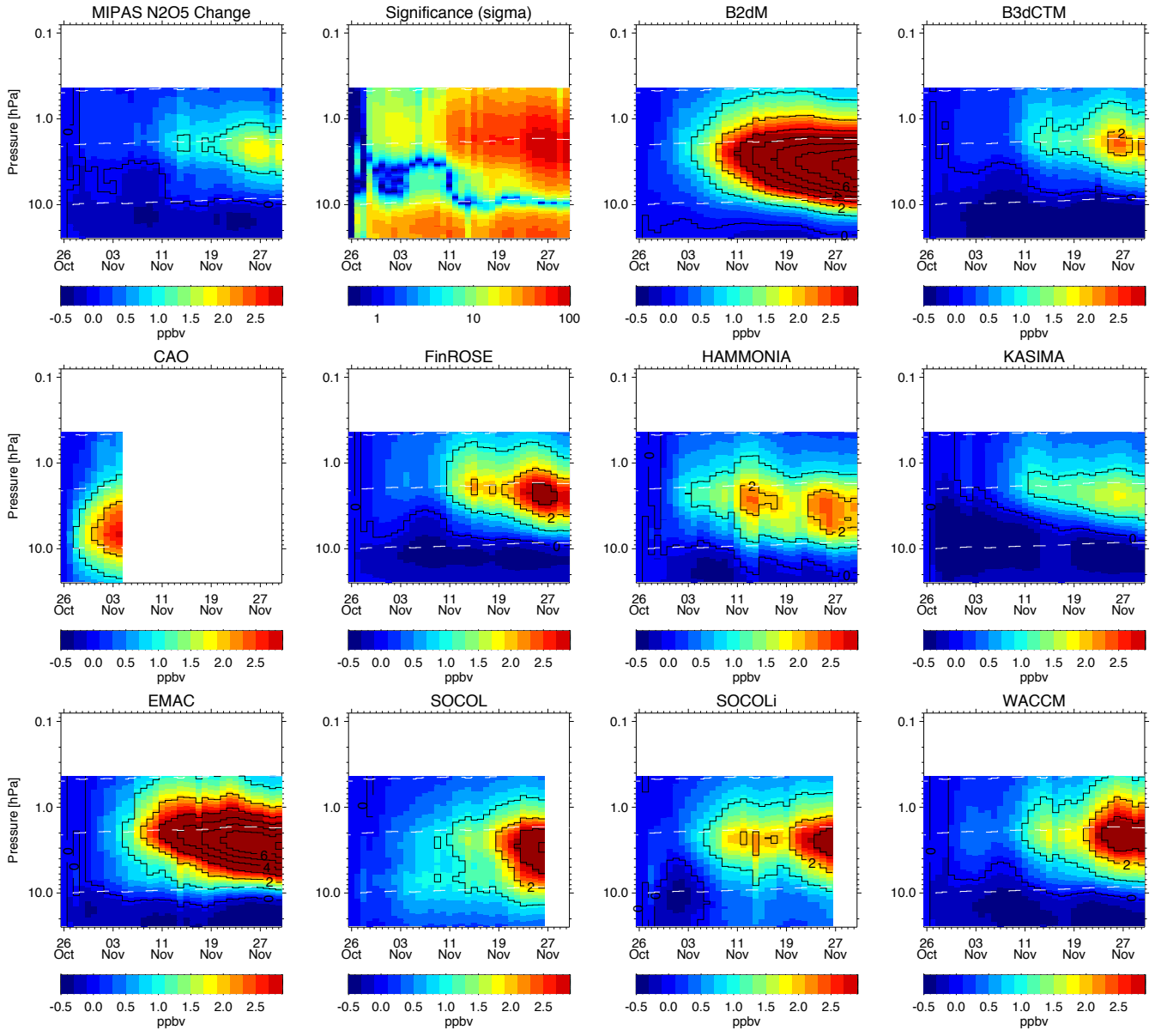

Fig. 21. Temporal evolution of area-weighted averages of N_2O_5 changes with respect to 26 October 2003 in MIPAS observations and model simulations at 70–90° N. Solid contour lines reflect 1 ppbv steps. The significance of observed N_2O_5 changes (in units of σ) is shown in the upper second panel (from the left).

however, have shown that the instantaneous HNO_3 increase after the proton forcing can only be reproduced by model calculations including ion-ion recombination between NO_3^- and H^+ cluster ions. The second enhancement of 1–5 ppbv started around 10 November and lasted until the end of December. Also in this case, attempts to reproduce the magnitude of the observed increases by model calculations including gas phase chemistry only, have failed (Jackman et al., 2008).

Figure 22 shows the observed and modeled temporal evolutions of the HNO_3 enhancements with respect to 26 October averaged over 70–90° N. Consistent with previous findings, the first instantaneous enhancement is considerably underestimated by all models, except FinROSE, which includes the ion chemistry proposed by Verronen et al. (2008). This model, however, overestimates the observed increases by up to a factor of 3. The overestimation below 50 km is surprising, given that 1-D simulations with the Sodankylä Ion and Neutral Chemistry (SIC) model which includes the ion-ion recombination were found to be in good agreement with the same MIPAS dataset at these altitudes. It should be noted, however, that different ionization rates have been used in the

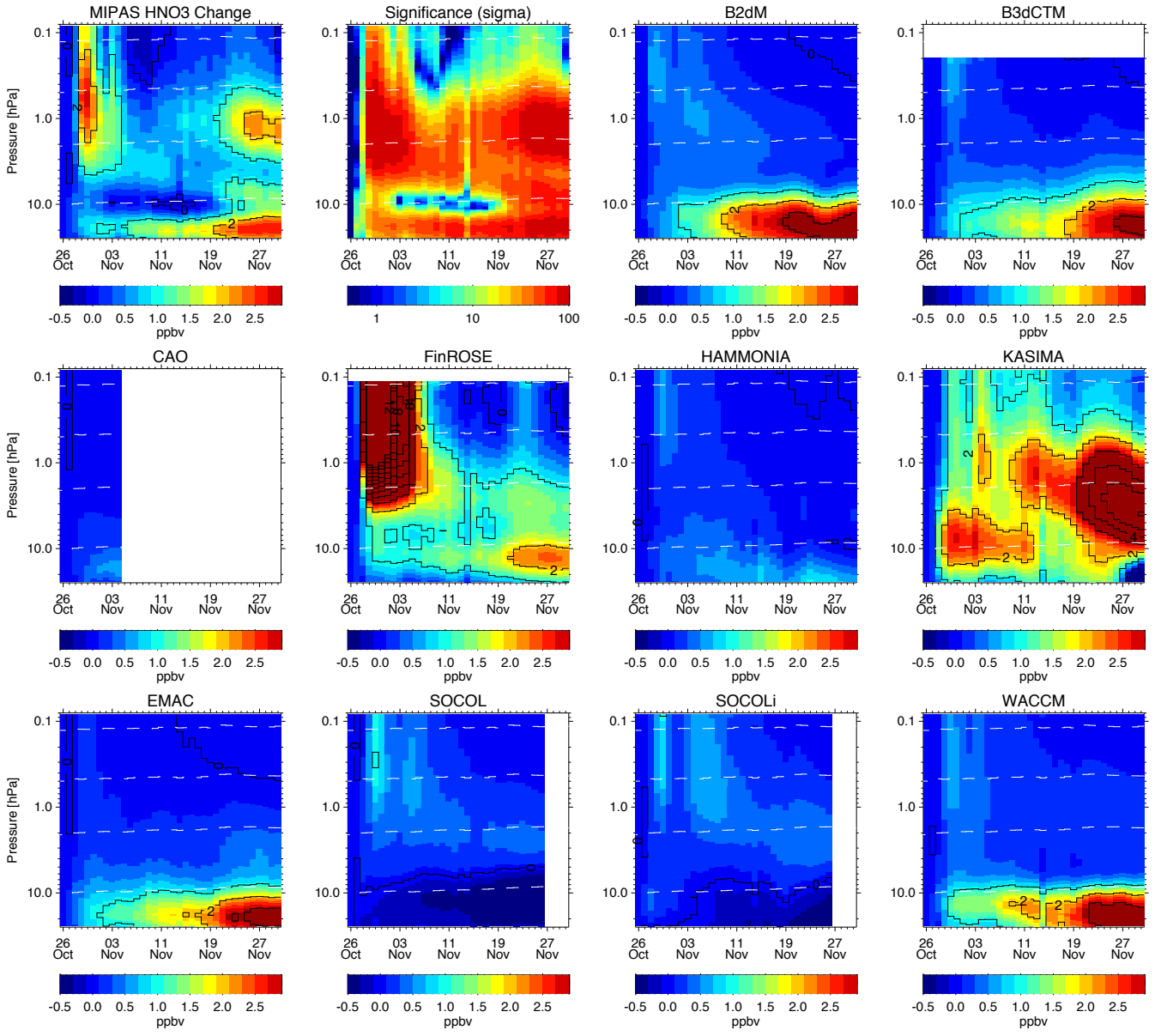

Fig. 22. Temporal evolution of area-weighted averages of HNO_3 changes with respect to 26 October 2003 in MIPAS observations and model simulations at 70–90° N. Solid contour lines reflect 1 ppbv steps. The significance of observed HNO_3 changes (in units of σ) is shown in the upper second panel (from the left).

SIC calculations of Verronen et al. (2008), and – probably even more important – that FinROSE uses a parameterization of the ion-ion recombination included in the full ion chemistry scheme of the SIC model.

The second enhancement, occurring around 15 November at 1–2 hPa, is only reproduced by KASIMA. In this case, however, the observed increases are overestimated by a factor of 3. Contrary to other models, KASIMA simulations account for HNO_3 formation via water cluster ions (Böhringer et al., 1983) combined with heterogeneous reactions on sulfate aerosols by means of a parameterization provided by de Zafra and Smyshlyaev (2001). At lower altitudes (i.e. below 10 hPa), midterm HNO_3 increases are visible in the observations, as well as in the B2dM, B3dCTM, EMAC, FinROSE, and WACCM model results. These increases are not related to the SPE and can be explained by seasonal variations.

In order to assess the repartitioning of the main NO_y species towards the end of November in a more quantitative way, we have analyzed their relative contributions to the total NO_y. This is necessary because of the encountered differences in the total amount of SPE-induced excess NO_y among

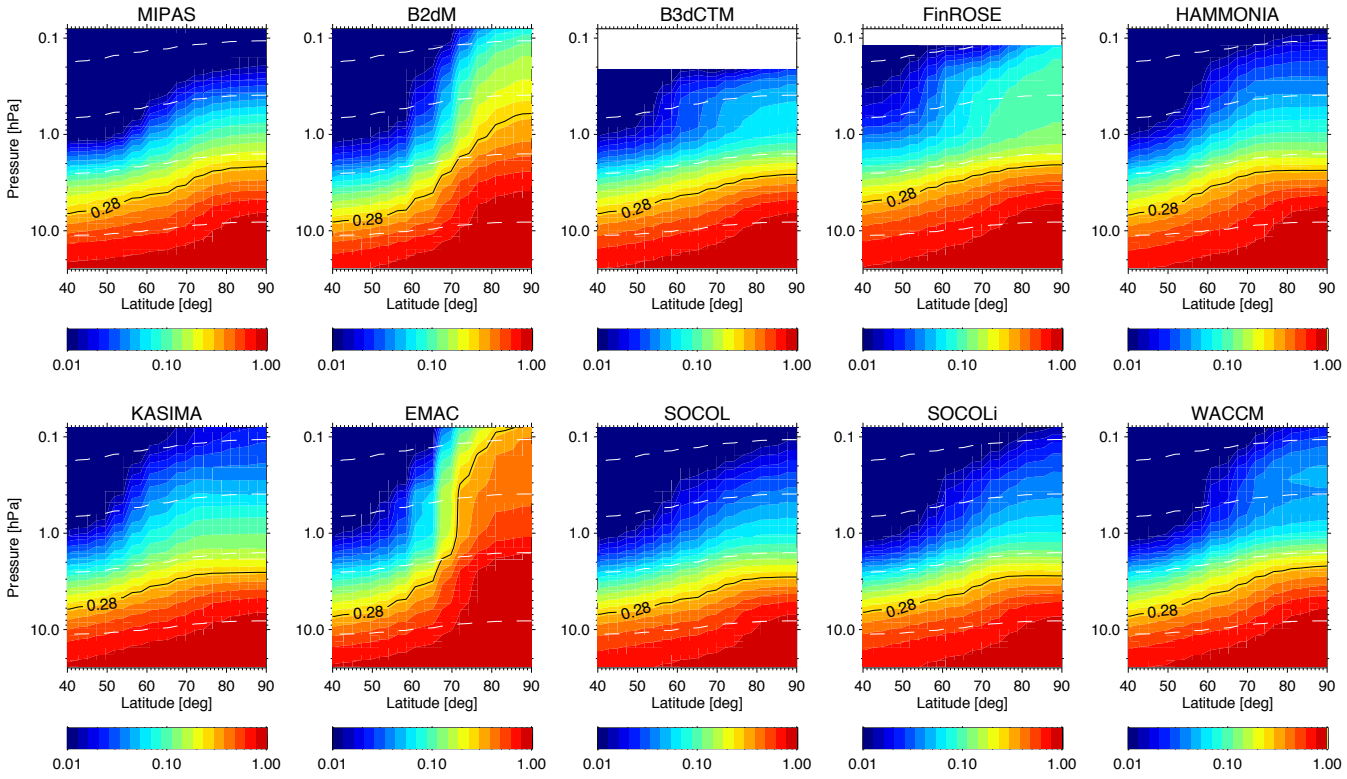

Fig. 23. Zonal mean $(2N_2O_5+HNO_3)/NO_y$ ratios averaged over the period 15–30 November in MIPAS observations and model simulations. The MIPAS ratio of 0.28, encountered at altitude of the maximum of the SPE-induced NO_y layer, is indicated by a black line.

the different models and the observations. Due to the observed conversion of N_2O_5 into HNO_3, we have looked, as a first step, at the relative contribution of the sum of both reservoir species to NO_y. Observed and simulated zonal mean $(2N_2O_5 + HNO_3)/NO_y$ ratios, averaged over the period 15–30 November, are shown in Fig. 23. The observed ratio of 0.28 at the peak height (∼0.2 hPa, see Fig. 15) of the NO_y enhancements in late November (indicated by a black line in Fig. 23) is very well reproduced by all models, except B2dM and EMAC. As discussed above, the disagreement found in these models is produced by too efficient buildup of N_2O_5 (see Fig. 21). The differences of the $(2N_2O_5 + HNO_3)/NO_y$ ratio in the observations and the B2dM simulations are, however, much less pronounced than those encountered in the absolute N_2O_5 abundances: while B2dM N_2O_5 exceeds the observed amounts by a factor of 4, the modeled $2N_2O_5 + HNO_3$ contribution to NO_y at its peak height is around 40 %, exceeding the observed contribution by only a factor of 0.5. The N_2O_5 overestimation in this model is hence mainly related to the higher amounts and more pole-centered distribution of the precursor NO_2. In contrast to B2dM , EMAC simulations obtain more than 90 % of the available NO_y at its peak altitude in the form of N_2O_5. This contribution decreases with altitude, but still exceeds 30 % in the mesosphere. Other models show, in some cases, a minor overestimation of the reservoir species fraction which can be partly explained by differences in the modeled temperatures and ozone abundances, controlling the efficiency of Reaction (R6).

The repartitioning between HNO_3 and N_2O_5 has been assessed by comparing the observed and modeled zonal mean $HNO_3/(2N_2O_5 + HNO_3)$ ratios averaged over the period 15–30 November (Fig. 24). As expected, the observed ratio is strongly underestimated above approximately 10 hPa by all models, except KASIMA. The qualtitative agreement of KASIMA simulations and MIPAS observations is very good, particularly regarding the vertical shape of this ratio. The modeled ratio, however, exhibits a positive bias of 0.2 with respect to the observations, most pronounced in the polar region. We conclude that the HNO_3 formation via water cluster ions and/or heterogeneous reactions on sulfate aerosols, both included in KASIMA by means of the parameterization of de Zafra and Smyshlyaev (2001), is the responsible mechanism for the observed HNO_3 enhancements in late November. However, some further work is required to adjust the parameterization quantitatively to the measurements.

6.3.3 Minor NO_y species

Also minor NO_y species were found to be enhanced in the aftermath of the Halloween SPE due to the repartitioning of initially produced NO_x. López-Puertas et al. (2005b) reported

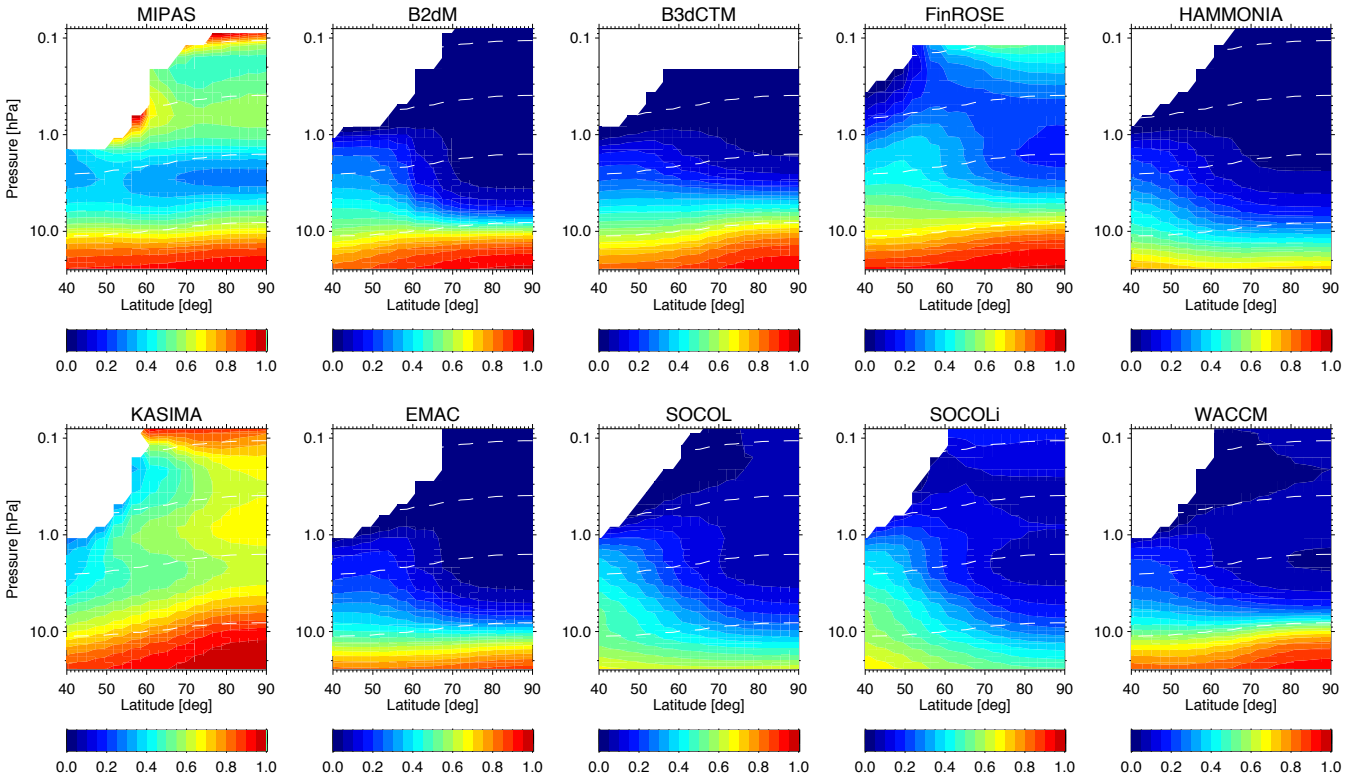

Fig. 24. Zonal mean $HNO_3/(2N_2O_5+HNO_3)$ ratios averaged over the period 15–30 November in MIPAS observations and model simulations. Regions with observed vmrs of $2N_2O_5+HNO_3$ smaller than 0.1 ppbv have been omitted.

$ClONO_2$ enhancements up to 0.4 ppbv a few days after the proton forcing from MIPAS observations. These observations are compared to the model simulations in Sect. 6.6, together with observations of other chlorine species. MIPAS has also observed enhanced HNO_4 during the first days of the Halloween SPE which have not been reported so far. These increases can be attributed to the termolecular reaction

$$HO_2 + NO_2 + M \rightarrow HNO_4 + M. \quad \text{(R8)}$$

Since at the altitude of the HNO_4 enhancements (around 2–3 hPa) SPE-related increases of the precursor NO_2 are relatively small (∼2 ppbv) compared to the background NO_2 abundance, the observed HNO_4 changes are mainly driven by enhanced HO_2 abundances, and hence, represent an indicator of SPE-generated HO_x in the middle stratosphere. At dark conditions, HO_x is in steady state even during a SPE, and its abundance is hence directly proportional to atmospheric ionization. Stratospheric HNO_4 is destroyed during the day by photolysis and by reaction with OH. Nighttime losses are negligible under quiescent conditions, and even during SPEs, OH-driven HNO_4 destruction is small compared to its production via Reaction (R8).

Due to problems with the gain calibration, particularly affecting this species (see discussion in Sect. 2), we restrict our analysis to data from the gain calibration period 28 October–5 November. Figure 25 shows the observed and modeled zonal mean distributions of HNO_4 vmrs during the first four days of the proton forcing (29 October–1 November). Model results for pre-SPE conditions (26 October) are also shown. HNO_4 model output is not available from CAO, EMAC, HAMMONIA, and FinROSE. Polar upper stratospheric enhancements of up to 0.18 ppbv are visible in the observations on 30 October, decreasing until 1 November by about 20 %. The HNO_4 enhancements are also simulated by the models in the first days of the SPE, but are generally overestimated. The overestimation is most pronounced in the B2dM, B3dCTM, and WACCM simulations (a factor 2–3), while SOCOLi shows smaller HNO_4 increases. The HNO_4 peak height is located at somewhat lower altitudes in SOCOLi which might be related to the relatively high abundances inside the ambient HNO_4 layer around 5 hPa. Both, the SPE-related and ambient peaks can not be vertically resolved and merge together after the application of MIPAS averaging kernels. The moderate decrease of HNO_4 in the following days is qualitatively reproduced by all models except B2dM. In this particular model, the HNO_4 enhancements are confined to the polar night region, hence experiencing less photochemical losses.

The differences in the magnitude of the HNO_4 enhancements in the simulations and the observations can partially be explained by differences in the abundances of the precursor NO_2. During the main proton forcing, modeled NO_2

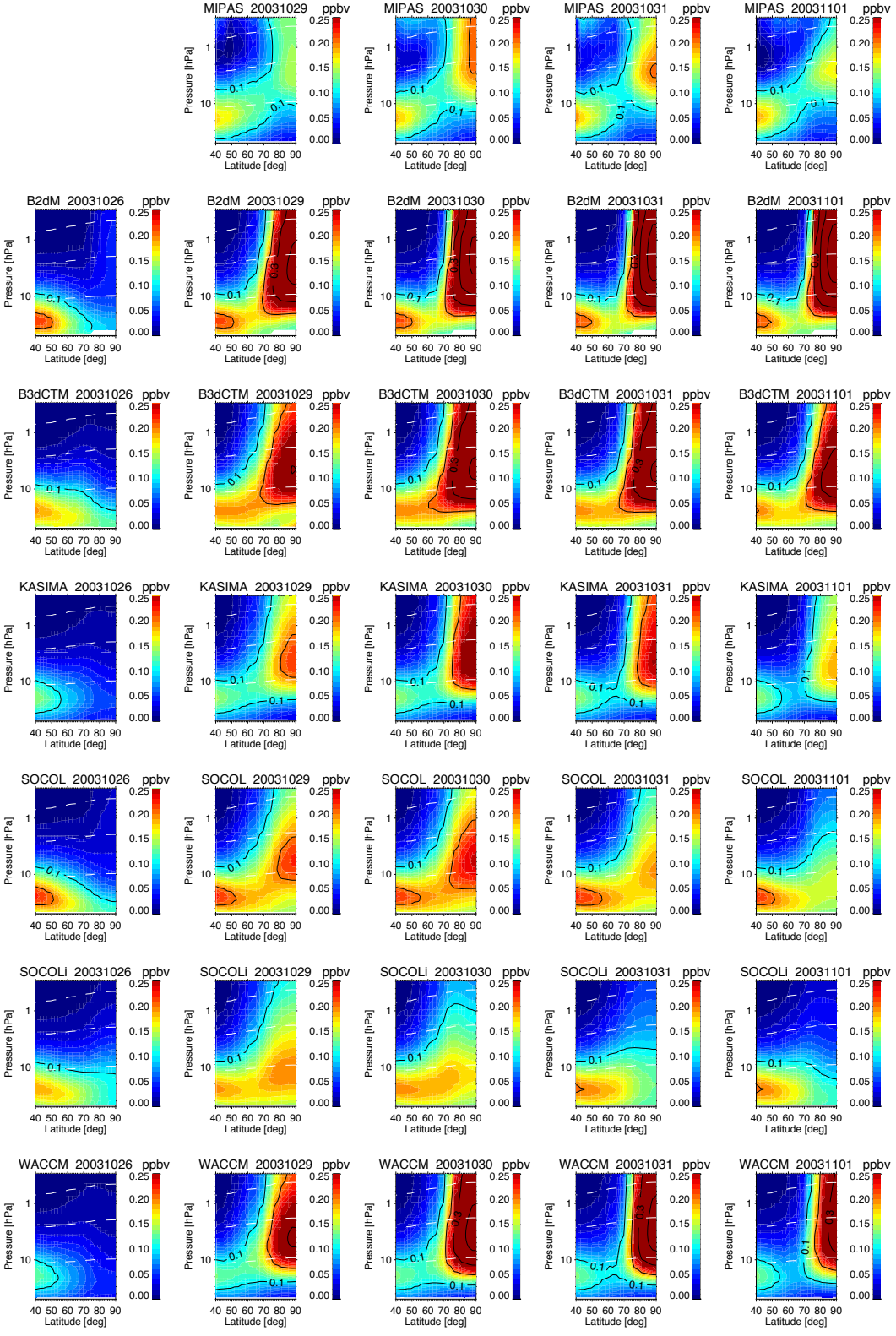

Fig. 25. Observed and modeled zonal mean HNO_4 vmrs for pre-SPE conditions (26 October) and during the main proton forcing (29 October–1 November). Solid contour lines reflect 0.1 ppbv steps. Note that MIPAS observations from 26 October have been omitted due to gain calibration problems.

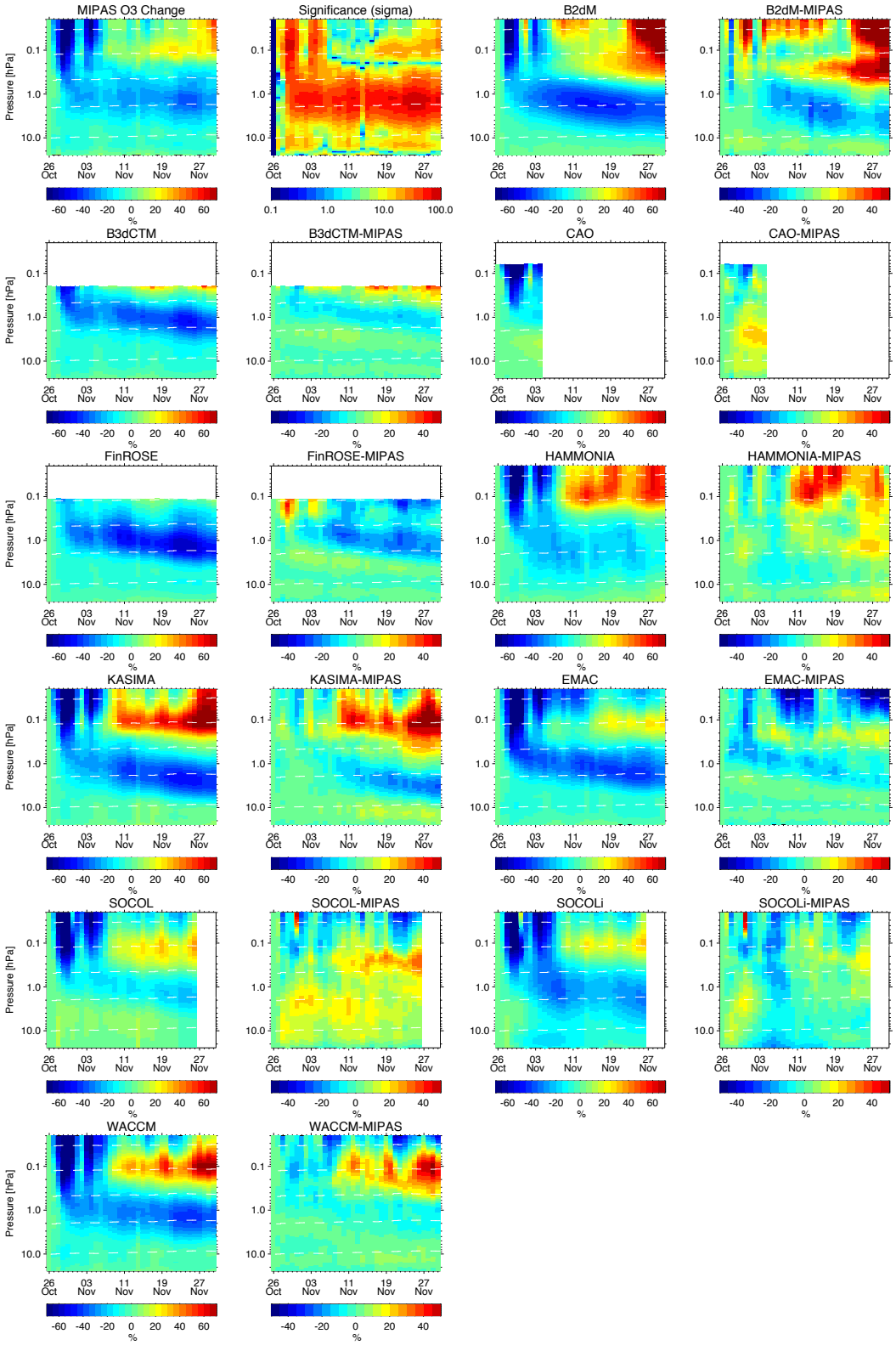

Fig. 26. Temporal evolution of area-weighted averages of relative O_3 changes with respect to 26 October 2003 in MIPAS observations and model simulations at 70–90° N, as well as differences between modeled and observed averages. The significance of observed O_3 changes (in units of σ) is shown in the upper second panel (from the left).

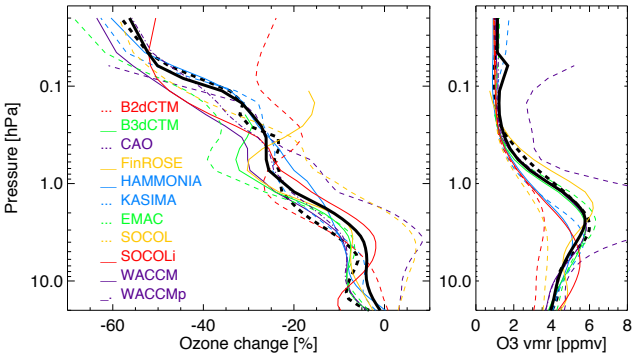

Fig. 27. Area-weighted averages (70–90° N) of observed and modeled relative O_3 changes during 29 October–4 November (left) with respect to the abundances on 26 October (right). Thick solid and dashed lines represent multi-model mean average and MIPAS observations, respectively. WACCMp denotes the WACCM simulation including proton ionization, only (excluded from the multi-model mean).

abundances at 70–90° N at the HNO_4 peak height are on average 50–100 % higher than the observed ones (not shown). The NO_2 overestimation in the models is mainly related to a weaker degree of denoxification compared to the observations already before the SPE event. Additionally, differences in the HO_2 availability might also play an important role in explaining the behavior of modeled HNO_4. At the peak height of the HNO_4 enhancements and in the absence of sunlight, HO_2 is the dominant HO_x compound in the presence of proton forcing. Since HO_x production by SPE-induced ionization is not expected to differ significantly among the models, different HO_2 abundances are most likely related to differences in the HO_x losses. These are dominated by the cannibalistic reaction

$$HO_2 + OH \rightarrow H_2O + O_2. \quad \text{(R9)}$$

In this sense, the HO_x partitioning plays a crucial role in the HO_2 availability at these altitudes despite the approximately 20 times smaller OH concentrations compared to HO_2.

It might also be possible that the HO_x partitioning is affected by ion chemistry. Several ion chemistry reactions are known which transfer H into OH^-, and therefore might act as a sink of HO_2; one reaction is known which transfers OH into HO_2. While it is beyond the scope of this investigation to determine whether these reactions really significantly affect the partitioning between odd hydrogen species, it might be worthwhile to investigate this point in the future.

6.4 Ozone loss

One of the most important aspects of the model-data intercomparison of SPE-induced composition changes during the Halloween event is the evaluation of the ability of the models to reproduce the observed ozone destruction caused by acceleration of catalytic HO_x and NO_x cycles. SPE-induced ozone losses have been observed by a variety of space-borne instruments during several of the stronger events of the past two solar cycles (see Jackman et al., 2000, for a review). Two different types of ozone destruction could be distinguished: HO_x-related short-time losses, acting principally in the mesosphere during the event itself, and NO_x-related midterm losses in the stratosphere which can last up to several months in the polar winter atmosphere. Such a behavior was also observed by MIPAS in the aftermath of the Halloween event. López-Puertas et al. (2005a) reported HO_x-driven mesospheric ozone losses up to 70 % and NO_x-driven stratospheric losses of around 30 %, the latter lasting for more than 2 weeks in the Northern Hemisphere.

Figure 26 shows the observed and modeled temporal evolutions of the relative O_3 changes with respect to 26 October, averaged over 70–90° N. The mesospheric ozone losses above 0.3 hPa, which exhibit two distinct peaks related to the proton events on 29 October and 4 November, are well reproduced by most of the models. Also the stratospheric O_3 losses during the following month, peaking around 1 hPa, are qualitatively reproduced by the simulations, however, with a more pronounced spread of the model results. This is not surprising since these losses are driven by NO_x which exhibits important differences between the models, particularly during the second half of November (see Sects. 6.2 and 6.3). Further, NO_x-induced ozone loss is driven by Reaction (R4) which is very sensitive to temperature differences. The midterm evolution in the mesosphere is characterized by ozone buildup which is related to seasonal variations (summer to winter transition), and which is generally more pronounced in the model simulations compared to the observations. This seasonal ozone buildup masks the residual ozone depletion related to the SPE.

In order to assess observed and modeled short-term ozone depletion in a more quantitative way, we have compared profiles of relative ozone changes at 70–90° N, averaged over the period of the main proton forcing (28 October–4 November), in Fig. 27. The agreement between observations and the multi-model average is excellent in the mesosphere, indicating a very good overall ability of the models to reproduce HO_x-related ozone losses under SPE conditions. Also, the models themselves agree reasonably well in this altitude range, except for B2dM. In the stratosphere, where NO_x-related losses are dominant, the agreement between the models is worse, though the model average is very close to the observations within 5 %. Ozone depletion around 1 hPa is overestimated by EMAC and B3dCTM. CAO and SOCOL results indicate a somewhat smaller ozone loss throughout the stratosphere. WACCM simulations performed with and without electron-induced ionization (WACCM and WACCMp, respectively in Fig. 27) indicate an additional ozone loss induced by electrons in the order of 5 % above 2 hPa.

Figure 28 shows the corresponding zonal mean distributions. Observed mesospheric losses extend to around 60° N in consonance with the expected cut-off latitude of proton

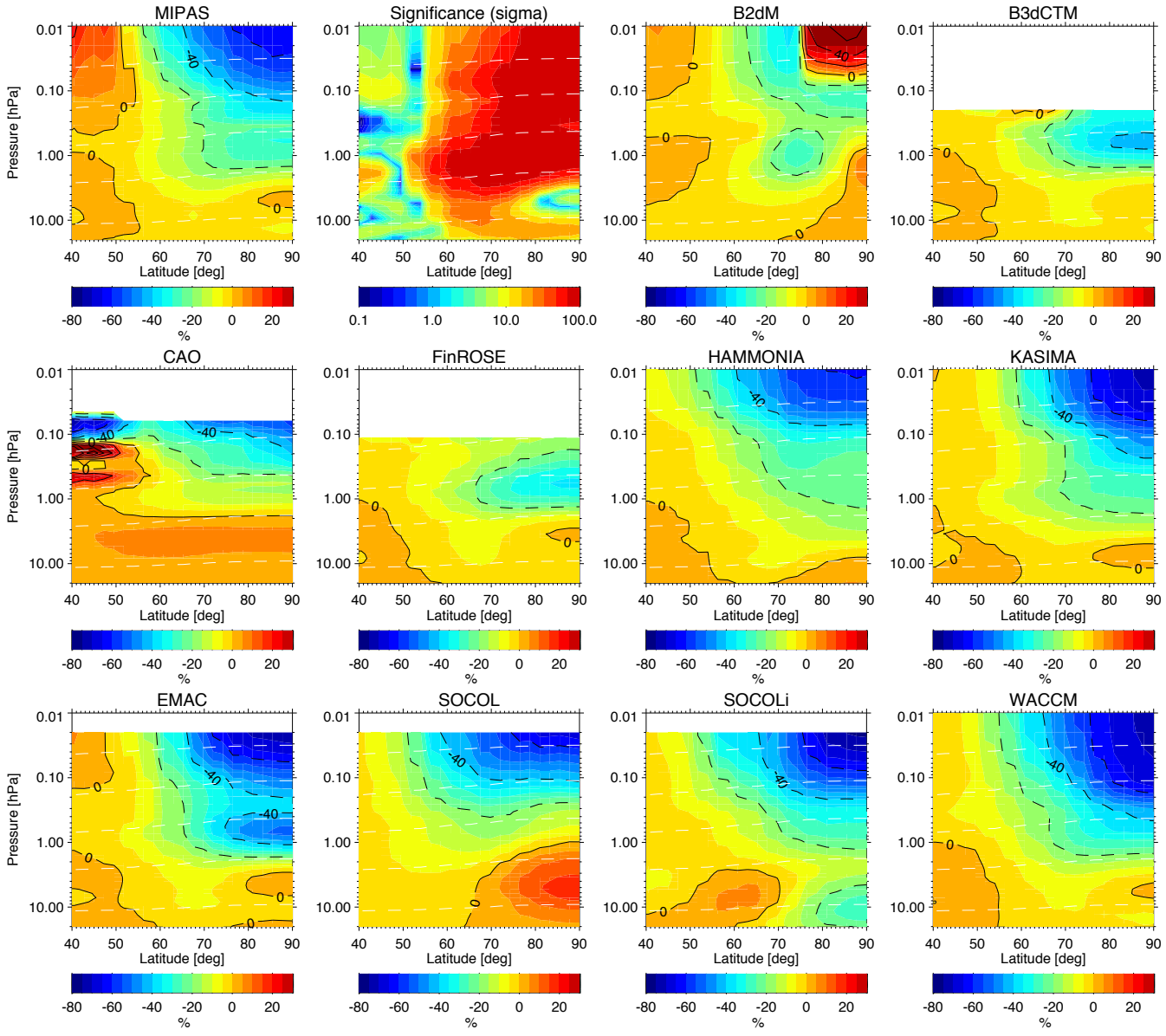

Fig. 28. Zonal mean relative O_3 changes with respect to 26 October averaged over the period 28 October–4 November in MIPAS observations and model simulations. Solid contour lines reflect 20 % steps. The significance of the observations is also shown (second top panel from the left, in units of σ).

precipitation. This latitudinal distribution is well reproduced by the models. B2dM shows a mesospheric ozone buildup poleward of 80° N related to seasonal changes, which overcompensates HO_x-related losses at these particular latitudes. This behavior, which can be attributed to deficient meridional mixing in the polar region, give rise to the apparent underestimation of mesospheric ozone losses of B2dM in Fig. 27. Oscillations encountered in the CAO ozone changes above 1 hPa at 40–50° N are related to the background O_3 and are not caused by the SPE.

The latitudinal extension of observed and modeled stratospheric ozone losses around 1 hPa correlates well with the area of NO_x increases shown in Fig. 14. In this altitude region, ozone depletion is restricted to latitudes poleward of 70° N. It is interesting to notice that B2dM simulations show no NO_x-induced ozone loss in the upper stratospheric polar night region, in contrast to the observations and other models. Indeed, the NO_x catalytic cycle is expected to be inefficient at dark conditions since NO_2 is not reconverted to NO. Strong mixing is hence required in order to obtain a homogeneous ozone distribution in the polar stratosphere as found

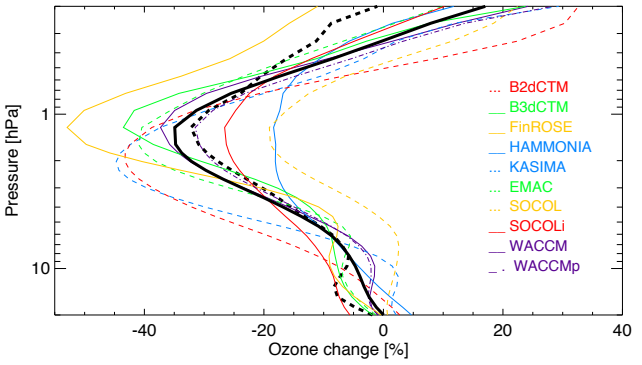

Fig. 29. Area-weighted averages (70–90° N) of observed and modeled relative O_3 changes with respect to 26 October during 16–26 November . Thick solid and dashed lines represent model mean average and MIPAS observations, respectively. WACCMp denotes the WACCM simulation including proton ionization, only (excluded from the multi-model mean).

in the observations. Ozone increases occur in the SOCOL simulation below 1 hPa which can be related to intrusions of mid-latitude air into the polar region, over-compensating the SPE-induced ozone losses.

Figure 29 shows profiles of stratospheric mid-term ozone changes at 70–90° N, averaged over the period 16–26 November. As expected, modeled ozone depletions have a larger spread than during the main proton forcing, ranging from 10 to 50 % at the peak height. The model average, however, is in very good agreement with the observed depletion of 30 % at 1–2 hPa. Only minor differences of 5 % are found at its maximum.

Figure 30 shows the corresponding zonal mean distributions. Generally, the magnitude of the stratospheric ozone loss at 70–90° N is anti-correlated to its latitudinal extension which, in turn, is linked to the spatial distribution of the SPE-related NO_x layer (see Fig. 17). Meridional redistribution is hence a key factor for explaining the differences in the modeled ozone depletions shown in Fig. 29. In particular, SOCOL simulations indicate strong meridional distribution around 1 hPa, resulting in higher polar ozone abundances than in the other models, despite the relatively high NO_y availability shown in Fig. 17. There, NO_x-driven ozone loss is partly compensated by in-mixing of O_3-rich air-masses from lower latitudes.

Observed mesospheric ozone changes in late November are characterized by a pronounced increase around the polar night terminator which is related to the buildup of the third ozone maximum (Marsh et al., 2001). This rapid buildup is responsible for the short lifetime of HO_x-related ozone depletion at these altitudes. Only in the polar night region, reduced ozone abundances are found until the end of November. This behavior is well reproduced by EMAC, KASIMA, WACCM and, to a lesser extent, HAMMONIA. B2dM behaves in an opposite way. A detailed investigation of the encountered differences in the seasonal ozone buildup among the models and the observations is beyond the scope of this paper, though an interesting topic for future studies.

In summary, SPE-related short- and midterm ozone changes are well reproduced by the atmospheric models on average, though individual model results can vary significantly due to differences in dynamical and meteorological background conditions. The good agreement between models and observations in the mesosphere can be interpreted as a verification of the parameterization of HO_x production by atmospheric ionization included in the models.

6.5 Enhancements of H_2O_2

MIPAS observed H_2O_2 increases of short duration immediately after the Halloween SPE in polar night stratosphere. H_2O_2 is formed by the reaction

$$HO_2 + HO_2 \rightarrow H_2O_2 + O_2 \quad \text{(R10)}$$

and is hence – together with HNO_4 – an indicator for SPE-generated HO_x in the stratosphere. During daytime, it is photolyzed within several hours to a day, or destroyed by the reaction

$$H_2O_2 + OH \rightarrow H_2O + HO_2. \quad \text{(R11)}$$

Chemical nighttime losses are negligible at quiescent conditions. The availability of OH during periods of proton forcing allows for H_2O_2 destruction also at night. These losses, however, are most important above the stratopause. In the dark stratosphere, Reaction (R11) is expected to deplete H_2O_2 by less than 10 %. Therefore, observed H_2O_2 increases are primarily driven by the production mechanism (R10).

Model output of H_2O_2 is available from B2dM, B3dCTM, FinROSE, HAMMONIA, KASIMA, and WACCM. Figure 31 shows observed and modeled zonal mean H_2O_2 changes during the period of the main SPEs (28 October–4 November). The observed increases of up to 0.1 ppbv are considerably overestimated by the simulations by a factor of 4–7. This huge difference between observed and modeled H_2O_2 increases can hardly be explained by a possible overestimation of the ionization rates by a factor of 1.2–2, as suggested from the comparison of NO_y increases. Although H_2O_2 production depends quadratically on HO_2, total HO_x scales with the square root of the ionization rate due to Reaction (R9), being the principal chemical loss mechanism at nighttime. Thus, 4–7 times lower ionization rates would be required in order to reduce modeled H_2O_2 increases to the observed values. As already mentioned in the discussion of HNO_4 enhancements, the availability of HO_2 during nighttime SPE conditions is largely controlled by the HO_x partitioning. At the peak height of the H_2O_2 increases (0.5–1 hPa), this dependence is even more pronounced than at the pressure levels of the HNO_4 enhancements (2–3 hPa) due to the increasing OH contribution to HO_x with altitude. Thus, the disagreement of observed and simulated H_2O_2 hints at

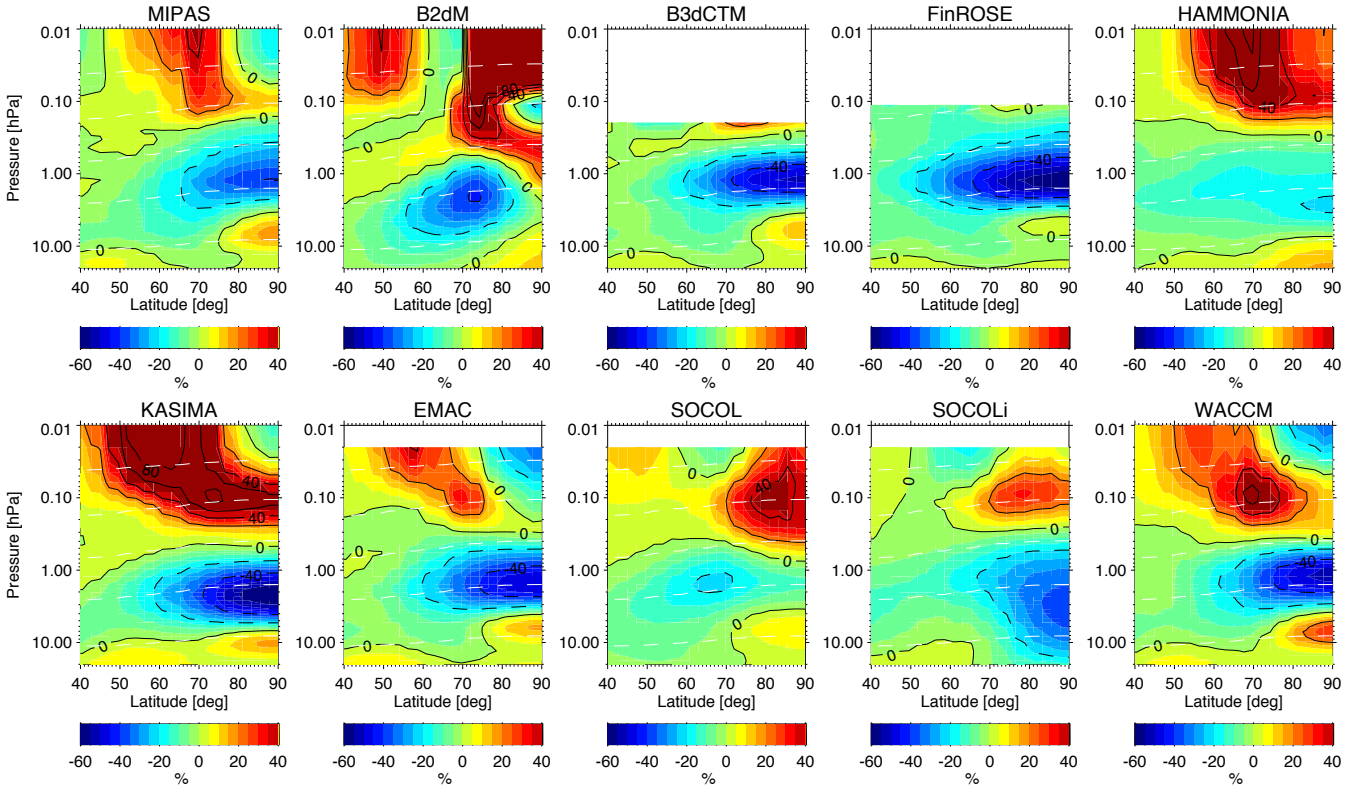

Fig. 30. Zonal mean relative O_3 changes with respect to 26 October averaged over the period 16–26 November in MIPAS observations and model simulations. Solid contour lines reflect 20 % steps.

an underestimation of the OH/HO_2 ratio in the upper polar stratosphere during the proton forcing. Alternatively, H_2O_2 formation by Reaction (R10) might be significantly overestimated in the models.

Meridional transport to illuminated latitudes, where H_2O_2 is photochemically destroyed, could also affect the magnitude of the SPE-related enhancements. H_2O_2 distributions simulated by B2dM, which has a very strong mixing barrier, might hence experience less photochemical losses than in other models. In fact, B2dM enhancements are more confined to the polar night region. Other models, however, show a similar meridional distribution as observed by MIPAS. It is thus unlikely, that differences in the efficiency of photochemical losses related to transport can explain the pronounced differences between observed and modeled H_2O_2 enhancements.

6.6 Enhancements and repartitioning of chlorine species

Enhancements of the chlorine species ClO, HOCl, and $ClONO_2$ have been detected by MIPAS in the aftermath of the Halloween SPE in the NH polar stratosphere (von Clarmann et al., 2005; López-Puertas et al., 2005b). Short-term ClO and HOCl increases of the order of 0.2 ppbv occurred immediately after the onset of the proton forcing on 29 October. $ClONO_2$ increases up to 0.4 ppbv appeared approximately 2 days later, remaining in the stratosphere for several weeeks. SPE-related HOCl increases have also been observed by MLS on Aura during the January 2005 proton event (Damiani et al., 2008). These enhancements were accompanied by a HCl decrease of similar magnitude, thus clearly demonstrating SPE-induced chlorine activation. The conversion of HCl to active species occurred in presence of enhanced OH via the reaction

$$HCl + OH \rightarrow Cl + H_2O. \quad \text{(R12)}$$

HCl can also be incorporated into negative ions, from which chlorine is released mainly in the form of atomic chlorine or chlorine monoxide. There are also reverse reactions releasing HCl, however, it has been shown in a recent publication (Winkler et al., 2009) that during large solar proton events, chlorine activation dominates, and negative ion reactions can act as a significant sink of HCl, and a source of active chlorine. Atomic chlorine is rapidly converted to ClO by

$$Cl + O_3 \rightarrow ClO + O_2. \quad \text{(R13)}$$

In the polar night stratosphere, where SPE-generated HO_x is dominated by HO_2, ClO is further converted to HOCl:

$$ClO + HO_2 \rightarrow HOCl + O_2. \quad \text{(R14)}$$

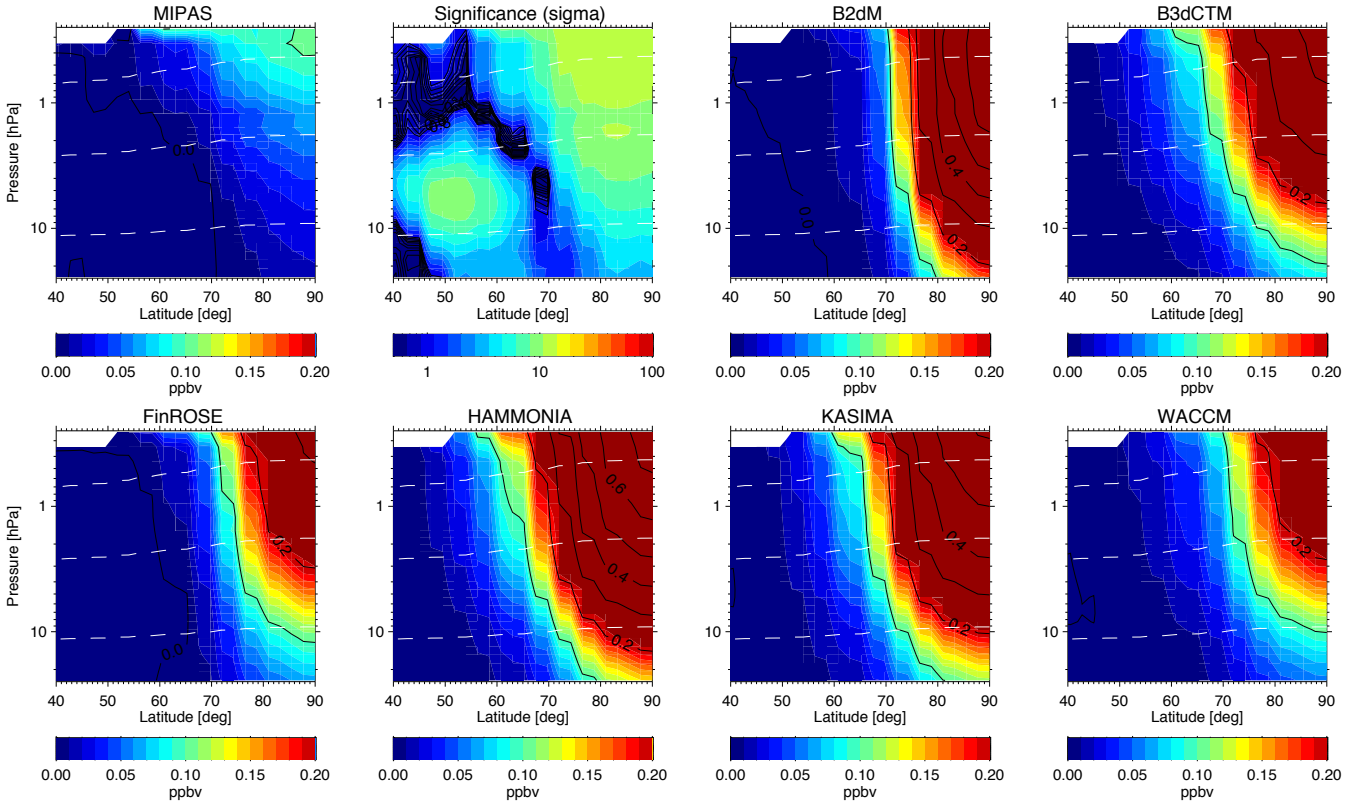

Fig. 31. Zonal mean H_2O_2 changes with respect to 26 October averaged over the period 28 October–4 November in MIPAS observations and model simulations. Solid contour lines reflect 0.1 ppbv steps. The significance of observed H_2O_2 changes (in units of σ) is shown in the upper second panel (from the left).

The chemical lifetime of nighttime HOCl is very long below the stratopause. Above and at sunlit conditions, HOCl is removed by the reaction

$$HOCl + OH \rightarrow ClO + H_2O \qquad (R15)$$

and rapid photo-dissociation. Due to the high HO_2/OH ratio in the nighttime stratosphere under SPE conditions, active chlorine is expected to be mainly in the form of HOCl. Hence, ambient ClO should be reduced in contrast to the results obtained by von Clarmann et al. (2005) from MIPAS observations during the Halloween SPE. On the other hand, OH is the dominant HO_x constituent during daytime and HOCl is quickly photolyzed even at high solar zenith angles. ClO enhancements might hence occur in the illuminated stratosphere, if SPE-related HO_x increases were well above the background concentration. In fact, the ClO enhancements observed by MIPAS on 29–30 October 2003 (von Clarmann et al., 2005) took place outside the polar night region.

The mid-term evolution of polar ambient ClO during the period of the Halloween event is characterized by a continuous decrease related to seasonal variations (see Fig. 3) which makes the analysis of SPE-induced changes on a longer timescale difficult. Therefore, we restrict our analysis to the period of the main proton event on 29–31 October. Figure 32 shows observed and modeled changes of the ClO zonal mean distribution, averaged over these days, with respect to 26–27 October. ClO increases of ∼0.1 ppbv are found in the MIPAS observations at latitudes around 60° N in qualitative agreement with the previous analysis of von Clarmann et al. (2005). These enhancements are reproduced by none of the models. Evidently, simulated daytime HO_x increases are too small compared to the ambient HO_x abundances to alter noticeably the ClO availability. Although the observed enhancements are significant at the 2σ-level with respect to the average measurement precision (see Fig. 32, second panel), this important difference between the observations and the simulations should be carefully interpreted due to a possible systematic bias related to gain calibration errors in the measurements (see Sect. 2), particularly because the observed ClO change has been calculated from temporal averages belonging to different gain calibration periods. In the polar night region, both, observations and models show a ClO decrease. The observed ClO reduction of up to 0.2 ppbv is considerably underestimated by the simulations, except for CAO. The latter model overestimates the ClO reduction by approximately a factor of 10. The unreasonably large ClO depletion in CAO is related to a high ClO availability before

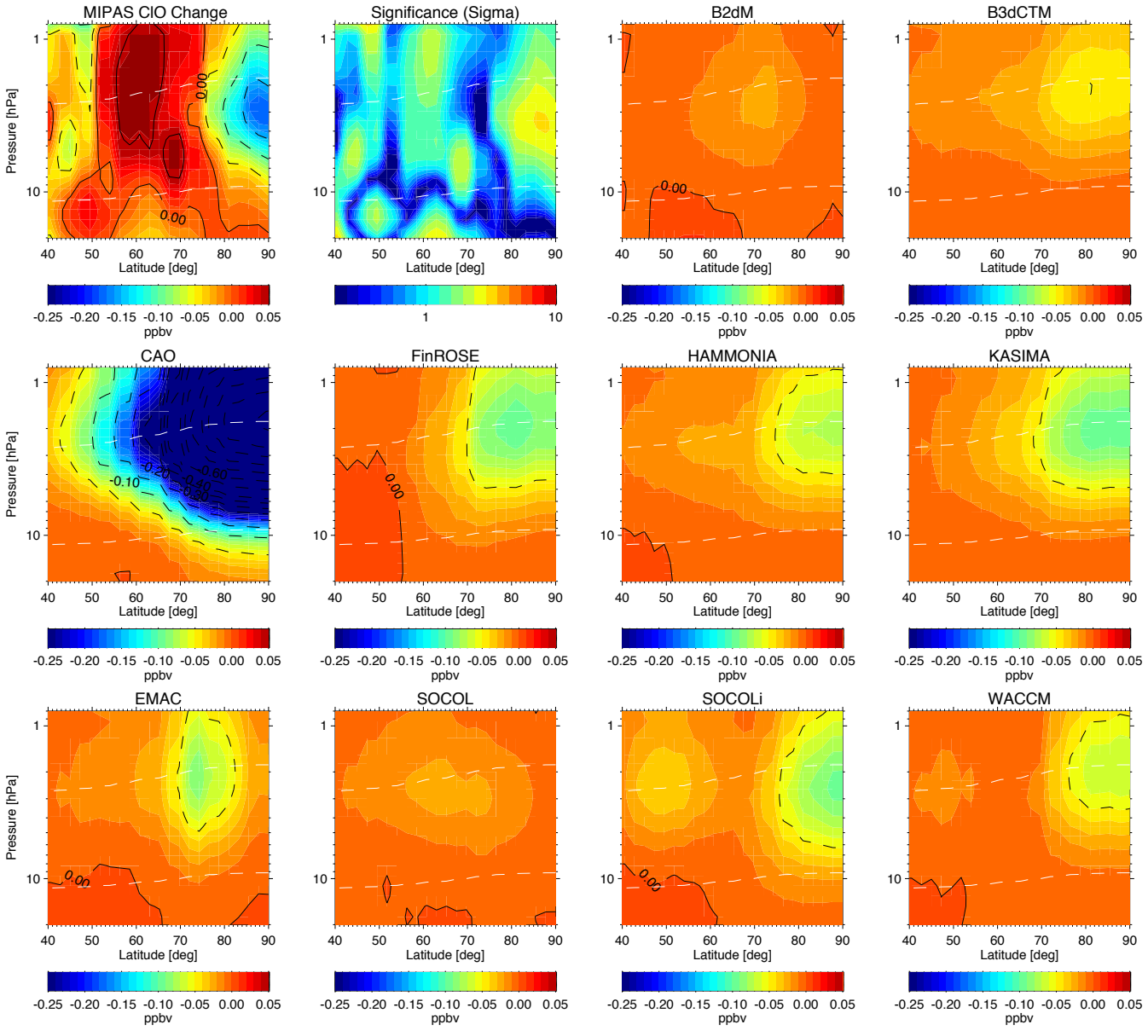

Fig. 32. Zonal mean ClO changes during the main proton forcing (29–31 October) with respect to 26–27 October in MIPAS observations and model simulations. Solid contour lines reflect 0.05 ppbv steps. The significance of observed ClO changes (in units of σ) is shown in the upper second panel (from the left).

the SPE and goes along with a $ClONO_2$ buildup of a similar magnitude (see below). The reason for the higher background ClO concentrations in this particular model is most probably related to the use of a family approach for ClO_y. In contrast to the observations, the ClO decreases obtained by B2dM, EMAC, and SOCOL are not pole-centered but shifted slightly to lower latitudes. The remaining models (except CAO) produce a very similar ClO signal.

The differences of observed and modeled ClO changes at latitudes poleward of 70° N are related to the background ClO abundances. Figure 33 shows the zonal mean distributions of ClO vmrs on 26–27 October prior to the onset of the proton forcing. ClO vmrs of more than 0.4 ppbv have been observed around 2 hPa in the entire NH with a slight decrease poleward of 70° N. Maximum abundances were found at 60–70° N, exactly at the same latitudes where the ClO increases during the following days occurred. Although we cannot exclude that the observed ClO in this latitude range is affected by gain calibration errors, this coincidence is somehow remarkable. In principle, the enhanced ClO abundances around 60–70° N can be related to differences in the latitudinal distributions of daytime OH and O, the first being responsible for ClO production and the latter for ClO removal.

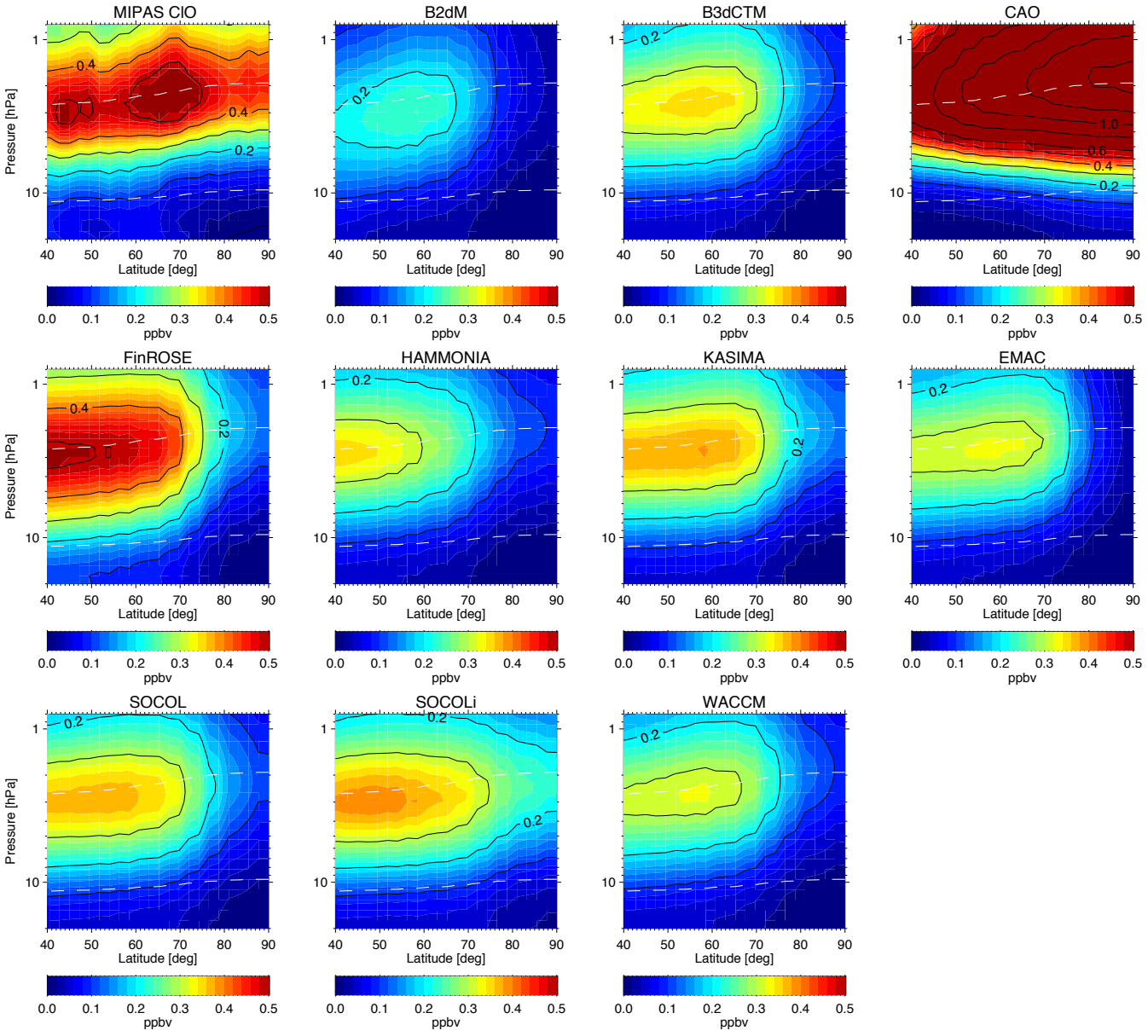

Fig. 33. Zonal mean ClO vmrs before the SPE 26–27 October in MIPAS observations and model simulations. Solid contour lines reflect 0.1 ppbv steps.

Modeled ClO abundances do not show this enhancement around 60–70° N. Simulated ClO vmrs are also generally lower by 50 % than those observed by MIPAS (except for FinROSE and CAO) and exhibit a pronounced decrease towards the polar night region. In some models (e.g. B2dM and EMAC) ClO has disappeared nearly completely at the pole. It is thus not surprising, that modeled ClO depletions at 70–90° N are less pronounced than in the observations in absolute terms. The much stronger modeled decrease of ClO towards the polar night region during pre-SPE conditions seems to be related to an overestimation of ClO losses. Since the sequestering into the Cl_2O_2 dimer is inefficient around 2 hPa and simulated HOCl or $ClONO_2$ distributions before the SPE do not indicate a conversion of ClO to these species, it is most likely that ClO is more efficiently converted to HCl than indicated by the observations. The faster conversion in the models might be related to the reaction path $ClO + OH \rightarrow HCl + O_2$ which has an uncertainty of its rate constant of several 100 % (Sander et al., 2006). However, also dynamical reasons (i.e. differences in the magnitude of meridional mixing) cannot be excluded.

The temporal evolution of observed and modeled HOCl changes at 70–90° N until mid November is shown in Fig. 34. HOCl started to increase rapidly on 29 October, reaching

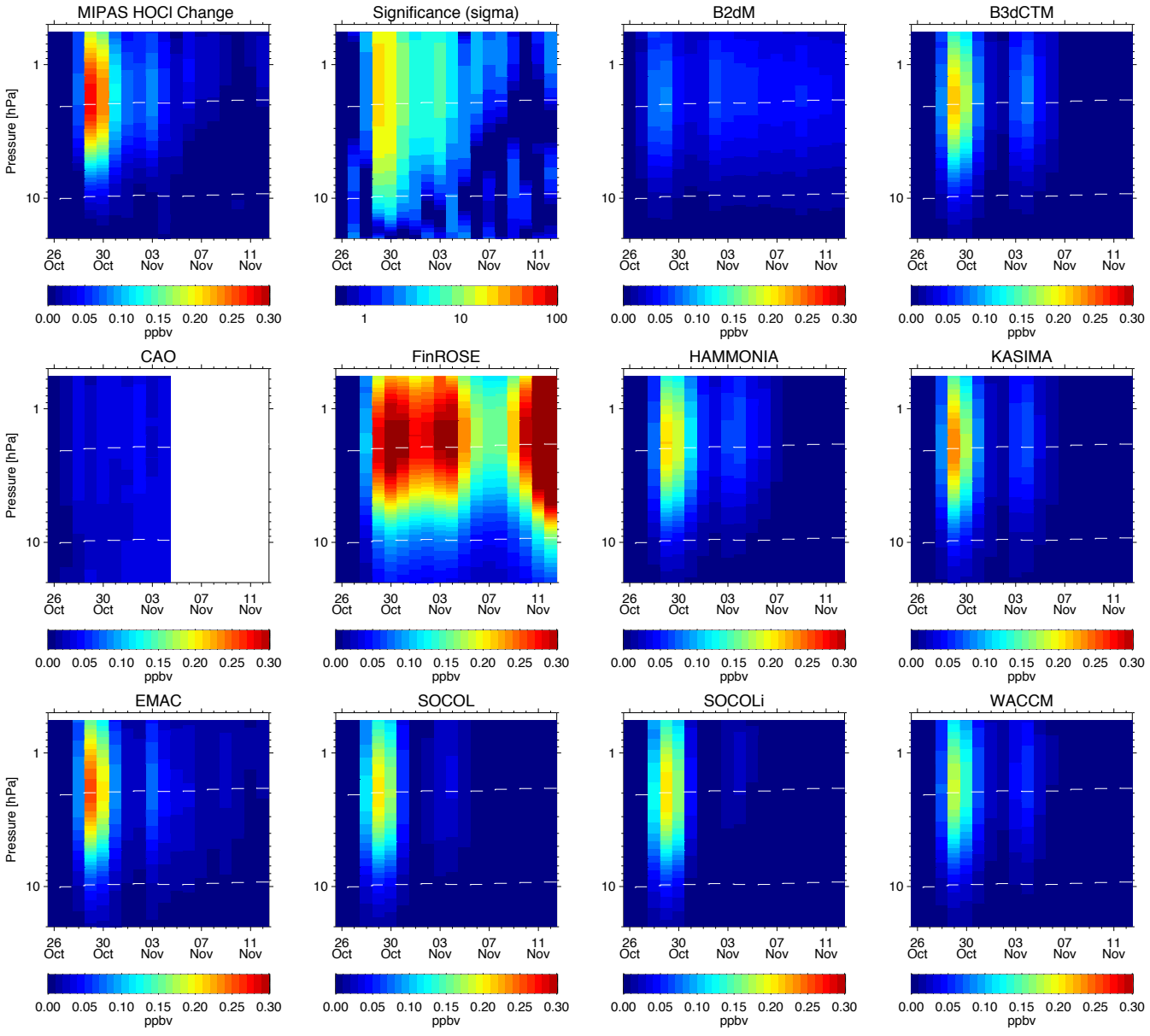

Fig. 34. Temporal evolution of area-weighterd averages of relative HOCl changes with respect to 26 October 2003 in MIPAS observations and model simulations at 70–90° N, as well as differences between modeled and observed averages. The significance of observed HOCl changes (in units of σ) is shown in the upper second panel (from the left).

values around 0.25 ppbv, and diminished after 1 November within a few days. A smaller second increase occurred on 3 November related to the second, weaker SPE. The simulations show generally smaller enhancements (approximately 30 % less on average), except FinROSE. This model overestimates significantly the observed enhancements by nearly a factor of 2. There, HOCl abundances remain enhanced after the SPE for nearly one week and show a second, even more pronounced enhancement around 11 November. A possible reason for the behavior of FinROSE could be the inclusion of the additional catalytic cycle

$$Cl + NO_2 + M \rightarrow ClNO_2 + M \quad \text{(R16)}$$

$$ClNO_2 + OH \rightarrow HOCl + NO_2, \quad \text{(R17)}$$

leading to additional HOCl production in the presence of NO_2.

Smallest HOCl enhancements are obtained by B2dM and CAO. In the former model, the smaller response seems to be related to the small latitudinal extent of the HOCl enhancements (as comes clear from Fig. 35), resulting in relatively low averages for the 70–90° N region. The small latitudinal extend in B2dM is related to a very strong but small

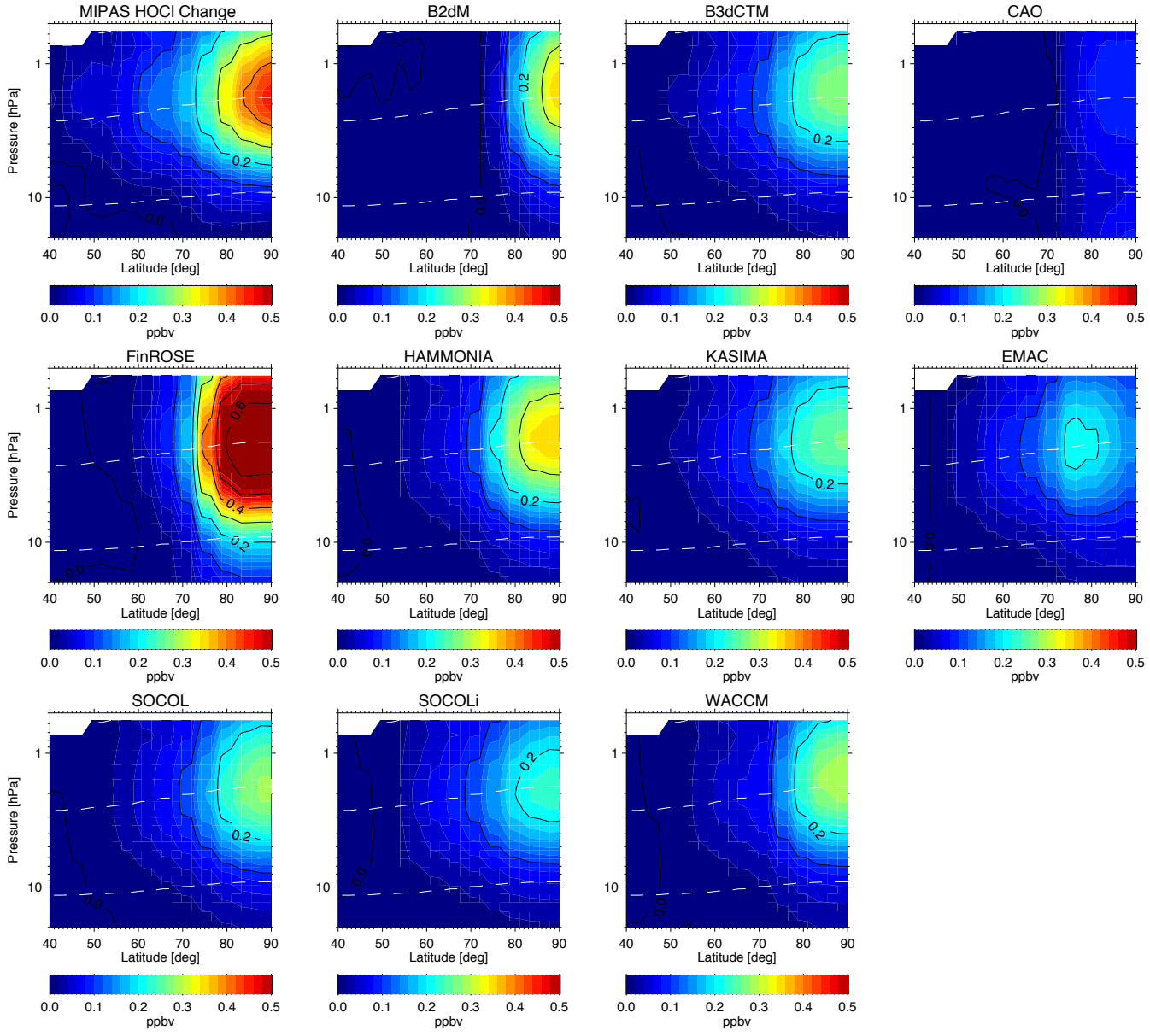

Fig. 35. Zonal mean HOCl changes during the main proton forcing (29–31 October) with respect to 26–27 October in MIPAS observations and model simulations. Solid contour lines reflect 0.1 ppbv steps.

vortex, probably as a result of the relatively poor horizontal resolution. Regarding the latter model, the small HOCl response is related to the unrealistic fast conversion of ClO to $ClONO_2$, compensating the increased HOCl buildup via Reaction (R14) by reduced ClO abundances.

Figure 35 shows observed and modeled changes of the HOCl zonal mean distribution averaged 29–31 October with respect to 26–27 October. The pronounced anti-correlation of HOCl increases and ClO decreases (compare Figs. 35 and 32) indicates that ambient ClO is quickly converted to HOCl via Reaction (R14) during nighttime in the presence of proton forcing. However, HOCl increases are higher than the corresponding ClO losses, resulting in a net increase of active chlorine by approximately 0.2 ppbv in the observations and most of the models. This can be explained by SPE-related chlorine activation via Reaction (R12). FinROSE, however, overestimates the chlorine activation by a factor of 3.

The sharp decline of the HOCl enhancements after the proton forcing observed by MIPAS, and also reproduced by most models, must occur in the sunlit atmosphere close to the polar night terminator, since losses via Reaction (R15) are negligible in the polar night stratosphere after the SPE. This is also the reason for the relatively long lifetime of the HOCl enhancements in B2dM where meridional redistribution is

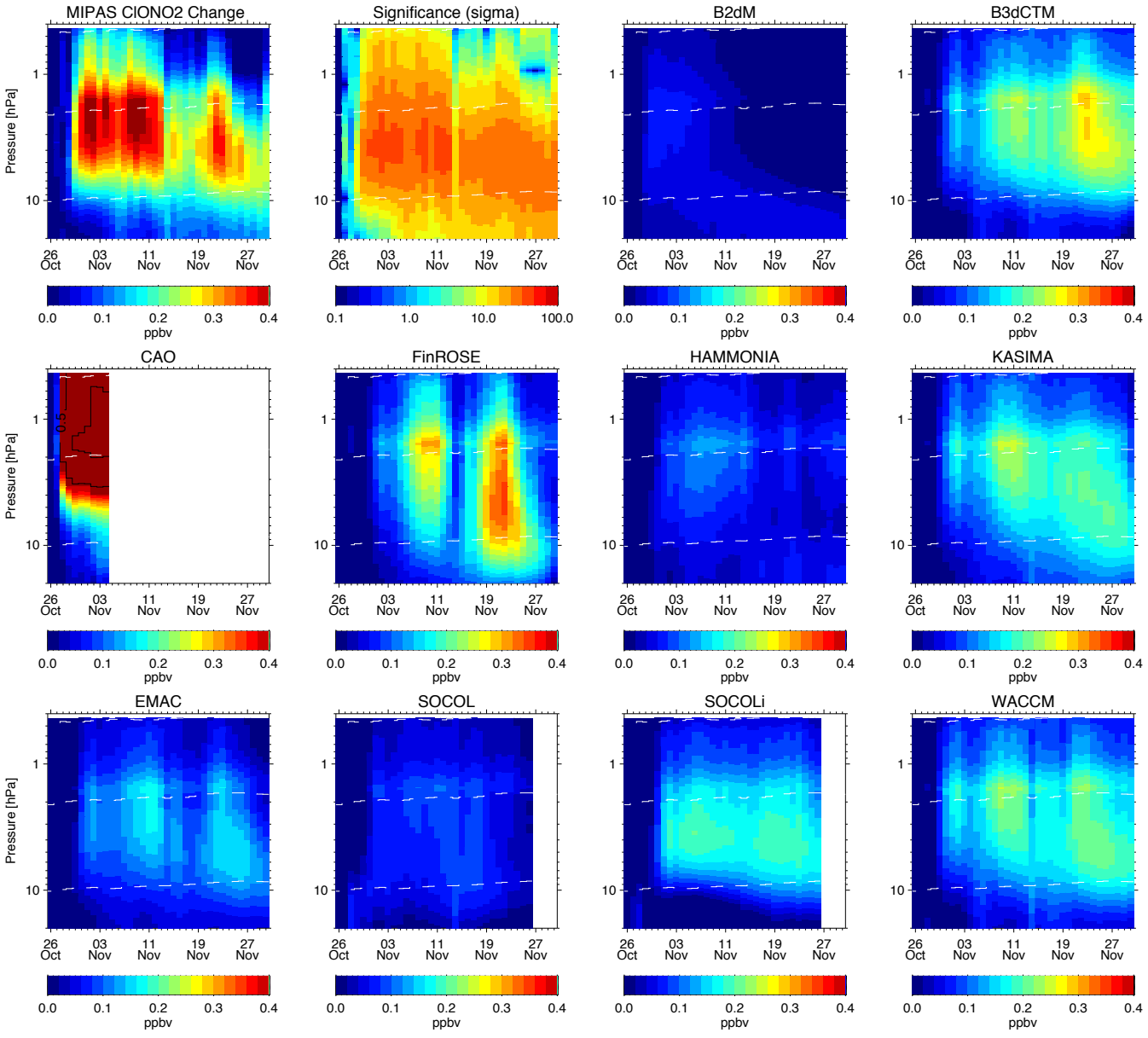

Fig. 36. Temporal evolution of area-weighted averages of relative $ClONO_2$ changes with respect to 26 October 2003 in MIPAS observations and model simulations at 70–90° N, as well as differences between modeled and observed averages. Contour lines reflect 0.5 ppbv steps. The significance of observed $ClONO_2$ changes (in units of σ) is shown in the upper second panel (from the left).

weak. This is not the case in the FinROSE model. There, the long lifetime of the HOCl enhancements related to the SPE, as well as the second buildup around 11 November, seem to be caused by an underestimation of chemical losses of HOCl.

$ClONO_2$ increases, occurring approximately two days after the SPE, are attributed to the termolecular reaction

$$ClO + NO_2 + M \rightarrow ClONO_2 + M. \quad \text{(R18)}$$

$ClONO_2$ is removed mainly by photolysis in the sunlit atmosphere and, to a lesser extent, by reaction with atomic oxygen. Due to its pressure dependence, $ClONO_2$ formation by Reaction (R18) is more effective at lower altitudes. Enhanced NO_2 availability related to the SPE, however, is increasing with altitude, leading to a peak height of the observed $ClONO_2$ enhancements around 3 hPa (∼36 km). This is slightly higher than reported by López-Puertas et al. (2005a) who based their analysis on an older MIPAS $ClONO_2$ data version than used here.

The temporal evolution of observed and modeled $ClONO_2$ changes at 70–90° N until the end of November is shown in Fig. 36. The observed enhancements of 0.4 ppbv after the SPE remained in the stratosphere for about two weeks.

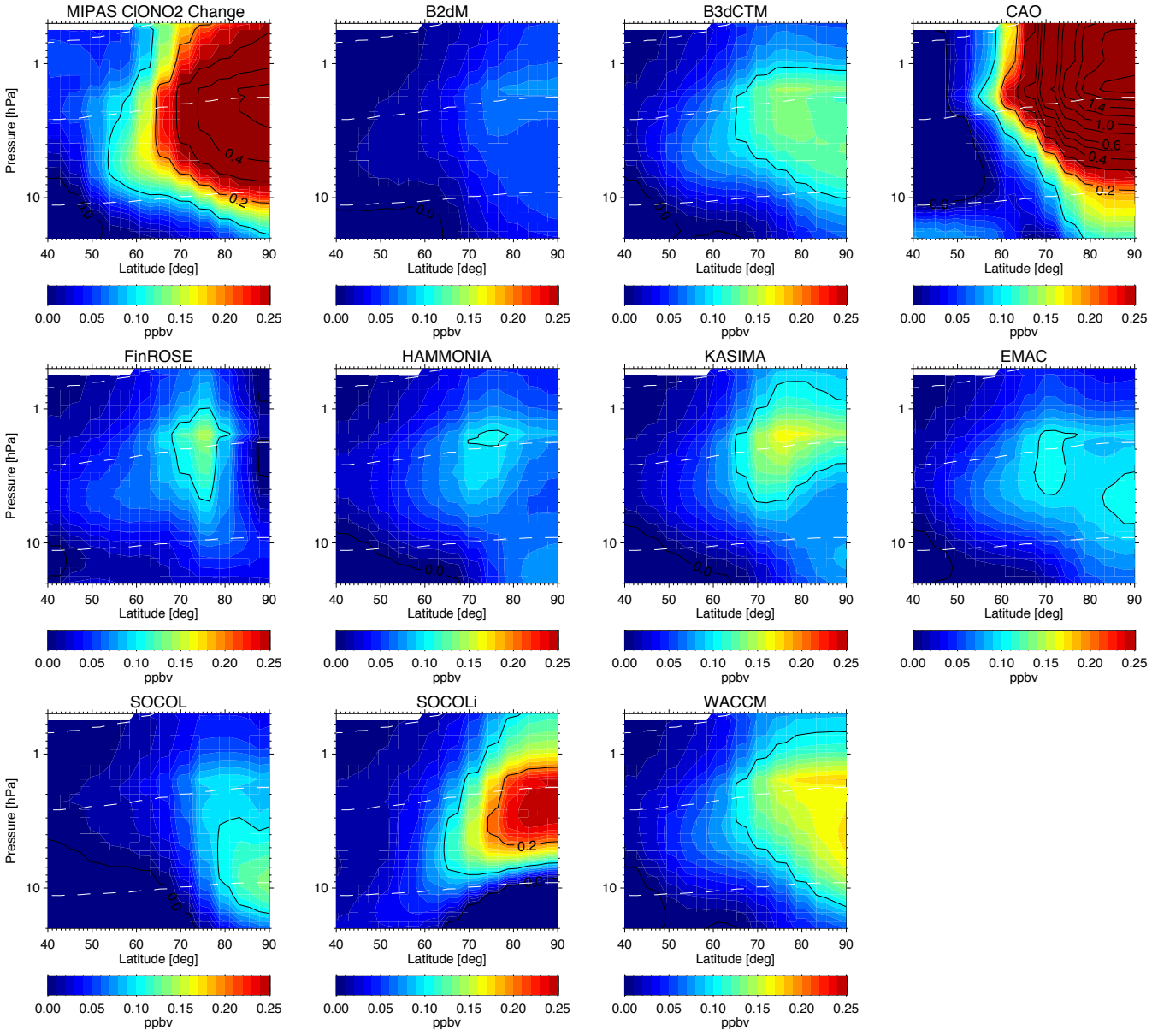

Fig. 37. Zonal mean $ClONO_2$ changes after the main proton forcing (1–5 November) with respect to 26–27 October in MIPAS observations and model simulations. Solid contour lines reflect 0.1 ppbv steps up to 0.6 ppbv and 0.2 ppbv steps above.

After a sudden decrease on 13 November, $ClONO_2$ abundances increased again on 19 November, reaching a second, weaker maximum around 22 November. The modeled $ClONO_2$ increases are generally smaller (except CAO, see discussion above) and show a different temporal evolution. The $ClONO_2$ underestimation in the simulations, particularly during the first enhancement starting on 1 November, is related to the reduced ClO availability compared to the observations. As an exception, CAO yields a quasi-instantaneous $ClONO_2$ increase with the onset of the proton forcing which can be explained by the use of a family approach for NO_y and ClO_y in this model.

Figure 37 shows the corresponding zonal mean distribution of the observed and modeled $ClONO_2$ enhancements averaged over 1–5 November. From the observations, it is clear that $ClONO_2$ is principally formed in the polar night region where high NO_2 abundances are available and no photochemical losses occur. Most of the model simulations, except CAO, SOCOLi and WACCM, show negligible enhancements there. Instead, $ClONO_2$ formation occurs around 70° N, were daytime losses are still small but ClO is available, however, with a considerably smaller magnitude than observed. SOCOLi and WACCM simulations, which have a similar latitudinal distribution of $ClONO_2$ changes as observed, exhibit

higher ClO abundances in the polar night region than other models.

The observed temporal evolution of the $ClONO_2$ changes in the second half of November is better captured by models based on ECMWF- and MERRA-driven meteorology up to the stratosphere (i.e. B3dCTM, FinROSE, KASIMA, and WACCM), which hints at a strong impact of vortex dynamics on the $ClONO_2$ abundances. Wave-driven vortex excursions to illuminated latitudes, alternated by reformation of a pole-centered vortex, are mainly responsible for the $ClONO_2$ variability and particularly for the decrease around 13 November. The descending NO_2 layer, formed during the SPE, acts as a reservoir for continuous $ClONO_2$ formation in the following weeks after the SPE. Due to the reduced ClO availability in the polar stratosphere towards the end of November, additional $ClONO_2$ buildup is observed only around 60–70° N, in agreement with most of the model results (not shown). B2dM, SOCOL, and HAMMONIA, however, show very small $ClONO_2$ increases in the second half of November. In the first model, this is related to the confinement of the NO_2 layer to high latitudes, where no ClO is available. In the latter model, strong meridional mixing led to a dilution of the SPE-generated NO_2 layer, such that insufficient NO_2 was available for additional $ClONO_2$ buildup.

7 Conclusions

We have compared stratospheric and mesospheric composition changes observed by MIPAS in the NH during and after the Halloween proton event with simulations performed with state-of-the-art GCMs and CTMs. The large number of models participating in the intercomparison exercise allowed for an evaluation of the overall ability of atmospheric models to reproduce observed atmospheric perturbations generated by SPEs, particularly with respect to NO_y and ozone changes. This model validation represents a mandatory first step towards an accurate implementation of particle precipitation effects in long-term climate simulations. It has also allowed to test and identify deficiencies in the chemical schemes, particularly with respect to nitrogen and chlorine chemistry, being relevant for stratospheric ozone.

Observed SPE-related short-time increases of the minor species HNO_4 and H_2O_2 have been identified for the first time and are qualitatively reproduced by the simulations. The observed enhancements of 0.2 and 0.1 ppbv, respectively, are overestimated by the models on average. Both observations and simulations give further evidence for an SPE-induced CO depletion. A clear isolation of these chemical losses from dynamical variability, however, is difficult.

In general, atmospheric models are able to reproduce most of the observed composition changes. In particular, simulated SPE-induced ozone losses agree within 5 % with the observations on average. This excellent agreement is found on a short-term scale (HO_x-driven) in the mesosphere, as well as on a mid-term scale (NO_x-driven) in the stratosphere. Simulated NO_y enhancements around 1 hPa are on average 30 % higher than indicated by the observations, while an underestimation of modeled NO_y of the same order was found in the mesosphere. The systematic behavior in the stratosphere suggests that these differences are related to the simulated ionization rate profile shape, though other error sources related to the models' atmospheric background state and/or transport schemes cannot be excluded. WACCM simulations without inclusion of electron-induced ionization allowed for distinguishing the electron and proton-related contributions to the NO_y enhancements. An upper stratospheric excess NO_y production by electron-induced ionization of 5–10 ppbv (20 % of the total SPE-induced production) could be identified from these simulations, particularly after the minor second event around 4–5 November. The excess ozone loss related to electron-induced ionization has been estimated to be around 5 %.

The impact of chemical NO losses due to reaction with atomic nitrogen (Reaction R2) on the SPE-induced NO_y increases has been studied in detail. An important dependence of the net NO_y generation on temperature and background NO_x due to this mechanism has been identified. In the stratosphere, SPE-related NO_y increases are reduced (enhanced) by approximately 10 % if temperatures were 10 K lower/higher. This behavior might be of relevance for future implications of SPE effects for climate when considering a stratospheric cooling trend related to climate change. The reduced NO_y production efficiency related to Reaction (R2) also implies limitations for models using family approaches in their chemical schemes, since this mechanism of NO_y destruction is not taken implicitly into account in these models.

The analysis of the observed and modeled NO_y partitioning in the aftermath of the Halloween SPE has clearly demonstrated the need to implement additional ion chemistry into the chemical schemes. Short-term HNO_3 increases can only be reproduced by model calculations including ion-ion recombination between NO_3^- and H^+ cluster ions (Verronen et al., 2008). The partitioning of HNO_3 and N_2O_5 in the following weeks after the SPE is significantly underestimated by the models that do not include HNO_3 formation via water cluster ions (Böhringer et al., 1983). However, further work is required to tune the parameterizations of these mechanisms such that quantitative agreement with the observations can be achieved.

The overestimation of observed H_2O_2 and HNO_4 enhancements by the models hints at an underestimation of the OH/HO_2 ratio in the upper polar stratosphere during the proton forcing. Further work is required to analyze in detail possible reasons for this behavior. The analysis of SPE-induced changes of the chlorine species ClO, HOCl and $ClONO_2$ has shown that the encountered differences between models and observations, particularly the underestimation of observed $ClONO_2$ enhancements, are related to a smaller availability of ClO in the polar region already before the SPE.

In general, the intercomparison has demonstrated that differences in the meteorology and/or initial state of the atmosphere in the simulations cause an important variability of the model results, even on a short timescale of only a few days. The model responses to the proton perturbation thus show a significant spread. On the other hand, this sensitivity of the simulated atmospheric responses to the background conditions, indicated by the spread in the model results, also implies that the real atmosphere's response to proton events depends strongly on the actual conditions.

Future HEPPA model-data intercomparison activities will focus on the assessment of indirect effects of energetic particle precipitation related to polar winter descent of upper atmospheric NO_x generated by electron precipitation. This is motivated, on one hand, by the higher potential of indirect effects to influence middle atmospheric composition on longer time scales compared to direct effects (i.e. SPEs) and, on the other hand, by its large variability related to dynamical modulations, making its representation in current atmospheric models challenging.

Acknowledgements. The IAA team was supported by the Spanish project AYA200803498/ESP and by the project 200950I081 of CSIC. The IMK, AIMOS, University of Bremen, and HAMMONIA groups were supported by the Priority Program CAWSES of the German science foundation (DFG). The input of CAO was supported by Russian Science Foundation for Basic Research (grant No. 09-05-009949) and by contract No. 1-6-08 under Russian Sub-Program "Research and Investigation of Antarctica". The SOCOLi team received funding from the European Community's Seventh Framework Programme (FP7/2007-2013) under grant agreement No. 218816. The development and applications of CCM SOCOL supported by the Swiss National Science Foundation under grant CRSI122-130642(FUPSOL). The WACCM team was supported by the NASA Living With a Star Targeted Research and Technology Program. The National Center for Atmospheric Research is sponsored by the National Science Foundation. We acknowledge the support of the German Climate Computing Center (DKRZ) where the HAMMONIA computations were performed. The authors gratefully acknowledge ESA for providing MIPAS spectra. The authors would also like to thank C. Randall and three anonymous reviewers for helpful comments and suggestions.

Edited by: W. Ward

References

Agostinelli, S., Allison, J., Amako, K., Apostolakis, J., Araujo, H., Arce, P., Asai, M., Axen, D., Banerjee, S., Barrand, G., Behner, F., Bellagamba, L., Boudreau, J., Broglia, L., Brunengo, A., Burkhardt, H., Chauvie, S., Chuma, S., Chytracek, R., Cooperman, G., and Cosmo, G.: GEANT4-a simulation toolkit, Nucl. Instr. Meth., 506, 250–303, doi:10.1016/S0168-9002(03)01368-8, 2003.

Baumgaertner, A. J. G., Jöckel, P., Riede, H., Stiller, G., and Funke, B.: Energetic particle precipitation in ECHAM5/MESSy – Part 2: Solar proton events, Atmos. Chem. Phys., 10, 7285–7302, doi:10.5194/acp-10-7285-2010, 2010.

Böhringer, H., Fahey, D. W., Fehsenfeld, F. C., and Ferguson, E. E.: The role of ion–molecule reactions in the conversion of N_2O_5 to HNO_3 in the stratosphere, Planet. Space. Sci., 31, 185–191, 1983.

Chipperfield, M. P. and Feng, W.: Comment on: Stratospheric Ozone Depletion at northern mid–latitudes in the 21st century: The importance of future concentrations of greenhouse gases nitrous oxide and methane, Geophys. Res. Lett., 30, 1389, doi:10.1029/2002GL016353, 2003.

Chipperfield, M. P. and Jones, R. L.: Relative influences of atmospheric chemistry and transport on Arctic ozone trends, Nature, 400, 551–554, 1999.

Chou, M.-D. and Suarez, M. J.: An Efficient Thermal Infrared Radiation Parameterization for Use in General Circulation Models, Technical Report Series on Global Modeling and Data Assimilation NASA/TM-1994-104606, vol. 9, Goddard Space Flight Center, Greenbelt, Maryland 20771, 1994.

Chou, M.-D. and Suarez, M. J.: A Solar Radiation Parameterization for Atmospheric Studies, Technical Report Series on Global Modeling and Data Assimilation NASA/TM-1999-104606, Vol. 15, Goddard Space Flight Center, Greenbelt, Maryland 20771, 1999.

Damiani, A., Diego, P., Laurenza, M., Storini, M., and Rafanelli, C.: Ozone variability related to several SEP events occurring during solar cycle no. 23, Adv. Space Res., 43, 28–40, doi:10.1016/j.asr.2008.06.006, 2008.

Damski, J., Thölix, L., Backman, L., Kaurola, J., Taalas, P., Austin, J., Butchart, N., and Kulmala, M.: A chemistry-transport model simulation of middle atmospheric ozone from 1980 to 2019 using coupled chemistry GCM winds and temperatures, Atmos. Chem. Phys., 7, 2165–2181, doi:10.5194/acp-7-2165-2007, 2007a.

Damski, J., Thölix, L., Backman, L., Taalas., P., and Kulmala, M.: FinROSE – middle atmospheric chemistry transport model, Boreal Env. Res., 12, 535–550, 2007b.

de Zafra, R. L. and Smyshlyaev, S. P.: On the formation of HNO_3 in the Antarctic mid to upper stratosphere in winter, J. Geophys. Res., 106, 23115–23125, doi:10.1029/2000JD000314, 2001.

Egorova, T., Rozanov, E., Zubov, V., Manzini, E., Schmutz, W., and Peter, T.: Chemistry-climate model SOCOL: a validation of the present-day climatology, Atmos. Chem. Phys., 5, 1557–1576, doi:10.5194/acp-5-1557-2005, 2005.

Egorova, T., Rozanov, E., Ozolin, Y., Shapiro, A., Calisto, M., Peter, T., and Schmutz, W.: The atmospheric effects of October 2003 solar proton event simulated with the chemistry-climate model SOCOL using complete and parameterized ion chemistry, J. Atmos. Solar-Terr. Phys., 73, 356–365, 2011.

Evans, D. and Greer, M.: Polar Orbiting Environmental Satellite Space Environment Monitor – 2: Instrument Descriptions and Archive Data Documentation, NOAA Technical Memorandum OAR SEC-93, Oceanic and Atmospheric Research Laboratories, Space Environment Center, Boulder, Colorado, 2000.

Fischer, H., Birk, M., Blom, C., Carli, B., Carlotti, M., von Clarmann, T., Delbouille, L., Dudhia, A., Ehhalt, D., Endemann, M., Flaud, J. M., Gessner, R., Kleinert, A., Koopman, R., Langen, J., López-Puertas, M., Mosner, P., Nett, H., Oelhaf, H., Perron, G., Remedios, J., Ridolfi, M., Stiller, G., and Zander, R.: MIPAS: an instrument for atmospheric and climate research, Atmos. Chem.

Phys., 8, 2151–2188, doi:10.5194/acp-8-2151-2008, 2008.

Fomichev, V. L., Blanchet, J.-P., and Turner, D. S.: Matrix parameterization of the 15 μm CO_2 band cooling in the middle and upper atmosphere for variable CO_2 concentration, J. Geophys. Res., 103, 11505–11528, doi:10.1029/98JD00799, 1998.

Funke, B., López-Puertas, M., Stiller, G. P., von Clarmann, T., and Höpfner, M.: A new non–LTE Retrieval Method for Atmospheric Parameters From MIPAS–ENVISAT Emission Spectra, Adv. Space Res., 27, 1099–1104, 2001.

Funke, B., López-Puertas, M., von Clarmann, T., Stiller, G. P., Fischer, H., Glatthor, N., Grabowski, U., Höpfner, M., Kellmann, S., Kiefer, M., Linden, A., Mengistu Tsidu, G., Milz, M., Steck, T., and Wang, D. Y.: Retrieval of stratospheric NO_x from 5.3 and 6.2 μm nonlocal thermodynamic equilibrium emissions measured by Michelson Interferometer for Passive Atmospheric Sounding (MIPAS) on Envisat, J. Geophys. Res., 110, D09302, doi:10.1029/2004JD005225, 2005.

Funke, B., López-Puertas, M., , Bermejo-Pantaleón, D., von Clarmann, T., Stiller, G. P., Höpfner, M., Grabowski, U., and Kaufmann, M.: Analysis of nonlocal thermodynamic equilibrium CO 4.7 μm fundamental, isotopic and hot band emissions measured by the Michelson Interferometer for Passive Atmospheric Sounding on Envisat, J. Geophys. Res., 112, D11305, doi:10.1029/2006JD007933, 2007.

Funke, B., García-Comas, M., López-Puertas, M., Glatthor, N., Stiller, G. P., von Clarmann, T., Semeniuk, K., and McConnell, J. C.: Enhancement of N_2O during the OctoberNovember 2003 solar proton events, Atmos. Chem. Phys., 8, 3805–3815, doi:10.5194/acp-8-3805-2008, 2008.

Funke, B., López-Puertas, M., García-Comas, M., Stiller, G. P., von Clarmann, T., Höpfner, M., Glatthor, N., Grabowski, U., Kellmann, S., and Linden, A.: Carbon monoxide distributions from the upper troposphere to the mesosphere inferred from 4.7 μm non-local thermal equilibrium emissions measured by MIPAS on Envisat, Atmos. Chem. Phys., 9, 2387–2411, doi:10.5194/acp-9-2387-2009, 2009.

Garcia, R. R., Marsh, D. R., Kinnison, D. E., Boville, B. A., and Sassi, F.: Simulation of secular trends in the middle atmosphere, J. Geophys. Res., 112, D09301, doi:10.1029/2006JD007485, 2007.

Glatthor, N., von Clarmann, T., Fischer, H., Grabowski, U., Höpfner, M., Kellmann, S., Kiefer, M., Linden, A., Milz, M., Steck, T., Stiller, G. P., Mengistu Tsidu, G., Wang, D. Y., and Funke, B.: Spaceborne ClO observations by the Michelson Interferometer for Passive Atmospheric Sounding (MIPAS) before and during the Antarctic major warming in September/October 2002, J. Geophys. Res., 109, D11307, doi:10.1029/2003JD004440, 2004.

Glatthor, N., von Clarmann, T., Fischer, H., Funke, B., Grabowski, U., Höpfner, M., Kellmann, S., Kiefer, M., Linden, A., Milz, M., Steck, T., Stiller, G. P., Mengistu Tsidu, G., and Wang, D. Y.: Mixing processes during the Antarctic vortex split in September/October 2002 as inferred from source gas and ozone distributions from ENVISAT-MIPAS, J. Atmos. Sci., 62, 787–800, 2005.

Gopalswamy, N., Yashiro, S., Michalek, G., Vourlidas, A., Kaiser, M. L., and Howard, R. A.: Coronal mass ejections and other extreme characteristics of the 2003 October–November solar eruptions, J. Geophys. Res., 110, A09S15, doi:10.1029/2004JA010958, 2005.

Heaps, M. G.: Parametrization of cosmic-ray ion-pair production-rate above 18 km, Planet. Space Sci., 26, 513–517, 1978.

Höpfner, M., von Clarmann, T., Fischer, H., Funke, B., Glatthor, N., Grabowski, U., Kellmann, S., Kiefer, M., Linden, A., Milz, M., Steck, T., Stiller, G. P., Bernath, P., Blom, C. E., Blumenstock, Th., Boone, C., Chance, K., Coffey, M. T., Friedl-Vallon, F., Griffith, D., Hannigan, J. W., Hase, F., Jones, N., Jucks, K. W., Keim, C., Kleinert, A., Kouker, W., Liu, G. Y., Mahieu, E., Mellqvist, J., Mikuteit, S., Notholt, J., Oelhaf, H., Piesch, C., Reddmann, T., Ruhnke, R., Schneider, M., Strandberg, A., Toon, G., Walker, K. A., Warneke, T., Wetzel, G., Wood, S., and Zander, R.: Validation of MIPAS $ClONO_2$ measurements, Atmos. Chem. Phys., 7, 257–281, doi:10.5194/acp-7-257-2007, 2007.

Jackman, C. H. and McPeters, R. D.: Solar Proton Events as Tests for the Fidelity of Middle Atmosphere Models, Physica Scripta., T18, 309–316, 1987.

Jackman, C. H., Fleming, E. L., and Vitt, F. M.: Influence of extremely large solar proton events in a changing stratosphere, J. Geophys. Res., 105, 11659–11670, 2000.

Jackman, C. H., DeLand, M. T., Labow, G. J., Fleming, E. L., Weisenstein, D. K., Ko, M. K. W., Sinnhuber, M., Anderson, J., and Russell, J. M.: The Influence of the Several Very Large Solar Proton Events in Years 2000–2003 on the Neutral Middle Atmosphere, Adv. Space Res., 35, 445–450, 2005a.

Jackman, C. H., DeLand, M. T., Labow, G. J., Fleming, E. L., Weisenstein, D. K., Ko, M. K. W., Sinnhuber, M., and Russell, J. M.: Neutral atmospheric influences of the solar proton events in October–November 2003, J. Geophys. Res., 110, A09S27, doi:10.1029/2004JA010888, 2005b.

Jackman, C. H., Marsh, D. R., Vitt, F. M., Garcia, R. R., Fleming, E. L., Labow, G. J., Randall, C. E., López-Puertas, M., Funke, B., von Clarmann, T., and Stiller, G. P.: Short- and medium-term atmospheric constituent effects of very large solar proton events, Atmos. Chem. Phys., 8, 765–785, doi:10.5194/acp-8-765-2008, 2008.

Jackman, C. H., Marsh, D. R., Vitt, F. M., Garcia, R. R., Randall, C. E., Fleming, E. L., and Frith, S. M.: Long-term middle atmospheric influence of very large solar proton events, J. Geophys. Res., 114, D11304, doi:10.1029/2008JD011415, 2009.

Jöckel, P., Sander, R., Kerkweg, A., Tost, H., and Lelieveld, J.: Technical Note: The Modular Earth Submodel System (MESSy) – a new approach towards Earth System Modeling, Atmos. Chem. Phys., 5, 433–444, doi:10.5194/acp-5-433-2005, 2005.

Jöckel, P., Tost, H., Pozzer, A., Brühl, C., Buchholz, J., Ganzeveld, L., Hoor, P., Kerkweg, A., Lawrence, M. G., Sander, R., Steil, B., Stiller, G., Tanarhte, M., Taraborrelli, D., van Aardenne, J., and Lelieveld, J.: The atmospheric chemistry general circulation model ECHAM5/MESSy1: consistent simulation of ozone from the surface to the mesosphere, Atmos. Chem. Phys., 6, 5067–5104, doi:10.5194/acp-6-5067-2006, 2006.

Kinnersley, J. S.: Interannual variability of stratospheric zonal wind forced by the northern lower-stratospheric large-scale waves, J. Atmos. Sci., 55, 2270–2283, 1998.

Kinnison, D. E., Brasseur, G. P., Walters, S., Garcia, R. R., Marsh, D. R., Sassi, F., Harvey, V. L., Randall, C. E., Emmons, L., Lamarque, J. F., Hess, P., Orlando, J. J., Tie, X. X., Randel, W., Pan, L. L., Gettelman, A., Granier, C., Diehl, T., Niemeier, U., and Simmons, A. J.: Sensitivity of chemical tracers to meteoro-

logical parameters in the MOZART-3 chemical transport model, J. Geophys. Res., 112, D20302, doi:10.1029/2006JD007879, 2007.

Klassen, A., Krucker, S., Kunow, H., Műller-Mellin, R., Wimmer-Schweingruber, R., Mann, G., and Posner, A.: Solar energetic electrons related to the 28 October 2003 flare, J. Geophys. Res., 110, A09S04, doi:10.1029/2004JA010910, 2005.

Kockarts, G.: Nitric oxide cooling in the terrestrial thermosphere, Geophys. Res. Lett., 7, 137–140, doi:10.1029/GL007i002p00137, 1980.

Kouker, W., Offermann, D., Küll, V., Reddmann, T., Ruhnke, R., and Franzen, A.: Streamers observed by the CRISTA experiment and simulated in the KASIMA model, J. Geophys. Res., 104, 16405–16418, 1999.

Krivolutsky, A. A. and Vyushkova, T. Y.: Three-dimensional photochemical transport model for the middle atmosphere (Basic variant), Scientific Report 1.3.2.15, Central Aerological Observatory, Russian Service for Hydrometeorology and Environmental Monitoring, 2002.

Krivolutsky, A. A., Kuminov, A. A., Repnev, A. I., Perejaslova, N. K., Nazarova, M. N., and Bazilevskay, G. A.: Model calculations of ozone response after solar proton event of November 1997, Geomagnetism and Aeronomy, 41, 243–252, 2001.

Krivolutsky, A. A., Klyuchnikova, A. V., Zakharov, G. R., Vyushkova, T. Y., and Kuminov, A. A.: Dynamical response of the middle atmosphere to solar proton event of July 2000: Three–dimensional model simulations, Adv. Space Res., 37, 1602–1613, doi:10.1016/j.asr.2005.05.115, 2006.

Kutepov, A. and Fomichev, V.: Application of the second-order escape probability approximation to the solution of the NLTE vibration-rotational band radiative transfer problem, J. Atmos. Terr. Phys., 55, 1–6, doi:10.1016/0021-9169(93)90148-R, http://www.sciencedirect.com/science/article/pii/002191699390148R, 1993.

Kylling, A., Albold, A., and Seckmeyer, G.: Transmittance of a cloud is wavelength – dependent in the UV-range: Physical interpretation, Geophys. Res. Lett., 24, 397–400, doi:10.1029/97GL00111, 1997.

López-Puertas, M., Funke, B., Gil-López, S., von Clarmann, T., Stiller, G. P., Höpfner, M., Kellmann, S., Fischer, H., and Jackman, C. H.: Observation of NO_x Enhancement and Ozone Depletion in the Northern and Southern Hemispheres after the October–November 2003 Solar Proton Events, J. Geophys. Res., 110, A09S43, doi:10.1029/2005JA011050, 2005a.

López-Puertas, M., Funke, B., Gil-López, S., von Clarmann, T., Stiller, G. P., Höpfner, M., Kellmann, S., Mengistu Tsidu, G., Fischer, H., and Jackman, C. H.: HNO_3, N_2O_5 and $ClONO_2$ Enhancements after the October–November 2003 Solar Proton Events, J. Geophys. Res., 110, A09S44, doi:10.1029/2005JA011051, 2005b.

Marsh, D., Smith, A., G-Brasseur, Kaufmann, M., and Grossmann, K.: The existence of a tertiary ozone maximum in the high-latitude middle mesosphere, Geophys. Res. Lett., 28, 4531–4534, 2001.

Marsh, D. R., Garcia, R. R., Kinnison, D. E., Boville, B. A., Sassi, F., Solomon, S. C., and Matthes, K.: Modeling the whole atmosphere response to solar cycle changes in radiative and geomagnetic forcing, J. Geophys. Res., 112, D23306, doi:10.1029/2006JD008306, 2007.

Mengistu Tsidu, G., von Clarmann, T., Stiller, G. P., Höpfner, M., Fischer, H., Glatthor, N., Grabowski, U., Kellmann, S., Kiefer, M., Linden, A., Milz, M., Steck, T., Wang, D.-Y., and Funke, B.: Stratospheric N_2O_5 in the austral spring 2002 as retrieved from limb emission spectra recorded by the Michelson Interferometer for Passive Atmospheric Sounding (MIPAS), J. Geophys. Res., 109, D18301, doi:10.1029/2004JD004856, 2004.

Minschwaner, K. and Siskind, D. E.: A new calculation of nitric oxide photolysis in the stratosphere, mesosphere, and lower thermosphere, J. Geophys. Res., 98, 20401–20412, 1993.

Morgenstern, O., Giorgetta, M. A., Shibata, K., Eyring, V., Waugh, D. W., Shepherd, T. G., Akiyoshi, H., Austin, J., Baumgaertner, A. J. G., Bekki, S., Braesicke, P., Brühl, C., Chipperfield, M. P., Cugnet, D., Dameris, M., Dhomse, S., Frith, S. M., Garny, H., Gettelman, A., Hardiman, S. C., Hegglin, M. I., Jöckel, P., Kinnison, D. E., Lamarque, J.-F., Mancini, E., Manzini, E., Marchand, M., Michou, M., Nakamura, T., Nielsen, J. E., Olivié, D., Pitari, G., Plummer, D. A., Rozanov, E., Scinocca, J. F., Smale, D., Teyssèdre, H., Toohey, M., Tian, W., and Yamashita, Y.: Review of the formulation of present-generation stratospheric chemistry-climate models and associated external forcings, J. Geophys. Res., 115, D00M02, doi:10.1029/2009JD013728, 2010.

Orsolini, Y. J., Manney, G. L., Santee, M. L., and Randall, C. E.: An upper stratospheric layer of enhanced HNO_3 following exceptional solar storms, Geophys. Res. Lett., 32, L12S01, doi:10.1029/2004GL021588, 2005.

Park, J. H., Ko, M. K. W., Jackman, C. H., Plumb, R. A., Kaye, J. A., and Sage, K. H. (Eds.): Models and Measurements Intercomparison II, NASA/TM-1999-209554, Langley Research Center, Hampton, Virginia, NASA-LARC, 1999.

Picone, J., Hedin, A., Drob, D., and Aikin, A.: NRLMSISE-00 empirical model of the atmosphere: Statistical comparisons and scientific issues, J. Geophys. Res., 107, 1468, doi:10.1029/2002JA009430, 2002.

Porter, H. S., Jackman, C. H., and Green, A. E. S.: Efficiencies for production of atomic nitrogen and oxygen by relativistic proton impact in air, J. Chem. Phys., 65, 154–167, doi:10.1063/1.432812, 1976.

Prather, M. J.: Numerical advection by conservation of second order moments, J. Geophys. Res., 91, 6671–6681, 1986.

Randall, C. E., Harvey, V. L., Manney, G. L., Orsolini, Y. J., Codrescu, M., Sioris, C., Brohede, S., Haley, C. S., Gordley, L. L., Zawodny, J. M., and Russell III, J. M.: Stratospheric effects of energetic particle precipitation in 2003–2004, Geophys. Res. Lett., 32, L05802, doi:10.1029/2004GL022003, 2005.

Reddmann, T., Ruhnke, R., Versick, S., and Kouker, W.: Modeling disturbed stratospheric chemistry during solar-induced NO_x enhancements observed with MIPAS/ENVISAT, J. Geophys. Res., 115, D00I11, doi:10.1029/2009JD012569, 2010.

Rienecker, M., Suarez, M., Todling, R., Bacmeister, J., Takacs, L., Liu, H.-C., Gu, W., Sienkiewicz, M., Koster, R., Gelaro, R., Stajner, I., and Nielsen, J.: The GEOS-5 Data Assimilation System Documentation of Versions 5.0.1, 5.1.0, and 5.2.0, Technical Report Series on Global Modeling and Data Assimilation, Volume 27 NASA/TM-2008-104606, vol. 27, Goddard Space Flight Center, Greenbelt, Maryland 20771, 2008.

Roble, R. G. and Ridley, E. C.: An auroral model for the NCAR thermospheric general circulation model (TGCM), Ann. Geophys., 5, 369–382, 1987.

Rodgers, C. D.: Inverse Methods for Atmospheric Sounding: Theory and Practice, vol. 2 of Series on Atmospheric, Oceanic and Planetary Physics, F. W. Taylor, ed., World Scientific, 2000.

Roeckner, E., Brokopf, R., Esch, M., Giorgetta, M., Hagemann, S., Kornblueh, L., Manzini, E., Schlese, U., and Schulzweida, U.: Sensitivity of Simulated Climate to Horizontal and Vertical Resolution in the ECHAM5 Atmosphere Model, J. Climate, 19, 3771–3791, 2006.

Rohen, G. J., von Savigny, C., Sinnhuber, M., Llewellyn, E. J., Kaiser, J. W., Jackman, C. H., Kallenrode, M.-B., Schrőter, J., Eichmann, K.-U., Bovensmann, H., and Burrows, J. P.: Ozone depletion during the solar proton events of October/November 2003 as seen by SCIAMACHY, J. Geophys. Res., 110, A09S39, doi:10.1029/2004JA010984, 2005.

Rusch, D. W., Gérard, J.-C., Solomon, S., Crutzen, P. J., and Reid, G. C.: The effect of particle precipitation events on the neutral and ion chemistry of the middle atmosphere. I – Odd nitrogen, Planet. Space Sci., 29, 767–774, 1981.

Sander, S. P., Friedl, R. R., Golden, D. M., Kurylo, M. J., Huie, R. E., Orkin, V. L., Moortgat, G. K., Kolb, C. E., Molina, M. J., and Ravishankara, A. R.: Chemical kinetics and photochemical data for use in atmospheric studies : Evaluation number 13, JPL Publication 00-3, Jet Propulsion Laboratory, California Institute of Technology, Pasadena, CA, 2000.

Sander, S. P., Finlayson-Pitts, B. J., Friedl, R. R., Golden, D. M., Huie, R. E., Kolb, C. E., Kurylo, M. J., Molina, M. J., Moortgat, G. K., Orkin, V. L., and Ravishankara, A. R.: Chemical kinetics and Photochemical Data for the Use in Atmospheric Studies. Evaluation Number 14, JPL publication 02-25, Jet Propulsion Laboratory, California Institute of Technology, Pasadena, CA, 2003.

Sander, S. P., Friedl, R. R., Ravishankara, A. R., Golden, D. M., Kolb, C. E., Kurylo, M. J., Molina, M. J., Moortgat, G. K., Keller-Rudek, H., Finlayson-Pitts, B. J., Wine, P., Huie, R. E., and Orkin, V. L.: Chemical kinetics and Photochemical Data for the Use in Atmospheric Studies. Evaluation Number 15, JPL publication 06-2, Jet Propulsion Laboratory, California Institute of Technology, Pasadena, CA, 2006.

Schmidt, H., Brasseur, G., Charron, M., Manzini, E., Giorgetta, M., Diehl, T., Formichev, V., Kinnison, D., Marsh, D., and Walters, S.: The HAMMONIA chemistry climate model: sensitivity of the mesopause region to the 11-year solar cycle and CO_2 doubling, J. Climate, 19, 3903–3931, 2006.

Schraner, M., Rozanov, E., Schnadt Poberaj, C., Kenzelmann, P., Fischer, A. M., Zubov, V., Luo, B. P., Hoyle, C. R., Egorova, T., Fueglistaler, S., Brönnimann, S., Schmutz, W., and Peter, T.: Technical Note: Chemistry-climate model SOCOL: version 2.0 with improved transport and chemistry/microphysics schemes, Atmos. Chem. Phys., 8, 5957–5974, doi:10.5194/acp-8-5957-2008, 2008.

Seppälä, A., Verronen, P. T., Kyrölä, E., Hassinen, S., Backman, L., Hauchecorne, A., Bertaux, J. L., and Fussen, D.: Solar proton events of October–November 2003: Ozone depletion in the Northern Hemisphere winter as seen by GOMOS/Envisat, Geophys. Res. Lett., 31, L19107, doi:10.1029/2004GL021042, 2004.

Shine, K.: The middle atmosphere in the absence of dynamical heat fluxes, Q. J. Roy. Meteorol. Soc., 113, 603–633, 1987.

Simmons, A., Uppala, S., Dee, D., and Kobayashi, S.: ERA-Interim: New ECMWF reanalysis products from 1989 onwards, ECMWF Newsletter 110 – Winter 2006/07, Data Services ECMWF, Shinfield Park, Reading, UK, 2006.

Sinnhuber, M., Burrows, J. P., Chipperfield, M. P., Jackman, C. H., Kallenrode, M.-B., Künzi, K. F., and Quack, M.: A model study of the impact of magnetic field structure on atmospheric composition during solar proton events, Geophys. Res. Lett., 30, 1818, doi:10.1029/2003GL017265, 2003a.

Sinnhuber, B.-M., Weber, M., Amankwah, A., and Burrows, J. P.: Total Ozone during the unusual Antarctic winter of 2002, Geophys. Res. Lett., 30, 1580, doi:10.1029/2002GL016798, 2003b.

Sinnhuber, B.-M., Sheode, N., Sinnhuber, M., Chipperfield, M. P., and Feng, W.: The contribution of anthropogenic bromine emissions to past stratospheric ozone trends: a modelling study, Atmos. Chem. Phys., 9, 2863–2871, doi:10.5194/acp-9-2863-2009, 2009.

Solomon, S. and Crutzen, P. J.: Analysis of the August 1972 Solar Proton Event Including Chlorine Chemistry, J. Geophys. Res., 86, 1140–1146, 1981.

Solomon, S. C. and Qian, L.: Solar extreme-ultraviolet irradiance for general circulation models, J. Geophys. Res., 110, A10306, doi:10.1029/2005JA011160, 2005.

Solomon, S., Rusch, D. W., Gérard, J.-C., Reid, G. C., and Crutzen, P. J.: The effect of particle precipitation events on the neutral and ion chemistry of the middle atmosphere. II - Odd hydrogen, Planet. Space Sci., 29, 885–892, 1981.

Steck, T., von Clarmann, T., Fischer, H., Funke, B., Glatthor, N., Grabowski, U., Hpfner, M., Kellmann, S., Kiefer, M., Linden, A., Milz, M., Stiller, G. P., Wang, D. Y., Allaart, M., Blumenstock, Th., von der Gathen, P., Hansen, G., Hase, F., Hochschild, G., Kopp, G., Kyrö, E., Oelhaf, H., Raffalski, U., Redondas Marrero, A., Remsberg, E., Russell III, J., Stebel, K., Steinbrecht, W., Wetzel, G., Yela, M., and Zhang, G.: Bias determination and precision validation of ozone profiles from MIPAS-Envisat retrieved with the IMK-IAA processor, Atmos. Chem. Phys., 7, 3639–3662, doi:10.5194/acp-7-3639-2007, 2007.

Stiller, G. P., von Clarmann, T., Brühl, C., Fischer, H., Funke, B., Glatthor, N., Grabowski, U., Höpfner, M., Jöckel, P., Kellmann, S., Kiefer, M., Linden, A., Lòpez-Puertas, M., Mengistu Tsidu, G., Milz, M., Steck, T., and Steil, B.: Global distributions of HO_2NO_2 as observed by the Michelson Interferometer for Passive Atmospheric Sounding (MIPAS), J. Geophys. Res., 112, D09314, doi:10.1029/2006JD007212, 2007.

Stiller, G. P., von Clarmann, T., Höpfner, M., Glatthor, N., Grabowski, U., Kellmann, S., Kleinert, A., Linden, A., Milz, M., Reddmann, T., Steck, T., Fischer, H., Funke, B., López-Puertas, M., and Engel, A.: Global distribution of mean age of stratospheric air from MIPAS SF_6 measurements, Atmos. Chem. Phys., 8, 677–695, doi:10.5194/acp-8-677-2008, 2008.

Strobel, D. F.: Parametrization of the Atmospheric Heating Rate from 15 to 120 km due to O_2 and O_3 Absorption of Solar Radiation, J. Geophys. Res., 83, 6225–6230, 1978.

Swinder, W. and Gardner, M. E.: On the accuracy of certain approximations for the Chapman function, in: Environmental Research Papers No. 272, Air Force Cambridge Research, Bedford, MA, USA, 1967.

Tikhonov, A.: On the solution of incorrectly stated problems and method of regularization, Dokl. Akad. Nauk. SSSR, 151, 501–504, 1963.

Turco, R. P. and Whitten, R. C.: A comparison of sev-

eral computational techniques for solving some common aeronomic problem, J. Geophys. Res., 79, 3179–3185, doi:10.1029/JA079i022p03179, 1974.

Verronen, P. T., Seppälä, A., Kyrölä, E., Tamminen, J., Pickett, H. M., and Turunen, E.: Production of odd hydrogen in the mesosphere during the January 2005 solar proton event, Geophys. Res. Lett., 33, L24811, doi:10.1029/2006GL028115, 2006.

Verronen, P. T., Funke, B., López-Puertas, M., Stiller, G. P., von Clarmann, T., Enell, C.-F., Turunen, E., and Tamminen, J.: About the Increase of HNO_3 in the Stratopause Region During the Halloween 2003 Solar Proton Event, Geophys. Res. Lett., 35, L20809, doi:10.1029/2008GL035312, 2008.

Versick, S.: Ableitung von H_2O_2 aus MIPAS/ENVISAT-Beobachtungen und Untersuchung der Wirkung von energetischen Teilchen auf den chemischen Zustand der mittleren Atmosphre, Ph.D. thesis, Karlsruhe, Karlsruher Institut für Technologie (KIT), urn:nbn:de:swb:90-197769, 2010.

von Clarmann, T., Glatthor, N., Grabowski, U., Höpfner, M., Kellmann, S., Kiefer, M., Linden, A., Mengistu Tsidu, G., Milz, M., Steck, T., Stiller, G. P., Wang, D. Y., Fischer, H., Funke, B., Gil-López, S., and López-Puertas, M.: Retrieval of temperature and tangent altitude pointing from limb emission spectra recorded from space by the Michelson Interferometer for Passive Atmospheric Sounding (MIPAS), J. Geophys. Res., 108, 4736, doi:10.1029/2003JD003602, 2003.

von Clarmann, T., Glatthor, N., Höpfner, M., Kellmann, S., Ruhnke, R., Stiller, G. P., Fischer, H., Funke, B., Gil-López, S., and López-Puertas, M.: Experimental Evidence of Perturbed Odd Hydrogen and Chlorine Chemistry After the October 2003 Solar Proton Events, J. Geophys. Res., 110, A09S45, doi:10.1029/2005JA011053, 2005.

von Clarmann, T., Glatthor, N., Grabowski, U., Höpfner, M., Kellmann, S., Linden, A., Mengistu Tsidu, G., Milz, M., Steck, T., Stiller, G. P., Fischer, H., and Funke, B.: Global stratospheric HOCl distributions retrieved from infrared limb emission spectra recorded by the Michelson Interferometer for Passive Atmospheric Sounding (MIPAS), J. Geophys. Res., 111, D05311, doi:10.1029/2005JD005939, 2006.

Wang, D. Y., Höpfner, M., Blom, C. E., Ward, W. E., Fischer, H., Blumenstock, T., Hase, F., Keim, C., Liu, G. Y., Mikuteit, S., Oelhaf, H., Wetzel, G., Cortesi, U., Mencaraglia, F., Bianchini, G., Redaelli, G., Pirre, M., Catoire, V., Huret, N., Vigouroux, C., De Mazière, M., Mahieu, E., Demoulin, P., Wood, S., Smale, D., Jones, N., Nakajima, H., Sugita, T., Urban, J., Murtagh, D., Boone, C. D., Bernath, P. F., Walker, K. A., Kuttippurath, J., Kleinböhl, A., Toon, G., and Piccolo, C.: Validation of MIPAS HNO_3 operational data, Atmos. Chem. Phys., 7, 4905–4934, doi:10.5194/acp-7-4905-2007, 2007.

Winkler, H., Sinnhuber, M., Notholt, J., Kallenrode, M.-B., Steinhilber, F., Vogt, J., Zieger, B., Glassmeier, K.-H., and Stadelmann, A.: Modeling impacts of geomagnetic field variations on middle atmospheric ozone responses to solar proton events on long timescales, J. Geophys. Res., 113, D02302, doi:10.1029/2007JD008574, 2008.

Winkler, H., Kazeminejad, S., Sinnhuber, M., Kallenrode, M.-B., and Notholt, J.: Conversion of mesospheric HCl into active chlorine during the solar proton event in July 2000 in the northern polar region, J. Geophys. Res., 114, D00I03, doi:10.1029/2008JD011587, 2009.

Wissing, J. M. and Kallenrode, M.-B.: Atmospheric Ionization Module OSnabrück (AIMOS) 1: A 3D model to determine atmospheric ionization by energetic charged particles from different populations, J. Geophys. Res., A06104, doi:10.1029/2008JA013884, 2009.

WMO: SPARC Report on the Evaluation of Chemistry-Climate Models, SPARC Report No. 5, WCRP-132, WMO/TD-No. 1526, 2010.

PUBL. III

Reprinted, with permission, from
Journal of Geophysical Research: Atmospheres, 118, 6837-6848,
doi:10.1002/jgrd.50486

JOURNAL OF GEOPHYSICAL RESEARCH: ATMOSPHERES, VOL. 118, 6837–6848, doi:10.1002/jgrd.50486, 2013

Observed effects of solar proton events and sudden stratospheric warmings on odd nitrogen and ozone in the polar middle atmosphere

S.-M. Päivärinta,[1] A. Seppälä,[1] M. E. Andersson,[1] P. T. Verronen,[1] L. Thölix,[1] and E. Kyrölä[1]

Received 14 December 2012; revised 10 May 2013; accepted 11 May 2013; published 26 June 2013.

[1] Here we use satellite observations from the ACE-FTS, MLS/Aura and SABER/TIMED to study the effects of solar proton events (SPEs) and strong sudden stratospheric warmings (SSWs) on the middle atmospheric odd nitrogen (NO_x) and ozone levels in the Northern Hemispheric polar region. Three winters (January–March) are considered: (1) 2005 (SPE), (2) 2009 (SSW), and (3) 2012 (SPEs and SSW). These different cases provide a good opportunity to study the roles that transport from the mesosphere-lower thermosphere region and in situ production due to particle precipitation have on stratospheric NO_x levels and the consequent effects on the middle atmospheric ozone. The observations show increases in NO_x after both the SPEs (days to weeks) and SSWs (weeks to months) by up to a factor of 25 between 40 and 90 km. The largest mesospheric NO_x increases are observed following the SSW in late January 2009, but the most substantial effects in the upper stratosphere are seen when both an SSW and in situ production by SPEs take place (2012), even though the in situ NO_x production in 2012 was relatively weak in magnitude compared to periods of much higher solar activity. In 2012, both short-term (days, due to SPEs and odd hydrogen) depletion and longer-term (months, due to several drivers) depletion of ozone of up to 90% are observed in the mesosphere and upper stratosphere, coinciding with the enhanced amounts of NO_x.

Citation: Päivärinta, S.-M., A. Seppälä, M. E. Andersson, P. T. Verronen, L. Thölix, and E. Kyrölä (2013), Observed effects of solar proton events and sudden stratospheric warmings on odd nitrogen and ozone in the polar middle atmosphere, *J. Geophys. Res. Atmos.*, *118*, 6837–6848, doi:10.1002/jgrd.50486.

1. Introduction

[2] Odd nitrogen ($NO_x = N + NO + NO_2$) is constantly produced in the lower thermosphere by solar EUV (extreme ultraviolet) radiation, soft X-rays, and energetic particles, i.e., auroral electrons [*Barth*, 1992]. In polar winter, in the absence of solar radiation, the chemical lifetime of NO_x is long and therefore the upper atmospheric NO_x can be transported inside the polar vortex to the middle atmosphere. *Solomon et al*. [1982] showed that if the descent continues down to stratospheric altitudes, NO_x can have an effect not only on the stratospheric NO_x amounts but also on ozone by destruction in catalytic chemical cycles. Mesospheric production of NO_x by energetic particle precipitation (proton and electron precipitation) can have an important role in intensifying the mesosphere-lower thermosphere (MLT) to stratosphere NO_x connection since the downward transport of thermospheric air masses through the mesopause (at ~90–100 km) is hindered by the wintertime upper atmospheric circulation patterns [*Smith et al*., 2011]. Stratospheric conditions are known to have an influence on the troposphere through top-down coupling [*Baldwin and Dunkerton*, 2001], and it has recently been suggested that changes in mesospheric-stratospheric NO_x and ozone concentrations could modulate the polar surface air temperatures by affecting the radiative budget and, through that, atmospheric circulation patterns [*Seppälä et al*., 2009; *Baumgaertner et al*., 2011].

[3] *Callis et al*. [1991a] studied the link between energetic particle precipitation, especially electrons, and stratospheric NO_x and ozone. They used satellite observations and a two-dimensional model to show that a connection between energetic particle precipitation and the middle and lower atmosphere exists. Further studies [e.g., *Callis et al*., 1991b; *Callis et al*., 1996a, 1996b; *Callis*, 1997; *Callis and Lambeth*, 1998] gave some indication that electron precipitation can, in fact, provide a significant source of NO_x between the upper stratosphere and mesosphere and that significant amounts of stratospheric ozone can be destroyed due to the enhanced NO_x concentrations. However, no strong conclusions on the long-term effects could be made due to scarcity of the observations.

[4] The NO_x connection between the MLT and stratosphere can be intensified by solar proton events (SPEs) and sudden stratospheric warmings (SSWs). SPEs are caused by

[1]Earth Observation Finnish Meteorological Institute, Helsinki, Finland.

Corresponding author: S.-M. Päivärinta, Earth Observation, Finnish Meteorological Institute, PO Box 503, Helsinki 00280, Finland. (sanna-mari.paivarinta@fmi.fi)

2169-897X/13/10.1002/jgrd.50486

large eruptions like coronal mass ejections in the Sun. During these eruptions, protons and heavier ions are emitted from the Sun and, when directed toward the Earth, are guided by the Earth's magnetic field to the polar regions where they precipitate into the atmosphere. SPEs occur on a sporadic basis but are more frequent during periods near solar maximum [*Jackman et al*., 2009]. SPEs have a direct effect in the mesosphere and stratosphere where they produce NO_x and odd hydrogen ($HO_x = H + OH + HO_2$) in situ through dissociation and dissociative ionization of neutral molecules (primarily N_2) in the atmosphere [e.g., *Jackman et al*., 2000; *López-Puertas et al*., 2005; *Seppälä et al*., 2004; *Verronen et al*., 2005; *Jackman et al*., 2008; *Seppälä et al*., 2008]. For example, the Halloween 2003 SPEs increased NO_x concentrations by an order of magnitude above 40 km, which lead to an ozone decrease of 20–60% over a period of several weeks [*Seppälä et al*., 2004]. Depending on the season, NO_x produced by the SPEs may influence the middle atmospheric chemistry for months or even years [*Jackman et al*., 2009]. SSWs, on the other hand, can intensify the downward transportation of NO_x from the MLT region to the stratosphere. Sudden stratospheric warming events are caused by vertically propagating planetary waves interacting with the zonal winds, leading to the breakdown or displacement of the polar vortex [*Matsuno*, 1971]. SSW events mainly occur in the Northern Hemisphere (NH) due to larger planetary wave activity. On average, an SSW event takes place about once every other winter. When the stratopause reforms after the SSW event, a period of strong downward transport of mesospheric and upper stratospheric air can take place, intensifying the descent inside the polar vortex.

[5] Several previous studies have discussed the MLT to stratosphere descent of NO_x and the possible influence on stratospheric ozone [e.g., *Funke et al*., 2005; *Randall et al*., 2006, 2009; *Funke et al*., 2011; *Salmi et al*., 2011; *von Clarmann et al*., 2013], but the roles of SPEs and SSWs as an NO_x source are still unclear. In the NH, NO_x descent events have been reported for early 2004, 2006, and 2009 [*Randall et al*., 2006, 2009]. Simultaneous ozone loss due to NO_x chemistry has been reported for the 2004 case [e.g., *Randall et al*., 2005; *Clilverd et al*., 2006, 2009]. The large NO_x amounts in the middle atmosphere in 2004 were most likely a result of the combined effects of increased particle precipitation from the massive SPEs in late 2003 and electron precipitation in early 2004 [*Clilverd et al*., 2009; *Semeniuk et al*., 2005] and the strong dynamical events following the December 2003 SSW [*Funke et al*., 2007; *Hauchecorne et al*., 2007].

[6] The aim of this investigation is to study the effects of SPEs and SSWs on middle atmospheric NO_x and ozone using satellite observations from the ACE-FTS, MLS/Aura, and SABER/TIMED. For our analysis, we have chosen the events that took place early in the years 2005, 2009, and 2012 because of their different characteristics: (1) SPEs occurred in 2005 and 2012 and (2) SSWs in 2009 and 2012. Other studies have also previously discussed the years 2005 (one SPE) [e.g., *Seppälä et al*., 2006; *Jackman et al*., 2011] and 2009 (a SSW event) [e.g., *Randall et al*., 2009; *Salmi et al*., 2011], and recently, *von Clarmann et al*. [2013] reported atmospheric responses to the 2012 SPEs. In this study we will contrast these three years with very different conditions while providing additional attention to year 2012, as this was a special case when several SPEs and a SSW took place, providing optimal conditions for the NO_x connection between MLT and the stratosphere to occur.

2. Data Description

2.1. ACE-FTS

[7] The ACE (Atmospheric Chemistry Experiment) satellite is a Canadian-led mission and was launched into low Earth circular orbit in 2003 [*Bernath et al*., 2005]. The satellite, also known as SCISAT-1, carries two instruments: FTS (Fourier Transform Spectrometer) and MAESTRO (Measurement of Aerosol Extinction in the Stratosphere and Troposphere Retrieved by Occultation). The FTS instrument is the primary instrument of the satellite and provides the main data (NO_x and O_3) used in this study. The ACE-FTS is a high spectral resolution instrument measuring the vertical distribution of trace gases and temperature. The measurements are carried out during sunset and sunrise, leading to a limited latitudinal coverage (Figure 1). The vertical resolution is about 4 km, covering the altitude range from the cloud tops up to about 150 km. We do not use any observations from the Southern Hemispheric polar region for this study as the number of observations in that area was very low during our study periods. In our analysis, we combined sunrise and sunset data neglecting possible NO_x asymmetry due to nighttime N_2O_5 buildup. However, this should make no significant impact on our results, because we only consider altitudes above 35 km where the N_2O_5 amounts are typically only a small fraction of those of NO_x.

[8] Measurement errors for NO_x vary with altitude and time. Below 25 km, the errors are over $\pm$40% and are hence not used. Between 25 and 45 km, the errors are quite small ($<$20%) but increase above 45 km ($>$20%). For NO and NO_2 separately, the errors are generally below 30% and 4–20% at around 50 km, respectively. The NO measurements become more unreliable with increasing altitude. For ozone, the errors are below 5% between 10–65 km and 85–95 km but can increase to $>$100% between these two regions (75–85 km).

2.2. MLS

[9] The Microwave Limb Sounder (MLS) instrument on board NASA's EOS Aura satellite was launched in 2004 and placed into a Sun-synchronous orbit at about 705 km altitude [*Waters et al*., 2006]. MLS observes thermal microwave emissions, scanning from the ground to 90 km every 25 s with daily global coverage of about 13 orbits per day. In this study, we use Version 3.3 Level 2 daily geopotential height (GPH), daily CO, and nighttime O_3 (solar zenith angles $>100°$), all screened according to the MLS data description and quality document [*Livesey et al*., 2011]. Details on validation of the MLS GPH, CO, and O_3 are given in *Schwartz et al*. [2008], *Pumphrey et al*. [2007], and *Jiang et al*. [2007], respectively. The vertical resolution of the MLS ozone measurements is about 2–3 km from the upper troposphere (12 km) to the middle mesosphere (65 km) and about 5 km above 65 km [*Jiang et al*., 2007]. The latitudinal coverage is 82°S–82°N, enabling the use of MLS data to look for hemispheric differences. The standard error of the mean for the MLS ozone data used in this study is, on average, $<$10% below 60 km and 10–20% above.

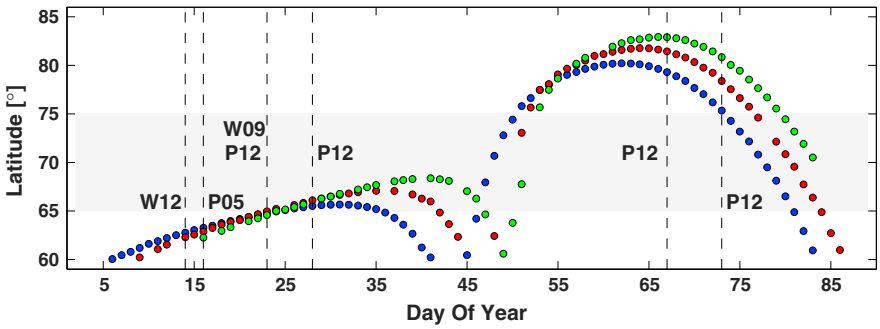

Figure 1. Daily averages of ACE-FTS measurement latitudes in January–March 2005 (blue), 2009 (red), and 2012 (green). The latitude range (65°N–75°N) used in the analysis of SABER and MLS measurements is marked in the figure with gray shading. The vertical dashed lines show the time points for SPEs (P) and SSWs (W) during 2005 (05), 2009 (09), and 2012 (12).

2.3. SABER

[10] SABER (Sounding of the Atmosphere using Broadband Emission Radiometry) is a 10-channel limb-scanning radiometer flying on NASA's TIMED satellite launched in 2002 [*Russell et al*., 1999]. SABER scans the Earth's limb from 400 km tangent height to the ground, simultaneously recording profiles of radiance in the spectral range from 1.27 to 15.4 μm [*Mlynczak et al*., 2005]. The instrument records approximately 1600 profiles per day. In this study we use the SABER (v1.07) ozone measurements derived from the infrared emission observations at 9.6 μm. The accuracy of the ozone measurements is of the order of 10% in the upper stratosphere-lower mesosphere region, with a positive bias increasing with altitude [*Rong et al*., 2009]. The vertical resolution of the observations is about 2 km [*Mlynczak*, 1997], and the latitudinal coverage changes with time, depending on the yaw period of the satellite, leading to the coverage changing from 83°S–52°N to 52°S–83°N every 60 days [*Rong et al*., 2009].

3. Definitions and Methods for Dynamics

[11] We use the World Meteorological Organization and *Charlton and Polvani* [2007] definition for sudden stratospheric warming events. The conditions for an SSW event are that (1) the zonal mean zonal wind is reversed (from westerly to easterly) at the 10 hPa level at 60°N and (2) the 10 hPa temperature gradient between 60°N and the pole becomes positive. If both conditions are fulfilled, the event is classified as a major SSW; otherwise, it is a minor SSW (e.g., when winds are reversed poleward of 60°N but not at 60°N). We used the operational zonal mean temperature and zonal mean zonal wind data from the European Centre for Medium-Range Weather Forecasts (ECMWF) and compared the 10 hPa zonal mean temperature/zonal wind at each latitude between 60°N and 90°N with the value at 60°N, 10 hPa. The results show that a major SSW took place on 23 January 2009 and that a strong minor warming took place on 14 January 2012.

[12] To characterize the dynamics in the polar regions even further and to examine the polar vortex conditions and mesosphere-to-stratosphere descent of air, we calculate the Northern Annular Mode (NAM) and CO Northern Annular Mode (CNAM) using EOF (empirical orthogonal function) analysis as described by *Baldwin and Dunkerton* [1999, 2001] and *Lee et al*. [2009, 2011]. The EOF analysis is carried out from MLS daily mean GPH and CO data for each altitude and on a 4° (latitude) × 8° (longitude) grid cell. The winter climatology over the 8 years of MLS measurements from 2005 to 2012 is then subtracted from the data, leaving GPH and CO anomalies. After area weighting the data, we computed the NAM and CNAM indices as the first EOF of the temporal covariance matrix (principal component). The NAM and CNAM indices are both normalized with the standard deviation of the indices. Details of applying EOF methods and further references can be found in *Baldwin and Dunkerton* [1999, 2001] and *Lee et al*. [2009, 2011].

4. Results

4.1. Middle Atmospheric Dynamics and EOF Analysis

[13] The NAM and CNAM indices for 2005, 2009, and 2012 in the NH are presented in Figure 2. In the figure, positive (red) NAM values are associated with a strong polar vortex and negative (blue) values with a weaker or displaced vortex. In all three years, the polar vortex either formed or was already formed in December and the NAM index shows a similar mesosphere-to-stratosphere progress of the vortex. While, in 2005, the vortex persisted until the end of February, in both 2009 and 2012, the vortex development was suddenly interrupted in late January (2009) and mid-January (2012). In addition, in late 2011 to early 2012, the NAM index turned negative in the upper stratosphere/lower mesosphere for a short period of time (~10 days), indicating a SSW event.

[14] An SSW took place also in both January 2009 and 2012, with slightly different timings. The effect of the SSWs can be seen from Figure 2 as an abrupt change of the NAM index from positive (strong polar vortex) to negative (vortex split/displacement) in both of these years. The changes after the SSWs in 2009 and 2012 are clear: The dynamics of the atmosphere were affected between about 10 and 95 km (2009) and between about 30 and 95 km (2012), with the effects of the 2009 SSW being more pronounced. In both cases, the polar vortex reformed at higher altitude after the stratospheric warming events and then progressed down to lower mesospheric and stratospheric altitudes. Regardless of the similarities in the upper mesospheric vortices after the SSW events in early 2009 and 2012, the polar vortex in the stratosphere before the SSWs was stronger

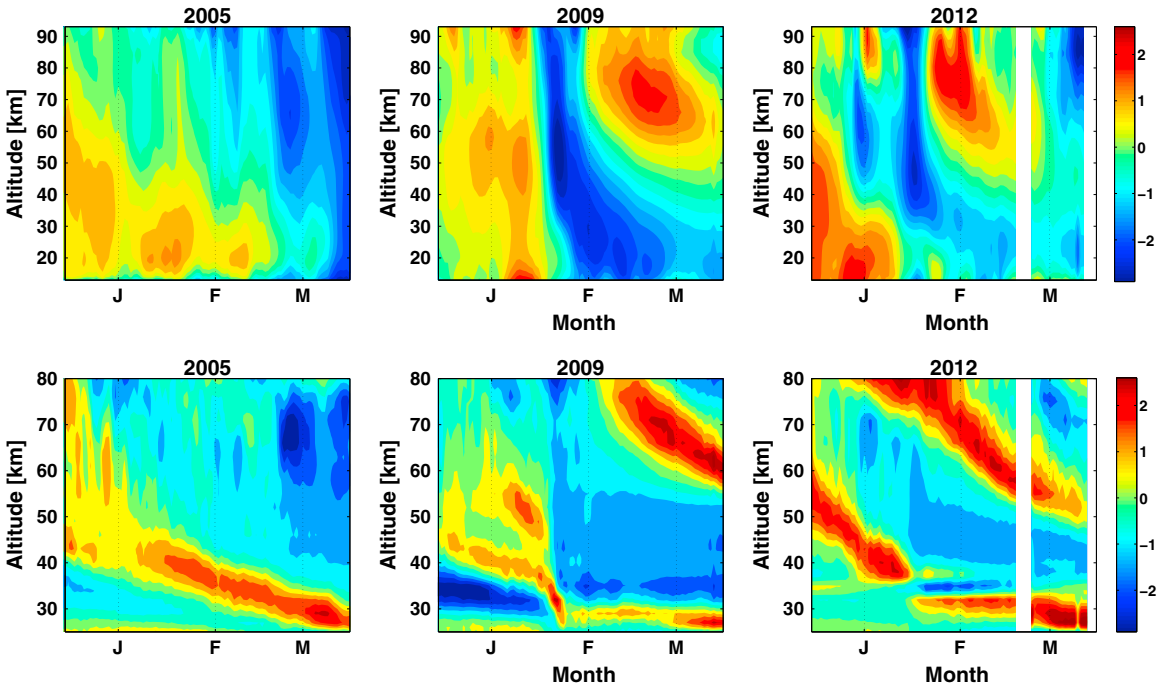

Figure 2. (top) NAM and (bottom) CNAM indices (see the text for more details) for 15 December to 15 March in 2005, 2009, and 2012 obtained from EOF analysis of the geopotential height and CO, respectively. Positive indices (red) represent conditions with a strong polar vortex (NAM) and a large amount of CO (CNAM), whereas negative indices (blue) represent conditions with a weak polar vortex (NAM) and only modest CO values (CNAM).

and more stable in 2012 than in 2009. In addition, the SSW in late 2011 to early 2012 affected the polar vortex at the mesospheric altitudes.

[15] The CNAM indices agree well with the NAM indices. The bottom panel of Figure 2 shows that there was mesosphere-to-stratosphere descent of CO in all three years. The rate of descent and the altitude range where the descent takes place appear to vary from year to year. During the 2004–2005 winter, the lower mesospheric air descended down to 25 km altitude with a descent rate of about 380 m/d which implies strong polar vortex conditions and low interference from atmospheric waves. In 2009 and 2012, SSWs took place in late January and mid-January, respectively, and interrupted the descent of the air. In both of these years, the descent continued, with increased descent rates, after the polar vortex reformed at a higher altitude following the warming events. By mid-March, the elevated CO values had descended to about 60 km (~570 m/d) and 50 km (~520 m/d) in 2009 and 2012, respectively.

4.2. Odd Nitrogen

[16] Figure 3 shows ACE-FTS observations of both daily mean NO_x (ppbv) and the change in NO_x (%) relative to the January–March mean in 2007–2008 in early 2005, 2009, and 2012 poleward from 60°N. The white dashed lines indicate the onset of SPEs, while the red solid lines indicate the onset of SSWs. The SPEs took place on 16 January 2005, 23 and 28 January 2012, and 7 and 13 March 2012.

[17] In 2005, the SPE (the proton fluxes have been described by *Seppälä et al.* [2006]) significantly affects NO_x volume mixing ratios between 45 and 80 km [see also *Jackman et al.*, 2011]. The ACE-FTS observations (Figure 3b, top) show 30–300% increases in NO_x right after the onset of the event. Because of the strong polar vortex in the stratosphere, NO_x was transported downward from early January, and elevated amounts (~10–20 ppbv) can be seen above about 45 km before the SPE onset (Figure 3a, top). The stratospheric vortex started to weaken in mid-February, reducing the levels of the SPE-produced NO_x in the stratosphere. Strong descent of mesospheric NO_x did not take place since; unlike in the stratosphere, the vortex was weak at higher altitudes (Figure 2) during the whole of early 2005.

[18] The major SSW in late January 2009 (23 January) and the following reformation of the stratopause at about 80 km altitude led to formation of a strong polar vortex that persisted until mid-March (Figure 2). The ACE-FTS observations (Figure 3a, middle) show NO_x descending inside the vortex from mesospheric altitudes down to about 50 km with mixing ratios of 20–300 ppbv, i.e., a factor of 10–25 higher than before the descent. The descent stops when the final vortex split takes place, just before the maximum of the NO_x descent feature reaches the stratosphere. This can also be seen in Figure 4, which presents the NO_x column densities around the stratopause during the different winters. The mesospheric NO_x enhancement is likely a result of the strong downwelling since no SPEs providing in situ production occurred. The overall geomagnetic activity was rather low in early 2009, which suggests that significant in situ production of NO_x by electron precipitation was also unlikely [*Randall et al.*, 2009]. Discontinuity in the data, i.e., lower abundances of NO_x (Figure 3a, middle) and decrease in NO_x (Figure 3b, middle), in the middle of the strong descent around mid-

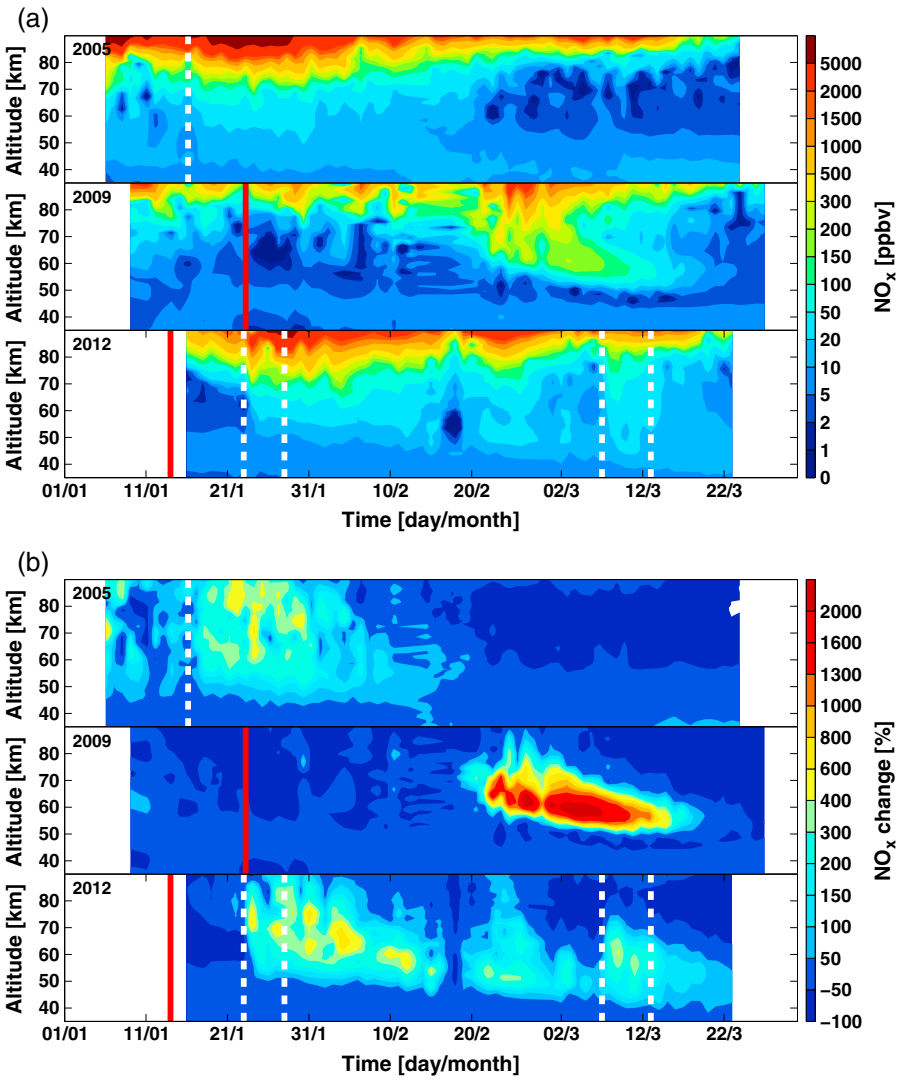

Figure 3. (a) NO_x mixing ratio (ppbv) and (b) change in NO_x (%) relative to the January–March mean in 2007–2008 calculated from ACE-FTS observations. For all figures, the observations shown are northward of 60°N in early 2005 ((a) and (b) top panels), 2009 (middle panels), and 2012 (bottom panels). The white dashed lines indicate the time points of the observed SPEs and the red solid lines the observed SSWs during these years.

February is due to the limited latitudinal coverage of the instrument (Figure 1): At this time, ACE-FTS was measuring at lower latitudes where the solar illumination and polar vortex conditions are already different to those farther in north. A similar effect is seen also in early February to mid-February 2012 (Figures 3a, bottom, and 3b, bottom).

[19] In 2012, a strong minor SSW took place in mid-January (14 January), i.e., earlier than the major SSW in 2009, and the CNAM indices (Figure 2) show descent of mesospheric air down to about 45 km by the end of March. A similar descent is seen in the ACE-FTS NO_x observations (Figures 3a, bottom, and 3b, bottom): Elevated amounts of NO_x reach altitudes of even 40 km by mid-March. Compared to the descent in 2009, the descent rates in 2012 were moderate (see section 4.1). However, lower altitudes were affected because the SSW, which started the descent event, occurred earlier than in 2009. In addition to the favorable dynamical conditions aiding the NO_x descent, there were several SPEs in early 2012, enabling in situ production of NO_x in the mesosphere and upper stratosphere. First, two SPEs took place in January (starting on 23 and 27 January). The >10 MeV proton fluxes, which will impact altitudes of about 70 km and below [*Turunen et al.*, 2009],were elevated for 9 days from the start of the first event, before returning to pre-SPE levels. It should be noted that the proton precipitation levels at lower energies were, in fact, elevated before the SPE, from 20 January. The peak >10 MeV proton flux was measured at 6310 pfu (particle flux unit, particles $cm^{-2}\,s^{-1}\,sr^{-1}$), making the event comparable with the January 2005 event (pfu of 5040; see *Seppälä et al.* [2006]). Another two SPEs took place in March (7 and 13 March), again with elevated precipitation starting earlier (5 March). The March events were comparable with the January events with a peak >10 MeV proton flux measured at 6530 pfu and a total duration from the start of the first SPE to return to pre-SPE levels taking 9 days.

[20] The ACE-FTS observations show NO_x descent already a couple of days after the SSW and a sudden, up to

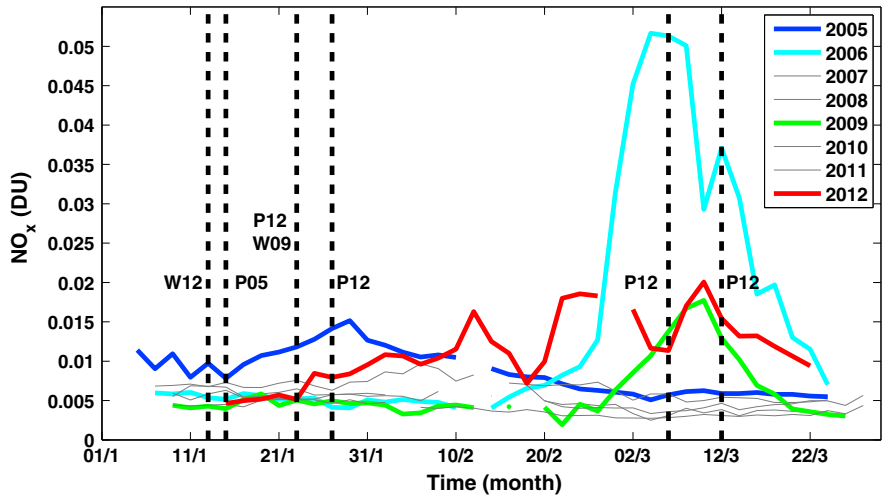

Figure 4. Two day mean NO_x column (DU) for altitude range 46–56 km calculated from ACE-FTS observations for the polar cap region (60°N–90°N). The dashed lines show the time points for SPEs (P) and SSWs (W) during 2005 (05), 2009 (09), and 2012 (12).

800% increase in NO_x mixing ratios above altitudes of about 50 km, with a 50–100% increase below 50 km, right after the first SPE (Figure 3b, bottom). The second proton event in late January seemed to have less of an effect on the already elevated NO_x levels. The first SPE in March, on the other hand, increased the amount of NO_x rapidly from 80 km down to even 40 km with a magnitude comparable to the first event in January, whereas the final SPE in mid-March caused an increase of 50–100% mainly between 40 and 45 km.

[21] Figure 4 compares the overall effects of particle precipitation activity and atmospheric dynamical processes on NO_x (Dobson unit, DU) around the stratopause between 46 and 56 km for years 2005–2012. The dashed lines show the onset times for SPEs and SSWs in 2005, 2009, and 2012. The figure shows that the amount of NO_x in the middle atmosphere in March is higher (>0.005 DU) during years with SSW events (2006, 2009, and 2012) than in dynamically nonactive years. These SSWs took place around January, but the effect on NO_x at stratopause altitudes is seen with a delay. This demonstrates the time needed for NO_x to descend from mesospheric altitudes down to the stratosphere inside the polar vortex. On the other hand, the NO_x increments due to SPEs are visible immediately after the events in January 2005 and January and March 2012. The changes in NO_x after these

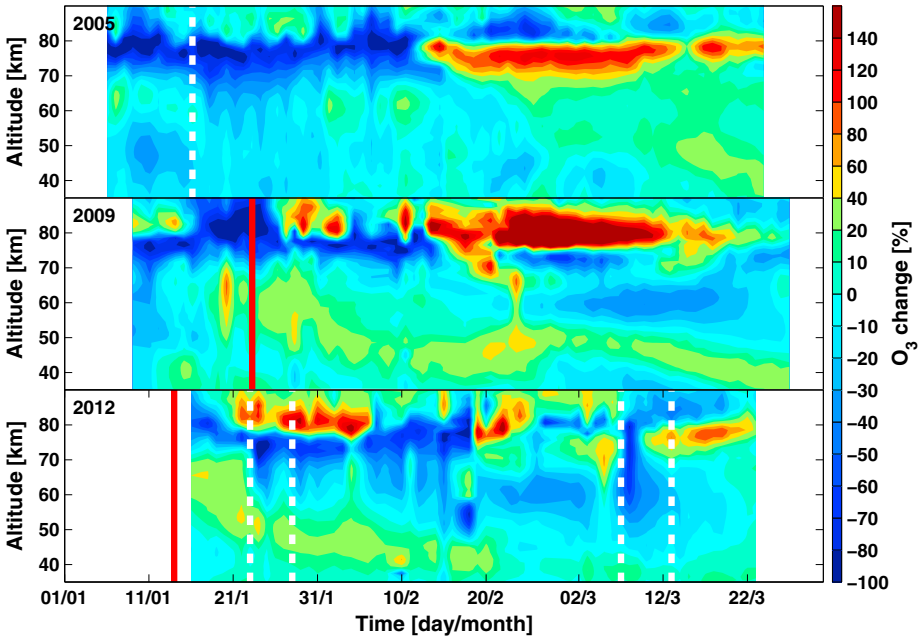

Figure 5. ACE-FTS observations of the change in O_3 (%) relative to the January–March mean in 2007–2008 northward of 60°N in (top) 2005, (middle) 2009, and (bottom) 2012. The white dashed lines indicate the time points of the observed SPEs and the red solid lines the observed SSWs during these years.

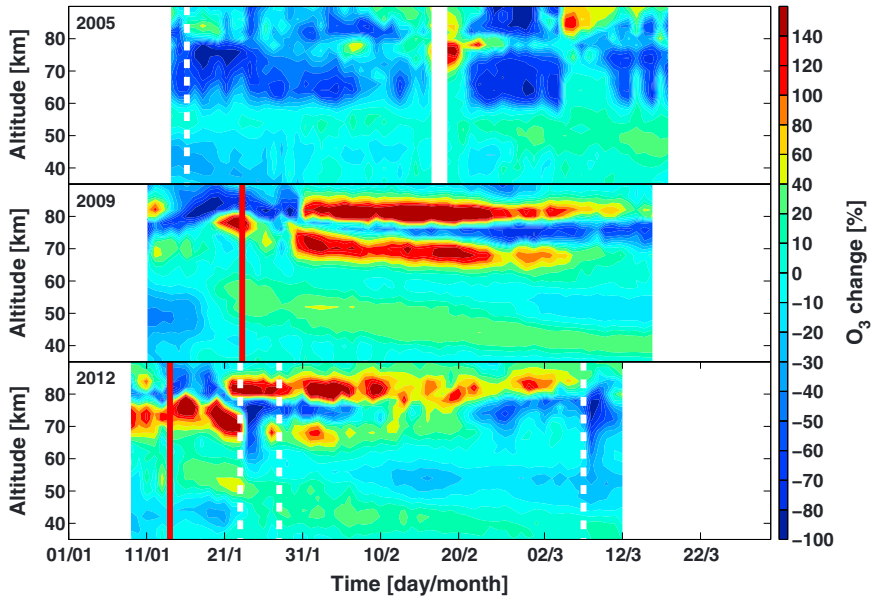

Figure 6. SABER observations of the change in O_3 (%) relative to the January–March mean in 2007–2008 between 65°N and 75°N in (top) 2005, (middle) 2009, and (bottom) 2012. Also, the observed SPEs (white dashed lines) and SSWs (red solid lines) are marked in the figure.

events last for varying periods of time (from couple to few days), also depending on atmospheric dynamics and the solar illumination conditions at the altitudes in question during these years. It is interesting to note that the largest NO_x amounts at the typical stratopause altitudes are observed in March 2006. This is observed despite the overall NO_x enhancements being larger during 2009 [see *Randall et al.*, 2009]. Like in 2009, as discussed earlier, the descent in 2006 stops before the maximum of the descending NO_x feature reaches ~50 km altitudes, limiting the main impact to mesospheric altitudes.

4.3. Ozone

[22] Ozone observations, which were available from ACE-FTS, SABER, and MLS, are shown in Figures 5–7, respectively. All three satellite instruments observe the NH polar cap region but use different techniques and have slightly different coverages. ACE-FTS only covers a narrow latitude band and is moving toward the south around mid-February and then returning back to higher latitudes (Figure 1), whereas both MLS and SABER observe all the latitudes except the very pole (here we use the latitude band

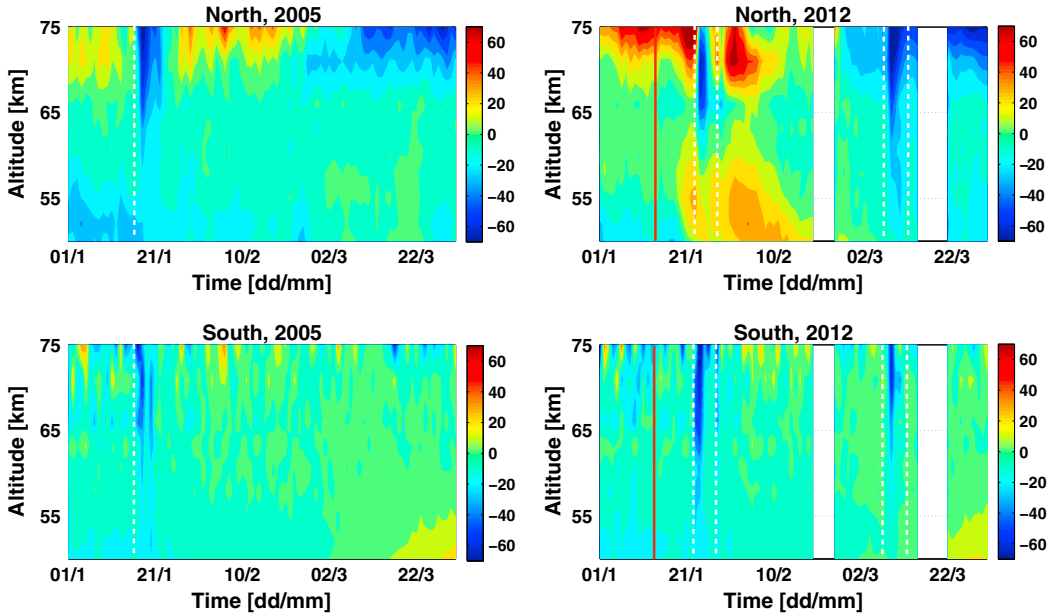

Figure 7. MLS observations of the change in nighttime O_3 at mesospheric altitudes for geomagnetic latitudes 65°N–75°N (top) and 65°S–75°S (bottom). The percent change is calculated relative to the January–March mean in 2007–2008. The white dashed lines indicate the observed SPEs and the red solid lines the SSW in 2012. Contour lines are shown in 10% steps between −70% and 70%.

Table 1. Changes in Ozone (%) After Solar Proton Events in January 2005 and in Early 2012 Relative to the January–March Mean in 2007–2008[a]

	ACE-FTS	MLS	SABER
	% (km)	% (km)	% (km)
2005	20–70 (45–80)	20–70 (50–80)	20–90 (55–80)
2012 (I)	10–80 (55–75)	10–70 (55–80)	10–90 (50–80)
2012 (II)	10–60 (55–75)	10–70 (63–80)	20–70 (70–80)
2012 (III)	10–70 (40–90)	10–70 (45–80)	20–90 (45–85)
2012 (IV)	20–30 (40–70)		

[a]The four cases for 2012 indicate the different SPEs that took place in January (I and II) and March (III and IV). In brackets is given the altitude range (in km) where the changes were observed. Empty fields stand for no available data.

65°N–75°N). Therefore, the results from the different instruments can reflect differences due to, e.g., different solar illumination and polar vortex conditions in the measurement locations. In addition, the instruments measure ozone with differing vertical resolutions as discussed earlier: The resolution is about 4 km for ACE-FTS, 2–3 km below 65 km and 5 km above for MLS, and about 2 km for SABER. It is important to note that this may affect how some features in the vertical profiles are seen by the different instruments. Because we use the MLS observations also to look at hemispheric differences in response to the SPEs, the MLS values are calculated for geomagnetic latitudes to ensure that a maximum amount of data is within the area where energetic particles precipitate. We also checked the results for geographic latitude, and the use of geomagnetic latitudes did not change the results significantly.

[23] The SPE-related ozone changes for 2005 and 2012, as seen in Figures 5–7, are summarized in Table 1. The changes are calculated relative to the January–March mean in 2007–2008 (no SSWs or SPEs) separately for every instrument. To help separate the individual 2012 SPEs, the results in Table 1 are given separately for the four SPEs in January and March 2012 and are labeled as I–IV according to their order of occurrence. The three satellite instruments all show reductions in ozone levels after the SPEs in 2005 and 2012. The depletion is restricted mainly to the altitude range of 50–80 km for 2005 and 40–80 km for 2012. The decreases are from about 20% up to 80% in 2005 and 10–90% in 2012. The reduction in ozone lasted longer in 2012 when a number of SPEs and a strong minor SSW occurred (in 2005, there was only one SPE): from late January to late March. While the short-term (few days) ozone losses observed directly after the SPEs are driven by chemical loss from enhanced SPE-produced HO_x [*Verronen et al.*, 2006], the observed longer-term depletion in lower mesospheric/upper stratospheric ozone in 2009 and especially in 2012 is more complex. In 2009, with only a major SSW affecting the middle atmosphere, the observations show (Figures 5 and 6) a decrease of 10–40% in ozone between about 45 and 75 km, coinciding with the NO_x descent maximum (Figure 3).

[24] For comparison of the SPE effects, we included MLS measurements also from the Southern Hemisphere (SH) summer in Figure 7. The January to March period in the south is summer/autumn season, i.e., non-polar-vortex conditions. The effect seen in ozone is thus only due to the SPE-driven chemical effects. The observations show that after the SPE in early 2005 (left), the amount of ozone decreases by 10–70% between 55 and 80 km. In 2012 (right), ozone decreases by 10–60% between 60 and 80 km (events I and III) and by 10–30% between 60 and 70 km (event II). For event IV, no MLS data were available. The magnitude of the ozone losses in the SH is comparable to those of the NH, but the NH changes last longer, due to lack of solar radiation and stable conditions inside the NH polar vortex at that time of the year, which prevent effective NO_x destruction.

5. Discussion

[25] In early 2012, when both a descent event of NO_x following a SSW in mid-January and in situ production of NO_x due to several SPEs during the period of January–March took place, both short-term and long-term ozone changes were observed. The SPE-related short-term (few days) ozone losses in early 2012 are driven by the enhanced HO_x, the main chemical catalyst of ozone loss in the mesosphere [e.g., *Grenfell et al.*, 2006].

[26] Understanding the longer-term (weeks) ozone depletion in the mesosphere and upper stratosphere is less straightforward. Figure 8 shows the changes in ozone in 2004–2012 relative to the 2007–2008 January–March mean from the ACE-FTS observations. The overlaid contours show the positive changes in NO_x (relative to the same period). It is clear that during years with enhanced NO_x in the middle atmosphere, e.g., in 2004 and 2012, also decreases in ozone are observed. In the mesosphere, the reaction rates of the NO_x catalytic cycles depleting ozone are dominated by those of the HO_x cycles, leading to the HO_x-driven ozone loss at those altitudes as discussed above. Closer to the stratopause region, and below, the catalytic NO_x cycles become comparable to the catalytic HO_x and chlorine cycles, becoming increasingly important to the chemical ozone balance.

[27] Changes in dynamics following SSW events are also likely contributing to the observed long-term ozone loss. *Sofieva et al.* [2012] suggested that during SSW events, the upper stratospheric and mesospheric ozone is affected by the negative temperature-ozone correlation and transport of ozone-poor air masses from higher altitudes. The ozone loss cycles could also be affected by the SSW-driven changes in temperatures, such as those reported by *Randall et al.* [2009]. It is also important to note that SSW events create a possibility for subtropical air to be transported to polar latitudes, further complicating the dynamical ozone balance in polar stratospheric air masses [*Konopka et al.*, 2007]. Due to the complexity of the situation, it is not possible to separate all these processes contributing to the ozone balance from observations alone to assess their relative importance. The detailed analysis of the different chemical and dynamical components requires the use of a chemistry transport model. This is, however, out of the scope of this paper and will be the topic of a further study focusing on the modeling aspect.

[28] Apart from ozone losses, the observations also indicate increases in ozone. In 2009 and 2012, ozone increases in the stratosphere are seen after the SSWs starting from above 50 km and descending down to ~40 km. These changes can be understood by polar vortex dynamics: When the vortex weakens, ozone-rich air from lower latitudes is mixed with the ozone-poor air inside the vortex, leading to the observed increases in ozone. This process can be clearly seen through the trace gases, such as CO and water vapor, which

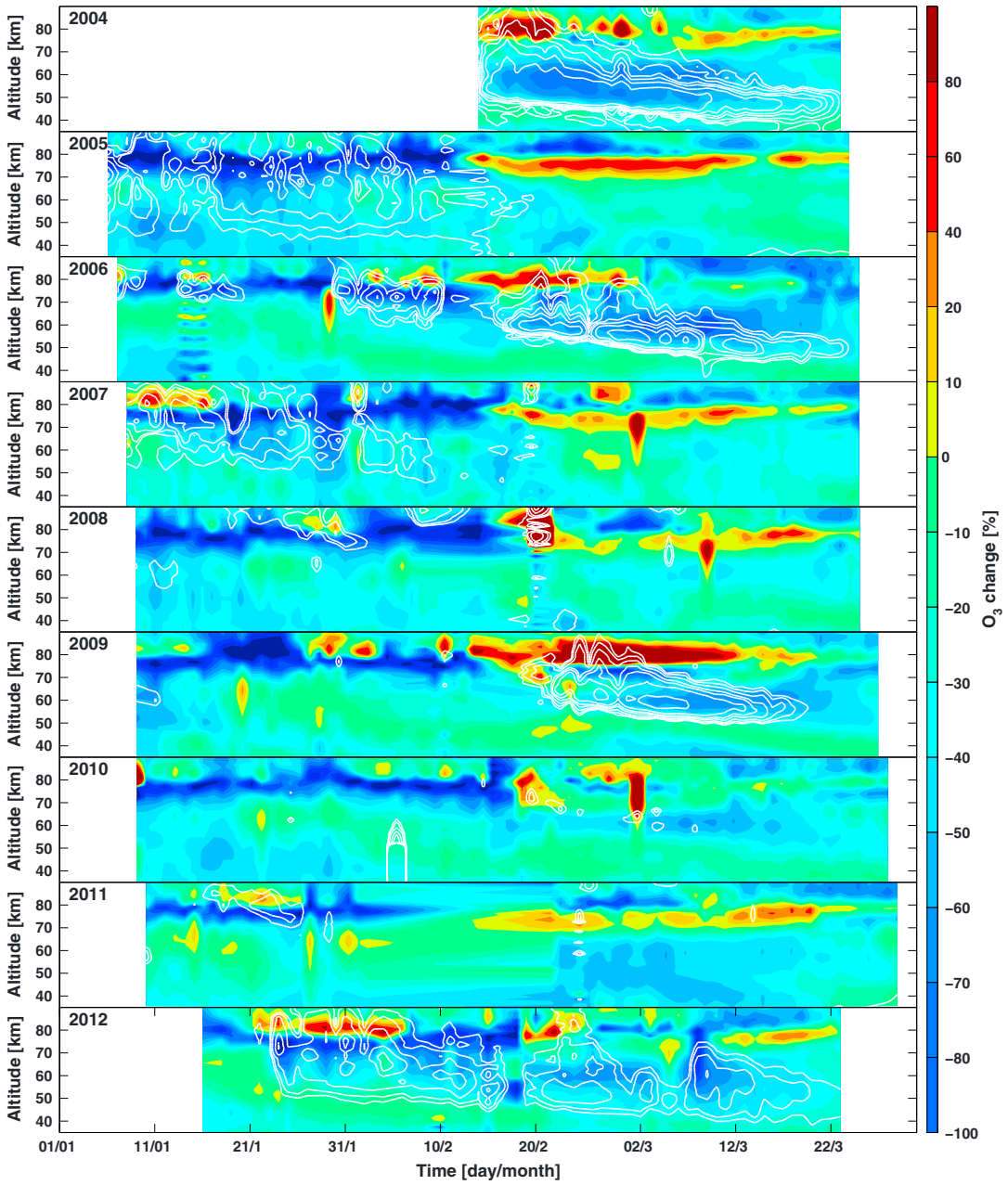

Figure 8. ACE-FTS observations of the change in O_3 (%) relative to the January–March mean in 2007–2008 northward of 60°N in 2004–2012. The overlaid contours are values of positive NO_x changes relative to the same period (50, 100, 200, 400, 600, 1000, and 2000%).

are mixed out of the vortex after SSW and transported into a strong reformed upper stratospheric/lower mesospheric vortex (as discussed by *Manney et al.* [2009] for the 2009 case). Higher up, in the MLT region, both the downward transport of the HO_x layer from the same altitude region and the descent of upper atmospheric air with high amounts of atomic oxygen increasing ozone production contribute to the increases [*Smith et al.*, 2009; *Damiani et al.*, 2010; *Sofieva et al.*, 2012]. In all cases, other effects, due to, e.g., the final warming timing and seasonal changes, need to be taken into account for a complete picture.

[29] Previous studies have shown a correlation between geomagnetic activity and the amount of NO_x in the NH stratosphere [e.g., *Seppälä et al.*, 2007; *Arnone and Hauchecorne*, 2012, and references therein]. Significant ozone losses following stratospheric NO_x enhancements have been reported on two different types of occasions: (1) following very large SPEs such as the Halloween event in 2003 [see, e.g., *Seppälä et al.*, 2004; *Jackman et al.*, 2009; *Funke et al.*, 2011] and (2) strong downward descent events following SSW, with existing NO_x enhancements from energetic particle precipitation such as the descent event in early 2004 [*López-Puertas et al.*, 2005; *Randall et al.*, 2005; *Clilverd et al.*, 2009]. Our results show that although the SPEs in 2005 and 2012 increased the amounts of NO_x in the mesosphere and upper stratosphere, the in situ production

was not sufficient enough to have a clearly NO_x-dominated effect on the middle atmospheric ozone. Similar results for mesospheric altitudes for the 2012 SPEs have now also been shown by *von Clarmann et al*. [2013] using a different satellite instrument than our study. The MIPAS observations reported by *von Clarmann et al*. [2013] suggest similar NO_x enhancements for the first three SPEs in 2012 as the ACE-FTS, MLS, and SABER observations we analyzed, but following the final SPE in mid-March, MIPAS shows lower increases (about 2–5 ppbv). *von Clarmann et al*. [2013] also report ozone losses coinciding with the NO_x enhancements at mesospheric altitudes following the January SPEs.

[30] It is important to note here that these SPEs were small to medium in strength, and much larger events have been observed in the past (including the 2003 SPEs). In fact, in January–February 2012, the monthly mean geomagnetic A_p index (available from the Space Physics Interactive Data Resource, http://spidr.ngdc.noaa.gov), used as a proxy for overall particle precipitation levels, was much lower (~7–9) than that at the same time in 2004 (~13–22) when enhanced amounts of NO_x due to energetic particle precipitation were transported to the stratosphere, and clear ozone losses were observed. For 2012, this means that the overall MLT NO_x production by energetic particle precipitation was very low. Consequently, any mesospheric air masses transported to the stratosphere would have relatively low concentrations of NO_x. Similar conditions low overall particle precipitation levels and, additionally, no SPEs for MLT NO_x production took place in 2009. Nevertheless, mesospheric production of NO_x can have an important role in intensifying the MLT NO_x-stratospheric ozone connection since the downward transport of thermosphere air masses through the mesopause is hindered by the upper atmosphere circulation patterns, and the transport from the lower thermosphere to the mesosphere arises mainly from diffusion processes [*Smith et al*., 2011].

[31] If the determining factor indeed is the level of NO_x production from the prevailing energetic particle precipitation, including SPEs, it is likely that the NO_x-ozone connection is more pronounced during and after solar maximum periods (2003–2004) than during and after solar minimum periods (the 2009 and 2012 events). Therefore, our results, which, for the strong descent event part, represent an exceptionally quiet solar minimum period, should not be used to draw conclusions for all situations but rather for conditions where the overall energetic particle precipitation levels influencing NO_x in the MLT were below average.

6. Conclusions

[32] The aim of this study was to compare years with SPEs and/or SSWs and the effects of different combinations of these events on middle atmospheric NO_x and ozone. The results show that the amount of NO_x increased due to both the SPEs (2005 and 2012) and SSWs (2009 and 2012) by a factor of 1 to 25 between 40 and 90 km depending on the year and event. Ozone losses, both short term and long term, of the order of 10–90% between 40 and 90 km were also observed. Comparing the three years, the largest mesospheric NO_x changes were observed in 2009 following the major SSW in late January. In 2012, when both SPEs and a SSW took place, enhanced amounts of NO_x were transported down to 40 km altitude, i.e., lower than in years 2005 and 2009. As a result, the largest NO_x changes in the upper stratosphere were seen in 2012.

[33] Our main result is that the combination of optimal dynamics, i.e., downward transport following a mid-January SSW, and in situ production of NO_x due to several moderate SPEs is not necessarily enough to produce a long-term and clearly NO_x-dominated effect on stratospheric ozone. Particularly in the case of 2012, (1) the SPEs were only medium size in strength and did not produce enough NO_x and (2) the overall production of NO_x by particle precipitation in the MLT region was low, leading to relatively low concentrations of NO_x being transported down to the stratosphere after the SSW. It should be noted that the cases presented in this paper are from an elongated period of relatively low solar activity. In order to fully understand the NO_x connection between the MLT and stratosphere and its influence on stratospheric ozone levels, periods of high solar activity (for high overall energetic particle precipitation) should be investigated as well. For this, the continuation of middle atmosphere measurements of NO_x and ozone is essential.

[34] **Acknowledgments.** The work of S.-M.P. was supported by the Academy of Finland through project 134325 (MIDAT: Middle atmosphere dynamics and chemistry in climate change), the work of A.S. was supported by the Academy of Finland through projects 258165 and 265005 (CLASP: Climate and Solar Particle Forcing), and the works of M.E.A. and P.T.V. were supported by the Academy of Finland through projects 136225 and 140888 (SPOC: Significance of Energetic Electron Precipitation to Odd Hydrogen, Ozone, and Climate). The Atmospheric Chemistry Experiment (ACE), also known as SCISAT, is a Canadian-led mission mainly supported by the Canadian Space Agency and the Natural Sciences and Engineering Research Council of Canada. We are grateful to NASA for providing the MLS Aura data and the SABER team for providing the SABER data.

References

Arnone, E., and A. Hauchecorne (2012), Stratosphere NO_y species measured by MIPAS and GOMOS onboard ENVISAT during 2002–2010: Influence of plasma processes onto the observed distribution and variability, *Space Sci. Rev.*, *168*, 315–332, doi:10.1007/s11214-011-9861-1.

Baldwin, M. P., and T. J. Dunkerton (1999), Downward propagation of the Arctic oscillation from the stratosphere to the troposphere, *J. Geophys. Res.*, *104*, 30,937–30,946, doi:10.1029/1999JD900445.

Baldwin, M. P., and T. J. Dunkerton (2001), Stratospheric harbingers of anomalous weather regimes, *Science*, *294*, 581–584, doi:10.1126/science.1063315.

Barth, C. A. (1992), Nitric oxide in the lower thermosphere, *Planet. Space Sci.*, *40*, 315–336.

Baumgaertner, A. J. G., A. Seppälä, P. Jöckel, and M. A. Clilverd (2011), Geomagnetic activity related NO_x enhancements and polar surface air temperature variability in a chemistry climate model: Modulation of the NAM index, *Atmos. Chem. Phys.*, *11*, 4521–4531, doi:10.5194/acp-11-4521-2011.

Bernath, P. F., et al. (2005), Atmospheric Chemistry Experiment (ACE): Mission overview, *Geophys. Res. Lett.*, *32*, L15S01, doi:10.1029/2005GL022386.

Callis, L. (1997), Odd nitrogen formed by energetic electron precipitation as calculated from TIROS data, *Geophys. Res. Lett.*, *24*, 3237–3240, doi:10.1029/97GL03276.

Callis, L. B., and J. D. Lambeth (1998), NO_y formed by precipitating electron events in 1991 and 1992: Descent into the stratosphere as observed by ISAMS, *Geophys. Res. Lett.*, *25*, 1875–1878, doi:10.1029/98GL01219.

Callis, L. B., D. N. Baker, J. B. Blake, J. D. Lambeth, R. E. Boughner, M. Natarajan, R. W. Klebesadel, and D. J. Gorney (1991a), Precipitating relativistic electrons: Their long-term effect on stratospheric odd nitrogen levels, *J. Geophys. Res.*, *96*, 2939–2976.

Callis, L. B., R. E. Boughner, M. Natarajan, J. D. Lambeth, D. N. Baker, and J. B. Blake (1991b), Ozone depletion in the high latitude lower stratosphere: 1979–1990, *J. Geophys. Res.*, *96*, 2921–2937.

Callis, L. B., et al. (1996a), Precipitation electrons: Evidence for effects on mesospheric odd nitrogen, *Geophys. Res. Lett.*, *23*, 1901–1904, doi:10.1029/96GL01787.

Callis, L. B., D. N. Baker, M. Natarajan, J. B. Blake, R. A. Mewaldt, R. S. Selesnick, and J. R. Cummings (1996b), A 2-D model simulation of downward transport of NO_y into the stratosphere: Effects on the 1994 austral spring O_3 and NO_y, *Geophys. Res. Lett.*, *23*, 1905–1908, doi:10.1029/96GL01788.

Charlton, A. J., and L. M. Polvani (2007), A new look at stratospheric sudden warmings. Part I: Climatology and modeling benchmarks, *J. Clim.*, *20*, 449–469, doi:10.1175/JCLI3996.1.

Clilverd, M. A., A. Seppälä, C. J. Rodger, P. T. Verronen, and N. R. Thomson (2006), Ionospheric evidence of thermosphere-to-stratosphere descent of polar NO_x, *Geophys. Res. Lett.*, *33*, L19811, doi:10.1029/2006GL026727.

Clilverd, M. A., A. Seppälä, C. J. Rodger, M. G. Mlynczak, and J. U. Kozyra (2009), Additional stratospheric NO_x production by relativistic electron precipitation during the 2004 spring NO_x descent event, *J. Geophys. Res.*, *114*, A04305, doi:10.1029/2008JA013472.

Damiani, A., M. Storini, M. L. Santee, and S. Wang (2010), Variability of the nighttime OH layer and mesospheric ozone at high latitudes during northern winter: Influence of meteorology, *Atmos. Chem. Phys.*, *10*, 14,583–14,610, doi:10.5194/acpd-10-14583-2010.

Funke, B., M. López-Puertas, S. Gil-Lopez, T. von Clarmann, G. P. Stiller, H. Fischer, and S. Kellmann (2005), Downward transport of upper atmospheric NOx into the polar stratosphere and lower mesosphere during the Antarctic 2003 and Arctic 2002/2003 winters, *J. Geophys. Res.*, *110*, D24308, doi:10.1029/2005JD006463.

Funke, B., M. López-Puertas, H. Fischer, G. P. Stiller, T. von Clarmann, G. Wetzel, B. Carli, and C. Belotti (2007), Comment on "Origin of the January–April 2004 increase in stratospheric NO_2 observed in northern polar latitudes" by Jean-Baptiste Renard et al., *Geophys. Res. Lett.*, *34*, L07813, doi:10.1029/2006GL027518.

Funke, B., et al. (2011), Composition changes after the "Halloween" solar proton event: The High-Energy Particle Precipitation in the Atmosphere (HEPPA) model versus MIPAS data intercomparison study, *Atmos. Chem. Phys.*, *11*, 9089–9139, doi:10.5194/acp-11-9089-2011.

Grenfell, J. L., R. Lehmann, P. Mieth, U. Langematz, and B. Steil (2006), Chemical reaction pathways affecting stratospheric and mesospheric ozone, *J. Geophys. Res.*, *111*, D17311, doi:10.1029/2004JD005713.

Hauchecorne, A., J.-L. Bertaux, F. Dalaudier, J. M. Russell, M. G. Mlynczak, E. Kyrölä, and D. Fussen (2007), Large increase of NO_2 in the north polar mesosphere in January–February 2004: Evidence of a dynamical origin from GOMOS/ENVISAT and SABER/TIMED data, *Geophys. Res. Lett.*, *34*, L03810, doi:10.1029/2006GL027628.

Jackman, C. H., E. L. Fleming, and F. M. Vitt (2000), Influence of extremely large solar proton events in a changing stratosphere, *J. Geophys. Res.*, *105*, 11,659–11,670.

Jackman, C. H., et al. (2008), Short- and medium-term atmospheric constituent effects of very large solar proton events, *Atmos. Chem. Phys.*, *8*, 765–785, doi:10.5194/acp-8-765-2008.

Jackman, C. H., D. R. Marsh, F. M. Vitt, R. R. Garcia, C. E. Randall, E. L. Fleming, and S. M. Frith (2009), Long-term middle atmospheric influence of very large solar proton events, *J. Geophys. Res.*, *114*, D11304, doi:10.1029/2008JD011415.

Jackman, C. H., et al. (2011), Northern Hemisphere atmospheric influence of the solar proton events and ground level enhancement in January 2005, *Atmos. Chem. Phys.*, *11*, 6153–6166, doi:10.5194/acp-11-6153-2011.

Jiang, Y. B., et al. (2007), Validation of Aura Microwave Limb Sounder ozone by ozonesonde and lidar measurements, *J. Geophys. Res.*, *112*, D24S34, doi:10.1029/2007JD008776.

Konopka, P., et al. (2007), Ozone loss driven by nitrogen oxides and triggered by stratospheric warmings can outweigh the effect of halogens, *J. Geophys. Res.*, *112*, D05105, doi:10.1029/2006JD007064.

Lee, J. N., D. L. Wu, G. L. Manney, and M. J. Schwartz (2009), Aura Microwave Limb Sounder observations of the Northern Annular Mode: From the mesosphere to the upper troposphere, *J. Geophys. Res.*, *36*, L20807, doi:10.1029/2009GL040678.

Lee, J. N., D. L. Wu, G. L. Manney, M. J. Schwartz, A. Lambert, N. J. Livesey, K. R. Minschwaner, H. C. Pumphrey, and W. G. Read (2011), Aura Microwave Limb Sounder observations of the polar middle atmosphere: Dynamics and transport of CO and H_2O, *J. Geophys. Res.*, *116*, D05110, doi:10.1029/2010JD014608.

Livesey, N. J., et al. (2011), EOS MLS Version 3.3 Level 2 data quality and description document, Rep. JPL D-33509, Jet Propul. Lab., Pasadena, Calif.

López-Puertas, M., B. Funke, S. Gil-López, T. von Clarmann, G. P. Stiller, M. Höpfner, S. Kellmann, H. Fischer, and C. H. Jackman (2005), Observation of NO_x enhancement and ozone depletion in the Northern and Southern Hemispheres after the October–November 2003 solar proton events, *J. Geophys. Res.*, *110*, A09S43, doi:10.1029/2005JA011050.

Manney, G. L., M. J. Schwartz, K. Krüger, M. L. Santee, S. Pawson, J. N. Lee, W. H. Daffer, R. A. Fuller, and N. J. Livesey (2009), Aura Microwave Limb Sounder observations of dynamics and transport during the record-breaking 2009 Arctic stratospheric major warming, *Geophys. Res. Lett.*, *36*, L12815, doi:10.1029/2009GL038586.

Matsuno, T. (1971), A dynamical model of the sudden stratospheric warming, *J. Atmos. Sci.*, *28*, 1479–1494.

Mlynczak, M. G. (1997), Energetics of the mesosphere and lower thermosphere and the SABER experiment, *Adv. Space Res.*, *20*, 1177–1183.

Mlynczak, M. G., et al. (2005), Energy transport in the thermosphere during the solar storms of April 2002, *J. Geophys. Res.*, *110*, A12S25, doi:10.1029/2005JA011141.

Pumphrey, H. C., et al. (2007), Validation of middle-atmosphere carbon monoxide retrievals from the Microwave Limb Sounder on Aura, *J. Geophys. Res.*, *112*, D24S38, doi:10.1029/2007JD008723.

Randall, C. E., et al. (2005), Stratospheric effects of energetic particle precipitation in 2003–2004, *Geophys. Res. Lett.*, *32*, L05802, doi:10.1029/2004GL022003.

Randall, C. E., V. L. Harvey, C. S. Singleton, P. F. Bernath, C. D. Boone, and J. U. Kozyra (2006), Enhanced NO_x in 2006 linked to upper stratospheric Arctic vortex, *Geophys. Res. Lett.*, *33*, L18811, doi:10.1029/2006GL027160.

Randall, C. E., V. L. Harvey, D. E. Siskind, J. France, P. F. Bernath, C. D. Boone, and K. A. Walker (2009), NO_x descent in the Arctic middle atmosphere in early 2009, *Geophys. Res. Lett.*, *36*, L18811, doi:10.1029/2009GL039706.

Rong, P. P., J. M. Russell, M. G. Mlynczak, E. E. Remsberg, B. T. Marshall, L. L. Gordley, and M. López-Puertas (2009), Validation of Thermosphere Ionosphere Mesosphere Energetics and Dynamics/Sounding of the Atmosphere using Broadband Emission Radiometry (TIMED/SABER) v1.07 ozone at 9.6 μm in altitude range 15–70 km, *J. Geophys. Res.*, *114*, D04306, doi:10.1029/2008JD010073.

Russell, J. M., III, M. G. Mlynczak, L. L. Gordley, J. Tansock, and R. Esplin (1999), An overview of the SABER experiment and preliminary calibration result, *Proc. Soc. Photo. Opt. Instrum. Eng.*, *3756*, 277–288.

Salmi, S.-M., P. T. Verronen, L. Thölix, E. Kyrölä, L. Backman, A. Y. Karpechko, and A. Seppälä (2011), Mesosphere-to-stratosphere descent of odd nitrogen in February–March 2009 after sudden stratospheric warming, *Atmos. Chem. Phys.*, *11*, 4645–4655, doi:10.5194/acp-11-4645-2011.

Schwartz, M. J., et al. (2008), Validation of the Aura Microwave Limb Sounder temperature and geopotential height measurements, *J. Geophys. Res.*, *113*, D15S11, doi:10.1029/2007JD008783.

Semeniuk, K., J. C. McConnell, and C. H. Jackman (2005), Simulation of the October–November 2003 solar proton events in the CMAM GCM: Comparison with observations, *Geophys. Res. Lett.*, *32*, L15S02, doi:10.1029/2005GL022392.

Seppälä, A., P. T. Verronen, E. Kyrölä, S. Hassinen, L. Backman, A. Hauchecorne, J. L. Bertaux, and D. Fussen (2004), Solar proton events of October–November 2003: Ozone depletion in the Northern Hemisphere polar winter as seen by GOMOS/Envisat, *Geophys. Res. Lett.*, *31*, L19107, doi:10.1029/2004GL021042.

Seppälä, A., P. T. Verronen, V. F. Sofieva, J. Tamminen, E. Kyrölä, C. J. Rodger, and M. A. Clilverd (2006), Destruction of the tertiary ozone maximum during a solar proton event, *Geophys. Res. Lett.*, *33*, L07804, doi:10.1029/2005GL025571.

Seppälä, A., P. T. Verronen, M. A. Clilverd, C. E. Randall, J. Tamminen, V. F. Sofieva, L. Backman, and E. Kyrölä (2007), Arctic and Antarctic polar winter NO_x and energetic particle precipitation in 2002–2006, *Geophys. Res. Lett.*, *34*, L12810, doi:10.1029/2007GL029733.

Seppälä, A., M. A. Clilverd, C. J. Rodger, P. T. Verronen, and E. Turunen (2008), The effects of hard-spectra solar proton events on the middle atmosphere, *J. Geophys. Res.*, *113*, A11311, doi:10.1029/2008JA013517.

Seppälä, A., C. E. Randall, M. A. Clilverd, E. Rozanov, and C. J. Rodger (2009), Geomagnetic activity and polar surface air temperature variability, *J. Geophys. Res.*, *114*, A10312, doi:10.1029/2008JA014029.

Smith, A. K., M. López-Puertas, M. García-Comas, and S. Tukiainen (2009), SABER observations of mesospheric ozone during NH late winter 2002–2009, *Geophys. Res. Lett.*, *36*, L23804, doi:10.1029/2009GL040942.

Smith, A. K., R. R. Rolando, D. R. Marsh, and J. H. Richter (2011), WACCM simulations of the mean circulation and trace species transport in the winter mesosphere, *J. Geophys. Res.*, *116*, D20115, doi:10.1029/2011JD016083.

Sofieva, V. F., N. Kalakoski, P. T. Verronen, S.-M. Päivärinta, E. Kyrölä, L. Backman, and J. Tamminen (2012), Polar-night O_3, NO_2 and NO_3 distributions during sudden stratospheric warmings in 2003–2008 as seen by GOMOS/Envisat, *Atmos. Chem. Phys.*, *12*, 1051–1066, doi:10.5194/acp-12-1051-2012.

Solomon, S., P. J. Crutzen, and R. G. Roble (1982), Photochemical coupling between the thermosphere and the lower atmosphere 1. Odd nitrogen from 50 to 120 km, *J. Geophys. Res.*, *87*, 7206–7220.

Turunen, E., P. T. Verronen, A. Seppälä, C. J. Rodger, M. A. Clilverd, J. Tamminen, C.-F. Enell, and T. Ulich (2009), Impact of different precipitation energies on NO_x generation during geomagnetic storms, *J. Atmos. Sol. Terr. Phys.*, *71*, 1176–1189, doi:10.1016/j.jastp.2008.07.005.

Verronen, P. T., A. Seppälä, M. A. Clilverd, C. J. Rodger, E. Kyrölä, C.-F. Enell, T. Ulich, and E. Turunen (2005), Diurnal variation of ozone depletion during the October–November 2003 solar proton events, *J. Geophys. Res.*, *110*, A09S32, doi:10.1029/2004JA010932.

Verronen, P. T., A. Seppälä, E. Kyrölä, J. Tamminen, H. M. Pickett, and E. Turunen (2006), Production of odd hydrogen in the mesosphere during the January 2005 solar proton event, *Geophys. Res. Lett.*, *33*, L24811, doi:10.1029/2006GL028115.

von Clarmann, T., B. Funke, M. López-Puertas, S. Kellmann, A. Linden, G. P. Stiller, C. H. Jackman, and V. L. Harvey (2013), The solar proton events in 2012 as observed by MIPAS, *Geophys. Res. Lett.*, doi:10.1002/grl.50119.

Waters, J. W., et al. (2006), The Earth Observing System Microwave Limb Sounder (EOS MLS) on the Aura satellite, *IEEE Trans. Geosci. Remote Sens.*, *44*, 1075–1092, doi:10.1109/TGRS.2006.873771.

PUBL. IV

Reprinted, with permission, from
Journal of Geophysical Research: Atmospheres, 121, 6085-6100,
doi:10.1002/2015JD024217

AGU PUBLICATIONS

JGR

Journal of Geophysical Research: Atmospheres

RESEARCH ARTICLE

10.1002/2015JD024217

Key Points:
- Effect of NO_x descent and SPEs on stratospheric ozone is studied using a chemistry transport model
- In early 2012, intensified descent after SSW leads to more NH stratospheric ozone loss than SPEs
- Model includes improved parameterization of NO_y upper boundary and SPE-driven ion chemistry

Correspondence to:
S.-M. Päivärinta,
sanna-mari.paivarinta@fmi.fi

Citation:
Päivärinta, S.-M., P. T. Verronen, B. Funke, A. Gardini, A. Seppälä, and M. E. Andersson (2016), Transport versus energetic particle precipitation: Northern polar stratospheric NO_x and ozone in January–March 2012, *J. Geophys. Res. Atmos.*, *121*, 6085–6100, doi:10.1002/2015JD024217.

Received 11 SEP 2015
Accepted 13 APR 2016
Accepted article online 3 MAY 2016
Published online 25 MAY 2016

Transport versus energetic particle precipitation: Northern polar stratospheric NO_x and ozone in January–March 2012

S.-M. Päivärinta[1,2], P. T. Verronen[1], B. Funke[3], A. Gardini[3], A. Seppälä[1], and M. E. Andersson[1]

[1]Earth Observation, Finnish Meteorological Institute, Helsinki, Finland, [2]Department of Physics, University of Helsinki, Helsinki, Finland, [3]Instituto de Astrofísica de Andalucía, CSIC, Granada, Spain

Abstract In early 2012, a strong sudden stratospheric warming (SSW) took place, accompanied by several medium-scale solar proton events (SPEs). Here we use a chemistry transport model (CTM) in order to assess the relative contributions of (1) intensified downward transport of odd nitrogen (NO_x) and (2) in situ production of NO_x by protons, on stratospheric NO_x and ozone during January–March 2012. The CTM is constrained by an upper boundary condition for reactive nitrogen (NO_y) species, based on satellite observations from Michelson Interferometer for Passive Atmospheric Sounding (MIPAS) on board Envisat, and includes a new parameterization of the SPE-caused effects on NO_y and odd hydrogen (HO_x) species. We found that the amount of NO_x increases due to both transport and in situ production effects, the intensified descent of NO_x dominating the middle and upper stratospheric impact. The model results indicate NO_x enhancements of 120–3300% (5–48 ppbv) between 38 and 50 km, caused by the transport of mesosphere/lower thermosphere NO_x down to the stratosphere following the SSW. The SPEs increase NO_x by up to 820–1200% (14–21 ppbv) at 33 to 50 km. The effect on the stratospheric ozone is larger following the downward transport of NO_x than during and after the SPEs. The model predicts ozone losses of up to 17% and 9% at around 40 km due to transport and SPE effects, respectively.

1. Introduction

Solar extreme ultraviolet radiation, soft X-rays, and auroral electrons produce odd nitrogen ($NO_x = N + NO + NO_2$) constantly in the upper mesosphere and lower thermosphere [*Barth*, 1992]. In the stratosphere, the main source for NO_x is the oxidation of nitrous oxide (N_2O). The photochemical lifetime of the mesosphere/lower thermosphere (MLT) NO_x ranges from days to months in the absence of solar radiation. During the dark polar winters NO_x can be transported from the MLT region down to the lower stratosphere [e.g., *Solomon et al.*, 1982; *Funke et al.*, 2014a]. In the stratosphere, below about 50 km, NO_x can take part in chemical catalytic cycles destroying ozone [e.g., *Callis et al.*, 1991]. A change in the middle atmospheric ozone balance, in turn, could have an effect on the middle atmospheric dynamics, i.e., temperatures and winds [*Langematz et al.*, 2003; *Lu et al.*, 2008; *Kvissel et al.*, 2012] and in the end, through interaction between atmospheric waves and the mean flow, also on the regional polar climate [*Rozanov et al.*, 2005; *Seppälä et al.*, 2013; *Baumgaertner et al.*, 2011; *Rozanov et al.*, 2012].

Downward transport of NO_x can be first interrupted and then intensified by dynamical events known as sudden stratospheric warmings (SSWs). According to *Andrews et al.* [1987] and *Charlton and Polvani* [2007], major SSW events occur on a quite regular basis taking place on average once every other winter or twice every three winters in the Northern Hemisphere (NH). Note that these are averaged occurrence rates for major SSWs and large variation takes place in the occurrence and that minor SSWs are even more frequent than the major ones. In the Southern Hemisphere (SH), only one SSW event has been observed [*Newman and Nash*, 2005; *Thompson et al.*, 2005]. The hemispherical differences in the SSW occurrence rates arises from the larger planetary wave activity driven by the distribution of seamasses and landmasses in the NH. A sudden warming of the stratosphere, cooling of the mesosphere, and weakening, or even reversal, of the zonal mean zonal wind are all associated with SSWs and are in fact linked to enhanced planetary wave activity and thus enhanced wave damping in the middle atmosphere [*Matsuno*, 1971; *Limpasuvan et al.*, 2012]. During SSW events the polar vortex is either split or displaced from the pole interrupting the downward transport of long-lived tracers

from the MLT region but also simultaneously allowing mixing of polar and midlatitude air masses. Intensified descent of MLT air down to the middle atmosphere takes place after strong SSWs when the stratopause reforms at very high (even about 80 km) altitudes after the recovery of the polar vortex [*Manney et al.*, 2008; *Orsolini et al.*, 2010].

Solar proton events (SPEs) are the most impulsive particle source producing NO_x directly in the middle atmosphere, especially in the stratosphere. SPEs are sporadic but tend to occur more frequently around the solar maximum [*Jackman et al.*, 2009]. During SPEs, protons and heavier ions emitted from the Sun are guided by the Earth's magnetic field to the polar regions where they precipitate into the Earth's atmosphere, simultaneously in both hemispheres. In the atmosphere, energetic particles produce NO_x and also odd hydrogen ($HO_x = H + OH + HO_2$) through dissociation and ionization processes [e.g., *Seppälä et al.*, 2004; *Jackman et al.*, 2005; *López-Puertas et al.*, 2005; *Verronen et al.*, 2005, 2006; *Seppälä et al.*, 2008]. The effects of the SPEs on NO_x are more pronounced in the winter hemisphere where the lower level of solar radiation results in a longer chemical lifetime and thus enables the downward transport. The photochemical lifetime of HO_x is relatively short, and as a result all HO_x driven effects are local, with no further downward transport taking place.

Several previous studies have discussed the separate effects of SPEs and SSWs, accompanied by the enhanced mesosphere-to-stratosphere descent, on the middle and upper atmospheric NO_x and the possible following effects on stratospheric ozone [e.g., *Manney et al.*, 2009; *Jackman et al.*, 2008; *Randall et al.*, 2009; *Funke et al.*, 2011; *Salmi et al.*, 2011]. *Holt et al.* [2013] concluded that the largest stratospheric NO_x increases occur after December to early January SSWs followed by an elevated stratopause. The only situations where NO_x reached stratospheric altitudes and a simultaneous signal on ozone was observed are those that took place in early 2004 [e.g., *Randall et al.*, 2005; *Semeniuk et al.*, 2005] and early 2012 [*Jackman et al.*, 2014; *Päivärinta et al.*, 2013]. The 2004 case started with a SSW already in late December 2003 and was followed by intensified downward transport of NO_x in early January 2004: large amounts of additional MLT NO_x, originally produced in the lower thermosphere due to low energy particle precipitation, was transported down to the stratosphere inside the strong polar vortex reformed after the December SSW [*Clilverd et al.*, 2006, 2009]. The 2012 case started with a later, mid-January SSW, and the enhanced descent of NO_x was accompanied by in situ production of NO_x due to four SPEs during January and March.

Päivärinta et al. [2013] studied the winter/spring of 2012 but could not separate the effects and the relative importance of transport and in situ production on the stratospheric NO_x and ozone levels based only on satellite observations. Here we use the FinROSE chemistry transport model (CTM) together with satellite observations from Michelson Interferometer for Passive Atmospheric Sounding (MIPAS)/Envisat and MLS (Microwave Limb Sounder) on board the Aura satellite in order to assess the separate contributions of (1) intensified NO_x transport after the January 2012 SSW and (2) NO_x in situ production due to the early 2012 SPEs, on stratospheric NO_x, and ozone levels.

2. Modeling

FinROSE is a global three-dimensional chemistry transport model (CTM) designed for middle atmospheric studies (further developed model version of the one described by *Damski et al.* [2007]). The model dynamics (e.g., temperature, horizontal winds, and pressure) are from external sources, i.e., changes in atmospheric composition do not affect the model dynamics. Vertical wind is calculated inside the model by using the continuity equation.

In this study FinROSE is run with 72 vertical levels (about 0–80 km), a horizontal resolution of 5° × 4° (longitude × latitude) and is driven by NASA's MERRA (Modern Era Retrospective-analysis for Research and Applications) data [*Rienecker et al.*, 2011]. The model calculates distributions of 41 species in the stratosphere and MLT region taking into account both chemistry and dynamics. Only the long-lived constituents are transported. The model includes about 120 homogeneous reactions and 30 photodissociation processes. Chemical kinetic data, reaction rate coefficients, and absorption cross sections are taken from look-up-tables based on the Jet Propulsion Laboratory compilation by *Sander et al.* [2006], including updates from the available supplements. Photodissociation frequencies are calculated using a radiative transfer model [*Kylling et al.*, 1997]. In addition to homogeneous chemistry, the model also includes heterogeneous chemistry, i.e., formation and sedimentation of polar stratospheric clouds (PSCs) and reactions on PSCs. Chemistry is not defined in the troposphere, but the tropospheric abundances are given as boundary conditions.

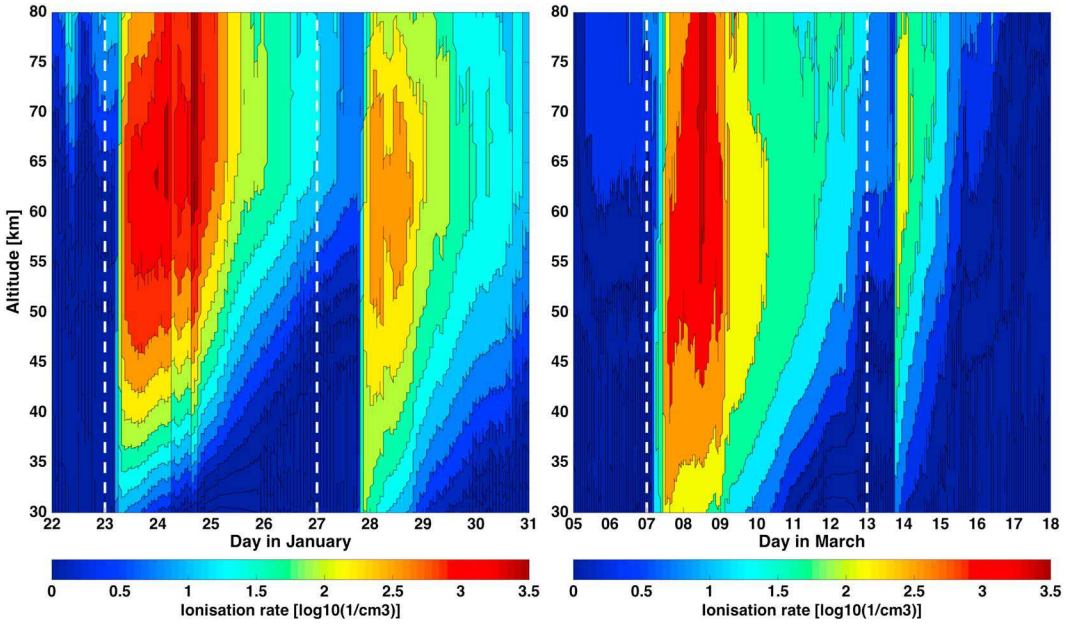

Figure 1. Ionization rates for the January and March 2012 SPEs in the upper stratosphere and mesosphere. White vertical dashed lines indicate the start days of the SPEs.

At the upper boundary, ozone is constrained by the MLS/Aura climatology and NO_y species (HNO_3, NO_2, NO, N_2O_5, and $ClONO_2$) by excess NO_y produced by energetic particle precipitation (EPP). The excess NO_y is derived from MIPAS/Envisat observations, using a tracer correlation method based on MIPAS CH4 and CO observations, and parameterized in terms of *Ap* index and seasonal evolution [*Funke et al.*, 2014a]. The upper boundary condition (UBC) in FinROSE is introduced on a daily basis only on the two upmost levels, at 0.0205 hPa (~75 km) and 0.0075 hPa (~80 km), in every model grid point in the polar areas between 70 and 90°S/N. The UBC is simply the sum of the excess NO_y and the model NO_y, calculated before the implementation of the condition. The purpose of the UBC is to give the model a source for thermospheric NO_y descending from altitudes above the model vertical grid and thus enable the downward transport of NO_x inside the polar vortex, especially following SSWs and elevated stratopause events.

Production of nitric acid (HNO_3) during SPEs has been one of the outstanding problems in understanding the atmospheric effects of EPP [*Jackman et al.*, 2008; *Funke et al.*, 2011]. Models describing atmospheric effects of EPP using the standard parameterization of HO_x and NO_x or ion chemistry too simplified for the lower ionosphere (*D* region) have greatly underestimated the amount of HNO_3 during solar proton events. FinROSE utilizes a new and revised parameterization of ion chemistry which considers the redistribution of NO_y due to negative ion chemistry [*Verronen and Lehmann*, 2013]. This parameterization is based on an ensemble of results from the Sodankylä Ion and Neutral Chemistry model [*Verronen et al.*, 2005], and it consists of a set of so-called P/Q numbers for 10 neutral species: H, OH, HNO_2, HNO_3, $N(^4S)$, $N(^2D)$, NO, NO_2, NO_3, and N_2O_5. The P/Q numbers vary with respect to the species, altitude, ionization rate, solar zenith angle, and season (through atmospheric conditions). They are used to calculate the rate of change (molecules cm^{-3} s^{-1}) for the neutral species, simply by multiplying them by the particle ionization rate. Ionization rates, in turn, are calculated using GOES 11 satellite proton flux data (available from, e.g., the NOAA National Geophysical Data Center World Wide Web server, www.ngdc.noaa.gov/stp/stp.html). GOES observations are converted to differential flux spectra, and ionization rates for every model time step, i.e., every 30 min, are then calculated using the empirical energy range relation of protons (for details, see *Verronen et al.* [2005, and references therein]). Ionization rates used in the model are presented in Figure 1.

The early 2012 SPEs in January and March were comparable with the medium scale January 2005 event with maximum proton fluxes of >6000 pfu (particles flux unit, particles cm^{-2} s^{-1} sr^{-1}). The proton fluxes during the first events both in January and in March were elevated for nine consecutive days before returning back to pre-SPE levels. More information on the 2012 SPEs is given in Table 1 and in, e.g., *Jackman et al.* [2014].

Table 1. Timings and Magnitudes of the Early 2012 SPEs[a]

	Start (Day/Month)	Peak (>10 MeV) (Day/Month)	Proton Flux (pfu)
SPE1	23/01	24/01	6310
SPE2	27/01	28/01	796
SPE3	07/03	08/03	6530
SPE4	13/03	13/03	469

[a]The four cases of SPEs indicate the different events that took place in January (SPE1 and SPE2) and March (SPE3 and SPE4).

In the text, we will refer to the January SPEs as SPE1 (first event) and SPE2 (second event) and to the March events as SPE3 (first) and SPE4 (second).

We use the World Meteorological Organization and *Charlton and Polvani* [2007] definition for major SSWs: (1) zonal mean zonal wind reversal at 10 hPa at 60°N and (2) positive temperature gradient at 10 hPa between 60 and 90°N. If only the second criterium is fulfilled, the SSW is classified as a minor SSW. According to this definition the central date for the 2012 SSW was 14 January 2012, and the warming can be classified as a strong minor SSW. The warming was followed by an elevated stratopause and intensified downward transport of MLT air. The event affected the dynamics and composition of all the middle atmosphere altitudes between 30 and 95 km. The meteorological background conditions have been discussed in more detail by *Päivärinta et al.* [2013].

We conducted four FinROSE simulations for the period of January–April 2012: (1) a control run, (2) an SPE run, (3) a UBC run, and (4) an all-encompassing run (UBC + SPE). Runs 1 and 2 were started from the same initial conditions obtained from a 10 year control run (2002–2012) with no UBC implemented for the NO_y species. Runs 3 and 4 were also started from the same initial conditions but now based on a 10 year run (2002–2012) with the UBC for NO_y implemented. Note that due to the different initial conditions of the model runs, the total effect in run 4 is not exactly the sum of runs 2 and 3 (although the difference is small).

We first, in section 4, analyze the overall behavior of FinROSE during early 2012 by contrasting the model NO_x, HNO_3, and O_3 against satellite observations from MIPAS and MLS, focusing on the SSW and SPE periods. To do this, MIPAS/Envisat and MLS/Aura averaging kernels (AKs) have been applied to the model NO_x and HNO_3 results, respectively, in order to make them comparable to the observations by eliminating issues related to the different vertical resolutions of the model and observations. For NO_x, we also show results without AKs in order to show the effect of the kernels on the agreement between the model and observations. AKs have not been applied to the FinROSE ozone results due to the very minor effect they had. For the comparison purposes we use measurements between 70 and 90°N, and model results colocated with the observation times and geolocations.

Then, in section 5, we assess the relative contributions of the intensified downward transport and the January/March SPEs on stratospheric NO_x and O_3 by comparing runs 2, 3, and 4 to the control run. In contrast to the model-measurement comparisons in section 4, where measurement AKs were applied to model results, this part of the analysis uses true polar averages (70–90°N) calculated from the "as is" model results (no AKs applied).

3. Satellite Observations

3.1. MIPAS/Envisat

MIPAS NO and NO_2 observations taken in the nominal observation mode [*Funke et al.*, 2014b] have been used to evaluate the modeled NO_x response. We use L2b version of NO (V5r_NO_221) and NO2 (V5r_NO2_221) provided by the Karlsruhe Institute of Technology/Instituto de Astrofísica de Andalucía research data processor [*von Clarmann et al.*, 2013]. In the middle- to high-latitude polar winters, typical vertical resolutions are 4–6 km in the stratosphere and 6–9 km in the mesosphere, while the single-profile precision is on the order of 5–15%. Systematic errors, dominated by non-LTE-related uncertainties, have been estimated to be less than 10%. Meaningful data are obtained in polar winters up to 70 km.

MIPAS O_3 observations (V5r_O3_225) were also taken in the nominal mode [*von Clarmann et al.*, 2013]. The single measurement precision ranges from 0.1 ppmv around the stratopause to 0.25 ppbv above and below. Vertical resolution is 3–4 km below 1 hPa and 5–7 km above. Meaningful data are obtained in the whole vertical range of interest (25–70 km).

3.2. MLS/Aura

We use observations from the MLS instrument on board the Aura satellite [*Waters et al.*, 2006] in order to study the HNO_3 response on the early 2012 SPEs. We utilize Version 4.2 Level 2 daily mean HNO_3 data for the whole period of interest and for the latitudinal band of 70–82.5° in the NH. The data were screened according to the MLS data description and quality document [*Livesey et al.*, 2015]. The recommended altitude range for MLS HNO_3 data is normally 40–45 km (2.15–1.5 hPa) [*Santee et al.*, 2007; *Livesey et al.*, 2015]. During large SPEs, however, significant HNO_3 enhancements in the upper stratosphere and lower mesosphere improve the signal-to-noise ratio of the observations. In fact, *Verronen et al.* [2011] have shown that it is possible to use the data to study SPE-related changes up to about 70 km (0.046 hPa). For this data, the standard error of the mean varies between 10 and 60% for the SPEs in January and early March above 45 km, i.e., in the region where the HNO_3 enhancements due to particle precipitation mainly takes place. For the mid-March SPE, the standard error of the mean (SEM) increases up to more than 600%, indicating worsening of the signal-to-noise ratio. The vertical resolution of HNO_3 above 30 km (10 hPa) varies between 3 and 5 km. Note that we only use MLS nighttime (solar zenith angle >100°) observations in our study.

4. Model-Measurement Comparison

Figure 2 shows the distribution of January to early April NO_x from MIPAS and FinROSE (SPE and UBC both applied, i.e., run 4) with (bottom row) and without (top row) AKs being applied to the model results and also the relative difference between them (FinROSE-MIPAS). The agreement between MIPAS and FinROSE is reasonably good: the timing of the descent, starting few days after the mid-January SSW, and the altitudes affected by the descent (~30–75 km) show very similar features, both in the observations and in the model results, both with and without the AKs. In fact, the 10 ppbv NO_x isolines of MIPAS and FinROSE agree well during the whole period from the mid-January SSW to early April.

From early to mid-January the model (AKs applied) shows enhanced amounts of NO_x (8–30 ppbv) between 37 and 65 km, not detected in the observations, leading up to 250% differences between the simulated and observed NO_x. Also, during the period of intensified descent, following the mid-January SSW, there is a model overestimation by up to 135% in the same altitude region. When strong in situ NO_x production occurs due the January SPEs, there is a better agreement between the model and observations. In the stratosphere, below about 40 km, FinROSE suggests up to 70% lower NO_x amounts than observed by MIPAS. Note that all the above differences are larger when AKs are not applied to FinROSE results. Above 65 km, the model without AKs overestimates NO_x before the mid-January SSW, whereas with AKs there is an underestimation by up to 60%.

The model underestimation below 40 km (Figure 2, bottom row, AKs applied) is related to a rather low NO_x background in FinROSE. This has been seen, for example, during multimodel-measurement comparisons (i.e., the so-called HEPPA2 project, not shown). The underestimation above 65 km is caused by two things:

1. The application of AKs in the case of NO is tricky because the NO retrieval response in the mesosphere is affected by the thermospheric column. In other words, the MIPAS AKs would work better if applied to the full NO profile (0–200 km). FinROSE (as many other models), however, has no thermosphere included.
2. The UBC used in the model runs is the parameterized MIPAS excess NO_y (not the observed one). The parameterization does neither account for dynamical intra-annual variability (not a big issue in 2012) nor for SPEs (an issue in 2012).

An important factor strongly affecting the model results and the simulated downward transport of NO_x is the meteorological data (see section 2) used in the model. When comparing temperature profiles between the observations and model (Figure 3), it is clear that the reanalysis temperatures are 5–25 K (4–14%) higher above 60 km than the MIPAS observations. This results in stronger downward transport of MLT air to the middle atmosphere in the simulations using the reanalysis data, explaining at least partly the larger NO_x abundances in the lower mesosphere after the SSW. Also, some features in early 2012, especially the elevated stratopause

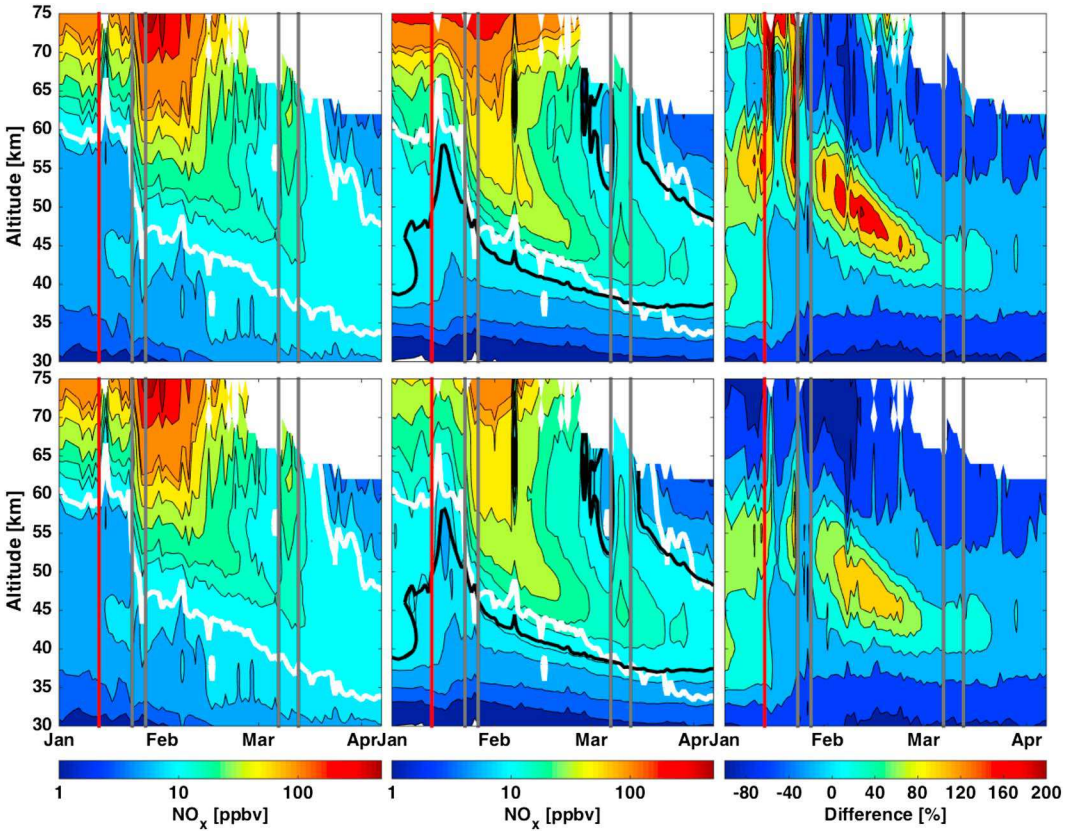

Figure 2. January to early April NO_x (ppbv) between 30 and 75 km from (left column) MIPAS and (middle column) FinROSE-CTM (UBC and SPE both applied) (top row) without and (bottom row) with averaging kernels being applied to the model results. (right column) The difference (%) between FinROSE and MIPAS. The overlaid contours are values of 1, 3, 5, 8, 10, 15, 20, 30, 50, 80, 100, 250, 500 ppbv and −100, −60, −20, 20, 60, 100, 150, 200% for the absolute values and difference, respectively. The white contour in Figure 2 (left and middle columns) denotes the MIPAS and the bold black contour in Figure 2 (middle column) the FinROSE 10 ppbv isoline for NO_x. The vertical red line shows the time point of the SSW and the vertical gray lines the time points of the SPEs.

after the SSW, are not perfectly prescribed since the UBC parameterization does not account for interannual dynamical variability.

In addition to the UBC, another factor strongly affecting the modeled NO_x is the parameterization of its production during the January and March SPEs. It is clear from Figure 2 that there is good agreement in timing of the SPEs between the simulation (with and without AKs) and observations. MIPAS shows that NO_x amounts increase substantially during the SPEs, and FinROSE is able to reproduce these enhancements reasonably well. For example, at 60 km SPE1 increases MIPAS NO_x by about 70 ppbv, while FinROSE underestimates the production by 28%, with AKs applied. Note that if AKs are not applied, the underestimation is less than 3%. Similarly, the NO_x production by SPE3 is underestimated, e.g., by 10–15 ppbv at 60 km.

Figure 4 shows time series of the observed and modeled (AKs applied) NO_x in the upper stratosphere (46 km) and lower mesosphere (60 km). In addition to the all-encompassing model run discussed earlier in this section, we also present model results from the control run (no SPEs or UBC for NO_x included), SPE run (only SPEs included) and UBC run (only UBC included). It is clear that by introducing the NO_y UBC to the model, the agreement between the observations and model improves drastically both in the upper stratosphere and lower mesosphere. By including only the effect of the SPEs, the model behavior in the upper stratosphere improves only during SPE1 and SPE2, but becomes worse after mid-February when the MLT NO_x, not included in the model in this model run, descends lower in the atmosphere. In the lower mesosphere, the SPE run underestimates the amount of NO_x throughout the period from January to early March. Due to the meteorological data and the too strong NO_x descent in the model, the all-encompassing run overestimates the amount of

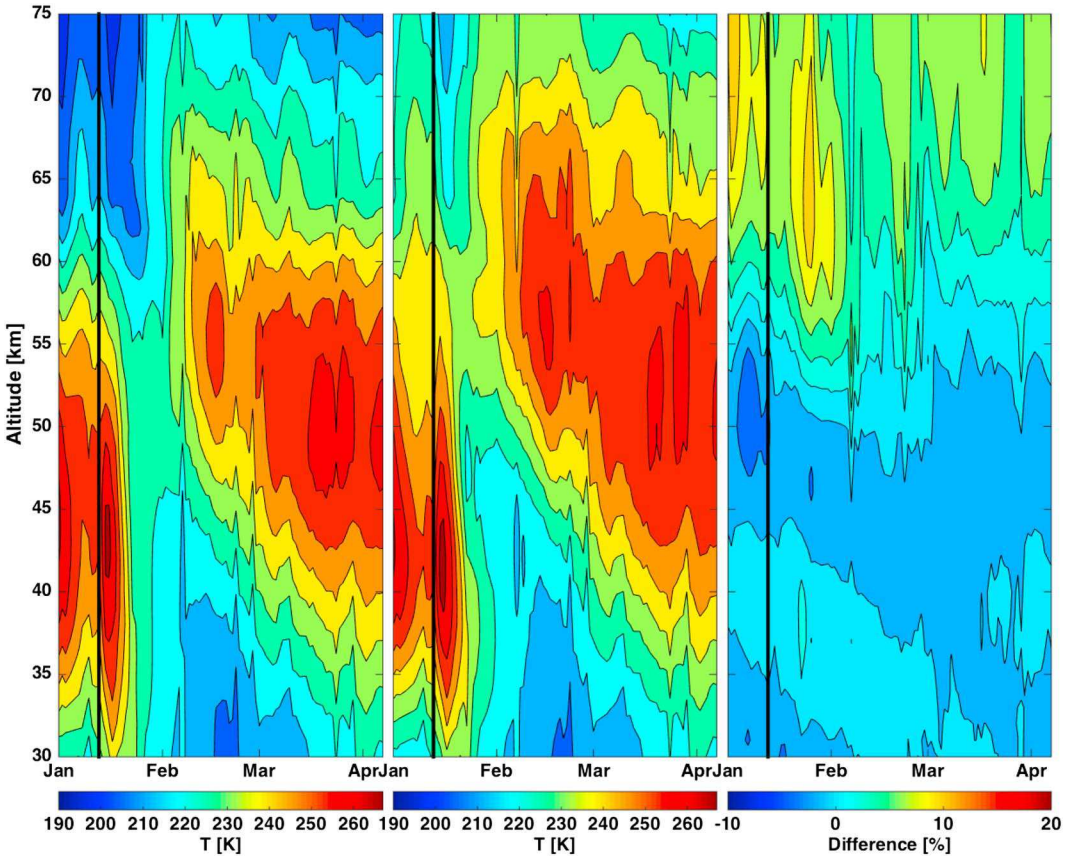

Figure 3. January to early April temperatures (K) between 30 and 75 km from (left) MIPAS and (middle) FinROSE-CTM with averaging kernels being applied to the model results. (right) The difference (%) between the observations and the CTM. The overlaid contours are values of 190–267 K with 7 K level step and −10–20% with 2% level step for the absolute values and difference, respectively. The vertical black line shows the time point of the SSW.

NO_x in the upper stratosphere, as discussed earlier in this section. The agreement between the observations and model is worst when no UBC or SPE parameterization is included in the model.

Figure 5 shows HNO_3 in early 2012 from the middle stratosphere to upper mesosphere as observed by MLS and simulated by the model (all-encompassing run 4). The background level of HNO_3 above 40 km is very similar in both (<1 ppbv), as well as the stratospheric HNO_3 maximum below 40 km (<4–5 ppbv). SPE1 increases HNO_3 by <3 ppbv between 45 and 75 km according to the observations, but even up to 6 ppbv in the simulation. This indicates more than 100% overestimation by the model during a time period when MLS measurement error is not more than about 20%. During SPE2 and SPE3, the agreement is reasonable with only 20–40% difference between 55 and 65 km, fitting inside the MLS measurement error limits of 20–100%. The overall effects extend from 45 to 70 km with HNO_3 increases up to ~2 ppbv both in MLS and in FinROSE. MLS shows, however, a rapid return of the HNO_3 back to the background levels above about 53 km 2 days after SPE3 and then again an increase back to the enhanced levels. This double peak structure is not captured by the model simulations and leads to an overestimation of about 1 ppbv followed by an underestimation of <3 ppbv. The model behavior reflects the SPE ionisation rates which start to decrease after 9 March and continue doing so until the next event on 13 March (see Figure 1). Also, the measurement error of MLS observations during this time period increases rapidly up to more than 600%, indicating a large uncertainty in the observations. SPE4 did not have a significant effect on HNO_3: according to the observations, only an increase of about 1 ppbv took place between 45 and 56 km, but this was not as clearly linked to the SPEs as the previous events, and the uncertainty of the observations was of the same magnitude as those following SPE3. In the model, SPE4 appears to have no effect on the HNO_3.

Figure 6 shows the ozone comparison between MIPAS and FinROSE (all-encompassing run 4). The overall distribution of ozone is more or less similar in the model and in the observations. The largest differences arise

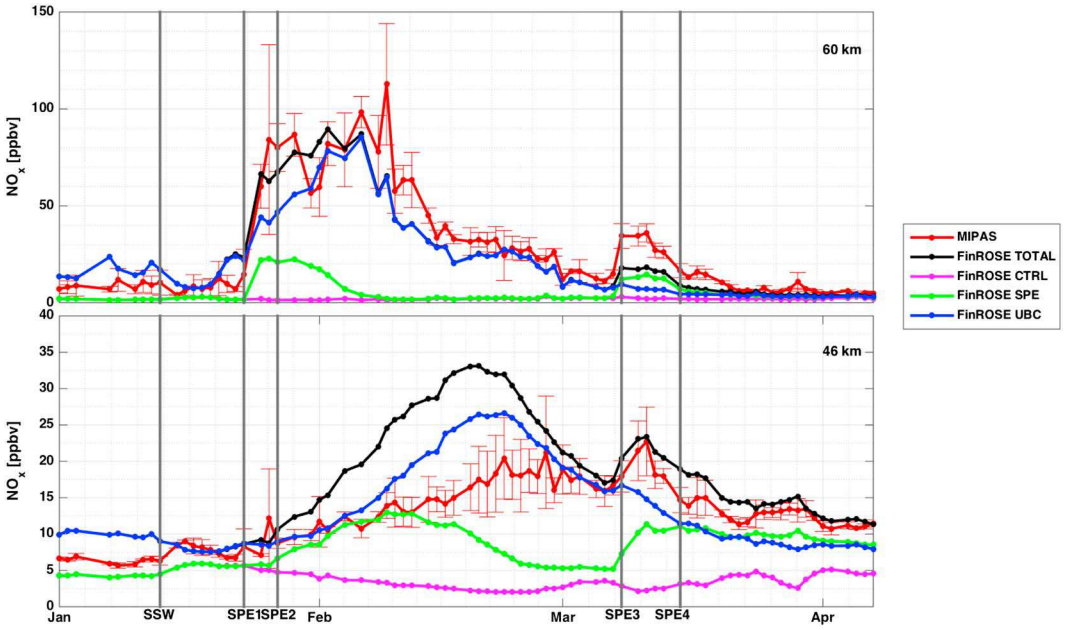

Figure 4. NO_x (ppbv) time series during January to early April in the lower mesosphere (top, 60 km) and the upper stratosphere (bottom, 46 km) as observed by MIPAS (red) and simulated by FinROSE-CTM (averaging kernels applied). All model runs are included in the figure: (1) control (magenta) run, (2) SPE (green) run, (3) UBC (blue) run, and (4) all-encompassing (black) run. MIPAS measuring errors (2*SEM) are plotted as error bars together with the observations. The vertical dark gray lines indicate the time points of the SSW and SPEs.

from the location of the stratospheric ozone layer (situated about 5 km lower in the middle atmosphere in FinROSE) and the mesospheric ozone amounts (generally about 70% lower in FinROSE). As mentioned above, the model/reanalysis temperature close to the stratopause is higher than observed. According to *Sofieva et al.* [2012], temperature and ozone are anticorrelated in the mesosphere and also in the upper stratosphere [e.g., *Smith*, 1995; *Smith et al.*, 2009; *Damiani et al.*, 2010]. In this case, the too low ozone values in the model mesosphere could thus be partly explained by the too high temperatures in the same region, but also due

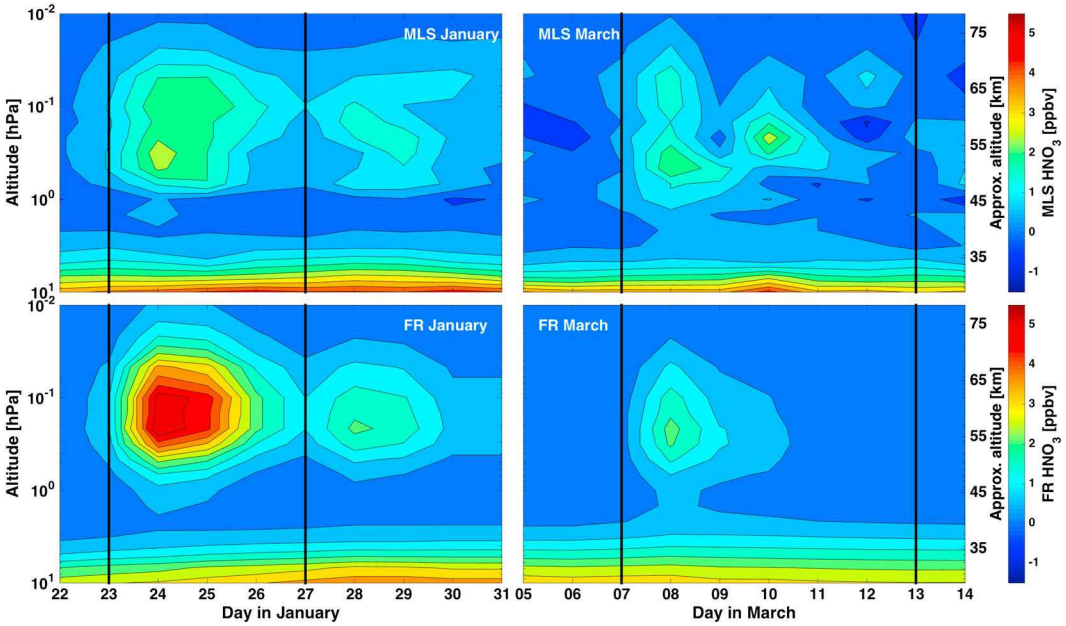

Figure 5. HNO_3 (ppbv) between 30 and 75 km from (top row) MLS and (bottom row) FinROSE-CTM (UBC and SPE both applied) for the (left column) January and (right column) March SPEs.

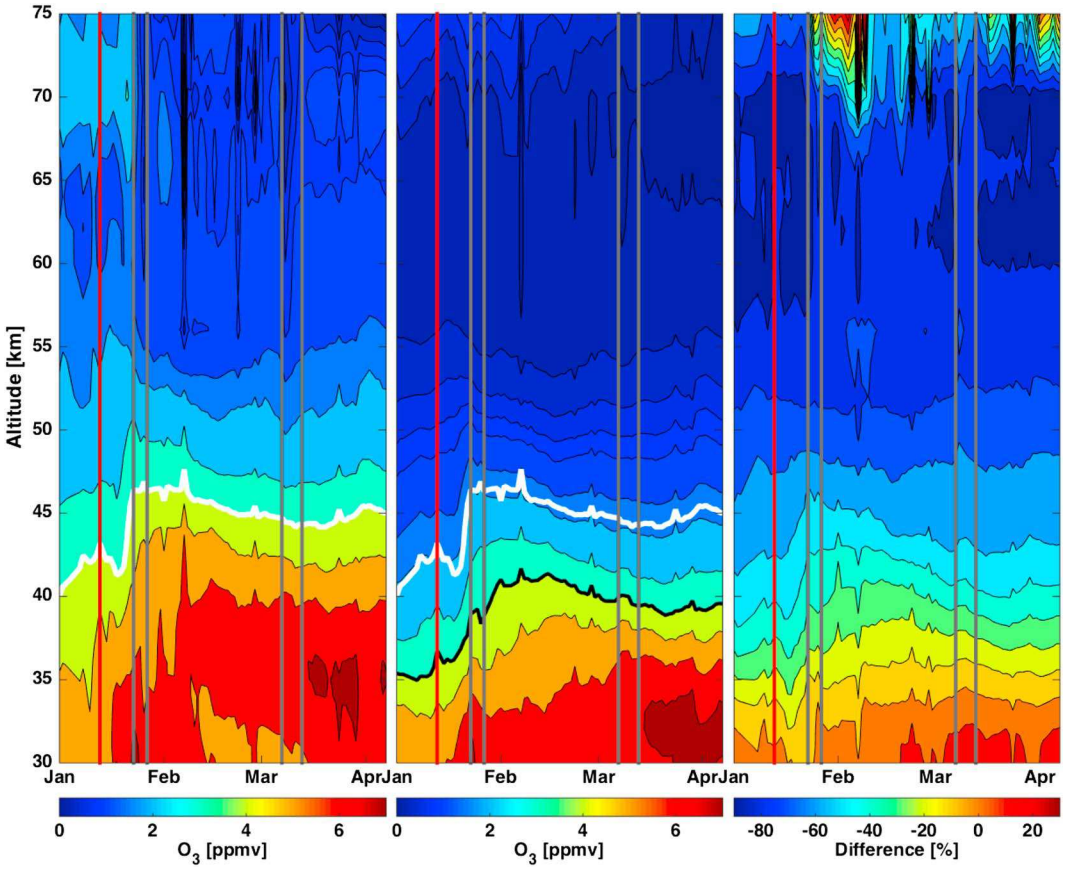

Figure 6. Same as Figure 2, but for ozone and without AKs. Here the overlaid contours are values of 0, 0.2, 0.4, 0.6, 0.8, 1, 1.5, 2, 3, 4, 5, 6, 7 ppmv and −90, −80, −70, −60, −50, −40, −30, −20,−10, 0, 10, 20, 30% for the absolute values and difference, respectively. (left and middle) The white contour denotes the MIPAS and the bold black contour in Figure 6 (middle) the FinROSE 4 ppmv isoline for O_3.

to the vicinity of the upper boundary and thus the possible lack of some MLT processes that would completely describe ozone in this region. On the other hand, the temperature comparison in Figure 3 indicates significant dynamical biases in the model relative to observations. This may be another reason for the ozone differences. A smaller part of the mesospheric differences can also be explained by the positive bias of MIPAS ozone observations [*Laeng et al.*, 2014].

The effects of the SPEs on observed ozone are evident in Figure 6. The observed amount of ozone decreases by 35–50% above 55 km after SPE1 and by up to 60% above 74 km after SPE2. In the middle mesosphere, above about 60 km, ozone starts to return back to the pre-SPE levels after SPE2, maximizing by the beginning of February. In the model, the timing of the ozone loss in connection to the SPEs is correct, but the magnitude of the absolute loss differs by 70–80%. Of course, the background level of the simulated ozone was lower already in the beginning, and therefore, all changes in ozone appear to be larger, at least farther away from the upper boundary. The vicinity of the upper boundary (MLS climatology) affects the altitudes above 75 km, possibly explaining at least some of the ozone differences in the upper mesosphere. However, the behavior of ozone in the middle mesosphere after SPE2, i.e., the increase in ozone back to the SPE preceding levels, is reproduced also by the model. Clear ozone losses are also observed after SPE3. The event has an effect even down to about 48 km with ozone decreasing by ∼10–40%, whereas SPE4 seems to have effect only above about 72 km, i.e., close to the upper limit of the observations, with ozone losses of up to 90%. For SPE4, the simulation and observations differ by 10–90% both in the middle and upper mesosphere.

Figure 7 shows time series of the observed and modeled ozone in the upper stratosphere (46 km) and lower mesosphere (60 km), similar to Figure 4 presented earlier. Due to the clearly lower absolute values of ozone in the model, we have multiplied the results with a factor of 4 and 2 in the stratosphere and mesosphere, respectively, in order to aid the comparison of variability. The general variability in ozone during January to

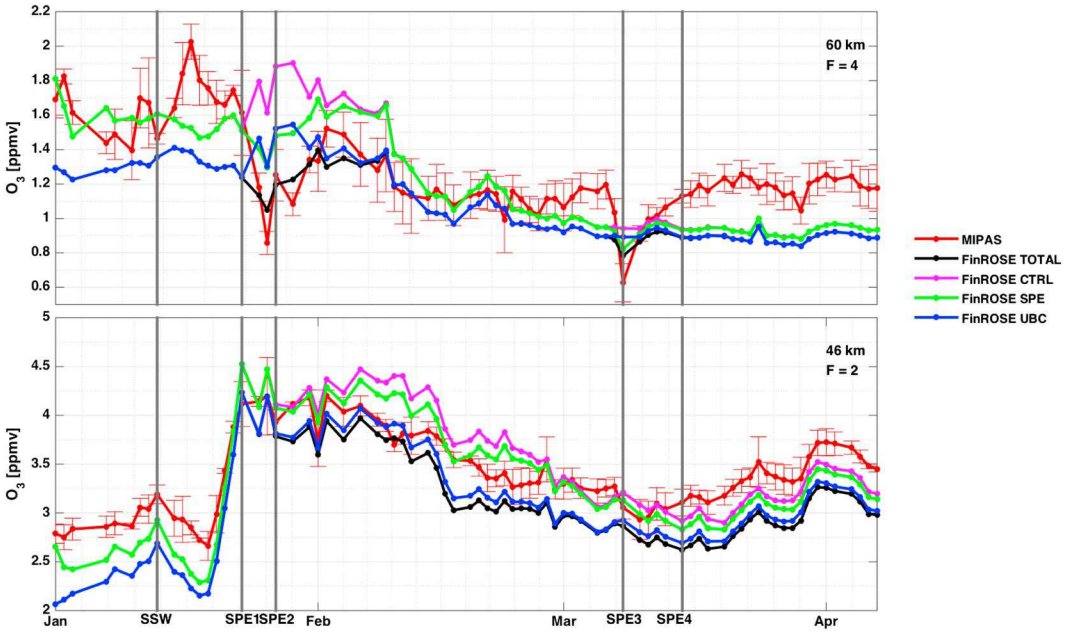

Figure 7. Same as Figure 4 but for ozone. The absolute values of the modeled ozone are multiplied with a factor of 4 ($F=4$) and 2 ($F=2$) in the mesosphere and stratosphere, respectively, in order to aid the comparison with the observed values.

early April is very similar in the model results and in the observations, although the absolute values differ greatly. However, only the all-encompassing and SPE run are able to reproduce the ozone depletion due to radicals such as NO_x and HO_x, the effect being stronger in the mesosphere. The NO_y UBC applied in the UBC and all-encompassing runs decrease the absolute values of ozone during the whole period of interest.

According to the model-observation comparison, the model performance seems to be in a reasonable agreement with the observations. This gives us a good basis for analyzing the separate contributions of transport and in situ forcing on the stratospheric NO_x and ozone. However, the comparison revealed also differences that might affect the contribution analysis to some extent. The downward transport of NO_x after the SSW in mid-January was stronger in the simulation and led up to 135% higher NO_x amounts during the most intense descent above about 40 km, possibly leading to an overestimation of the respective ozone loss in the stratosphere. Differences of up to 110% took place also after the SPEs in the mesosphere, but the agreement (~20%) in the stratosphere was reasonably good. The simulated amount of ozone in the stratosphere was lower down to ~33 km, and NO_x produced ozone losses above this level may thus be overestimated since the model is sensitive to even quite small changes. Due to the stronger NO_x descent from the MLT down to the stratosphere and the lower ozone amounts in the same region in the simulations, the contribution analysis should be considered to represent the maximum changes in both NO_x and ozone in the middle atmosphere.

5. Contributions of Transport and In Situ Forcing

Figure 8 shows NO_x in the control run, averaged over 70–90°N, and the changes due to UBC and SPEs (applied separately and together in runs 2–4) compared to the control run. The largest effect in the mesosphere, above about 50 km, arises from the implementation of the UBC (shown also in Figure 4). Changes of the order of 4–80 ppbv between 50 and 70 km are visible already from the beginning of the year due to descent of MLT NO_x inside the polar vortex (not seen by MIPAS, see section 4). The descent was interrupted by the mid-January SSW but continued again after reformation of the polar vortex shortly after the SSW. Between 70 and 80 km NO_x increases by 35–650 ppbv in early to mid-January, propagating with elevated levels down to about 50 km after the SSW in mid-January. Strongest descent of NO_x lasts until the end of March bringing 4–7 ppbv (100–300%) more NO_x down to even 45 km, although signs of increased NO_x are visible still in late April.

The mesospheric effects of the January/March SPEs on NO_x maximize during the events with magnitudes of even 36 ppbv above 60 km. The enhanced NO_x is transported downward inside the polar vortex so that the effects of the January SPEs are visible only about 2 weeks above 60 km with NO_x increases of 0.1–36 ppbv but

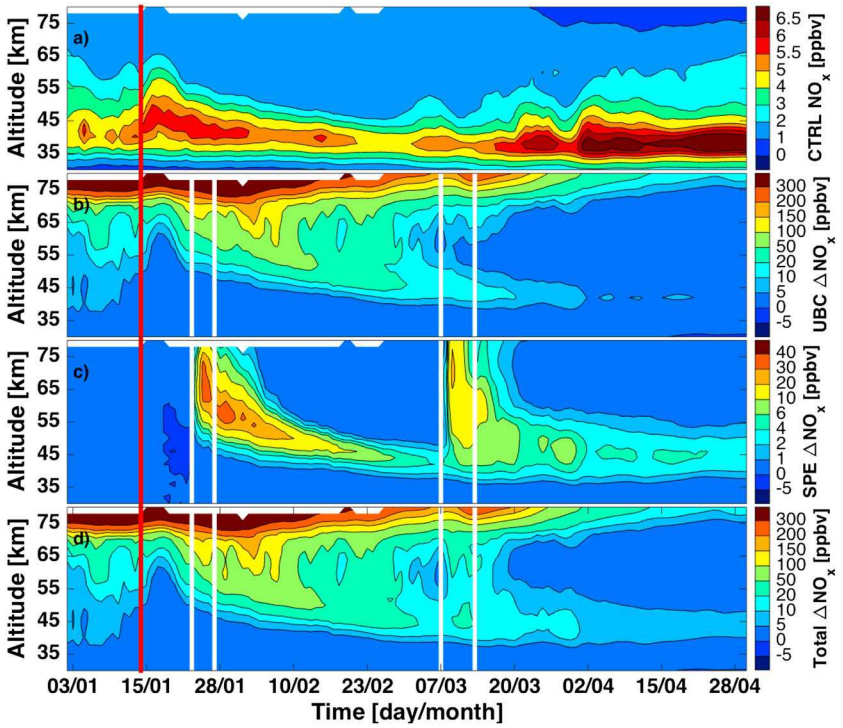

Figure 8. FinROSE NO_x results in January–April 2012. (a) Run 1 (control). (b) Difference between the UBC and control runs. (c) Difference between the SPE and control runs. (d) Difference between the all-encompassing (UBC + SPE) and control runs. White lines indicate the time points of the SPEs and the red solid line the SSW.

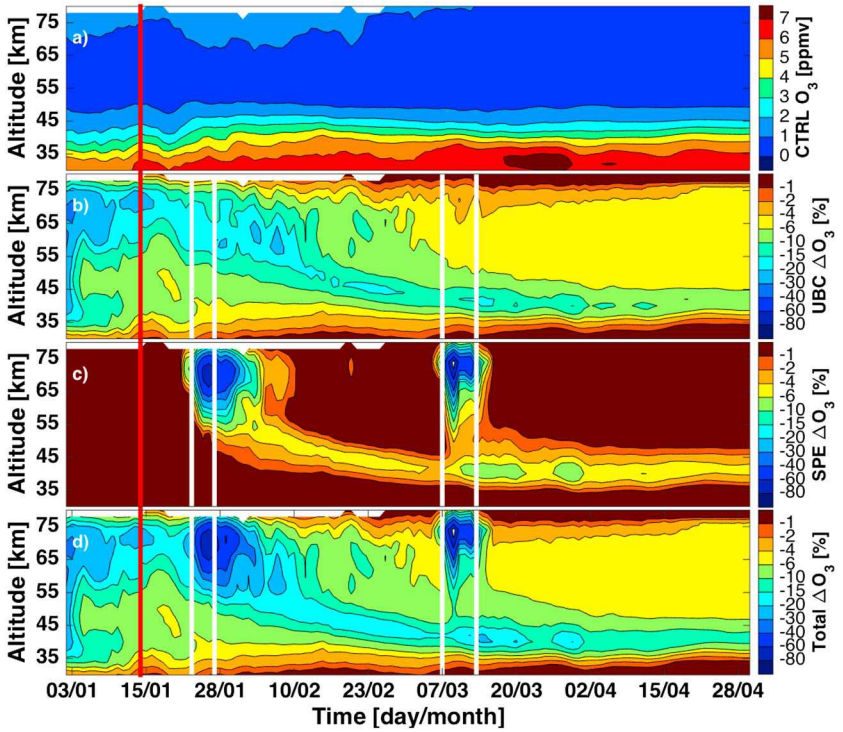

Figure 9. Same as Figure 8 but for ozone.

Table 2. Maximum Ozone Loss (%) After Sudden Stratospheric Warming and Solar Proton Events in Early 2012[a]

	30–50 km (%)	50–60 km (%)	60–75 km (%)
SPE	9	22	87
UBC	17	24	24

[a]Changes are calculated separately for the SPE (all events included) and UBC effects for the given altitude ranges in the stratosphere and mesosphere.

remain even longer than 1 month below 60 km with same order of magnitude increases. The March SPEs have a more constant effect on NO_x in the vertical direction due to the already weakened downward transport after the SSW in January. Above 50 km NO_x increases by 0.1–22 ppbv after SPE3, and the effect seems to remain from 1 to 2 months at upper to lower mesospheric altitudes, respectively. SPE4 increases the amounts only between 53 and 67 km by 0.2–15 ppbv.

In the stratosphere, below about 50 km, NO_x descends down to about 36 km with mixing ratios of ~1.3 ppbv by early March, indicating an increase of at least about 30% only due to the implementation of the UBC. Just at and below the stratopause region the changes are maximizing with NO_x increases up to 60 ppbv between early and late February. When analyzing the SPE run, it is clear that the in situ production, taken into account at all stratospheric altitudes, causes NO_x to increase by up to 21 ppbv after the January and 14 ppbv after the March SPEs. The effect of the January SPEs descends down to about 35 km by SPE3, after which the effect can be seen as low as 33 km altitude. The NO_x increase after the March SPEs does not descend much lower in the stratosphere, but the effect stays visible until the end of April.

Figure 9 shows the corresponding changes in ozone. The UBC effect on mesospheric ozone is visible already in the beginning of January with ozone losses of 30–40%, coinciding with the enhanced amounts of NO_x in the model. After the mid-January SSW, ozone losses are around 15–20% during the most intense NO_x descent but recover by about 10% by early March. The stratospheric ozone changes are less pronounced compared to those in the mesosphere: the implementation of the UBC, and the following downward transport of NO_x, causes ozone to decrease by up to ~30% in January before the SSW and up to ~15% after the SSW from 30 to 50 km.

Contrary to the NO_x enhancements, which are largely due to descent, the most substantial ozone decrease in the mesosphere is caused by the SPEs. The decrease is clear throughout the whole mesosphere during and shortly after (from days to couple of weeks) the SPEs, maximizing around 70 km with ozone losses up to ~90%. According to previous studies of the effects of different SPEs in the middle and upper atmosphere [e.g., *Verronen et al.*, 2006], the in situ mesospheric ozone losses during the SPEs are mainly caused by the increased HO_x production in the same region. Note that FinROSE ozone response is in agreement with the results presented for the same SPEs by *Jackman et al.* [2014].

Between 50 and 60 km, up to ~20% ozone loss is still visible 1–4 weeks after the SPEs due to downward transport of the SPE produced NO_x. The altitude range (30–50 km) for the stratospheric ozone changes is very similar for both UBC and SPE cases. However, in this region, the SPE effects on ozone are about a factor of 2 smaller compared to the UBC effects, and the model suggests ozone losses of up to about 10% after the January/March SPEs. Ozone changes due to the indirect UBC effect (NO_x downward transport) and SPE effect at different mesospheric and stratospheric altitudes, calculated from the SPE and UBC runs, are presented in more detail in Table 2.

6. Discussion

Päivärinta et al. [2013] showed that both short-term and long-term ozone changes were observed in early 2012 after intensified NO_x descent from MLT down to the stratosphere, following a SSW in mid-January, and in situ production of NO_x due to several SPEs in January/March. They concluded that the short-term (few days) ozone losses in the mesosphere were driven by HO_x chemistry, but they could not separate the effects of transport and SPEs on the longer-term (weeks) ozone depletion in the mesosphere and upper stratosphere by using only satellite observations. Our model results show that the indirect UBC effect brings much larger NO_x amounts (7–48 ppbv) below the stratopause level than the SPE effect (<21 ppbv) for these particular events.

The enhanced NO_x in the stratosphere, in turn, further affects the stratospheric ozone levels. According to the model, the indirect UBC effect on ozone is double (see Table 2) compared to the SPE effect, directly connected to the NO_x amounts in the stratosphere.

An interesting feature in the model results is the middle mesospheric ozone decrease (e.g., 30–40% at 65–75 km in early January) caused by the NO_y UBC forcing (Figure 9). The same effect is also seen in the all-encompassing run before the January SPEs as well as between the January and March SPEs. The NO_x catalytic cycles depleting ozone are not important in mesosphere [e.g., *Grenfell et al.*, 2006]. Thus, the ozone decrease seems to be related to changes in the HO_x nighttime partitioning and loss caused by the NO_x enhancement, which lead to increase in the daytime HO_x amount and ozone loss rates [*Verronen and Lehmann*, 2015]. Indeed, comparing the UBC and control runs, we find that the nighttime HO_x partitioning changes below 75 km (not shown). As seen in Figure 9, this leads to a longer-term effect on ozone lasting from early January to mid-February, contrary to the short-term (but larger) effect caused by the direct HO_x increase during SPEs. The stronger ozone effect in January, compared to February when the model actually shows larger NO_x amounts, is due to the enhanced amounts of NO_x strongly affecting ozone already in late 2011 (not shown). NO_x decreases from the December values in January due to polar vortex dynamics, which leads to ozone recovery in early January (Figure 9). However, this recovery is relatively slow, and thus, the January ozone depletion is higher than what is seen in February. Also, the HO_x partitioning effect caused by high NO_x is relatively stronger in January than in February (not shown).

Funke et al. [2011] reported the effects of the 2003 October/November SPEs on the middle and upper atmosphere composition by using both observations and several atmospheric models, including the FinROSE-CTM. They concluded that models using an incomplete SPE parameterization in order to reproduce the observed HNO_3 increases seem to, in general, underestimate the HNO_3 amounts considerably. The new and revised parameterization used in this study shows significant improvement in reproducing of HNO_3 observations during the SPEs. Although the model somewhat overestimates the amount of HNO_3 when contrasted to the observations (a factor of <2.7 in January and <1.4 in March), the simulated results are clearly in reasonable agreement with the observed magnitude and altitude extent of the enhancements. MLS errors (standard error of the mean) grow up to 60% and 100% above 45 km during the January (SPE1 and SPE2) and March (SPE3) events, respectively, possibly explaining part of the differences. Note that uncertainties in the parameterization of HNO_3-producing ion chemistry are not the main reason for the model overestimation during SPE1 (in fact, during all other SPEs the modeled values are in much better agreement with the observations). First, understanding of the ionic reactions and rates affecting HNO_3 is satisfactory [*Verronen et al.*, 2011]. Second, although the parameterized HNO_3 production factors used here have additional uncertainty due to assumptions made on atmospheric composition when deriving them, according to *Verronen and Lehmann* [2013], this should be of the order of 24%. Instead, the FinROSE-MIPAS differences are better explained by relatively large measurement uncertainty (as mentioned above), and uncertainties of the reanalysis data (temperature, winds, and total density) used in the model (see final paragraph of this section). The reanalysis data are important here because they drive polar vortex dynamics that have been shown to have a strong effect on the day-to-day distribution of SPE-produced HNO_3 [*Verronen et al.*, 2011].

Note that the early 2012 SPEs took place during a rather weak solar maximum, and the background MLT NO_x production by energetic particles was low. Relatively low amounts of NO_x were transported down to the stratosphere, and although combined with the small to medium-strength SPEs, a clear NO_x-dominated impact on stratospheric ozone was not observed [*Päivärinta et al.*, 2013]. The FinROSE results do, however, show that the transport from MLT to lower atmosphere plays a very important role in the stratospheric NO_x-ozone connection, even on a time scale of weeks to months.

The results of the contribution analysis in this study are based on CTM results only. Although the model performs reasonably well when compared to observations, the results have to be considered as an estimation. As already mentioned in section 4, the too strong NO_x descent from MLT down to the stratosphere in FinROSE, and lower ozone amounts in the same region, indicates that our results could overemphasize the transport effect during periods of intensified descent. Nevertheless, the overlapping timing of the different events at this time provided us with an opportunity to utilize an atmospheric model to separate the roles of in situ (i.e., SPE) and transport effects on middle atmospheric composition. This is not straightforward with most satellite observations. The meteorological input for the CTM is reanalysis data, i.e., produced by numerical models, and thus a source for uncertainty, even though they are based on assimilating observations into the

models. Differences in various reanalysis data have been discussed by, e.g., *Martineau and Son* [2010] and *Lawrence et al.* [2015]. In fact, some further testing (not shown) suggests that using another reanalysis data set leads to a different vertical and horizontal distribution of the simulated species, e.g., through changes in the descent rates, although the main features of the SPE effect and indirect UBC effect still remain the same. However, the differing dynamical variables seem to lead to, e.g., lower modeled HNO_3 amounts during the January/March SPE periods. A detailed analysis of the impact of changing the meteorological input in the CTM is beyond the scope of this paper and a topic of a future study. Yet this emphasizes the real need of reliable meteorological input data for atmospheric models in order to reproduce the observed fields as well as possible but also the need of continuous satellite observations in the stratosphere and MLT region to be used in both assimilation processes and validating the models.

7. Conclusions

We have assessed the relative contributions of indirect and direct effects on the stratospheric NO_x and ozone in the Northern polar cap area (70–90°), using a CTM with an UBC for the NO_y species and an improved parameterization scheme for the early 2012 SPEs. The results show that the amount of NO_x increased due to both effects, but more pronounced stratospheric impact, was caused by the intensified downward transport of NO_x after the mid-January SSW. The model suggests NO_x enhancements of up to 3300% (<48 ppbv) just below the stratopause level (~50 km), and even up to 120% (5 ppbv) as low as 38 km altitude. The SPE effect on NO_x was visible at the same stratospheric altitudes as increased NO_x amounts of up to 1200% (<21 ppbv) above 35 km and up to 820% (<14 ppbv) above 33 km were simulated after the January and March SPEs, respectively. The following effect on the stratospheric ozone was greater for the indirect UBC effect, leading to ozone losses of up to 17%, whereas the SPE effect caused ozone losses of 9%.

Although the conditions in early 2012 were not ideal, due to the small/medium magnitude of the SPEs and low background production of NO_x in the MLT region, stratospheric signal on both NO_x and ozone was still evident in both cases. This emphasizes the importance of both middle atmosphere dynamics and the geomagnetic activity on the chemical composition of the stratosphere, possibly propagating farther down into the troposphere. Continuation of middle atmosphere observations and high-quality reanalysis data is needed in order to investigate the MLT-stratosphere connection also during periods of high solar activity when the combination of optimal dynamics (i.e., intensified downward transport following SSWs), and EPP is likely to have even greater impact in the stratosphere.

Acknowledgments

The work of S.M.P., P.T.V., A.S., and M.E.A. was supported by the Academy of Finland through the projects 276926 (SECTIC: Sun-Earth Connection Through Ion Chemistry), 258165, and 265005 (CLASP: Climate and Solar Particle Forcing). The work of B.F. and A.G. was supported by the Spanish MCINN under grant AYA2011-23552 and EC FEDER funds. MIPAS/Envisat and MLS/Aura data are provided by European Space Agency (ESA) and National Aeronautics and Space Administration (NASA), respectively. The FinROSE data supporting the analysis and conclusions have been archived and are available upon request from the corresponding author.

References

Andrews, D. G., J. R. Holton, and C. B. Leovy (1987), *Middle Atmosphere Dynamics*, pp. 259–260, Academic Press, New York.

Barth, C. A. (1992), Nitric oxide in the lower thermosphere, *Planet. Space Sci.*, *40*, 315–336.

Baumgaertner, A. J. G., A. Seppälä, P. Jöckel, and M. A. Clilverd (2011), Geomagnetic activity related NO_x enhancements and polar surface air temperature variability in a chemistry climate model: Modulation of the NAM index, *Atmos. Chem. Phys.*, *11*, 4521–4531, doi:10.5194/acp-11-4521-2011.

Callis, L. B., D. N. Baker, J. B. Blake, J. D. Lambeth, R. E. Boughner, M. Natarajan, R. W. Klebesadel, and D. J. Gorney (1991), Precipitating relativistic electrons: Their long-term effect on stratospheric odd nitrogen levels, *J. Geophys. Res.*, *96*, 2939–2976.

Charlton, A. J., and L. M. Polvani (2007), A new look at stratospheric sudden warmings. Part I: Climatology and modeling benchmarks, *J. Clim.*, *20*, 449–469, doi:10.1175/JCLI3996.1.

Clilverd, M. A., A. Seppälä, C. J. Rodger, P. T. Verronen, and N. R. Thomson (2006), Ionospheric evidence of thermosphere-to-stratosphere descent of polar NO_x, *Geophys. Res. Lett.*, *33*, L19811, doi:10.1029/2006GL026727.

Clilverd, M. A., A. Seppälä, C. J. Rodger, M. G. Mlynczak, and J. U. Kozyra (2009), Additional stratospheric NO_x production by relativistic electron precipitation during the 2004 spring NO_x descent event, *J. Geophys. Res.*, *114*, A04305, doi:10.1029/2008JA013472.

Damiani, A., M. Storini, M. L. Santee, and S. Wang (2010), Variability of the nighttime OH layer and mesospheric ozone at high latitudes during northern winter: Influence of meteorology, *Atmos. Chem. Phys.*, *10*, 10,291–10,303, doi:10.5194/acp-10-10291-2010.

Damski, J., L. Thölix, L. Backman, J. Kaurola, P. Taalas, J. Austin, N. Butchart, and M. Kulmala (2007), A chemistry-transport model simulation of middle atmospheric ozone from 1980 to 2019 using coupled chemistry GCM winds and temperatures, *Atmos. Chem. Phys.*, *7*, 2165–2181.

Funke, B., et al. (2011), Composition changes after the "Halloween" solar proton event: The High-Energy Particle Precipitation in the Atmosphere (HEPPA) model versus MIPAS data intercomparison study, *Atmos. Chem. Phys.*, *11*, 9089–9139, doi:10.5194/acp-11-9089-2011.

Funke, B., M. López-Puertas, G. P. Stiller, and T. von Clarmann (2014a), Mesospheric and stratospheric NO_y produced by energetic particle precipitation during 2002–2012, *J. Geophys. Res. Atmos.*, *119*, 4429–4446, doi:10.1002/2013JD021404.

Funke, B., M. López-Puertas, L. Holt, C. E. Randall, G. P. Stiller, and T. von Clarmann (2014b), Hemispheric distributions and interannual variability of NO_y produced by energetic particle precipitation in 2002–2012, *J. Geophys. Res. Atmos.*, *119*, 13,565–13,582, doi:10.1002/2014JD022423.

Grenfell, J. L., R. Lehmann, P. Mieth, U. Langematz, and B. Steil (2006), Chemical reaction pathways affecting stratospheric and mesospheric ozone, *J. Geophys. Res.*, *111*, D17311, doi:10.1029/2004JD005713.

Holt, L. A., C. E. Randall, E. D. Peck, D. R. Marsh, A. K. Smith, and V. L. Harvey (2013), The influence of major sudden stratospheric warming and elevated stratopause events on the effects of energetic particle precipitation in waccm, *J. Geophys. Res. Atmos.*, *118*, 11,636–11,646, doi:10.1002/2013JD020294.

Jackman, C. H., M. T. DeLand, G. J. Labow, E. L. Fleming, D. K. Weisenstein, M. K. W. Ko, M. Sinnhuber, and J. M. Russell (2005), Neutral atmospheric influences of the solar proton events in October–November 2003, *J. Geophys. Res.*, *110*, A09S27, doi:10.1029/2004JA010888.

Jackman, C. H., et al. (2008), Short- and medium-term atmospheric constituent effects of very large solar proton events, *Atmos. Chem. Phys.*, *8*, 765–785, doi:10.5194/acp-8-765-2008.

Jackman, C. H., D. R. Marsh, F. M. Vitt, R. R. Garcia, C. E. Randall, E. L. Fleming, and S. M. Frith (2009), Long-term middle atmospheric influence of very large solar proton events, *J. Geophys. Res.*, *114*, D11304, doi:10.1029/2008JD011415.

Jackman, C. H., C. E. Randall, V. L. Harvey, S. Wang, E. L. Fleming, M. López-Puertas, B. Funke, and P. F. Bernath (2014), Middle atmospheric changes caused by the January and March 2012 solar proton events, *Atmos. Chem. Phys.*, *14*, 1025–1038, doi:10.5194/acp-14-1025-2014.

Kvissel, O.-K., Y. J. Orsolini, F. Stordal, I. S. A. Isaksen, and M. L. Santee (2012), Formation of stratospheric nitric acid by a hydrated ion cluster reaction: Implications for the effect of energetic particle precipitation on the middle atmosphere, *J. Geophys. Res.*, *117*, D16301, doi:10.1029/2011JD017257.

Kylling, A., A. Albold, and G. Seckmeyer (1997), Transmittance of a cloud is wavelength—Dependent in the UV-range: Physical interpretation, *Geophys. Res. Lett.*, *24*(4), 397–400, doi:10.1029/97GL00111.

Laeng, A., et al. (2014), Validation of MIPAS IMK/IAA V5R_O3_224 ozone profiles, *Atmos. Meas. Tech.*, *7*(11), 3971–3987, doi:10.5194/amt-7-3971-2014.

Langematz, U., M. Kunze, K. Kruger, K. Labitzke, and G. L. Roff (2003), Thermal and dynamical changes of the stratosphere since 1979 and their link to ozone and CO_2 changes, *J. Geophys. Res.*, *104*(D1), 4027, doi:10.1029/2002JD002069.

Lawrence, Z. D., G. L. Manney, K. Minschwaner, M. L. Santee, and A. Lambert (2015), Comparisons of polar processing diagnostics from 34 years of the ERA-Interim and MERRA reanalyses, *Atmos. Chem. Phys.*, *15*, 3873–3892, doi:10.5194/acp-15-3873-2015.

Limpasuvan, V., J. H. Richter, Y. J. Orsolini, F. Stordal, and O.-K. Kvissel (2012), The roles of planetray and gravity waves during a major stratospheric sudden warming as characterized in WACCM, *J. Atmos. Sol. Terr. Phys.*, *78–79*, 84–98, doi:10.1016/j.jastp.2011.03.004.

Livesey, N. J., et al. (2015), EOS MLS Version 4.2x Level 2 data quality and description document, *JPL D-33509*, Jet Propul. Lab., California Inst. Technol., Pasadena, Calif.

López-Puertas, M., B. Funke, S. Gil-López, T. von Clarmann, G. P. Stiller, M. Höpfner, S. Kellmann, H. Fischer, and C. H. Jackman (2005), Observation of NO_x enhancement and ozone depletion in the Northern and Southern Hemispheres after the October–November 2003 solar proton events, *J. Geophys. Res.*, *110*, A09S43, doi:10.1029/2005JA011050.

Lu, H., M. J. Jarvis, and R. Hibbins (2008), Possible solar wind effect on the northern annular mode and Northern Hemispheric circulation during winter and spring, *J. Geophys. Res.*, *113*, D23104, doi:10.1029/2008JD010848.

Manney, G. L., et al. (2008), The evolution of the stratopause during the 2006 major warming: Satellite data and assimilated meteorological analyses, *J. Geophys. Res.*, *113*, D11115, doi:10.1029/2007JD009097.

Manney, G. L., M. J. Schwartz, K. Krüger, M. L. Santee, S. Pawson, J. N. Lee, W. H. Daffer, R. A. Fuller, and N. J. Livesey (2009), Aura Microwave Limb Sounder observations of dynamics and transport during the record-breaking 2009 Arctic stratospheric major warming, *Geophys. Res. Lett.*, *36*, L12815, doi:10.1029/2009GL038586.

Martineau, P., and S.-W. Son (2010), Quality of reanalysis data during stratospheric vortex weakening and intensification events, *Geophys. Res. Lett.*, *37*, L22801, doi:10.1029/2010GL045237.

Matsuno, T. (1971), A dynamical model of the sudden stratospheric warming, *J. Atmos. Sci.*, *28*, 1479–1494.

Newman, P. A., and E. R. Nash (2005), The unusual Southern Hemisphere stratosphere winter of 2002, *J. Atmos. Sci*, *62*, 614–628, doi:10.1175/JAS-3323.1.

Orsolini, Y. J., J. Urban, D. P. Murtagh, S. Lossow, and V. Limpasuvan (2010), Descent from the polar mesosphere and anomalously high stratopause observed in 8 years of water vapor and temperature satellite observations by the odin sub-millimeter radiometer, *J. Geophys. Res.*, *115*, D12305, doi:10.1029/2009JD013501.

Päivärinta, S.-M., A. SeppäLä, M. E. Andersson, P. T. Verronen, L. ThöLix, and E. KyröLä (2013), Observed effects of solar proton events and sudden stratospheric warmings on odd nitrogen and ozone in the polar middle atmosphere, *J. Geophys. Res. Atmos.*, *118*, 6837–6848, doi:10.1002/jgrd.50486.

Randall, C. E., et al. (2005), Stratospheric effects of energetic particle precipitation in 2003–2004, *Geophys. Res. Lett.*, *32*, L05802, doi:10.1029/2004GL022003.

Randall, C. E., V. L. Harvey, D. E. Siskind, J. France, P. F. Bernath, C. D. Boone, and K. A. Walker (2009), NO_x descent in the Arctic middle atmosphere in early 2009, *Geophys. Res. Lett.*, *36*, L18811, doi:10.1029/2009GL039706.

Rienecker, M. M., et al. (2011), MERRA: NASA's modern-era retrospective analysis for research and applications, *J. Clim.*, *24*, 3624–3648, doi:10.1175/JCLI-D-11-00015.1.

Rozanov, E., L. Callis, M. Schlesinger, F. Yang, N. Andronova, and V. Zubov (2005), Atmospheric response to NO_y source due to energetic electron precipitation, *Geophys. Res. Lett.*, *32*, L14811, doi:10.1029/2005GL023041.

Rozanov, E., M. Calisto, T. Egorova, T. Peter, and W. Schmutz (2012), The influence of precipitating energetic particles on atmospheric chemistry and climate, *Surv. Geophys.*, *33*, 483–501, doi:10.1007/s10712-012-9192-0.

Salmi, S.-M., P. T. Verronen, L. Thölix, E. Kyrölä, L. Backman, A. Y. Karpechko, and A. Seppälä (2011), Mesosphere-to-stratosphere descent of odd nitrogen in February–March 2009 after sudden stratospheric warming, *Atmos. Chem. Phys.*, *11*, 4645–4655, doi:10.5194/acp-11-4645-2011.

Sander, S. P., et al. (2006), Chemical kinetics and photochemical data for use in atmospheric studies, *Eval. Num. 15, JPL Publ. 06-2*, Jet Propulsion Lab., Calif. Inst. of Tech., Pasadena, Calif.

Santee, M. L., et al. (2007), Validation of the aura microwave limb sounder HNO_3 measurements, *J. Geophys. Res.*, *112*, D24S40, doi:10.1029/2007JD008721.

Semeniuk, K., J. C. McConnell, and C. H. Jackman (2005), Simulation of the October–November 2003 solar proton events in the CMAM GCM: Comparison with observations, *Geophys. Res. Lett.*, *32*, L15S02, doi:10.1029/2005GL022392.

Seppälä, A., P. T. Verronen, E. Kyrölä, S. Hassinen, L. Backman, A. Hauchecorne, J. L. Bertaux, and D. Fussen (2004), Solar proton events of October–November 2003: Ozone depletion in the Northern Hemisphere polar winter as seen by GOMOS/Envisat, *Geophys. Res. Lett.*, *31*, L19107, doi:10.1029/2004GL021042.

Seppälä, A., M. A. Clilverd, C. J. Rodger, P. T. Verronen, and E. Turunen (2008), The effects of hard-spectra solar proton events on the middle atmosphere, *J. Geophys. Res.*, *113*, A11311, doi:10.1029/2008JA013517.

Seppälä, A., H. Lu, M. A. Clilverd, and C. J. Rodger (2013), Geomagnetic activity signatures in wintertime stratosphere wind, temperature, and wave response, *J. Geophys. Res. Atmos.*, *118*, 2169–2183, doi:10.1002/jgrd.50236.

Smith, A. K. (1995), Numerical simulation of global variations of temperature, ozone, and trace species in the stratosphere, *J. Geophys. Res.*, *100*, 1253–1269, doi:10.1029/94JD02395.

Smith, A. K., M. López-Puertas, M. García-Comas, and S. Tukiainen (2009), SABER observations of mesospheric ozone during NH late winter 2002–2009, *Geophys. Res. Lett.*, *36*, L23804, doi:10.1029/2009GL040942.

Sofieva, V. F., N. Kalakoski, P. T. Verronen, S.-M. Päivärinta, E. Kyrölä, L. Backman, and J. Tamminen (2012), Polar-night O_3, NO_2 and NO_3 distributions during sudden stratospheric warmings in 2003–2008 as seen by GOMOS/Envisat, *Atmos. Chem. Phys.*, *12*, 1051–1066, doi:10.5194/acp-12-1051-2012.

Solomon, S., P. J. Crutzen, and R. G. Roble (1982), Photochemical coupling between the thermosphere and the lower atmosphere 1. Odd nitrogen from 50 to 120 km, *J. Geophys. Res.*, *87*, 7206–7220.

Thompson, D. W. J., M. P. Baldwin, and S. Solomon (2005), Stratospher–troposphere coupling in the Southern Hemisphere, *J. Atmos. Sci.*, *62*, 708–715, doi:10.1175/JAS-3321.1.

Verronen, P. T., and R. Lehmann (2013), Analysis and parameterisation of ionic reactions affecting middle atmospheric HO_x and NO_y during solar proton events, *Ann. Geophys.*, *31*, 909–956, doi:10.5194/angeo-31-909-2013.

Verronen, P. T., and R. Lehmann (2015), Enhancement of odd nitrogen modifies mesospheric ozone chemistry during polar winter, *Geophys. Res. Lett.*, *42*, 10,445–10,452, doi:10.1002/2015GL066703.

Verronen, P. T., A. Seppälä, M. A. Clilverd, C. J. Rodger, E. Kyrölä, C.-F. Enell, T. Ulich, and E. Turunen (2005), Diurnal variation of ozone depletion during the October–November 2003 solar proton events, *J. Geophys. Res.*, *110*, A09S32, doi:10.1029/2004JA010932.

Verronen, P. T., A. Seppälä, E. Kyrölä, J. Tamminen, H. M. Pickett, and E. Turunen (2006), Production of odd hydrogen in the mesosphere during the January 2005 solar proton event, *Geophys. Res. Lett.*, *33*, L24811, doi:10.1029/2006GL028115.

Verronen, P. T., M. L. Santee, G. L. Manney, R. Lehmann, S.-M. Salmi, and A. Seppälä (2011), Nitric acid enhancements in the mesosphere during the January 2005 and December 2006 solar proton events, *J. Geophys. Res.*, *116*, D17301, doi:10.1029/2011JD016075.

von Clarmann, T., B. Funke, M. López-Puertas, S. Kellmann, A. Linden, G. P. Stiller, C. H. Jackman, and V. L. Harvey (2013), The solar proton events in 2012 as observed by MIPAS, *Geophys. Res. Lett.*, *40*, 2339–2343, doi:10.1002/grl.50119.

Waters, J. W., et al. (2006), The Earth Observing System Microwave Limb Sounder (EOS MLS) on the Aura satellite, *IEEE Trans. Geosci. Remote Sens.*, *44*, 1075–1092, doi:10.1109/TGRS.2006.873771.